# PARAMETERS DEFINING FLOW RESISTANCE AND THE FRICTION FACTOR BEHAVIOR IN LIQUID ANNULAR SEALS WITH DELIBERATELY ROUGHENED SURFACES

A Dissertation

by

LARRY ALFONSO VILLASMIL URDANETA

Submitted to the Office of Graduate Studies of
Texas A&M University
in partial fulfillment of the requirements for the degree of

DOCTOR OF PHILOSOPHY

August 2006

Major Subject: Mechanical Engineering

# PARAMETERS DEFINING FLOW RESISTANCE AND THE FRICTION FACTOR BEHAVIOR IN LIQUID ANNULAR SEALS WITH DELIBERATELY ROUGHENED SURFACES

A Dissertation

by

LARRY ALFONSO VILLASMIL URDANETA

Submitted to the Office of Graduate Studies of
Texas A&M University
in partial fulfillment of the requirements for the degree of

DOCTOR OF PHILOSOPHY

Approved by:

| | |
|---|---|
| Co-Chairs of Committee, | Dara W. Childs |
| | Hamn-Ching Chen |
| Committee Members, | Gerald L. Morrison |
| | Alí Beskök |
| Head of Department, | Dennis L. O'Neal |

August 2006

Major Subject: Mechanical Engineering

# ABSTRACT

Parameters Defining Flow Resistance and the Friction Factor Behavior in Liquid Annular Seals with Deliberately Roughened Surfaces. (August 2006)

Larry Alfonso Villasmil Urdaneta, B.S., Universidad del Táchira, Venezuela;

M.S., Texas A&M University

Co-Chairs of Advisory Committee: Dr. Dara W. Childs
Dr. Hamn-Ching Chen

Non-contacting annular seals are internal sealing devices used in rotating machinery, such as multistage centrifugal pumps and compressors. Their design affects both efficiency and rotor stability. Traditional plain and labyrinth seals are being replaced with stators containing different roughness patterns to reduce leakage and enhance rotor response. Several roughened seal experiments with liquid and air have produced leakage data indicating that the friction factor increases as the seal clearance is increased. Simplified models based on bulk flow theory and Moody's approach to characterize wall friction in pipes cannot explain this outcome.

This research is an extension of a 2-D numerical analysis of flat plate experiments with water which found that friction factor of these surfaces is governed by the roughness' ability to develop high static pressures. An exhaustive 3-D numerical analysis of several experiments with liquid annular seals has been performed using a CFD code. Direct numerical simulations (DNS) of turbulent channel flow and smooth seals were replicated within 1% using Reynolds-averaged Navier-Stokes (RANS) equations and turbulence modeling. Similarly, measured groove seal leakage rates were reproduced within 2%. On the other hand, no turbulence model combination predicts the leakage in most 3-D pattern roughened seals with the same accuracy. Present results reproduce the friction factor 'plateau' behavior predicted with the 2-D analysis and observed in the flat plate experiments. They also reproduce the friction-factor-to-clearance indifference behavior, the maximum friction factor observed in a specific roughness pattern size is independent of the

actual clearance in a certain Reynolds number range, but clarify the role of the roughness length-to-clearance ratio and the actual roughness size in defining the friction-factor-to-clearance proportionality.

All simulations indicate that roughened surface area and roughness aspect ratios are the parameters defining the friction factor at a given seal clearance. The roughness pattern size, relevant in determining the friction-factor-to-clearance proportionality, plays a moderate role once the above cited ratios are defined. In any shape and size, shallow patterns are predicted and observed to provide larger friction factors than deep patterns. Predictions also confirm limited experimental data showing that friction factor is affected by the mean flow orientation relative to the roughness pattern.

Solving RANS equations is sufficient to model simple seal geometries but might not be enough to replicate turbulent flow in liquid annular seals with roughened surfaces.

# DEDICATION

To the infinite source of wisdom and understanding…

"God does not play dice"

Albert Einstein

To Gladys, an exceptional human being, mother, my first teacher and best mentor...

To Yanelys, my wife, who has supported me unconditionally in this journey…

…a journey that I started alone while leaving her in a hospital bed, soon after losing our first conceived soul…a brave 25-week term boy that lived for several minutes desperately trying to simply be able to breathe…Lawrence Abraham…

In his memory…

# ACKNOWLEDGEMENTS

I would like to thank my committee co-chairs, Dr. Dara W. Childs, his support and encouragement was crucial, and Dr. Hamn-Ching Chen, his guidance was enlightening.

Thanks to all my friends in the Turbomachinery Laboratory, a truly special place to do research…particularly to Eddie Denk, the soul behind the smooth operation of the Laboratory facilities…

I would also like to acknowledge the support of the Advanced Research and Technology Program of the Texas Engineering Experiment Station.

Lastly, thanks to all the friends, students, and faculty I have the opportunity to interact with. In Aggie land, I have been able to pursue numerical modeling in one of the most challenging subject in fluid dynamics…turbulence.

# TABLE OF CONTENTS

# TABLE OF CONTENTS (cont.)

# LIST OF FIGURES

# LIST OF FIGURES (cont.)

# LIST OF FIGURES (cont.)

# LIST OF FIGURES (cont.)

# LIST OF FIGURES (cont.)

# LIST OF FIGURES (cont.)

# LIST OF FIGURES (cont.)

# LIST OF FIGURES (cont.)

# LIST OF FIGURES (cont.)

# LIST OF FIGURES (cont.)

# LIST OF TABLES

# NOMENCLATURE

| | |
|---|---|
| $\alpha$ | loss coefficient, -. |
| B | groove depth, mm. |
| $\beta$ | linear pressure gradient, total loss coefficient ($\alpha_I + \alpha_E$), Pa/m, -. |
| $C_r$ | radial clearance, mm, μm. |
| d | roughness pattern depth, mm. |
| $\varepsilon$, $\lvert\varepsilon\rvert$ | turbulent dissipation, relative error magnitude, $m^2/s^3$, -. |
| F | Force, N. |
| $F_S$ | safety factor (the GCI of Roache [31]), -. |
| $f$, $\bar{f}$ | friction factor, function, friction factor ratio, -. |
| $\phi$ | flow field variable, diameter, -, m. |
| $\Gamma$ | roughened surface are ratio, %. |
| h | head, grid size, m, μm. |
| k | turbulent kinetic energy, $m^2/s^2$. |
| L, l | generic length, roughness pattern length, mm. |
| $\dot{m}$ , $\overline{m}$ | mass flow rate, mass flow rate ratio, kg/s, -. |
| $\mu$ | dynamic viscosity, cPoise. |
| N | Number, -. |
| P, $\widetilde{P}$ | pressure, periodic static pressure, Pa. |
| p | observed order of convergence, -. |
| $\Delta$P, $\overline{P}$ | pressure gradient, pressure gradient ratio, Pa/m, -. |
| Q | volumetric flow rate, $m^3/s$. |
| R, r | numeric residual, grid size ratio, radius, -, m. |
| Re,$R_n$ | Reynolds number, -. |
| $\rho$ | Density, $kg/m^3$. |
| $\tau_w$ | wall shear stress, Pa. |
| $u_\tau$ | friction velocity, $\sqrt{\tau_w/\rho}$ , m/s. |
| $U^+$, $U^*$ | mean flow velocity normalized by the friction velocity [24], -. |

# NOMENCLATURE (cont.)

| | |
|---|---|
| u | x-coordinate velocity component, m/s. |
| V, $\overline{V}$ ,v | flow velocity, averaged mean flow velocity, y coordinate velocity component, m/s. |
| ν, ν* | kinematic viscosity, wall friction velocity, $m^2/s$, m/s. |
| w | z-coordinate velocity component, roughness pattern width, m/s, m. |
| x | stream wise coordinate. |
| y | vertical coordinate, distance from the wall. |
| $y^+$, $y^*$ | wall units [24]. |
| z | span wise coordinate. |

Subscripts

| | |
|---|---|
| E | exit. |
| F | friction. |
| g | groove. |
| I | inlet. |
| l | losses, per unit length. |
| N | number in a sequence. |
| O | outlet. |
| p | Pattern. |
| R | rotor. |
| ref | reference. |
| S | seal. |
| T | total (subscript). |

Acronyms

| | |
|---|---|
| DNS | Direct Numerical Simulation |
| EWT | Enhanced Wall Treatment |
| GCI | Grid Convergence Index |
| PISO | Pressure-Implicit with Splitting of Operators |

## NOMENCLATURE (cont.)

| | |
|---|---|
| PRESTO | Pressure Staggering Option |
| RANS | Reynolds-averaged Navier-Stokes equations |
| SIMPLEC | Semi-Implicit Method for Pressure-Linked Equations Consistent |
| RNG | Re-normalization Group Theory k-ε turbulence model |
| RSM | Reynolds Stress Model |
| STD | Standard k-ε turbulence model |
| SWF | Standard Wall Functions |
| TLZ | Two Layer Zonal turbulence model |

# 1. INTRODUCTION

Non-contacting annular seals are internal sealing devices normally used in a wide range of rotating machinery, including multistage centrifugal pumps and compressors. Their design affects both machinery performance and rotor stability. From a rotor dynamics perspective, long seals affect rotor stability the most; therefore manufacturers and researchers focus their attention on the balance piston of straight-through machines and central seals of back-to-back arrangements. The internal surfaces of these long seals (L/D > 1) are frequently smooth in pumps and stepped- or labyrinth-like in compressors. Manufacturing standards regulate seal clearances and a typical clearance-to-radius ratio, Cr/R, is around 0.002.

The stator to rotor interaction in annular seals is normally estimated with a linear reaction-force/seal-motion model that is valid for small motions about a centered position, Childs [1]. To estimate the coefficients of this linear model for a particular seal, traditional theoretical analyses use the bulk-flow approach, which was originally developed by Hirs [2] to predict the behavior of turbulent hydrodynamic bearings. These bulk-flow models use averaged values across the clearance for fluid pressure and flow velocities, while the wall shear stress is the only energy dissipation mechanism and is defined in terms of the wall friction factor. Bulk-flow models provide reasonable predictions for plain, smooth seals for either parallel seal displacements or combined displacement and tilting, Childs [1], and they are still in use for day-to-day rotor dynamic stability analysis, Moore [3]. Based on the simplicity of the method, several authors have made contributions to the bulk-flow approach; most recently, Arghir and Frene [4] extended the analysis of Florjancic [5] to analyze an eccentric circumferentially grooved liquid annular seal. Their leakage predictions agreed well with the experiments of Marquette and Childs [6], within 2.5%, while tuning empirical coefficients for zero eccentricity. On the other hand, dynamic coefficients are either over or under predicted ranging from 20% up to 120%.

To reduce leakage and enhance rotor response, plain and labyrinth seals are sometimes being replaced with stators containing different combinations of roughness patterns. Figure 1 illustrates a gas annular “honeycomb” seal. This seal leaks less than an equivalent labyrinth seal and has shown potential in reducing serious vibration problems and

---

This dissertation follows the style and format of the *International Journal for Numerical Methods in Fluids*.

instabilities. This potential is associated with a dramatic increase in the seal's effective damping. Bulk-flow models predict lower circumferential average velocities in a roughened stator seal; leading to a predicted increase in the threshold speed of instability associated with a reduction in the seal cross-coupled stiffness, and indeed, extending the stable operation range of the machinery. Liquid seals with artificially roughened stators are commonly referred as to "damper" seals, Von Pragenau [7].

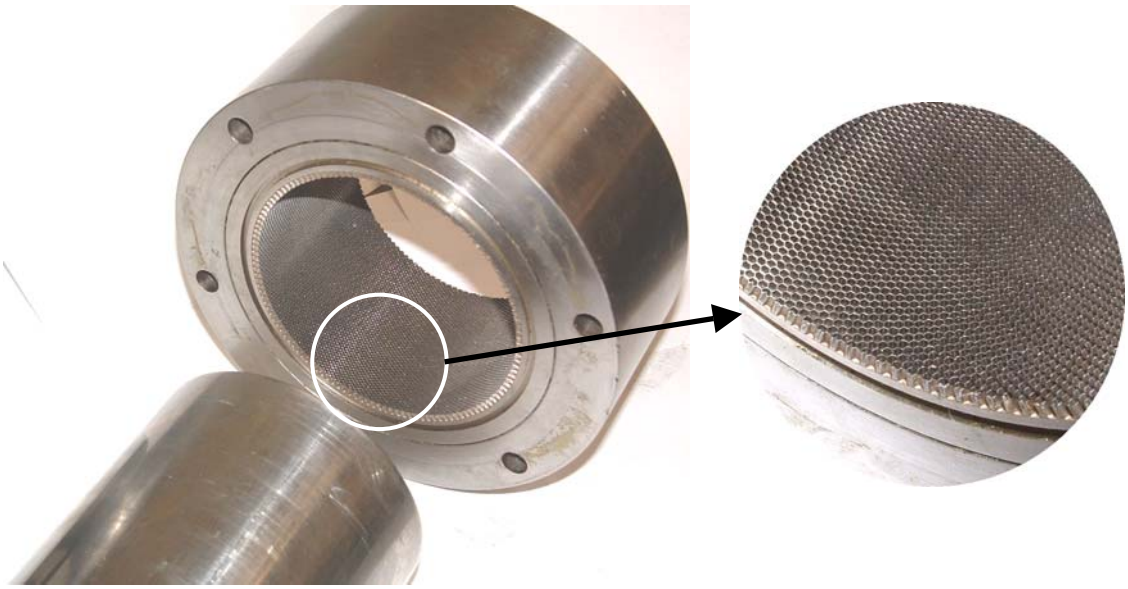

Figure 1. Honeycomb-stator seal with a smooth-rotor [1].

Experimental tests of Childs and Fayolle [8] in 1999 confirmed that damper seals have smaller cross-coupled stiffness values, but they also found that the direct stiffness coefficient or centering force is also considerably reduced and sometimes becomes even negative. To explain this outcome, they introduced a perturbation model for the friction factor, separately accounting for the contributions of the mean flow Reynolds number and the actual clearance of the seal. Moody's friction data diagram for pipe flow shows that the total effect is additive in all turbulent cases. Therefore, a bulk-flow theory based on Moody's data predicts a decrease in the friction factor as the seal clearance is increased due to both effects, namely, an increase in the Reynolds number and a decrease in the relative roughness. But the leakage data [8] showed that the contribution of increasing the clearance, reducing the relative roughness, is positive and opposes the decreasing effect on

the friction factor of a higher Reynolds number in the loose side of the seal, for reasonable clearance ranges. Because the net effect is reduced, the friction factor changes little, and the ability of the seal to develop the restoring force is reduced. Analysis using this data also predicted that this term accounts for most of the stabilizing effect of the damper seal, versus the conventional view that roughnesses primarily reduce the fluid rotation. Separate flat-plate test results by Ha and Childs [9] in 1992 for air, and DeOtte et al. [10] in 1994 for water, had already shown the positive contribution of an increasing clearance in the friction factor perturbation model. More recent static tests of honeycomb annular gas seals, Al-Qutub et al. [11], also show that the friction factor increases with increasing clearance in roughened seals with relatively small clearances.

Acknowledging the shortcomings of the bulk-flow approach to predict the behavior of grooved seals, Dietzen and Nordmann [12] introduced in 1986 a finite difference technique to calculate rotor dynamic coefficients while solving the time averaged Navier-Stokes equations using turbulence modeling within the seal clearance. Their results showed a modest improvement in the predictions of the dynamics coefficients of a plain smooth seal over the bulk-flow results of Childs [13], but deviations were still significant and included trends with rotor speed not observed in the experiments. Their predictions in grooved seals did not include any comparison with experiments. Following Dietzen and Nordmann, Rhode et al. [14] developed in 1992 a finite difference method for determining rotor-dynamic forces on an eccentric whirling labyrinth cavity, assuming that the rotor whirls in a circular orbit about the seal geometric center. Their results are in close agreement with the referenced experiment. In a more recent work, Moore [3] reported in 2001 a three dimensional analysis of gas labyrinth seals. The study used a proprietary CFD code, SCISEAL, a 3-D whirling method developed by Athavale et al. [15], and the experiments of Pelleti [16] as a benchmark case. For a given leakage, the predicted pressure gradient was considerably lower. This discrepancy was attributed to an uncertainty in the actual seal clearance of the original experiment. To match the experimental leakage, simulations were performed with the clearance reduced by 33%. In addition, the upstream and downstream portions of the seal were included in the numerical model to improve the dynamic coefficient predictions. Overall results are better than those obtained with codes based on bulk-flow theory but they are not yet within reasonable margins when compared to the

experimental figures.

While concentrating on leakage only, Schramm et al. [17] studied the influence of the honeycomb facing on the flow through a stepped labyrinth seal, performing several experiments in a 4:1 scaled-up planar model. They analyzed three different clearances, but ran only a numerical simulation of the largest clearance with commercial CFD software. The flow discharge coefficients determined numerically were within 6.8% of the experimental findings.

Introducing an original scaling procedure to treat the compressible flow around repeated geometries as periodic, Chochua [18] thermo-physically modeled the flow within flat plates with smooth and honeycomb-surfaces based on the experimental work of Ha and Childs [9]. He included a comparison of the predicted friction factor against the experimental values for three test cases. The agreement is excellent for the case where both plates were smooth. In a second test case with honeycomb plates, the friction factor is over-predicted from 75% up to 165%. On the other hand, the friction factor is under-predicted from 30% up to 80% in the third test case, with shallower honeycomb plates. Note that in the latter case, the original experiments reported a sudden increase in the friction factor in what it is referred as the "friction factor jump", Ref. 9. Neither this singular observation nor the friction-factor-to-clearance direct proportionality behavior were addressed.

In annular seal applications, the turbulence model combination used to solve the Reynolds-averaged Navier-Stokes equations largely determines the quality of the results for turbulent flows [18,19]. All numerical work cited previously used the standard $k$-$\varepsilon$ approach for turbulence modeling. Even past numerical studies in annular flow [3,17] rely on this first order closure approach to model isotropic turbulence, while some others prefer some variations of it such as the so-called renormalization group $k$-$\varepsilon$ (RNG) or the $k$-$\omega$ model of Wilcox [20]. Recent numerical analyses for turbomachinery flow [21] and wall-bounded flows with separation [22] suggest that second order turbulence closure models are better suited for calculating flows with significant mean streamline curvature, rapid variation, swirling, and presence of secondary flows; all characteristics of the flow in annular seals. In the 2-D numerical analysis [19] of Nava's experiments, observed friction factor trends were better reproduced when using the Reynolds Stress Model [23]. Major drawbacks of using

such models in the 3-D approach are that computational requirements are heavily increased because six additional equations need to be solved The uncertainty in the modeling of closure terms also increases (many of such terms can neither be experimentally measured nor validated), and even grid quality and refinement are more demanding.

Regarding the near wall treatment of turbulence, likewise, most researchers use the wall function method of Launder and Spalding [20]. Only Chochua [18] and Villasmil [19] have recently reported the use of low Reynolds number approaches to model the flow over deliberately roughened surfaces. Chochua [18] compared the performance of this approach against the "low-Reynolds number" model of Chien [24] and found that predictions using the latter are in better agreement with the experiments. Similarly, Villasmil [19] found that predictions obtained with the combination of the two-layer zonal approach [25] and the Reynolds stress model [23] reproduced better the relative behavior of the friction factor within clearances and roughness sizes.

Low-Reynolds number and separation are pervasive effects in fluid flow within this kind of annular seals. The wall function approach is less reliable in such cases. Despite several attempts to develop single turbulence models that are valid all the way to the wall [21], [24], [26], [27], the two-layer formulation introduced by Chen and Patel [25], [28] appears to be the preferred numerical approach when modeling wall-bounded flows is crucial, [22]. Gerolymos [21] introduces a wall-normal-free model by using a pseudo normal direction defined by the gradients of turbulence length scale and anisotropy tensor invariants. Although the model reproduced the relaminarization measured in turbulent channel flow with span wise rotation, it predicted a dependence on the rotation strength for the wall friction velocity not observed in the experiments. Also, the calculated mean velocity profile differed noticeable from the measurements near the inner rotating wall. Also, avoiding using the distance wall as a parameter, Rahman [29] defined an alternative turbulent Reynolds number calculated from the mean velocity, the turbulent kinetic energy, and the modified turbulent dissipation, to slightly improve the skin friction predictions only away from the reattachment location in backward facing step flow. Similarly, Hsieh [22] showed a modest improvement in the predictions for the reattachment length and the Nusselt number on a non-isothermal sudden expansion, by defining the two-layer-model interface by the value of the damping function and not the turbulent Reynolds number.

Major drawbacks of the two-layer formulation are that computational grids need to be fine enough to resolve the laminar sub-layer, and that solutions in the outer layer do not always match with the two-layer formulation, impeding solution convergence [23]. Although high grid resolution near the wall cannot be avoided when using the two-layer formulation, the use of blending functions to match either the turbulent viscosity values predicted by the outer and inner models or the linear (laminar) profile and logarithmic (turbulent) laws-of-the-wall could improve the convergence rate of a given problem. This approach is called "Enhanced Wall Treatment" in Ref. [23].

Computational grid requirements are not determined solely by the restrictions of the turbulence model being used. A numerical solution is said to be grid independent when the errors introduced by the discretization of the governing equations are sufficiently small. In the steady 2-D numerical analysis, Villasmil [19], performed in the symmetry plane of each roughness pattern tested by Nava [30], found grid independent solutions by comparing results obtained in multiple grids, uniform, non-uniform, boundary layer type with different stretching factors, and varying the distance of the first grid point near the wall. Such an ad hoc and labor-intensive approach proved to be prohibitive in terms of time consumed. Extending the numerical analysis to three dimensions would be far more challenging. To be time effective, a more systematic approach is required.

Citing the inconsistent and confusing reporting of grid convergence studies in the engineering and scientific literature, Roache [31] proposed the Grid Convergence Index (GCI) in 1994 for the uniform reporting of grid convergence studies in CFD and related disciplines. This method is based upon a grid convergence error estimator derived from the generalized Richardson extrapolation. Arghir [32] used of this technique when analyzing incompressible, laminar, shear-driven flow over a macro roughness cell. Although special considerations are required for problems involving turbulence modeling [31], the GCI has been successfully utilized to estimate the numerical accuracy for the flow field in a hydraulic turbine draft tube [33]. Even though systematic, the use of the GCI as a global convergence indicator is also laborious. Numerical calculations shall be made with grid resolutions in the asymptotic range. For practical purposes, three grid solutions per case are necessary to determine the rate of convergence and estimate the error. Roache [31] also discuss several single grid calculation error estimators, like the use of higher and lower

order accuracy solutions on the same grid or the convergence study of higher order quadratures.

The present research is an extension of the work "Understanding the Friction Factor Behavior in Liquid Annular Seals with Deliberately Roughened Surfaces, A CFD Approach", Ref. 19, where an extensive numerical analysis in two dimensions of the experiments of Nava [30] and Hess [34] led to the main conclusions that the friction-factor behavior in highly roughened surfaces is governed by the roughness' ability to develop a high static pressure in the trailing face of the roughness cavity, and the maximum friction factor observed in a certain Reynolds number range is barely affected by the actual clearance in a specific roughness pattern size.

In terms of numerical predictions, Villasmil [19] reproduced the shift in proportionality of the friction-factor-to-clearance behavior and the friction-factor plateau phenomenon observed in the original experiments, pointing to the cavity-length to clearance-ratio as the key dimension. On the other hand, friction factor estimations obtained with the 2-D numerical approach clearly over-predicted the values of the experimental data in a range from 60% to 200%, with better agreement in the knurl geometries, i.e., a triangular pattern in two dimensions. At the time, the infinite width 2-D cavity was thought to perturb the flow more than the actual finite size 3-D cavity. Each stream wise plane of a knurl cavity is a "ditch" of different size and could be considered as a linear combination of all sizes. This design probably would damp the span wise turbulence more effectively, therefore promoting a more stable mean flow stream wise recirculation, and the 2-D symmetry approach would be closer to the 3-D reality. In the recess geometry, each stream wise plane has a different length-to-depth ratio, and with a constant depth, the recess should not damp turbulence in the span wise direction as effectively as the knurl, and should promote recirculation in several patterns.

From a modeling perspective, overall results and the analysis included in Ref. [19] indicated that, with all turbulence modeling restrictions fulfilled, the Reynolds stress model predicts higher friction factors than those obtained with any of the k-ε type models, with the so-called renormalization group theory of the latter predicting the lowest friction factor. Nevertheless, predictions obtained with the combination of the former and the two-layer

zonal approach better reproduced the relative behavior of the friction factor within clearances and roughness sizes of the original experiments by Nava [30]. Finally, the wall function approach as near wall treatment of turbulence for this particular flow application was extremely sensitive to the location of the first grid point near the wall, while the two-layer zonal model was more consistent. Predictions did not vary with the location of this point provided it was within 1 and 10 wall units. These results translated into the conclusion that grid independent solutions were not consistently found when using the law of the wall, due to the grid coarseness required to fulfill its modeling restrictions given the low Reynolds number nature of the flow, whereas the consistency of the two-layer zonal approach translates into well-defined grid independent solutions.

Extending the numerical analysis to 3-D was believed to produce better predictions for the friction factor. As seen in the paragraphs above, there is evidence in the literature suggesting that leakage flow and dynamic coefficients predictions for annular seals with roughened walls based on solving the Reynolds averaged Navier Stokes equations improve the estimations of the much simpler bulk-flow approach, but the deviations in terms of absolute values and trending are still significant.

The present research provides an exhaustive numerical evaluation of several experiments with liquid annular seals. Direct numerical simulations of turbulent channel flow at medium Reynolds number [35], and smooth seal experiments at low Reynolds number [36,37] have been replicated within 1%, using the periodic approach in 2-D and 3-D numerical domains with first order closure turbulence models (STD and RNG $k$-$\varepsilon$) and the enhanced wall treatment [23] (equivalent to the two-layer zonal model [25]). These analyses validated using both local refined grids and highly stretched conformal single grids for modeling 3-D roughness patterns when the enhanced wall treatment was used as a near-wall turbulence model. Rectangular groove seal experiments at low Reynolds number [38] were also replicated within 2% using the periodic approach in a 2-D numerical domain with the simplest near-wall treatment, standard wall functions. This analysis validated the original 2-D approach [19] developed to simulate Nava's flat plate tests. On the other hand, using the periodic approach in 3-D numerical domains with any turbulence model combination can not replicate most of the experiments with liquid roughened seals under

scrutiny within the same accuracy in terms of leakage measurements. Indeed, only the results of Childs and Fayolle [8] for the deep pattern at the largest clearance has been duplicated with comparable accuracy.

Numerical results presented herein have been extensively scrutinized for accuracy and consistency. Grid independent results were sought by several methods including the GCI (Grid Convergence Index of Roache [31]). The GCI performed satisfactorily when modeling laminar flow and 2-D turbulent flow with uniform grids designed to be used with standard wall functions. On the other hand, the GCI was not consistent in indicating convergence when applied to grids that were locally refined or created in a boundary layer style to be used with more complex turbulence models, in either 2-D or 3-D numerical domains. Therefore, numerical convergence was established on a case-by-case basis analyzing the relative error of the parameters under study, namely mass flow rate and friction factors. In addition, modeling approaches such as prescribing the stream wise pressure gradient rather than the mass flow rate or the use of periodicity and symmetry as boundary conditions were also validated.

Results include a detailed analysis on the effect of the clearance in the friction factor predictions for the two seal patterns that experimentally provide the larger resistance to flow. While predictions in the smaller pattern indicate that the ‘traditional’ friction factor behavior is expected; namely, decreasing values with increasing clearances, a friction factor ‘plateau’ is predicted for the larger roughness pattern. Coincidentally, this ‘plateau’ is predicted at the intermediate clearance value from the original experiments of Nava [30]. Although larger turbulence levels and static pressure force ratios are predicted at the ‘plateau’ clearance, more research is needed to explain why the ‘plateau’ occurs at this particular clearance, given the uncertainty of the actual data in the original experiments.

2-D and 3-D predictions agree in indicating that the roughened surface area ratio, the actual fraction of the wall occupied by the roughness pattern, and the aspect ratio of the roughness pattern (depth over the stream wise length), are the primary parameters defining the flow resistance, indeed the friction factor, at any given clearance. The actual size of the roughness pattern, although relevant in determining the friction-factor-to-clearance proportionality [19], plays only a moderate role in the actual friction factor once the primary parameters are established. In any shape and size, shallow patterns are predicted to

provide larger friction factors than deep patterns in any Reynolds number range for turbulent flow. On the other hand, a non-fully symmetric pattern (axi-symmetric holes are the only possibility for a fully-symmetric pattern) is predicted to offer significantly different resistance to flow, a.k.a. friction factor, depending on the mean flow incidence angle relative to the pattern orientation at a sufficiently large size.

From a turbulence modeling perspective, most results included herein were obtained by first order closure models (STD and RNG $k$-ε). The Reynolds stress model [23] appears to be extremely sensitive to the larger grid stretching factors required to create reasonably sized conformal grids when using more elaborated near wall turbulence treatment in 3-D numerical domains, as the Reynolds number of the mean flow in the annular clearance of the seal is increased. Contrary to the findings described in the original 2-D numerical analysis[19] of Nava's experiments, current simulations predict comparable trends in the friction-factor-to-clearance proportionality of the two 3-D patterns studied the most with either near-wall approach of turbulence, standard wall functions or the enhanced wall treatment, with the former providing larger friction factors. As already mentioned above, some experiments were better replicated with the enhanced wall treatment and others with the standard wall functions.

What all the literature related to roughened seals modeling cited herein have in common is that leakage in labyrinth and grooved seal experiments is fairly replicated, while leakage in seals with 3-D roughness patterns is significantly either over predicted or under predicted in most cases. Regarding turbulence modeling, most authors propose subtle variations of either the original model of Launder and Spalding [20], or the two-layer zonal model of Chen and Patel [25], where the improvement in the predictions associated with the modifications are moderate at best. In the present research, both approaches were evaluated intensively while analyzing the leakage behavior of several seal experiments and comparing turbulence modeling predictions to direct numerical simulation results to conclude that a fair estimation of the averaged turbulent flow might not be sufficient to replicate the flow field in seals with deliberately roughened surfaces. This outcome is similar to a test case of turbulent flow and heat transfer in a channel with surface mounted cubes that have been a challenge to current Reynolds-averaged Navier-Stokes (RaNS) models [39].

# 2. ANALYSIS IN TWO-DIMENSIONS

This section presents a critical review of the original 2-D modeling approach developed by the author in simulating flat-plate-channel-water-flow experimental tests [19]. This review is driven by the fact that predictions fairly reproduced the friction-factor-to-clearance proportionality and the friction-factor plateau effect but over-predicted the absolute value for the friction factor by 60 to 100% in the knurl geometries, and by 100 to 200% in the recesses or round holes geometries [40]. For validation, pilot simulations on 3-D geometries based on the 2-D domains created for the large knurl and tiny recess patterns [19]. These sizes reflected the friction-factor-to-clearance indifference behavior [19], an overlooked phenomenon present in the original experiments[30]. In addition, recent experimental tests by Ha [41] with roughness geometries comparable to those of Nava [30] were examined.

Likewise, a numerical analysis of the experimental tests of Iwatsubo [38] is included. These tests were performed in seals with square grooved stators and a smooth rotor, and included leakage data with no rotation and the rotor located in the centered position. Indeed, these experiments are an ideal benchmark to validate the author's 2-D modeling approach. Finally, a parametric analysis in the effect on leakage of the groove depth, groove length, and the groove-to-land area ratio, was performed starting from the original seal dimensions of the referenced experiments.

## *2.1. Summary of the original 2-D modeling of Nava's experiments*

Nava's experiments covered five basic flat-plate configurations, smooth against smooth walls, and rough walls with two periodic patterns in two different sizes against a smooth wall. Tests included six clearances per plate configuration. Tested patterns were a half diamond indentation or knurl, and a round cylindrical hole or recess. To depict any possible scale effect, a small and a large size of each pattern was tested. The small size was half of the large size. On the other hand, the actual sizes of each pattern did not overlap. The small recess was bigger than the large knurl by roughly 60 % (recess diameter vs. stream wise knurl length). No reference was given for the selection of the actual physical dimensions.

2-D numerical results fairly reproduced: (i) the friction-factor-to-clearance direct proportionality and plateau behaviors in both knurl sizes, (ii) the fact that friction-factor

values in the large knurl are larger than in any other pattern, and (iii) that both knurls exhibited larger friction factors than both recesses. Although 2-D numerical results in the recesses reproduced the friction-factor-to-clearance direct proportionality behavior, they did not consistently reproduce the plateau behavior, and values predicted in the large recess were lower than those predicted in the small recess, in contradiction to the experimental data.

To better evaluate the predicted trends in the friction factor, two additional sizes per pattern were simulated. Acknowledging the scaling approach of the experiments, new "big" geometries were devised as twice the large ones, and new "tiny" geometries were devised as half the small ones. In the new geometries, the numerical analysis was concentrated in the larger clearances of the original experimental set-up. Friction factor calculation were based on Darcy's definition and the Reynolds number was estimated with twice the clearance as the hydraulic diameter:

$$\mathrm{Re} = \frac{2}{\mu}\dot{m}_l \tag{1}$$

$$f = 4 \cdot \rho \cdot \frac{\Delta P_x}{\dot{m}_l^2} \cdot C_r{}^3 \tag{2}$$

Figures 2 and 3 compare predicted friction factor values of all knurl and recess geometries versus the data of the experimental sizes. As in the original figures, a scaled drawing of each pattern is included on each sub-figure, with horizontal lines showing the largest clearances. Please note that the friction-factor axis scale is linear and not the traditional logarithmic one. These new figures include revised numerical friction-factor data extended to the whole Reynolds number range for all pattern sizes; whereas' the originals included only predictions based strictly on the pressure gradients extracted from the experiments, even for the additional pattern sizes. Following are the most relevant observations extracted from references [19], [40], and [42]:

In the knurl geometries, the large size has the highest friction factor for a clearance equal to or larger than 20 mils (508 μm). The friction factor varies inversely with clearance in the large, small, and tiny sizes for a clearance equal to or larger than 20 mils (508 μm). However, friction factor of 20 and 30 mils (508 and 762 μm) in the small and tiny sizes

seem to merge into a single curve above a certain Reynolds number. In contrast, the friction factor increases with clearance in the big size.

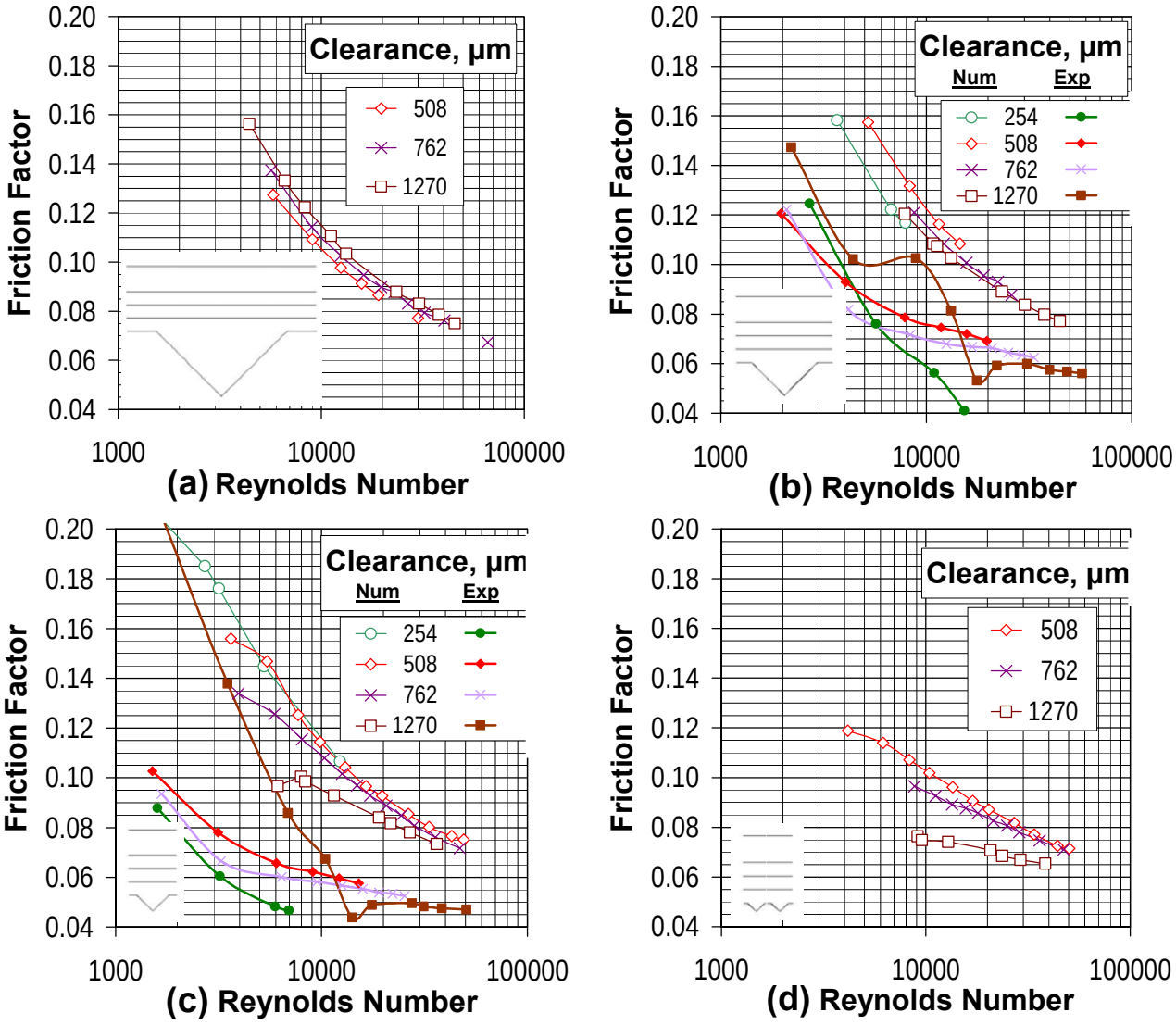


Figure 2. Numerical friction factors in 2-D knurl geometries. (a) Big (b) Large (c) Small (d) Tiny.

In the recess geometries, the tiny size emerges as the pattern with the highest friction factor in every clearance, with the exception of the 50 mils (1270 µm). The friction factor is nearly independent of the clearance in this size for Reynolds number larger than $10^4$. The friction factor increases with clearance in all other sizes. The big size has the lowest friction factor for all clearances. However, friction factor of all clearances in every size seems to

either merge into a single curve above a certain Reynolds number or cross over like in the tiny size.

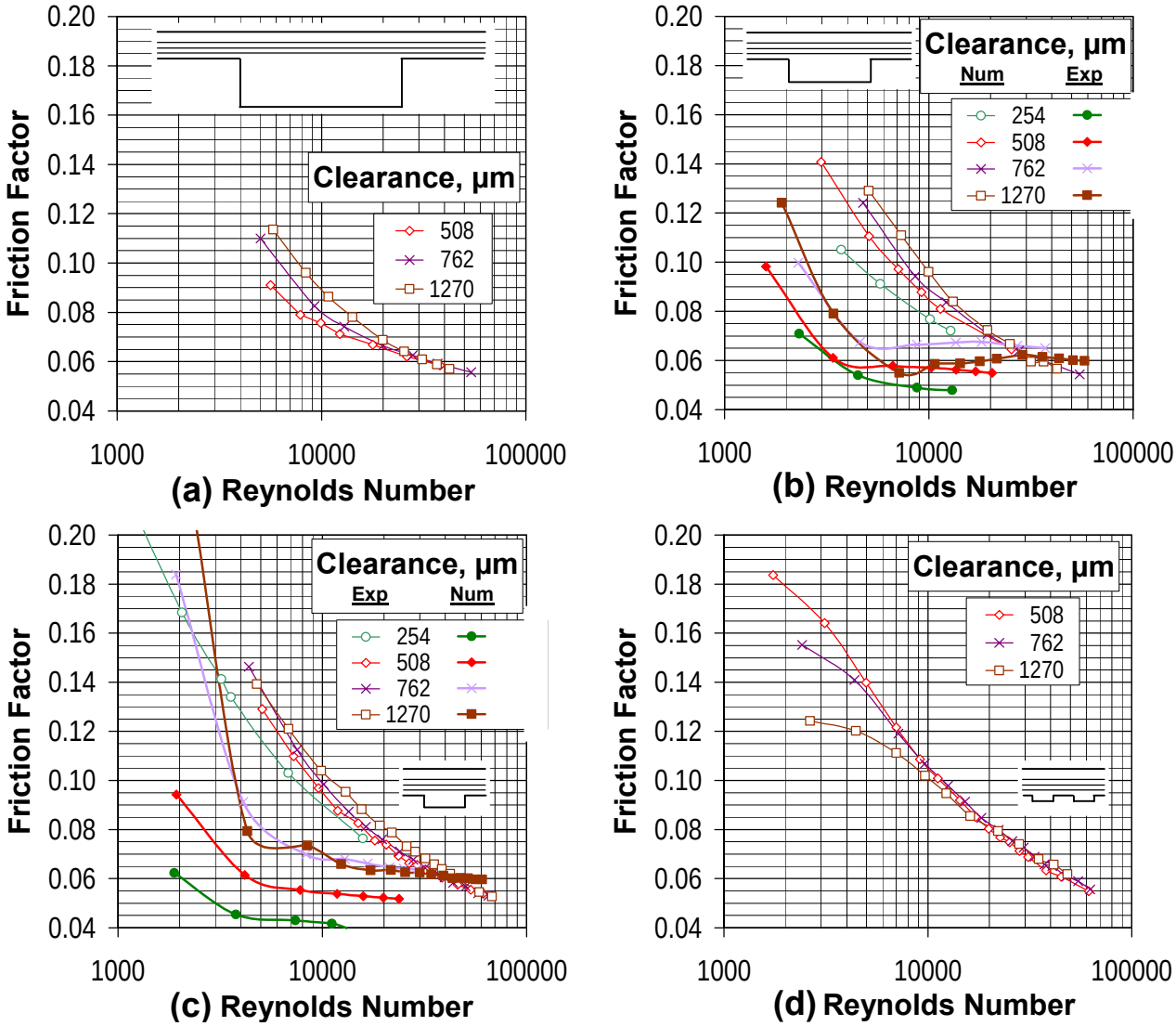


Figure 3. Numerical friction factor in 2-D round-hole geometries. (a) Big (b) Large (c) Small (d) Tiny.

In summary, predictions obtained with the newly proposed sizes of experimental patterns outline a particular trend. For every roughness pattern, the friction factor has a maximum that is insensitive to changes in clearance at a specific pattern size. This behavior was observed in the large size of the knurl pattern and the tiny size of the recess pattern. In a larger pattern size, the friction factor reduces and it decreases as the clearance decreases.

In a smaller pattern size, the friction factor becomes inversely proportional to the clearance, but has less dependence on the clearance, in a given Reynolds number range.

As erratum to the original figures included in reference [19], note that original the predictions were calculated with mass flow rate values derived from the streamline function feature of the CFD software used. By definition, streamlines can be either positive or negative, depending on the location within the domain where the numerical integration of the velocity field is started. The software feature is programmed to present only positive values for the streamlines. In case of recirculation flows that yield negative streamline values, the maximum streamline value is calculated by adding the recirculation flow to the actual mass flow rate. Therefore, original friction-factor predictions were calculated with an "inflated" mass flow rate. Fortunately, deviations did not affect friction factor trends and the main conclusions derived from the original 2-D numerical analysis, although recirculation increases significantly with pattern size and reducing the channel clearance.

Figure 4 repeats the summary of the friction-factor-to-clearance behavior in all numerical geometries, references [19, 40]. Clearances and pattern geometries are drawn to scale. Those with comparable size are depicted side by side, recalling that LR, LK, SR, and SK correspond to the experimental sizes. The expressions on the right summarize the observed behavior of numerical simulation while those on the left, that of the experiments. Relative to the pattern geometry, simulations reproduced the observed friction-factor-to-clearance behavior shifted one size down with the exception of the large size of the recess. The shift down in one size was then attributed to the fact that 2-D simulations might over predict turbulence intensity within the cavities, which indeed are numerically equivalent to a ditch in the knurl cases and to a groove in the recess geometries. Finally, the similarities on the friction-factor predictions of comparable numerical sizes, small recess vs. big knurl and tiny recess vs. large knurl, the original qualitative scaling analysis [19], and the correlation of leakage with groove length to be presented in following sections, indicate that the absence of overlapping in sizes of the original experiments was a drawback because the pattern length plays a dominant role in the friction factor.

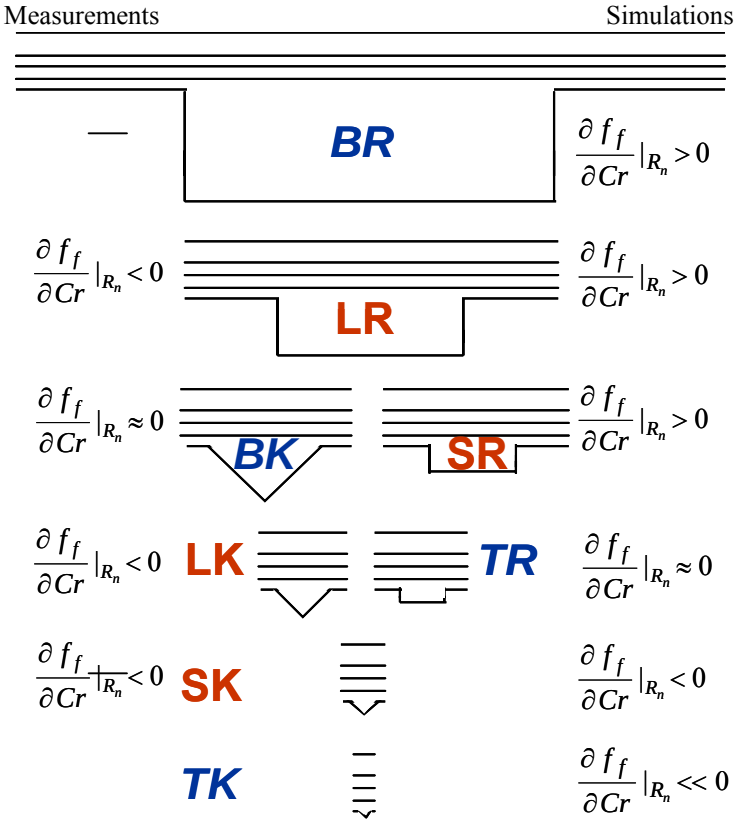


Figure 4. Summary of friction-factor-to-clearance behavior in the 2-D periodic unit geometries.

### *2.2. 3-D validation of the original 2-D modeling*

Extending the 2-D modeling to include the third dimension is not an easy and straightforward task. Initial 3-D simulations were halted due to time constraints plus the success of the 2-D approach in qualitatively reproducing the plateau effect and the friction factor to clearance proportionality [19,42]. Similarly, preliminary results of 3-D simulations for the large knurl and the small recess patterns, to be discussed in the next section, are consistent with the simpler 2-D approach results in over predicting friction factor values.

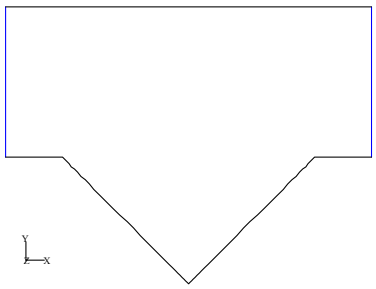

(a) 2-D large knurl geometry

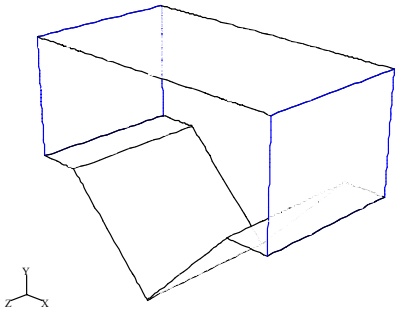

(b) 3-D projection of the 2-D large knurl geometry

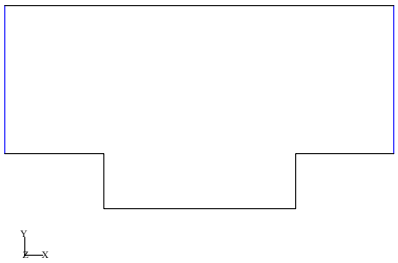

(c) 2-D tiny recess geometry

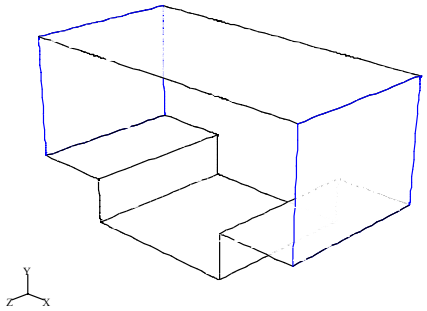

b) 3-D projection of the 2-D tiny recess geometry

Figure 5. Original 2-D geometries and 3-D projections, Nava's experiments, clearance = 762µm (30 mils.)

One simple way to validate the 2-D modeling consistency, numerical approach and CFD software performance, is to project the 2-D periodic unit, the symmetry plane of the roughness pattern, into the third dimension. With this analysis, 3-D predictions should replicate the original 2-D numerical results.

The friction-factor-to-clearance indifference behavior was predicted in the 2-D geometries with comparable size, the large knurl and the tiny recess. Figure 5 presents the original 2-D periodic units of these geometries and their 3-D projections for the 762 µm (30 mils) clearance. This clearance value is the smallest showing the above-mentioned behavior

for both geometries. Simulations are executed with similar numerical parameters, boundary conditions, equal turbulence models, and the projections are based in the 2-D final grid of each original periodic unit. This approach was chosen to assure that numerical results and resultant conclusions address exclusively the effect of the third dimension.

Figure 6 compares the friction factor predictions of the 3-D projections with the original 2-D symmetry plane results. Results correspond to the power law discretization scheme for all variables, the PRESTO scheme for pressure, and the PISO option for the pressure-velocity linking algorithm. The standard k-ε model was used in the core flow with the enhanced wall treatment as near-wall treatment (some of the original 2-D simulations correspond to the two layer zonal model).

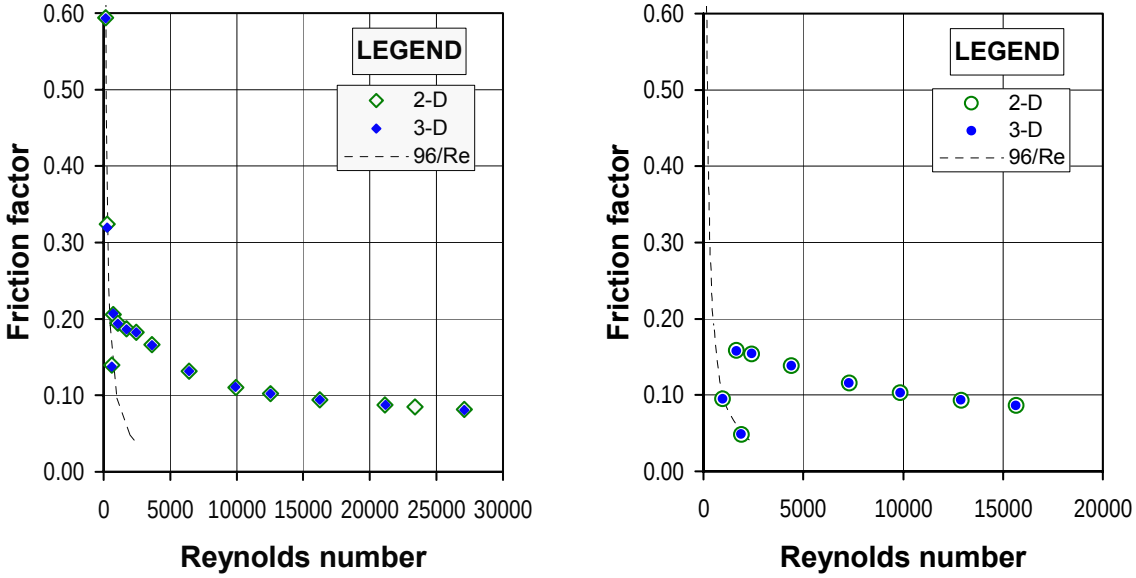


(a) Large knurl geometries (b) Tiny recess geometries

Figure 6. 2-D vs. 3-D projection friction factor predictions, laminar and turbulent flow regimes.

Deviations in predicted friction factor in the large knurl geometries vary from 1.54% in laminar flow to 0.21% in the turbulent regime. Similarly, predicted deviations in the tiny recess geometries vary from 0.57% in laminar flow to 0.31% in the turbulent regime. Prior two-layer zonal results differ from new enhanced wall treatment predictions by 1.85% or less. In summary, the 3-D solver and the 2-D numerical approach developed in [19] are consistent and predict similar results in terms of mass flow rate and friction factors.

### *2.3. How the original 2-D modeling results compare with other experiments*

While looking for explanations about the consistent over-prediction of both 2-D and 3-D modeling approaches, original 2-D numerical predictions [19,40] were discussed with some colleagues, to find out results fairly agree with very recent experimental tests for round-hole roughness surfaces in channel flow where flow range, actual clearances, and geometric characteristics are all comparable to those of the small recess flat plate in Nava's experimental tests [30], see table I. Figure 7 compares the friction factor observations of the latter, the original 2-D modeling results (Reynolds stress and two layer zonal modeling), and the experimental results of Ha [43].

Table I. Roughness pattern dimensions, Nava[30], Ha [40], and 2-D numerical analysis[19]

| Experiment | Pattern | Characteristic length, l | Depth, h | Hole Area, Γ | Clearance, $C_r$ |
|---|---|---|---|---|---|
| Nava | Round-hole | ~ 1.98 | 0.56 | 38.5 % | 0.076 to 1.270 |
| 2-D approach | Groove | 1.98 | 0.56 | 46.6 % | 0.076 to 1.270 |
| Ha | Round-hole | ~ 2.00 | 0.75 | 37.4 % | 0.200 to 0.800 |

Note: all dimensions in mm.--

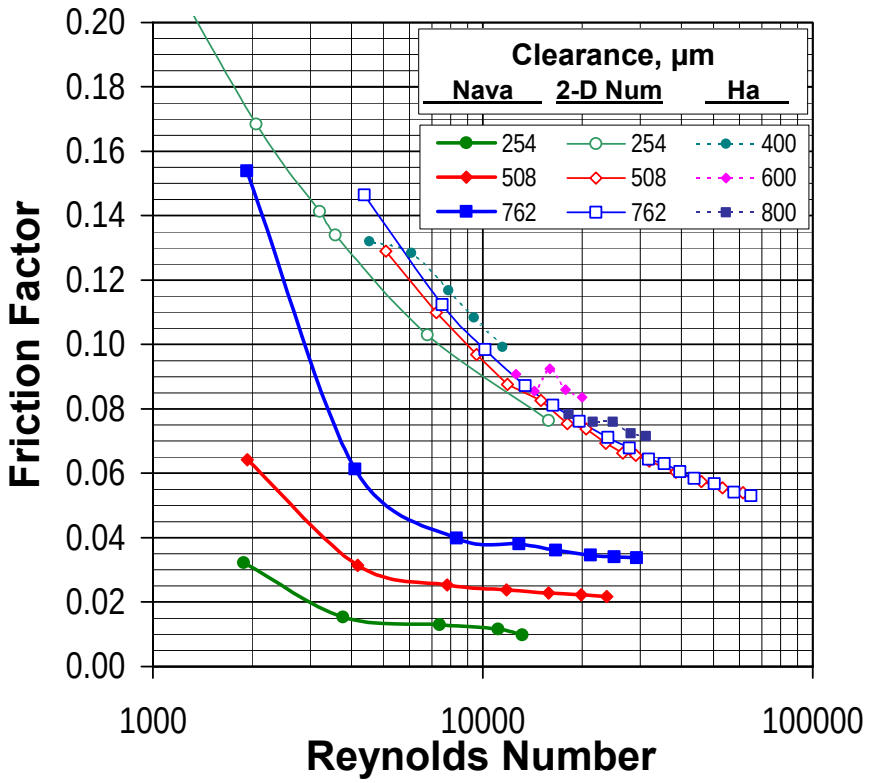


Figure 7. Friction factor in recess pattern geometries, experiments and predictions.

These results raise doubts in the certainty of the original experiments of De Otte [10], Nava [30], and Hess [34], at least in terms of the absolute values. On the other hand, these recent tests by Ha also display a slight dependence on clearance for the friction factor, and even a possible plateau for the 0.6 mm clearance. Nevertheless, the author neglected this bare dependence when modeling the friction factor using a Moody like approach, in spite of the fact that the flow range among tested clearances did not overlap.

Available electronic data and records of the original experiments was again scrutinized to find two inconsistencies. First, actual friction factor equations in Nava's data reduction program are not in agreement with the formulation included in the text[30]. On the other hand, such formulation is in concordance with both Hess' reduction programs and theoretical expressions [34]. Second, friction factor curves for the small and large knurls in the original experiments are strikingly similar for the three largest clearances at Reynolds number above $10^4$. Even pressure measurements along the top plate tabs appear to be directly proportional when comparing corresponding data points. Data sets for both patterns even included the same number of flow points per clearance.

Although remote, the possibility that original data might have been miscalculated can not be discarded. These observations emphasize the importance of recording both primitive variables and post-processed data instead of uniquely recording the latter.

### *2.4. Numerical analysis of a true 2-D experiment*

While looking for explanations about the consistent over-prediction of both modeling approaches, 2-D and 3-D, annular groove seals were examined as a possibly better benchmark to the developed 2-D numerical approach rather than insisting on the data of the original experiments[30].

Following the original numerical approach [19], a leakage analysis of the experiments by Iwatsubo [38] with parallel grooved seals has been performed. Figure 8 shows the basic dimensions of 'Seal 1' and the minimum stream wise periodic unit used for simulations, which were limited to the experimental cases involving no shaft rotation.

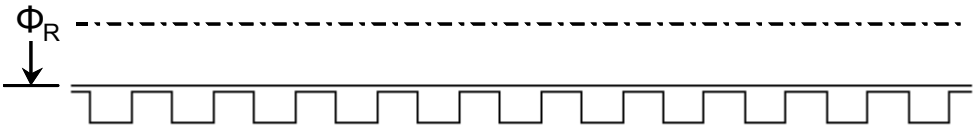


(a) Smooth rotor on a grooved stator (to scale).

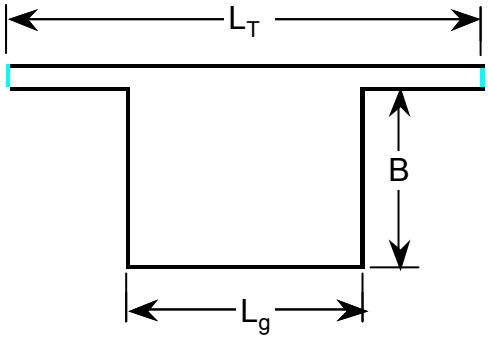


(b) Minimum periodic unit

| | | | |
|---|---|---|---|
| $L_T$ | = | 3.2 | mm |
| Lg | = | 1.6 | mm |
| B | = | 1.2 | mm |
| $\phi_R$ | = | 70.0 | mm |
| Cr | = | 0.175 | mm |
| Ng | = | 11 | |

(c) Dimensions

Figure 8. 'Seal 1' configuration, Iwatsubo [38].

Leakage is predicted within 2% in 'Seal 1' while using wall functions as near wall treatment and the RNG *k*-ε turbulence model for the core flow. On the other hand, leakage in 'Seal 2' is under-predicted by roughly 20%. 'Seal 2' geometry is identical to 'Seal 1' but has twice the length. Figure 9 compares leakage measurements from the experiments against numerical predictions.

From a modeling perspective, only one periodic unit was required to simulate both seals. They are equivalent numerically, and only the pressure gradient imposed on their boundaries differs. Values on 'Seal 2' are half the ones on 'Seal 1'. On the other hand, the

periodic approach requires the a priori knowledge of the pressure gradient within the roughened surfaces of the seal. Without such knowledge, the pressure gradient is estimated as the quotient of the total pressure differences measured in the experiments and each seal length. This approximation is equivalent to assume that inlet and exit losses are negligible, a fair approximation in long seals. L/D ratios are 0.5 in 'Seal 1' and 1.0 in 'Seal 2'.

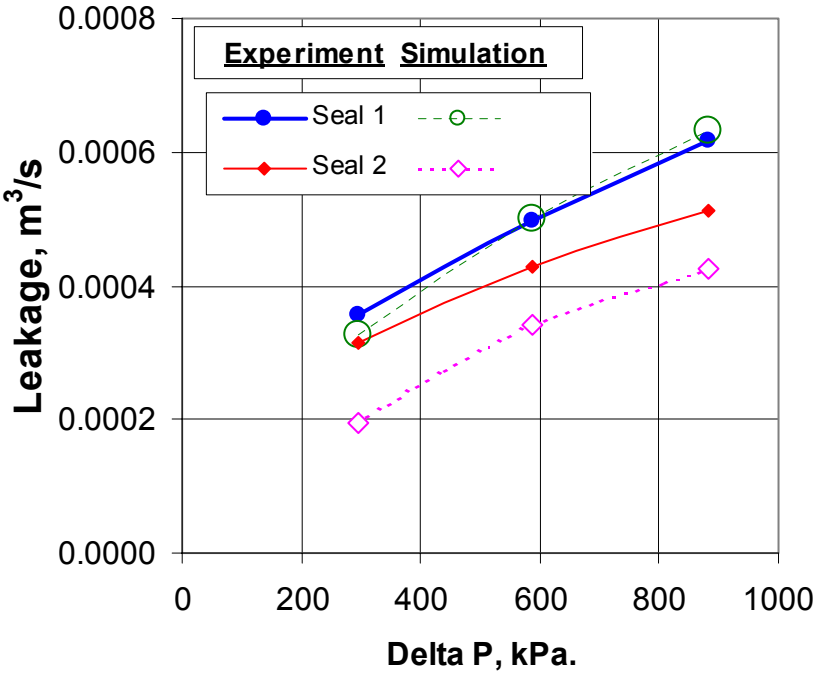


Figure 9. Leakage predictions vs. experiments, groove seals of Iwatsubo [38].

To improve the predictions, the only option is to quantify inlet and exit losses thus refining pressure gradient values. With the data from the experiments, this task can be accomplished in two ways. First, inlet and exit losses can be extracted combining 'Seal 1' and 'Seal 2' results. Secondly, the whole seal can be modeled using a 2-D axisymmetric approach including inlet and exit geometries.

Several numerical tests by the present author and others indicate that the flow reaches the fully developed condition shortly after entering the annulus of a roughened seal. In this seal geometry, the condition is achieved after the flow passes the first groove due to the low Reynolds number nature of the flow in the tests, see section 4.1.1. Under this premise, it is fair to assume that at equal flow rates, the pressure gradient on both seals will be the same

and constant along the whole length of each seal. Following is the formulation used to extract the pressure gradient and inlet/exit losses from the experiments.

The total pressure difference head on each seal can be expressed as:

$$h_{l_T} = h_{l_I} + h_{l_F} + h_{l_E} \tag{3}$$

With the help of Bernoulli's equation and the assumption of constant pressure gradient:

$$h_{l_T} = \frac{P_I - P_O}{\rho} = \alpha_I \cdot \frac{\overline{V}^2}{2} + \frac{1}{\rho} \cdot \left|\frac{\Delta P}{\Delta x}\right| \cdot L_S + \alpha_E \cdot \frac{\overline{V}^2}{2} \tag{4}$$

Combining inlet and exit losses into one term, a two equation system can be formed. The two unknowns are losses coefficient and pressure gradient, for a given mean flow velocity in the overlapped range in both seals experiments.

$$\begin{aligned} (P_I - P_O)_1 &= \beta_N \cdot \overline{V}_N^2 + L_{S_1} \cdot \left|\frac{\Delta P}{\Delta x}\right|_N \\ (P_I - P_O)_2 &= \beta_N \cdot \overline{V}_N^2 + L_{S_2} \cdot \left|\frac{\Delta P}{\Delta x}\right|_N \end{aligned} \tag{5}$$

Where:

$$\beta_N = \frac{\rho}{2} \cdot (\alpha_I + \alpha_E)_N \tag{6}$$

$$\overline{V}_N \cong \frac{Q_N}{\pi \cdot \phi_R \cdot C_r} \tag{7}$$

Using polynomial regression to fit the data in the overlapping flow range of the two seals, calculated ($\alpha_I + \alpha_E$) values vary from 4.84 to 4.09, approximately twice of what it is expected in liquid annular seals [1]; see total losses coefficient in table II. In his analysis, Iwatsubo [38] specified this value as a constant, 2.26 (1.50 + 0.76). A larger total loss coefficient indicates that 'actual' pressure gradient values within the grooved surfaces are much smaller than assumed and estimated as less than half the original differential pressure measured in the experiments; see calculated differential pressure in table II. Simulations on the periodic unit with such reduced pressure gradients would have not been valuable.

An alternative calculation is to estimate the mean $\beta$ value that gives the best correlation for a polynomial fit of the combined pressure gradients versus the mean flow velocity. A linear regression produces the best correlation fit, r = 0.998, resulting in a mean ($\alpha_I$ + $\alpha_E$) value of 4.28. Puzzled by extracting ($\alpha_I$ + $\alpha_E$) values roughly twice of those used by Iwatsubo[38] theoretical analysis, the whole seal configuration was simulated with a 2-D axisymmetric model. On the other hand, actual dimensions of the inlet and exit regions of the actual seal test rig are unknown; therefore, numerical models included few educated guesses. Figure 10 compares two of the 'whole' seal geometries that were evaluated.

Table II. Inlet losses coefficient and pressure gradient, grooved seal experiments of Iwatsubo[38]

| Experiment | | | Analysis | | |
|---|---|---|---|---|---|
| Mean Flow velocity | Seal '1' | Seal '2' | Total losses coefficient | Seal '1' | Seal '2' |
| $\overline{V}_N$ , m/s | Original differential pressure, kPa | | $\beta_N$ , - | Calculated differential pressure, $L_S \cdot \lvert \Delta P / \Delta X \rvert_N$ , kPa. | |
| 13.31 | (622) | 882 | 4.09 | 259.8 | 519.5 |
| 12.93 | 588 | (825) | 4.20 | 237.4 | 474.8 |
| 11.14 | (438) | 588 | 4.64 | 150.3 | 300.6 |
| 9.22 | 294 | (383) | 4.83 | 88.7 | 177.4 |

(second order polynomial interpolation)

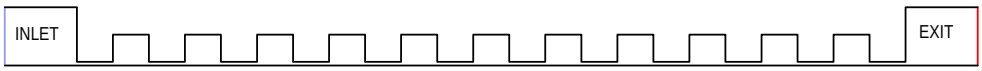


(a) Equal inlet and exit geometries with pressure inlet and outlet boundary conditions

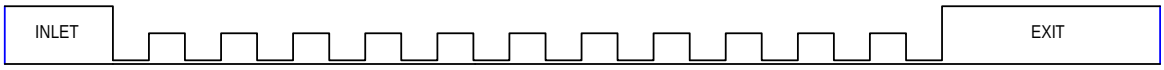


(b) Enlarged inlet and exit geometries with periodic boundary conditions

Figure 10. Whole seal geometry 2-D configuration for the Seal '1' of Iwatsubo[38].

Again, simulations were performed using wall functions and the RNG *k*-ε turbulence model. Leakage predictions and inlet/exit losses coefficient estimates were not affected by the choice of the inlet/exit geometries. Calculated leakage is under-predicted by 10% to 20% when compared to the experimental values and the numerical calculations in the periodic unit of Seal '1'. Contrary to the assumption in the theoretical analysis by Iwatsubo, combined inlet/exit losses coefficients extracted from simulations depend on the mean flow velocity, although values are comparable in magnitude. It was only at very low Reynolds

numbers for laminar flow, that such coefficients reached values larger than 4.0. Table III summarizes calculated inlet/exit losses coefficients, including the theoretical values used by Iwatsubo[38], and the ones extracted from the experiments (Table II) as reference.

Providing a strict explanation of these findings is well beyond the scope of the present research. It shall be mentioned that the experimental analysis did not include a leakage uncertainty analysis, and that a quick review of the data shows an 'outlier' affecting the regressions, lowest Reynolds number is 2800. Indeed, 'Seal 2' could have been operating in a flow regime that was not fully turbulent. Similarly, the fact that calculated pressure gradients and mean flow velocity correlated better with a linear regression is an indication that the flow regimes was note the same in both seals, a linear regression is more consistent with a laminar like regime.

Table III. Inlet losses coefficient from numerical simulations based on the grooved seal of Iwatsubo[38]

| Experiment, Seal '1' | | | | | 'Whole' Seal '1' Simulations | | |
|---|---|---|---|---|---|---|---|
| Original ΔP, kPa | Re | $\overline{V}_N$, m/s | Theory | Extracted | | $\overline{V}_N$, m/s | Re |
| | | | $\beta_N$, - | | | | |
| (17600) | | | | | **1.62** | 44.82 | 25305 |
| (5000) | | | | | **1.68** | 37.25 | 12843 |
| 882 | 5517 | 16.00 | | | **1.73** | 14.37 | 4955 |
| 588 | 4458 | 12.93 | **2.26** | **4.20** | **1.75** | 11.45 | 3949 |
| 294 | 3178 | 9.22 | | **4.83** | **1.83** | 7.39 | 2547 |
| (14) | | | | | **2.67** | 1.43 | 391 |
| (5) | | | | | **4.55** | 0.47 | 161 |
| (1) | | | | | **13.03** | 0.11 | 39 |

(additional values for simulations)

In summary, the original 2-D numerical approach developed in reference [19] reproduced quite well the leakage observed in experiments with groove seals, particularly in the Seal '1' configuration of Iwatsubo[38], where there is certainty in the fully turbulent nature of the flow. In contrast, the inlet-losses analysis performed while combining results from both seal configurations and the friction factor versus Reynolds number behavior indicate that Seal '2', the longer seal configuration, was tested in a condition where the flow inside the seal was not fully turbulent. Therefore, the 2-D numerical approach could be considered as entirely validated, and the constant over-prediction of friction factor values when modeling the experiments of Nava's experiments was not a numerical flaw.

### *2.5. Parametric effect on leakage of the groove dimensions*

Encouraged now by a quantitative validation of the 2-D numerical approach originally developed in reference [19], the possibility of finding similarity in either the leakage rate or the friction factor behavior using appropriate ad-hoc dimensional scaling of the 2-D roughness actual size and the clearance value was reviewed once again.

As mentioned in section 2.1, experimental tests were conducted in plates with two sizes of each roughness looking for scale effects. The original analysis of such tests did not find any scale effect while focusing on friction factors at the smaller clearances. Although an overlooked phenomenon indeed present in the original experiments was numerically predicted, the friction-factor-to-clearance indifference behavior, it shall be acknowledged that it is extremely difficult to find scaling parameters when all dimensions seem to have a measurable effect in both the friction factor observations, and the original 2-D predictions. Considering only geometric characteristics, following is a list of the parameters that potentially have an effect in the leakage performance of roughened seals:

- Roughness pattern length, l.
- Roughness pattern depth, d.
- Roughness pattern width, w (infinite for a grooved seal).
- Roughened surface area, Γ, proportion of the seal land surface covered by the patterns.
- Roughness pattern shape (any quadrilateral shape in a grooved seal).
- Roughness pattern orientation (fixed in this analysis).

Any combination of these parameters must include the seal clearance. Note that the list refers only to roughness characteristics affecting leakage in a straight trough seal of a smooth rotor (just one surface is roughened). Other parameters such as the use of stepped or converging/diverging clearances are left out. In reference [19], a qualitative scaling analysis suggested the friction-factor-to-clearance indifference behavior is present when the pattern length is roughly twice the clearance, without specific details about possible design practices. Using the 2-D model developed in the previous section, a parametric analysis was performed varying length, depth, and grooved to land area ratio, starting from the groove configuration of Iwatsubo [38] while maintaining the original clearance, 175 μm (~ 7 mils).

Figure 11 shows all groove depths simulated within the initial periodic unit based on the original ‘Seal 1’ configuration [14]. In this configuration, the grooved area ratio is

equivalent to a Γ of 50%.

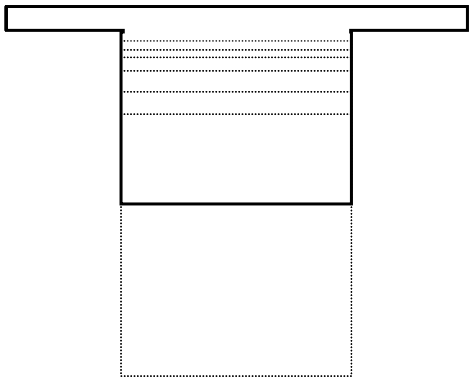


Figure 11. Minimum periodic unit of the 'Seal 1' configuration and the depths simulated.

Table IV includes the dimensions of the family of groove configurations simulated, grouped by Γ percentages. No hole area or Γ equal to 0 % is the basic smooth seal configuration, and Γ equal to 100% is equivalent to a labyrinth seal with zero thickness teeth. Bold font corresponds to the original dimensions of 'Seal 1'.

Table IV. Simulated grooved seal geometries

| **Γ, %** | 25 | | 50 | | | | 75 | | | 100 | |
|---|---|---|---|---|---|---|---|---|---|---|---|
| **$L_g$,** mm | 0.175 | 0.350 | 0.175 | 0.400 | 0.800 | **1.600** | 0.600 | 1.200 | 2.400 | 0.175 | 0.700 |
| **$L_T$,** mm | 0.700 | 1.400 | 0.350 | 0.800 | 1.600 | **3.200** | 0.800 | 1.600 | 3.200 | 0.175 | 0.700 |
| **D**, mm. | 0.015 | 0.015 | 0.030 | 0.030 | 0.030 | 0.090 | 0.030 | 0.060 | 0.060 | 0.015 | 0.029 |
| | 0.030 | 0.060 | 0.060 | 0.060 | 0.090 | 0.150 | 0.060 | 0.120 | 0.300 | 0.030 | 0.087 |
| | 0.090 | 0.090 | 0.090 | 0.090 | 0.120 | 0.210 | 0.090 | 0.240 | 0.480 | 0.045 | 0.175 |
| | 0.175 | 0.150 | 0.120 | 0.120 | 0.150 | 0.300 | 0.120 | 0.300 | 0.600 | 0.060 | 0.350 |
| | | 0.300 | 0.175 | 0.240 | 0.180 | 0.450 | 0.180 | 0.450 | 1.200 | 0.090 | 0.700 |
| | | | | 0.360 | 0.240 | 0.600 | 0.240 | 0.600 | 1.800 | 0.175 | |
| | | | | | 0.300 | **1.200** | 0.300 | 0.750 | 2.400 | | |
| | | | | | 0.600 | 2.400 | 0.450 | | | | |

As in the previous section, simulations were performed using wall functions and the RNG *k*-ε turbulence model. Several alternatives to make results non-dimensional and be presented in a meaningful way were explored. Of the possible combinations of parameters (Cr, l, d, Γ), the aspect ratio of the groove (depth to length ratio, d/l) is the one that seems to

group the otherwise independent and dispersed resistance flow behavior of each groove configuration. Within a certain groove length interval and a Reynolds number range, the flow behavior is clearly grouped, i.e., defined by the percentage of the grooved area, i.e., Γ.

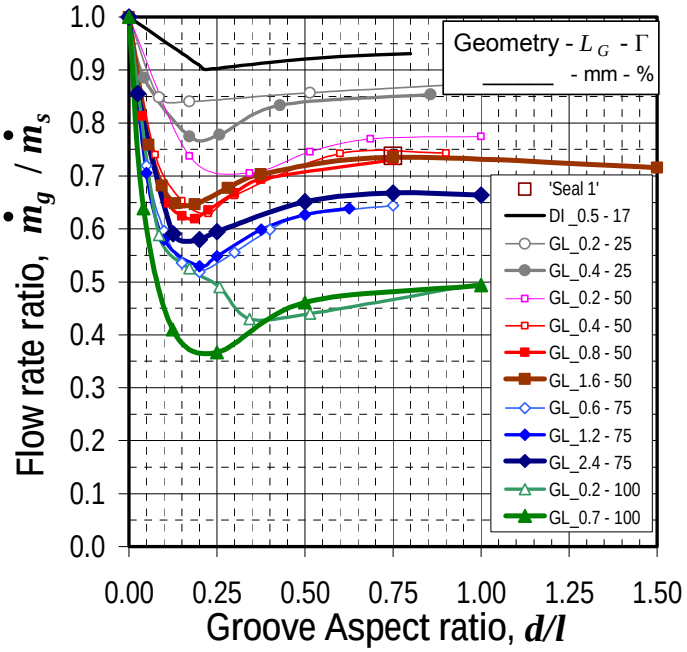


(a) Low Reynolds number (2.2~ $6.0 \cdot 10^3$), $\Delta P_X$ = 16.7 MPa/m.

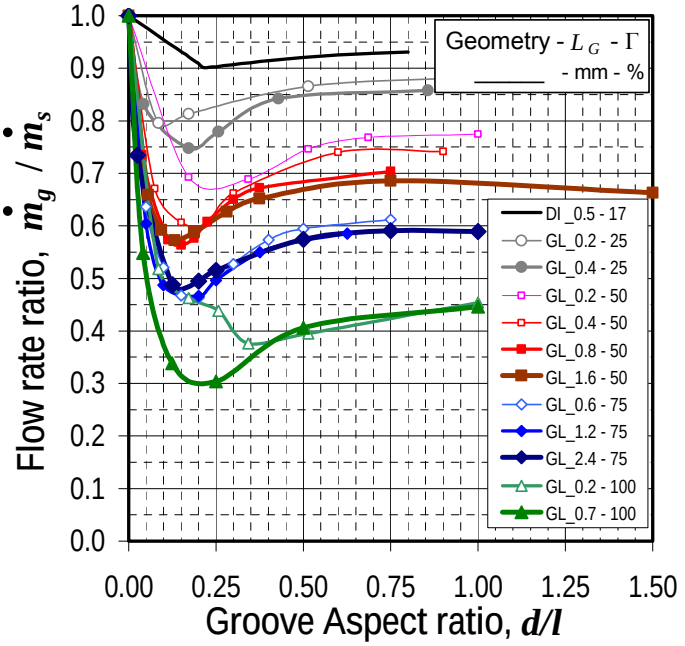


(b) Medium Reynolds number (1.3~ $4.3 \cdot 10^4$), $\Delta P_X$ = 500 MPa/m.

Figure 12. Groove seal parametric analysis

DI = Dietzen [12] ($\Delta P_X$ = 31 MPa/m) GL = Groove Length.

Figure 12 includes the predicted leakage behavior for particular ranges of Reynolds numbers. Results are made non-dimensional by dividing the predicted leakage flow rate in a given grooved geometry by the expected flow rate in the smooth seal, subjected to the same differential pressure. The non-dimensional scale ratio refers to the groove aspect ratio. Figure 12(a) corresponds to simulations at the median differential pressure of the original experiments. The experimental data is added as reference, a single point in the graph. Also, to put the leakage analysis into perspective, the numerical data of the pioneer work of Dietzen and Normann [12] on CFD of liquid grooved seals was included. Similarly, Figure 12(b) corresponds to results at the largest differential pressure simulated.

Three main features are common in the Reynolds number range analyzed. First, the resistance to the flow increases as the grooved percentage area, Γ, of the seal is increased. Secondly, each groove configuration has an optimum aspect ratio where the leakage is minimized. Lastly, although the optimum aspect ratio depends on the actual Reynolds number, such dependence is very weak.

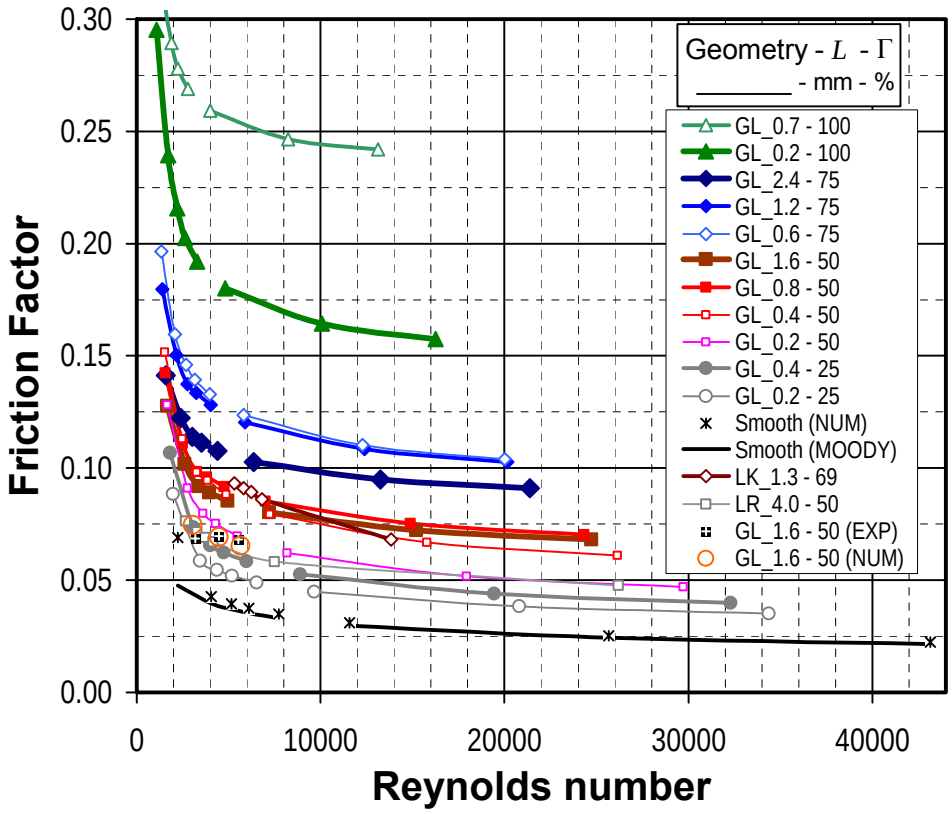


Figure 13. Friction factor behavior in the optimum aspect ratio groove configuration.

These results are now compared with previous 2-D predictions [19] in Nava's [30] experiments. Figure 13 presents the friction factor behavior versus Reynolds number for each groove configuration at the optimum aspect ratio, including predicted behavior in the large knurl and recess geometries [19] at a comparable clearance, 0.127 mm (5 mils), and the original Seal '1' data, recalling that experiments had a groove aspect ratio that is not the predicted optimum. Moody's smooth friction factor curve and 2-D predictions of a smooth seal are included to validate the basic grid used for the calculations.

Following are the most relevant observations:

- A larger Γ leads to a larger friction factor.
- The effect of groove length on the friction factor increases as the Γ ratio is increased.
- At a constant Γ, the friction factor is the largest at a particular groove length (at the optimum aspect ratio), roughly 3 to 5 times the clearance.
- The large knurl (LK_1.3) numerical data, actual Γ of 69%, lays within the groove numerical data with Γ equal to 50%, while the large recess (LR_4.0) numerical data, actual Γ of 50%, lays atop the groove numerical data with Γ equal to 25% at low Reynolds number, but lays atop of the GL_0.2 – 50% curve at the largest Reynolds number plotted.

Nava's numerical data confirm the trend that for a given clearance, larger Γ ratios lead to larger friction factors, recalling that was generated at the experimental d/l ratios, not necessarily the optimum in each particular geometry.

Finally, Figure 14 presents how the optimum aspect ratio correlates with the groove length and Γ ratio of each groove configuration. Taking into account that the data was generated with discrete and not continuous variation of both the depth for each particular geometry and the Γ ratio, the apparently scattered data indicate a particular trend, best shown in the Γ ratios of 50% and 75%. As the groove length is increased, the optimum aspect ratio for a given Γ appears to reach a constant value. In other words, at a sufficient large size of the groove relative to the clearance, the optimum aspect ratio is universal for that particular groove at the given clearance.

New simulations with geometries sized around the aspect ratio of each groove configuration that leaks the least are required to refine predictions of the optimum aspect ratio; including more groove lengths for Γ ratios of 50% and 75%, to confirm the apparent universality predicted for the optimum aspect ratio for a grooved seal. Similarly, a Γ ratio of

100% is unrealistic; labyrinth seal teeth have a certain minimum thickness. Typical labyrinth seals have tooth thickness and pitch [1] resulting in Γ ratios ranging from 80% to 95%. The performance of real labyrinth seals is hidden between the predicted behavior of Γ ratios of 75% and 100%.

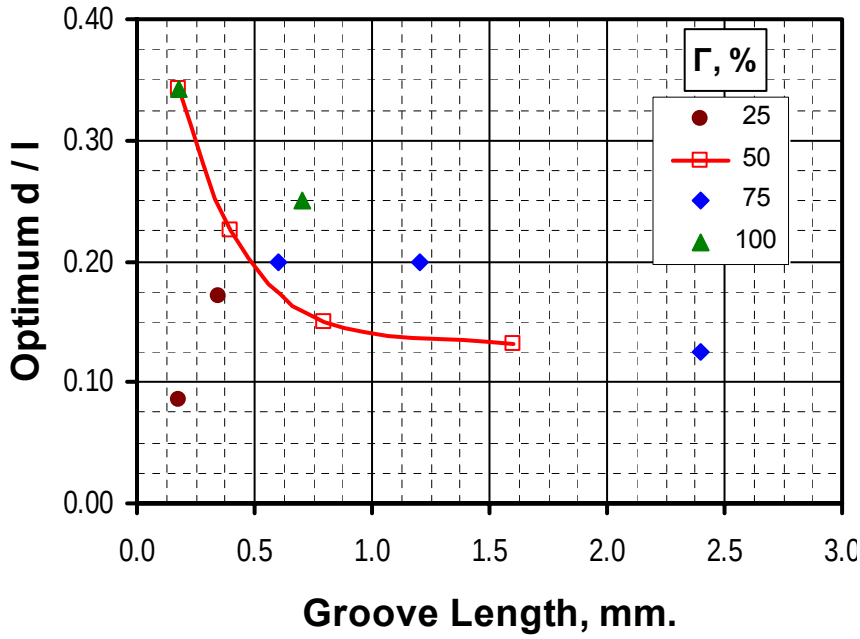


Figure 14. Optimum aspect ratio groove configuration vs. groove length.

# 3. ANALYSIS IN THREE-DIMENSIONS

This section includes the results of all 3-D simulations performed in term of friction factor. First, a comparison of selected 3-D predictions, 2-D modeling results [19], and the original Nava's experiments [30] is presented. Secondly, preliminary 3-D predictions based on the experiments of Fayolle [8], Iwatsubo [36], and Kaneko [37] are discussed. Then, an extensive analysis on the friction-factor-to-clearance behavior of the two roughness geometries that provided higher resistant to Poiseuille flow, experimentally and numerically is laid out. The analysis includes the clearance of the experiments, 175 μm (6.9 mils) in the isogrid seal of Iwatsubo [36] and 176 μm (6.9 mils) in the honeycomb-like seal of Kaneko [37], plus four additional larger clearances based on the flat-plate tests of Nava [30].

Finally, still in progress but revealing simulations are examined regarding the effect of the roughness orientation relative to the mean flow direction in the friction factor.

## *3.1. Preliminary 3-D modeling of Nava's experiments*

The large knurl roughness geometry provided the maximum friction factor in Nava's experiments [30], with the plateau occurring in the 508 μm (20 mils) clearance. Following grid techniques developed in the 2-D numerical approach [19], regarding cell shape and wall distance, simulations in the minimum 3-D periodic unit of the large knurl geometry were performed at this particular clearance. Figure 15(a) shows the minimum 3-D periodic unit geometry with the symmetry plane that defined the 2-D model geometry clearly identified; X is the stream wise-flow coordinate. A detailed numerical review is included in Section 4.

In the 3-D geometries, friction-factor calculations are performed with the same equations developed for the 2-D numerical analysis, but the mass flow rate per unit length is estimated as follows:

$$\dot{m}_l = \frac{\dot{m}}{w} \tag{8}$$

where $w$ is the periodic unit width. Figure 15(b) compares friction factor results of the 3-D simulations, previous 2-D solutions, and the original experimental data. 3-D and 2-D predictions obtained with the standard k-ε model and wall functions are comparable within

10%, and both over predict the observed friction factor by approximately 50%. 3-D predictions obtained with the standard k-ε model and the enhanced wall treatment are comparable within 5% to the 2-D predictions obtained with the Reynolds Stress model and the two-layer zonal approach. Both over predict the observed friction factor by roughly 80%.

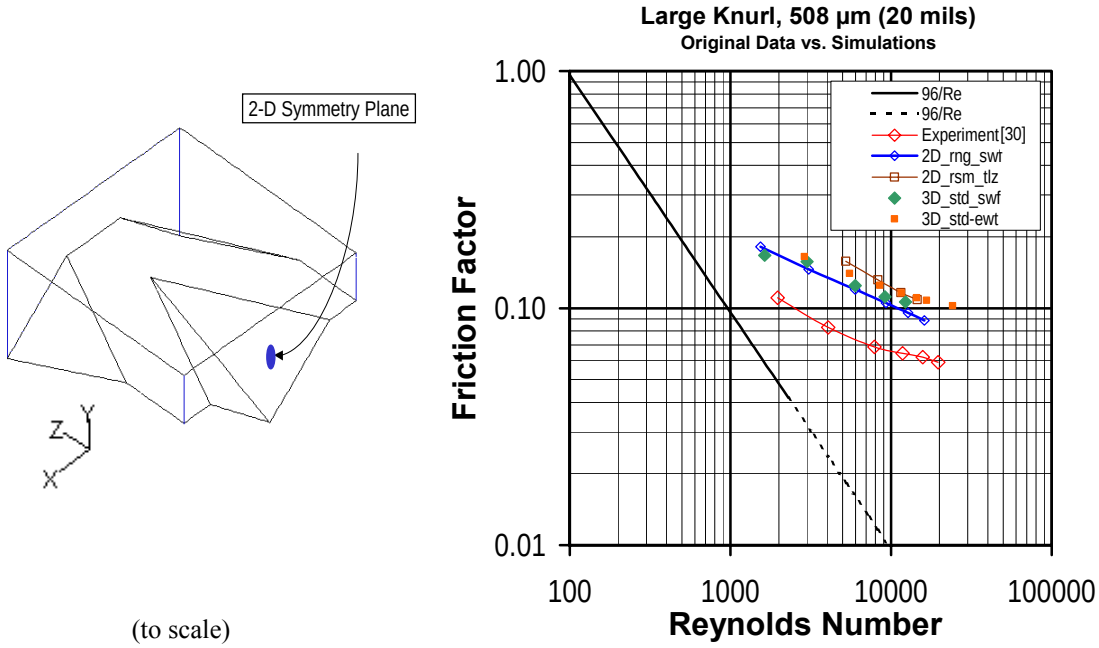


(to scale)

(a) Large knurl minimum periodic unit.

(b) Friction factor vs. Reynolds number

Figure 15. Flat plate test results vs. numerical predictions, smooth against large knurl pattern surfaces.

Figure 16(a) shows (to scale) the minimum periodic unit of the small recess geometry for the clearance of 254 µm (10 mils) with the symmetry plane clearly identified. Similarly, Figure 16(b) shows the corresponding full periodic unit; X is the stream wise-flow coordinate. Figure 16(c) compares both 3-D simulation results, 2-D solutions, and the experimental data.

Laminar solutions fall slightly below the 96/Re line but 2-D and both of the 3-D predictions are consistent. On the other hand, turbulent predictions with the 3-D approach lie within the 2-D results, over predicting by several times the experimental friction factor.

At low Reynolds number, 3-D predictions based on wall functions are larger than their 2-D counterparts by roughly 40%, due to differences in actual $y^+$ values. On the other hand,

all wall function predictions are comparable within 5% at medium to large Reynolds number, where $y^+$ modeling restrictions are fulfilled in all solutions.

Similarly, 3-D predictions based on the two-layer zonal approach and the enhanced wall treatment are mutually consistent, and both are lower than 2-D two-layer zonal predictions by 20%. Modeling differences, in dimensions and turbulence treatments, do not explain the staggering 400% over-prediction when compared to the original experiments.

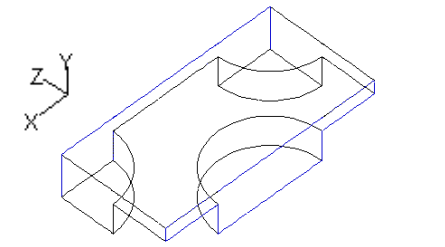


(a) Minimum periodic unit (to scale)

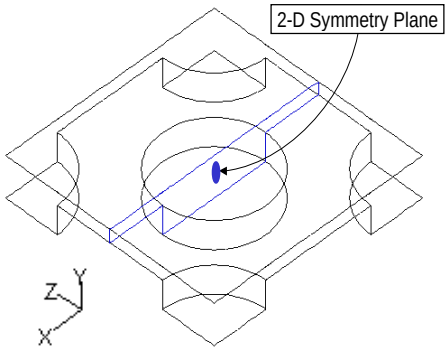


(b) Full periodic unit (to scale).

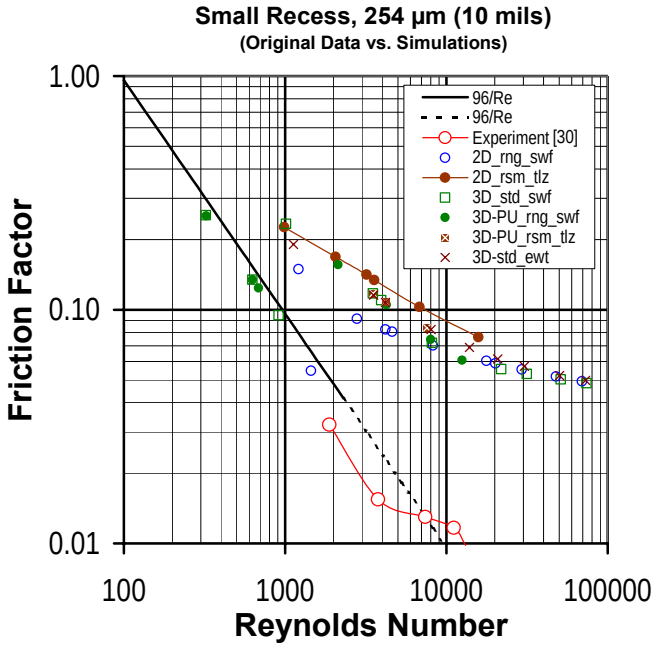


(c) Friction factor vs. Reynolds number

Figure 16. Flat plate test results vs. numerical predictions, smooth against small recess pattern surfaces.

Figure 17(a) again shows (to scale) the minimum periodic unit of the small recess geometry but for the clearance of 508 µm (20 mils). Figure 17(b) compares numerical results with the experiments, including three 3-D solutions, varying turbulence models, and including coarse (cg) and fine grid (fg) solutions. 3-D numerical solutions appear to be grid independent but actual values are comparable with the 2-D approach results that over-predicted the friction factor by roughly 250% when compared to the experimental values.

All preliminary 3-D solutions consistently over predict the friction factor when compared to the values derived from the original experiments. Improvements in the predictions for adding the third dimension are minor. While deviations between predictions

and measurements in the knurl geometries are reasonable, they are excessive in the recesses (round-holes). On the other hand, the consistency of all modeling predictions, 2-D and 3-D, the fact that experiments by others in similar geometries compare well with the original 2-D predictions as reviewed in section 2.3, and the replication of a true 2-D turbulent flow experiment as discussed in sections 2.4, indicate that recorded/registered friction factor values in the original experiments of Nava[30] and Hess[34] might not correspond to the actual values measured.

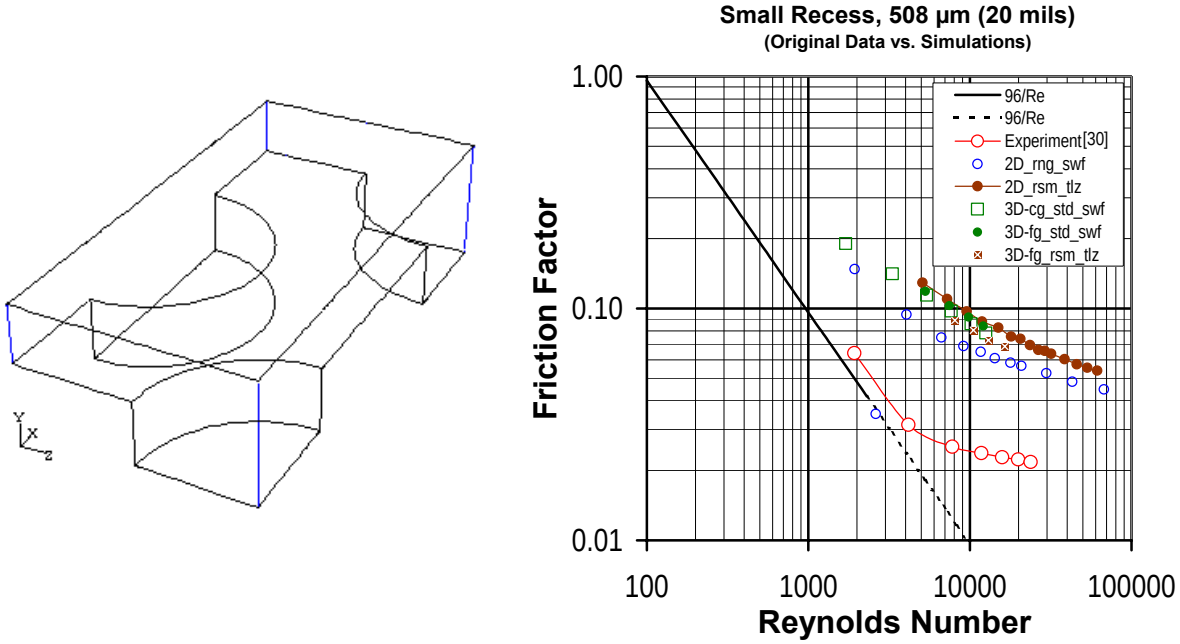


(a) Minimum periodic unit (to scale) (b) Friction factor vs. Reynolds number

Figure 17. Flat plate test results vs. numerical predictions, smooth against small recess pattern surfaces.

### *3.2. Preliminary 3-D modeling of several roughened seal experiments.*

As stated in the previous section, friction factor values recorded in the original Nava's experiments were not quantitatively reproduced within reasonable margins. Nonetheless, section 2.4 discussed a truly 2-D experiment that was reproduced with confidence with the same numerical approach developed in Villasmil [19], casting doubts in the absolute magnitude of the recorded friction factor values, although it shall be emphasized that the friction-factor-to-clearance dependence observed in the original experiments is not in doubt. Therefore, other experiments regarding 'damping' seals' flow were evaluated, to broaden the evaluation effectiveness of the numerical approach in modeling the flow over roughened surfaces. Figure 18 shows (to scale) the minimum periodic unit of each roughness pattern at the maximum clearance seal arrangement for the experimental works of Childs and Fayolle [8], Iwatsubo and Sheng [36], and Kaneko et al. [37].

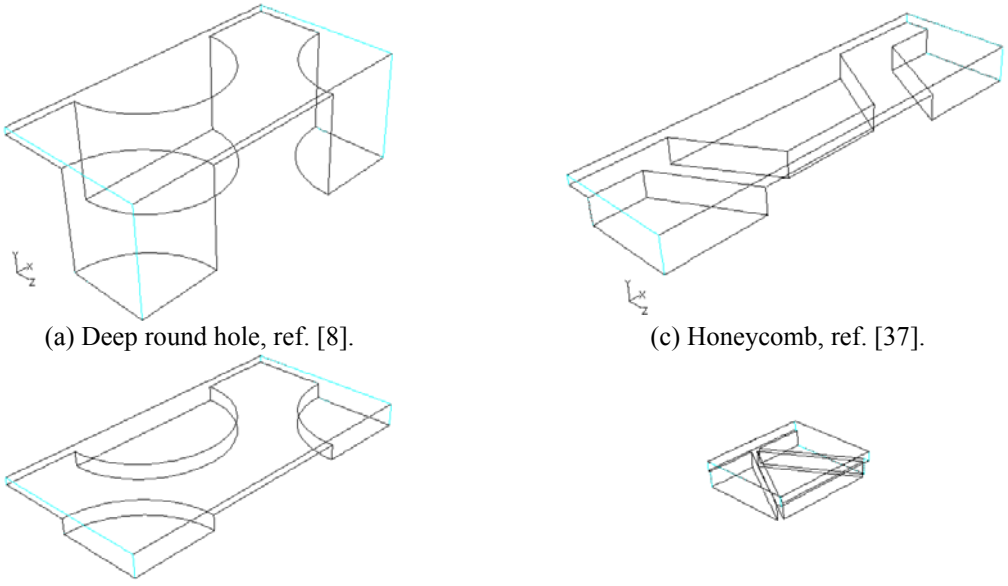

(a) Deep round hole, ref. [8].

(c) Honeycomb, ref. [37].

(b) Shallow round hole, ref. [8].

(d) Isogrid, ref. [36].

Figure 18. 3-D Minimum periodic units (to scale), X is the stream wise-flow coordinate.

Childs and Fayolle studied three clearances and two depths of round holes as roughness patterns. To the best of the author's knowledge, their work was the first to identify the friction-factor-to-clearance direct proportionality behavior in roughened annular seals, a phenomena observed previously in the flat plate tests of Ha [9] and Nava [30]. An private

report [44] on a study of the friction factor behavior of surfaces with the roughness pattern of Von Pragenau [7], constant depth holes with an equilateral triangle as sectional area (commonly referred as "Isogrid"), indicated that such surfaces presented larger resistance to flow than the large knurl of Nava's [30], in a similar flat plate arrangement. A smaller "Isogrid" pattern by Iwatsubo [36] provided even larger friction factors in a single-clearance annular seal arrangement. Finally, another single-clearance seal experiment, Kaneko [37], showed the largest friction factor of all experiments with flat plates and liquid seals reviewed, although the data was generated only for one differential pressure at an extremely low Reynolds number. Table V summarizes the characteristics of the seal roughness of these experiments. Nava's [30] patterns are included as a reference.

Table V. Roughness pattern dimensions, Fayolle[8], Iwatsubo[36], Kaneko[37]

| Experiment | Pattern | Characteristic length, l | Depth, d | Hole Area, Γ | Clearance, $C_r$ |
|---|---|---|---|---|---|
| Childs & Fayolle | Round hole | 3.175 | 2.00, 0.28 | 44.4 % | 0.076, 0.10, 0.12 |
| Iwatsubo | Isogrid | ~ 2.00 | 0.30, 0.50 | 83.4 % | 0.175 |
| Kaneko | Honeycomb | ~ 4.00 | 0.50 | 60.2 % | 0.176 |
| Nava | Knurls | 0.64, 1.27 | 0.32, 0.64 | 46.6 % | 0.076 to 1.270 |
| Nava | Round-hole | ~ 2.00, 4.00 | 0.56, 1.18 | 38.5 % | 0.076 to 1.270 |

Note: all dimensions in mm.

Numerical simulations were performed in the cases that involved no shaft rotation. Modeling and boundary conditions are discussed in section 4. Figure 19 compares predicted friction factors with the data extracted from each experiment.

In the deep round-hole pattern, predictions are within 2% of the experiments. On the other hand, friction factor is over-predicted by roughly 25% in the shallow round-hole pattern. Similarly, predictions for the isogrid pattern are within 50% of the experiments, while numerical results under-predict the friction factor in the honeycomb pattern by 19%. Overall, these deviations are reasonable and can be considered a success when compared to the over-prediction by as much as 400% in the 2-D and 3-D numerical analysis of the recesses geometries of Nava [30]. On an individual basis, the numerical results confirm that shallow round-holes provide larger resistance to flow than deep round-holes, although the predicted difference is larger than the one reported in the experiments of Childs and Fayolle [8]. On the other hand, maximum friction factor is predicted in the isogrid pattern, Iwatsubo[36]. In the experiments, the honeycomb pattern of Kaneko [37] provided the

largest resistance.

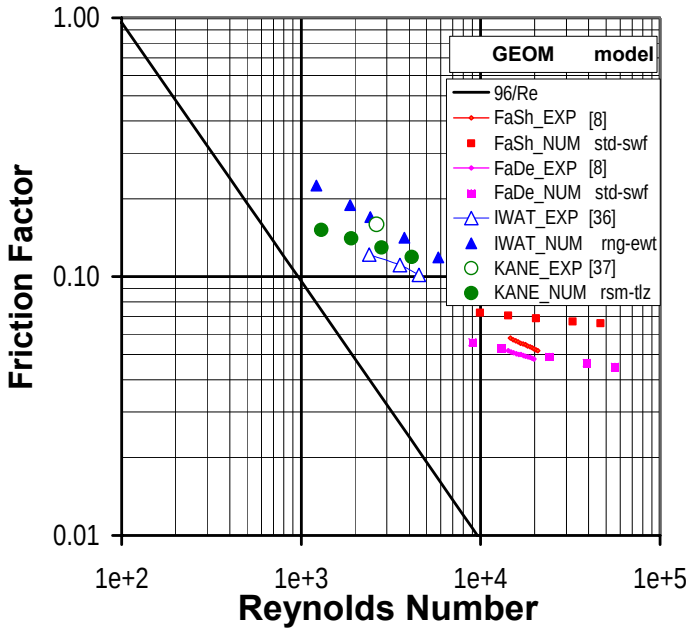


Figure 19. Annular seal test results vs. numerical predictions, smooth rotor and roughened stator.

In summary, these predictions indicate that the 3-D modeling approach pursued in the present research reproduces reasonably the observations of several experiments with annular seals with deliberately roughened surfaces.

### *3.3. Friction-factor-to-clearance behavior predictions, isogrid pattern of Iwatsubo[36]*

As discussed in the previous section, the two patterns that experimentally and numerically consistently provide the largest resistance to flow are the Isogrid pattern and the Honeycomb pattern. In this section, an extensive analysis of the predictions in terms of the friction-factor-to-clearance behavior is presented for the Isogrid roughness pattern of Iwatsubo [36]. Figure 20(a) includes basic dimensions of the Isogrid periodic pattern while Figure 20(b) shows the periodic unit used for simulation purposes with the studied clearances, the 175 μm (~ 6.9 mils) test clearance and values of 254, 508, 762 and 1270 μm ( 10, 20 , 30 and 50 mils.), following Nava's experiments.

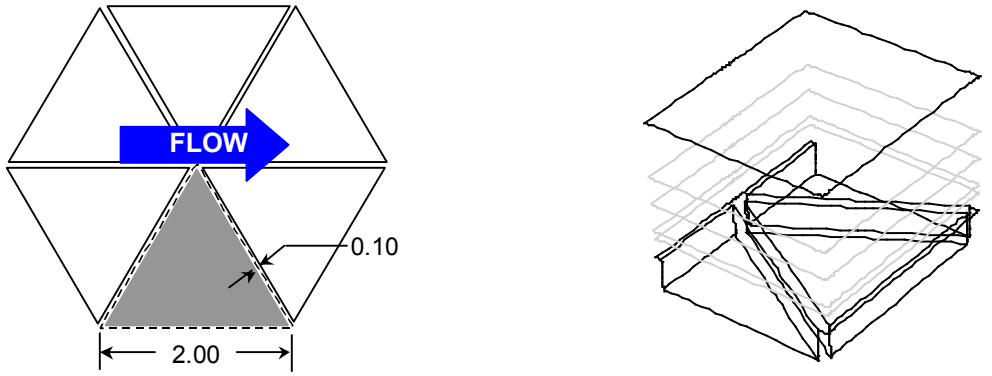


(a) Pattern Dimensions (b) Periodic unit with all clearances

Figure 20. Isogrid [36] pattern.

Figure 21 compares friction factor curves derived from Iwatsubo's experimental results and the numerical predictions for the original clearance of 175 μm ( 6.890 mils) and a pattern depth of 300 μm (the one providing the largest resistance to flow). Simulations were obtained with the standard $k$-ε turbulence model and the enhanced wall treatment [24] for the near-wall modeling. In terms of absolute values, simulations over predict the observed friction factor by roughly 55% (50% by using the RNG $k$-ε, section 3.2). On the contrary, the dependence on Reynolds number is reproduced within 8%, evaluated as the exponent in a simple power law correlation of the friction factor versus Reynolds number.

To explain the deviations in the predictions, many numerical tests have been executed, including multiple grid analysis, closest-to-the-wall cell distance evaluation, and unsteady simulations using LES, verifying that the model and the equations are being solved properly

and accurately. All numerical details are discussed in the following section. The source of the deviations is either the modeling itself or the experimental uncertainty. Although, a combination of both might be more reasonable.

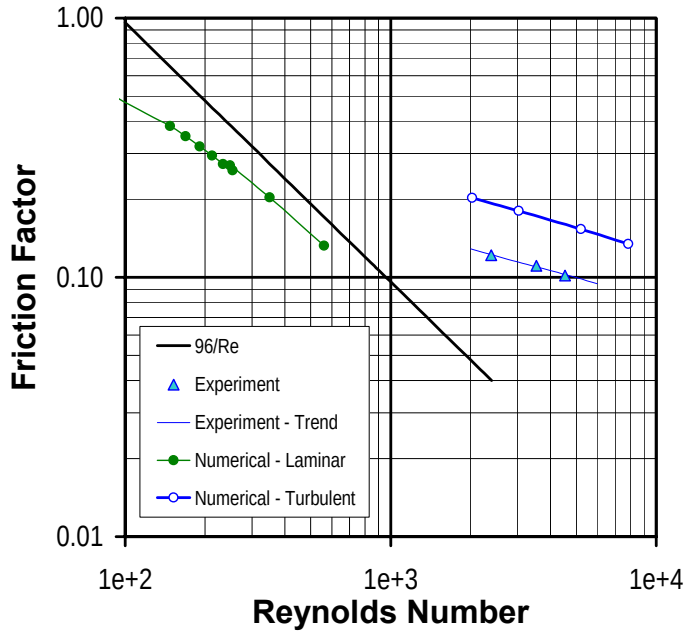


Figure 21. Iwatsubo's annular seal test Results (no-rotation) vs. numerical predictions, Cr = 175 μm

The model has two main sources of uncertainties. As in section 2.4, a periodic approach was used using the total pressure difference in the experiment divided by the seal length as the pressure gradient, neglecting the significance of the inlet and exit losses and the location of the actual pressure measurements tabs. Secondly, recall the very low Reynolds number nature of the flow in the actual experiments. The experimental range from 2000 to 5000 might be better defined as transitional flow rather than turbulent flow, and expecting turbulence modeling to replicate such flows might be optimistic, although preliminary LES modeling solutions in the experimental cases seem to confirm the friction factor predictions of the RANS approach within 10%. Regarding the data extracted from the original experiments, there are two main sources of uncertainty, the actual clearance of the seal, and the accuracy of the leakage, pressure, and temperature measurements. None of the two was addressed by Iwatsubo [36]. While uncertainty in flow and pressure measurements normally amounts to low single digits, accuracy is certainly an issue when measuring the actual

clearance and fluid temperature. The effect of leakage and pressure measurements in the Reynolds number and friction factor calculations is relatively low, because such effect is either equivalent or roughly twice the accuracy. On the other hand, a small variation in either the absolute temperature or in the actual clearance of the seal affects greatly the calculated Reynolds number and friction factor. A 3% variation in the water temperature of the experiment, 293°K (20°C), is equivalent to a 25% variation in the dynamic viscosity. With the experimental setup described in the original paper, a ±2.5 % deviation in the actual clearance, as measured or in centering the rotor, is estimated to be equivalent to a 16.2 % difference in the calculated friction factor. Therefore, predicted deviations are reasonable considering a 5% deviation in either the absolute water temperature or the actual clearance is quite probable.

Figure 22 presents the predicted friction factor behavior in the isogrid pattern of Iwatsubo[36] for the 175 μm (7 mils) test clearance and values of 254, 508, 762 and 1270 μm ( 10, 20 , 30 and 50 mils.). Simulation results correspond to the power law discretization scheme for all variables, the PRESTO scheme for pressure, and the PISO option for the pressure-velocity linking algorithm. Regarding turbulent calculations, the standard k-ε model was used in the core flow with the enhanced wall treatment as near-wall treatment. Multiple grids and local refinement were required to comply with $y^+$ modeling restrictions in the whole Reynolds number range analyzed. Numerical details are included in section 4.3.

Following are the more relevant observations:

- Laminar Solutions:
  - Friction factor is predicted to increase with clearance. At Re~350, the predicted value for the 1270 μm clearance is larger than the value predicted at the 175 μm test clearance by roughly 21%.
  - The smooth channel solution, 96/Re line, appears to be the limiting value of all clearance predictions as the Reynolds number is increased. Deviations from the smooth-channel solution increase in each clearance, as the Reynolds number is decreased. They are associated with the flow reattaching to the bottom walls of the roughness pattern.

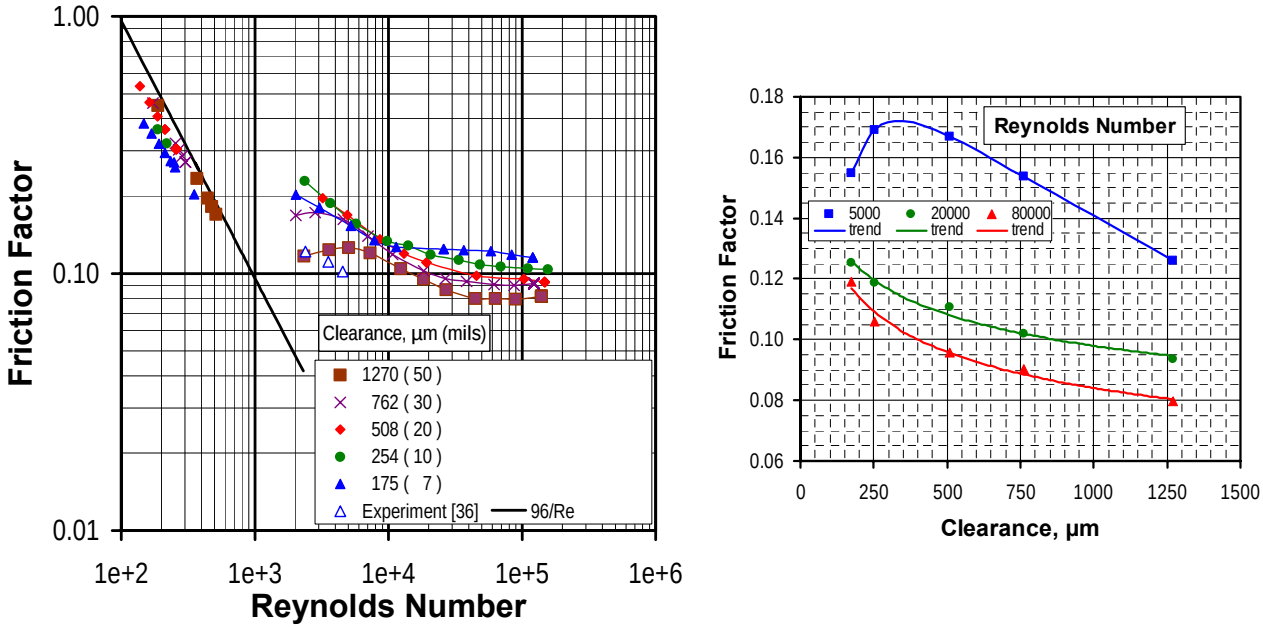


(a) Friction factor versus Reynolds number (b) Friction factor versus clearance

Figure 22. Friction-factor-to-clearance analysis in Iwatsubo's pattern.

- Turbulent Solutions ($Re<10^4$):
  - Friction factor is proportional to the clearance up to the 508 μm value. At Re~5000, the predicted value for this clearance value is larger than the one predicted at the original 175 μm clearance by roughly 10%. Although significant, the difference is comparable to the numerical uncertainty.
  - Friction factor is inversely proportional to the clearance from the 508 μm value to the largest clearance of 1270 μm. At Re~5000, the predicted value for this clearance value is smaller than the one predicted at the 508 μm clearance by roughly 25%. This difference is significant and smaller than the numerical uncertainty.
- Turbulent Solutions ($Re>10^4$):
  - Friction factor becomes inversely proportional to the clearance in all values. At $Re\sim6\cdot10^4$, predicted value at the largest clearance of 1270 μm is smaller than the one predicted at the original 175 μm clearance by roughly 35%. This difference is significant and much larger than the numerical uncertainty.
  - Friction factor dependence on Reynolds number increases with clearance but it is weak in all clearance values. Predicted friction factors become asymptotic, independent of the Reynolds number, for $Re > 10^5$.

### *3.4. Friction-factor-to-clearance behavior predictions, honeycomb pattern of Kaneko[37]*

As with the previous section, predictions in terms of the friction-factor-to-clearance behavior are now addressed for the Honeycomb pattern of Kaneko [37]. Figure 23(a) includes basic dimensions of the Honeycomb periodic pattern while Figure 23(b) shows the periodic unit used for simulation purposes with the studied clearances, the test clearance of 176 μm (~ 6.9 mils) and values of 254, 508, 762 and 1270 μm ( 10, 20 , 30 and 50 mils.), again following Nava's experiments.

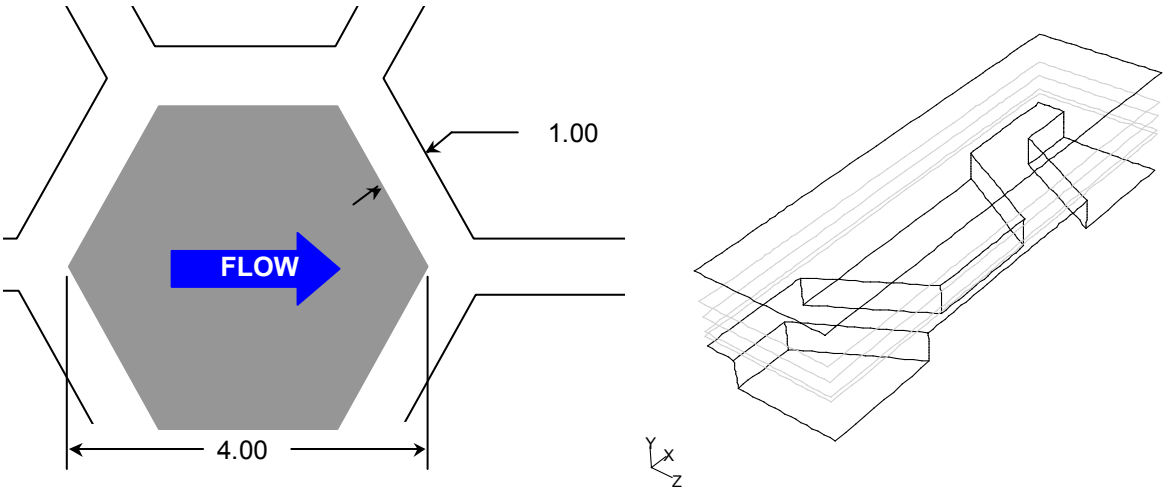


(a) Pattern Dimensions (b) Periodic unit with all clearances

Figure 23. Honeycomb [37] pattern.

In contrast to Iwatsubo [36], Kaneko [37] only tested one pressure difference. Figure 24 includes the friction factor value calculated with the single data point of the experiments at zero speed, the numerical prediction for the original clearance of 176 μm ( 6.929 mils), and for comparison purposes, results and predictions in the original clearance of Iwatsubo's experiment. Matching previous section simulations, predictions were obtained with the standard *k*-ε turbulence model and the enhanced wall treatment [24]. In terms of absolute values, the simulation under predicts the observed friction factor by roughly 27% (by 19% when using the Reynolds stress model, section 3.2). With just one data point at zero speed, no evaluation in the friction factor dependence versus Reynolds number can be made.

Similarly, the model developed and the solving of the equations have been numerically scrutinized for consistency and accuracy. The deviation is most likely related to a

combination of both modeling flaws and experimental uncertainty.

Regarding modeling, Kaneko [37] measured the axial pressure distribution thus eliminating uncertainties in the pressure gradient associated with inlet and exit losses and location of pressure tabs. His experiment was also conducted at a very low Reynolds number, roughly 2600 - in the author's opinion transitional rather than turbulent flow.

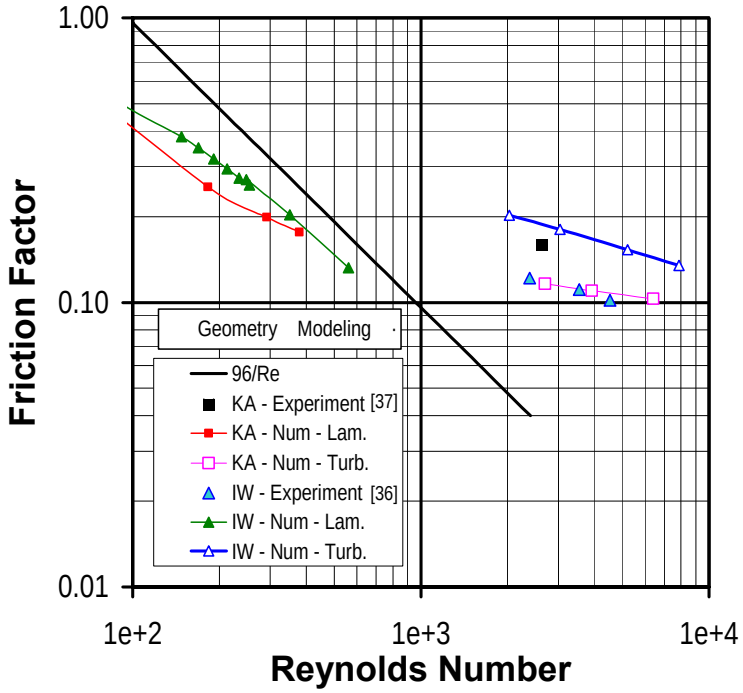


Figure 24. Kaneko vs. Iwatsubo annular seal test results (no-rotation) vs. numerical predictions.

In contrast to Iwatsubo [36], Kaneko described the method used to perform the uncertainty analysis in all measurements, and included averaged values. Pressure and leakage flow rate measurements average uncertainties were estimated at 5% each. There is no mentioning about accuracy of the actual clearance. Friction factor deviations are roughly 5 to 10 % considering given uncertainties for pressure and leakage respectively. Kaneko [37] and Iwatsubo [36] experimental setups are similar; therefore, expected deviations due to clearance uncertainty are numerically the same. A ±2.5% deviation in the clearance is equivalent to a 16.2 % difference in friction factor. Therefore, predicted deviation is reasonable, considering a 5% deviation in the actual clearance is quite possible. No information about the water temperature is given in the original paper.

Figure 25 presents the predicted friction factor behavior in the honeycomb pattern of Kaneko[37] for the 176 µm (~ 6.9 mils) test clearance plus values of 254, 508, 762 and 1270 µm ( 10, 20 , 30 and 50 mils.). Simulation results correspond to the power law discretization scheme for all variables, the PRESTO scheme for pressure, and the PISO option for the pressure-velocity linking algorithm. Regarding turbulent calculations, the standard k-ε model was used in the core flow with the enhanced wall treatment as near-wall treatment. Multiple grids and local refinement were required to comply with $y^+$ modeling restrictions in the whole Reynolds number range analyzed. Numerical details are included in section 4.3.

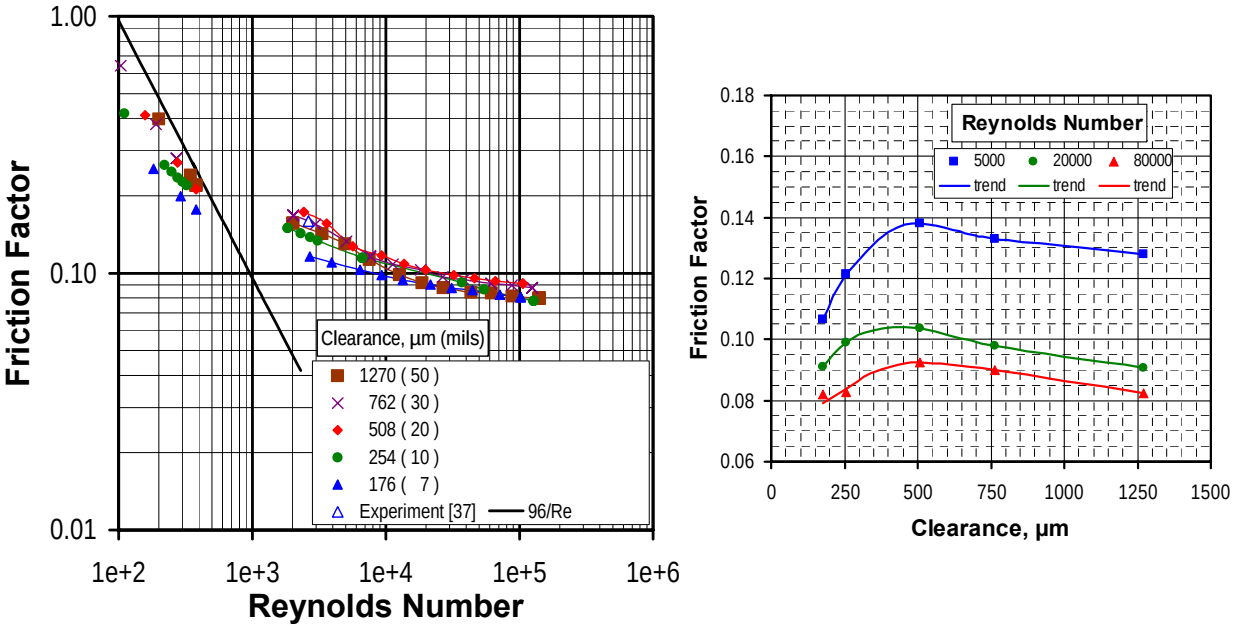


(a) Friction factor versus Reynolds number (b) Friction factor versus clearance

Figure 25. Friction-factor-to-clearance analysis in Kanekos's pattern.

Following are the more relevant observations:

- Laminar Solutions:
  - Friction factor is predicted to increase with clearance. At Re~100, the predicted value for the 762 µm clearance is larger than the one predicted at the 254 µm clearance by 50%.
  - The smooth channel solution, 96/Re line, appears to be the limiting value of all

clearance predictions as the Reynolds number is increased. Deviations from this solution increase in each clearance, as the Reynolds number is decreased. They are associated with the flow reattaching to the bottom walls of the roughness pattern.

- Turbulent Solutions ($Re<10^4$):
  - Friction factor predictions are proportional to the clearance up to the 508 μm value. At Re~9000, the predicted friction factor value for this clearance value is larger than prediction for the 176 μm clearance by roughly 20%. This difference is significantly larger than the numerical uncertainty.
  - Friction factor predictions are inversely proportional to the clearance from 508 μm to 1270 μm. At Re~7500, the predicted value for the 1270 μm clearance is smaller than the one predicted at 508 μm by roughly 4%. This difference is comparable to the numerical uncertainty. In fact, friction factor values for the larger clearances, 254 to 1270 μm, are comparable within 4% in the $5 \cdot 10^3$-$10^4$ Reynolds number flow range. Predictions in these clearance values differ up to 21% at Re~2300, where the turbulence modeling capabilities might be questionable.
- Turbulent Solutions ($Re>10^4$):
  - Friction factor predictions remain proportional to the clearance up to the 508 μm value. At $Re\sim10^5$, the predicted value at 508 μm is larger than the one predicted at the 176 μm test clearance by roughly 13%. This difference is significant and larger than the numerical uncertainty.
  - Friction factor dependence on Reynolds number is predicted to increase from the 176 μm test clearance to Cr = 508 μm but to decrease from Cr = 508 μm to 1270 μm. Predicted friction factors still depend on the Reynolds number, for $Re > 10^5$.
  - Predicted friction factors in the smaller clearance values, 176 μm and 254 μm, and the largest clearance of 1270 μm are comparable within 4% for Reynolds number larger than $5 \cdot 10^5$. Similarly, predictions at 508 and 762 μm clearances are comparable within 4% but both are larger than predictions at 176, 254, and 1270 μm by 13%. Predictions indicate that the clearance value of 508 μm is likely a plateau for the honeycomb pattern of Kaneko[37].

### *3.5. Effect of the pattern orientation on the friction factor*

As shown in Ref [39] for 2-D simulations, numerical simulations indicated that the flow must be resolved up to the laminar sub-layer to capture the dependence of the friction factor versus clearance. The use of simpler near-wall modeling approaches derived from the logarithmic law of the wall seemed to neglect the effect of the clearance in the predicted friction factor behavior. That is not the case in the present 3-D simulations where both approaches predict comparable friction-factor-to-clearance proportionality in the isogrid and honeycomb pattern for Reynolds numbers above $10^5$. The turbulence modeling performance is extensively discussed in section 4.3.

From a numerical perspective, including or adding each roughness pattern in the domain of an annular seal is cumbersome because the actual volume of the pattern is several order of magnitudes larger that seal clearance gap. In addition, resolving rigorously the laminar sub-layer at high Reynolds number requires a considerable number of nodes and special care in the grid generation near the walls. Certainly, using law-of-the-wall approaches ease the numerical burden. Recent numerical studies [17,18,45] show promise in reducing computational efforts by either employing a simplified empirical model with extended wall functions or replacing the original gap in the roughened seal with an effective or equivalent smooth seal clearance, indeed avoiding including each roughness in the numerical domain.

These studies either used a planar model (no change in mean flow direction) or evaluated the flow behavior in round-hole seals, a perfectly symmetric pattern. Contrary to round holes, experiments with non-fully symmetric patterns such as knurls [30], isogrid [36,44] and honeycomb [37] show larger resistance to flow. Likewise, numerical predictions [19] reproduced observations that knurls are better than round holes. Also, present simulations indicate that either honeycomb or isogrid patterns are better than round holes in terms of flow resistance.

Since an exhaustive numerical evaluation of the predicted friction factor behavior for the isogrid of Iwatsubo [36] and the honeycomb of Kaneko [37] patterns had already been performed, to carry out an analysis on the effect of the roughness orientation in the friction factor was straightforward. Figure 26 shows sketches (to scale) of both patterns including the primary flow direction according to each original experiment set-up and the most

different or counter flow direction. Because both patterns are based on an equilateral triangle shape, the primary flow direction is repeated every 60°. Therefore, the counter flow direction is 30° apart from the primary flow direction.

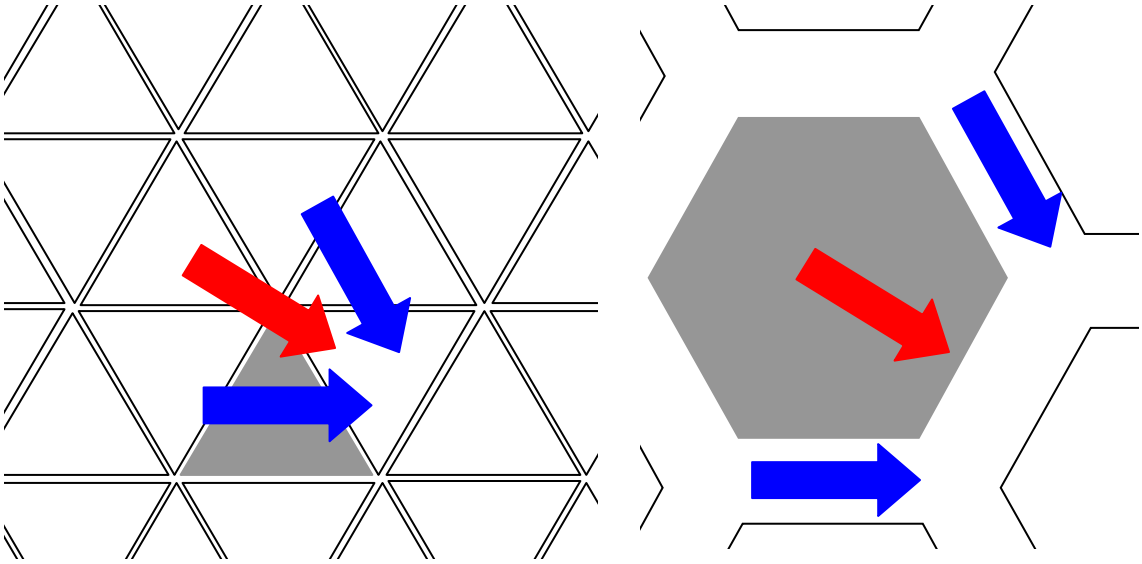

(a) Isogrid pattern [36] (b) Honeycomb pattern [37]

Figure 26. Primary (blue) and counter flow (red) direction in non-symmetric roughness patterns.

Figure 27 shows the periodic unit of both patterns. For simulation purposes, test clearance values of 175 and 176 μm (~ 6.9 mils), and an additional 508 μm clearance (20 mils and plateau clearance in Nava's [30] experiments and honeycomb predictions of the previous section). The periodic units are basically the same shown in Figures 20(b) and 23(b) but divided along symmetry lines in constant X coordinate planes, and duplicated in the Z direction, to reach periodicity. Flow in the Z direction on these figures is referred to as the counter flow direction.

Figure 28 compares the predicted friction factor behavior in the original flow direction to the counter flow direction for the isogrid pattern of Iwatsubo[36]. Simulation results correspond to the power law discretization scheme for all variables, the PRESTO scheme for pressure, and the PISO option for the pressure-velocity linking algorithm. Regarding turbulent calculations, the standard k-ε model was used in the core flow with the enhanced wall treatment as near-wall treatment. Multiple grids and local refinement were required to comply with $y^+$ modeling restrictions in the Reynolds number range analyzed. Numerical

details are included in section 4.3.

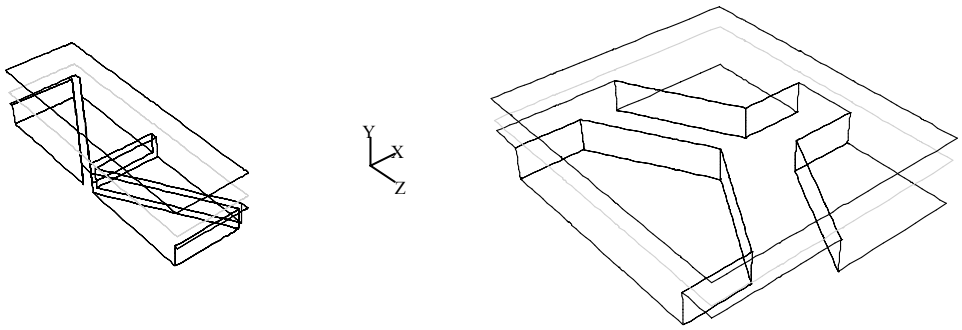


(a) Isogrid pattern, Iwatsubo [36]. (b) Honeycomb pattern, Kaneko [37]

Figure 27. Minimum periodic units of the non-fully symmetric roughness pattern (to scale). Z is the main flow direction for calculation purposes but labeled as counter flow direction.

Following are the more relevant observations:

- Laminar Solutions:
  - Predicted friction factors in both directions in the test clearance of 175 μm are comparable within 2%.
  - Predicted friction factors in both directions in the 508 μm clearance value are comparable within 1%.
  - Given the numerical uncertainty, predicted friction behavior is not affected by the mean flow direction in the laminar flow regime.
- Turbulent Solutions ($Re<10^4$):
  - Predicted friction factor in the counter flow direction is roughly 4% larger than predictions in the original direction for the clearance of 175 μm.
  - Predictions in the counter flow direction for the clearance of 508 μm are roughly 5% larger than predictions in the original direction.
  - Given the numerical uncertainty, predicted friction behavior is not affected by the mean flow direction in the turbulent flow regime at low Reynolds number.
- Turbulent Solutions ($Re>10^4$):
  - Predicted friction factor in the original flow direction is roughly 6% larger than predictions in the counter flow direction for the clearance of 175 μm.
  - At the intermediate clearance of 508 μm, predictions in both directions are

comparable within 3%.

- Given the numerical uncertainty, predicted friction behavior is not significantly affected by the mean flow direction in the turbulent flow regime at medium to high Reynolds number.

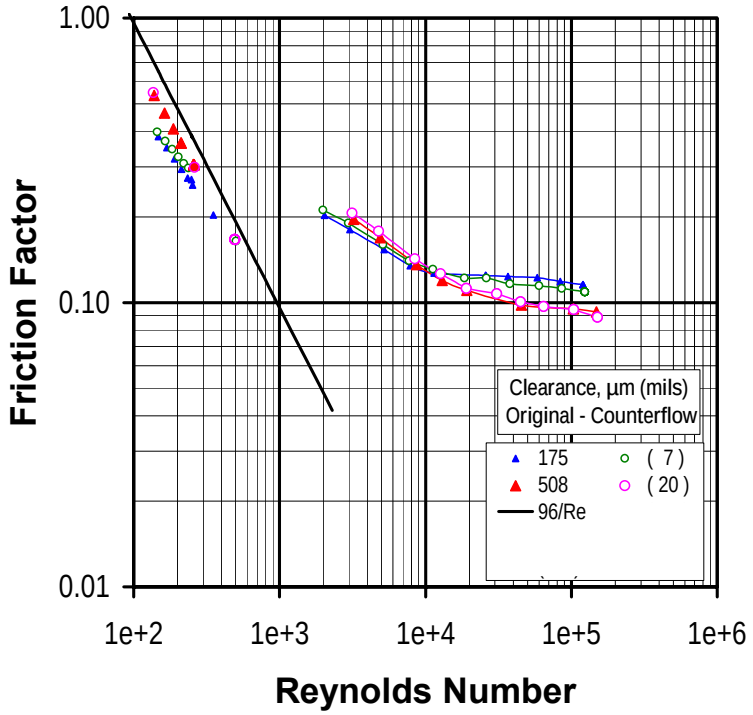


Figure 28. Effect of the mean flow orientation in the isogrid [36] pattern.

Figure 29 compares the predicted friction factor behavior in the original flow direction to the one predicted in the counter flow direction for the honeycomb pattern of Kaneko[37]. Similar numerical schemes and modeling approach to the isogrid pattern were followed; details are included in section 4.3. Following are the more relevant observations:

- Laminar Solutions:
  - Predicted friction factors in the counter flow direction for the original clearance of 176 µm are larger than those predicted in the original direction from 2.7% to 3.8%.
  - Similarly, predicted friction factors in the counter flow direction for the 508 µm clearance are comparable to those predicted in the original direction within 2.2%.
  - Given the numerical uncertainty, predicted friction behavior is not significantly affected by the mean flow direction in the laminar flow regime although the original

flow direction appears to provide larger resistance.

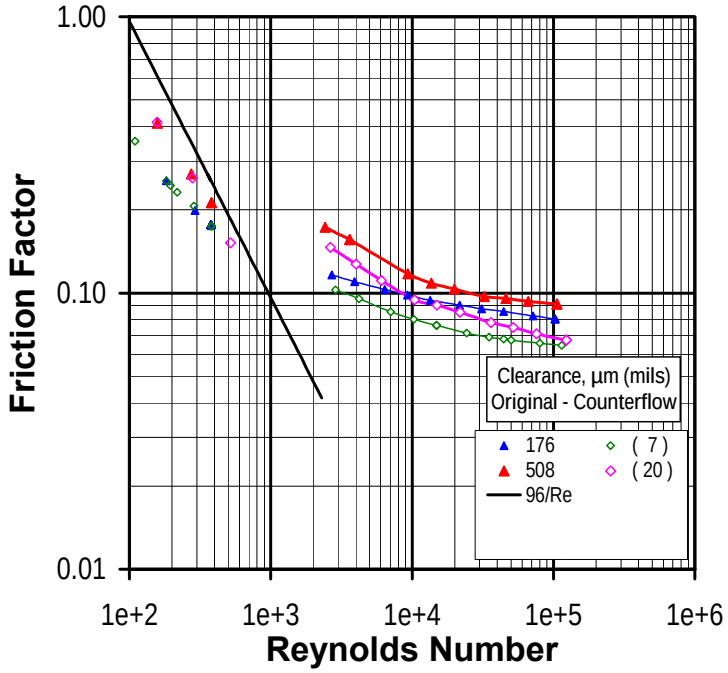


Figure 29. Effect of the mean flow orientation in the Honeycomb [37] pattern.

- Turbulent Solutions:
  - Predicted friction factors in the original flow direction are consistently larger than predictions in the counter flow direction for the original clearance of 176 µm. Differences amount to 10% to 15% at low Reynolds number and increase up to 21% at the largest Reynolds number simulated.
  - Similarly, predicted friction factors in the original flow direction for the 508 µm clearance are consistently larger than predictions in the counter flow direction. Differences amount to 13% to 18% at low Reynolds number and increase up to 26% at the largest Reynolds number simulated.
  - Given the numerical uncertainty, predicted friction behavior is significantly affected by the mean flow direction in the turbulent flow regime in the whole Reynolds number flow range under scrutiny.

A thorough discussion on turbulence modeling is included in section 4.3, while flow field contours and recirculation paths on each pattern are discussed in section 5.

# 4. MODELING VALIDATION AND VERIFICATION

"*No one believes the CFD results except the one who performed the calculation, and everyone believes the experimental results except the one who performed the experiment." [31, Chapter 9].*

This section in its entirety is devoted to verify that each and every numerical model developed was solved properly. Several numerical tools were employed to assure that modeling, convergence, and discretization errors were reduced to a minimum so any trend or fluid behavior extracted from the predictions is certainly an expected condition if a true experiment were run under similar conditions. A special effort has been made to follow the numerical terminology and definitions described in Ref [31].

First, the basic modeling procedure followed is introduced. Secondly, a validation of the boundary conditions used for modeling is presented, simply assessing the credibility of the simulation model within its domain of applicability. Thirdly, the question on how accurate the validated model was solved is addressed. Uncertainty, grid convergence, and iterative convergence are without doubt problem dependent. Lastly but not least important, a comparison is made on how several turbulence models performed in predicting the flow behavior in channel or annular flow with walls that have been deliberately roughened with a specific pattern.

In summary, this section is an extension of the extensive numerical 2-D analysis included in Refs. [19,42]. Both proven and "ad-hoc" techniques have been used to confirm that the governing equations of validated models are being properly and accurately solved.

## *4.1. Basic modeling*

Figure 30 shows (to scale) the minimum periodic unit of each roughness pattern at the test clearance for the experimental works of Childs and Fayolle [8], Iwatsubo and Sheng [36], and Kaneko et al. [37]. The boundary conditions are set as follows:

- Periodicity. Along the stream wise direction, X, the inlet and exit faces of the domain, with the same meshing, are linked for using the periodic approach.
- Walls. Along the vertical direction, Y, the no-slip and no-penetration conditions are enforced in both the top smooth wall of the domain and the bottom wall containing

each roughness pattern.

- Symmetry. Across the span wise direction, Z, the symmetry condition is invoked in both planes defining the width of each pattern domain.

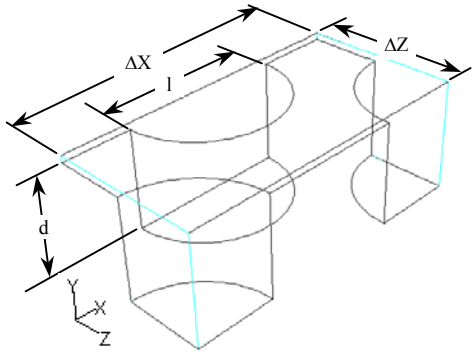


(a) Deep round hole, ref. [8].

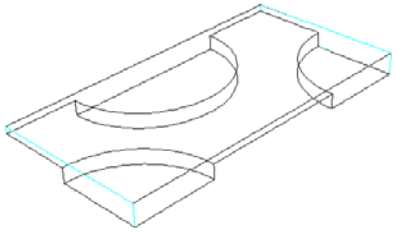

(b) Shallow round hole, ref. [8].

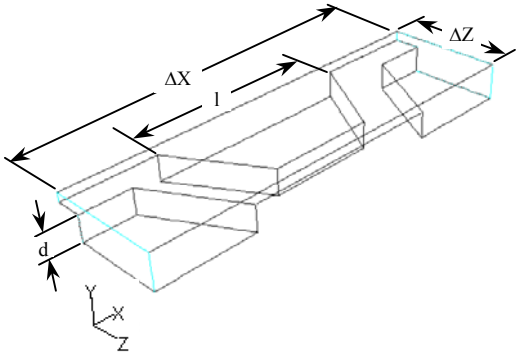


(c) Honeycomb, ref. [37].

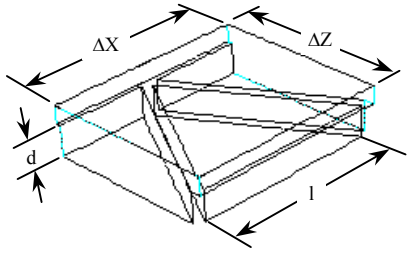


(d) Isogrid, ref. [36]. (twice the scale)

All experiments were run with water. Table VI summarizes main dimensions of each roughness pattern, the actual size of the minimum periodic, and the properties of the water used for simulations (extracted from each original experiment).

Table VI. Roughness pattern minimum periodic unit dimensions, water properties.

| Pattern | Γ, % | $C_r$, μm | l, mm | d, mm | ΔX, mm | ΔZ, mm | ρ, kg/m$^3$ | μ, cP. |
|---|---|---|---|---|---|---|---|---|
| Deep round-hole [8] | 44.4 | 130 | 3.175 | 2.000 | 5.944 | 3.000 | 986.0 | 0.495 |
| Shallow round-hole [8] | 83.4 | 175 | 3.175 | 0.280 | 5.944 | 3.000 | 986.0 | 0.495 |
| Isogrid [36] | 83.4 | 175 | 1.827 | 0.300 | 7.732 | 2.232 | 999.8 | 1.015 |
| Honeycomb [37] | 60.2 | 176 | 4.000 | 0.500 | 2.000 | 1.732 | 999.8 | 1.015 |

Numerical simulations were performed in the cases that involved no shaft rotation. The typical procedure for solving the RANS equations is as follows:

- Generate the geometry and the grid.
- Assign fluid properties and boundary conditions.

- Impose the pressure gradient.
- Choose flow solver/model (steady, laminar, turbulent, near-wall treatment, etc.).
- Initialize the flow field and run simulation until convergence (iterative).
- Store the converged flow field.
- Repeat process for each experimental run, when modeling specific data points from each experiment. Numerical trends outside the flow range tested are created by imposing larger pressure gradients.
- Assure numerical errors are minimized by using multiple grids, and grid convergence analysis techniques such as the relative error or the Grid Convergence Index [31].

## *4.2. Validation of the boundary conditions*

### *4.2.1. Periodicity*

A deliberately roughened seal with a moderate Γ ratio could contain easily several thousands of individual patterns. Our numerical tests indicate that the minimum number of grid nodes or cells using the periodic approach [46] to solve properly the flow features in the Reynolds number flow and clearance ranges under scrutiny are in the order of the ten thousands per roughness pattern. Therefore, considering only the seal gap and the volume occupied by each pattern one could be dealing with coarse grids easily exceeding ten millions of nodes per case. With actual computer power, few runs in a complete model is reasonable achievable. Thousands of simulations to perform a parametric analysis are still practically impossible. If the seal is manufactured with a pattern that is periodically repeated and the clearance is maintained along the seal length, the computational effort is substantially reduced by assuming and verifying that the flow can reach the fully developed condition within a very short distance from the seal inlet. As extensively discussed in Refs. [18,19,42], if the flow is fully developed the numerical domain can be reduced to a "small computational box" containing basically the seal/plate gap and one full pattern, indeed, the minimum periodic unit.

In section 3.7 of Ref. [19], an extensive analysis was included on the pressure gradient measured in Nava's experiments and several 2-D numerical tests to validate that the flow reached the fully developed condition after passing over very few roughness patterns. Those

experiments showed a long entry region in the larger clearances at very low Reynolds number, either laminar or transition flow. On the other hand, the flow was fully developed after a very short region in smaller clearances for Reynolds number above $10^5$. In liquid annular seals, smaller clearances and moderate to high Reynolds numbers are the norm. Numerically speaking, the periodic approach is expected to be valid when modeling constant clearance seals that are roughened with uniform patterns under no shaft rotation.

The numerical analysis of a true 2-D experiment described in section 2.4 included axisymmetric calculations performed on the whole seal to primarily estimate inlet and exit losses but valuable to validate the periodic unit approach used to in the parametric analysis of section 2.5, an approach that is the rock foundation of the whole analysis included in reference [19] and the present research.

Figure 31 present the 2-D axisymmetric model of "Seal 1" of Iwatsubo [38] experiments. To determine numerically the developing flow region, the local pressure gradient ratio was calculated as follows:

$$p_i = \frac{\Delta Px_i}{\Delta Px_{Ng}} \qquad i = 1,2,\ldots,Ng \tag{9}$$

A local pressure gradient ratio close to unity would indicate that the pressure gradient in that particular groove is equal to the one extracted from the last groove in the seal, when the flow is expected to be fully developed. Figure 32(a) presents predicted laminar flow local pressure gradient ratios along the seal for selected Reynolds number values.

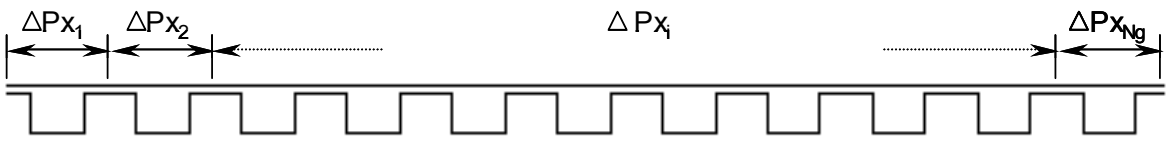


Figure 31. "Seal 1" axisymmetric model (inlet/exit regions not shown), local pressure gradient calculation.

At the lowest Reynolds number simulated shown in Figure 32(a), Re=39, the flow enters the annular seal gap practically undisturbed. At Re=161, the pressure gradient on the first groove is only 0.05% smaller than the reference. As the Reynolds is increased further,

the effect of the entry region is more noticeable, although the flow can be considered fully developed within 1% after the it has passed just two grooves in the largest Reynolds number case fully converged, Re = 391. The Re = 493 curve corresponds to a pressure gradient where the steady laminar solver did not reach a converged solution. It was included just as a reference on how turbulent pressure gradient ratios might look like.

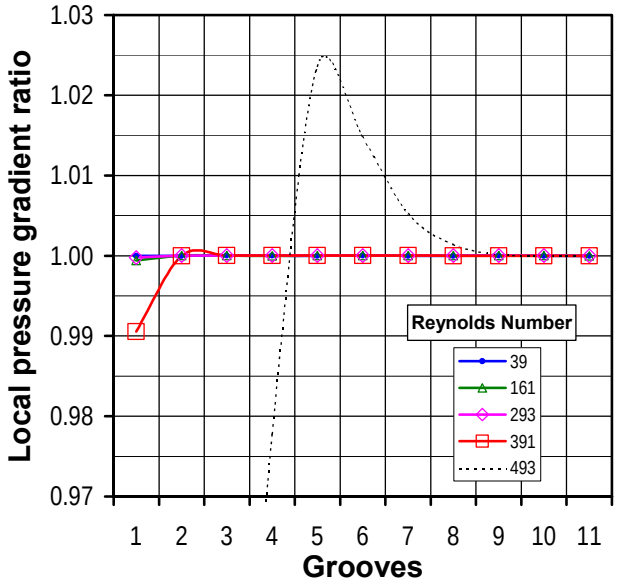


(a) Laminar flow calculations

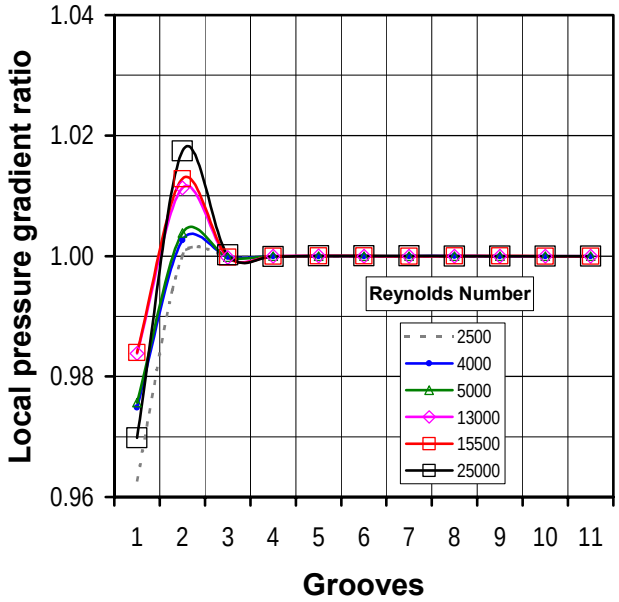


(b) turbulent flow calculations

Figure 32. Local pressure gradient ratio along “Seal 1” model.

Likewise, Figure 32(b) presents predicted turbulent flow local pressure gradient ratios along the seal for selected Reynolds number values. Like in section 2.4, results correspond to the RNG k-ε turbulence model for the core flow and wall functions as near wall treatment.

In the Reynolds number flow ranging from 2.5 to $5.0 \cdot 10^3$, the flow is fully developed within 1% after it has passed just the first groove. As the Reynolds number is increased further, the second groove is also part of the entry region, but the effect on the local pressure gradient is less than 2%.

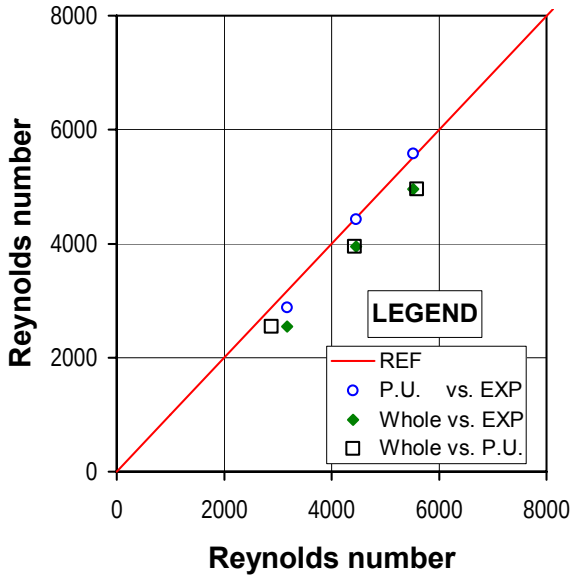


Figure 33. Predictions and 'Seal 1' measurements, 2-D periodic vs. 2-D whole seal axisymmetric modeling.

Finally, Figure 33 compares predictions of the 2-D periodic unit approach, the 2-D axisymmetric model, and the original flow measurements of 'Seal 1' in terms of the Reynolds number. While the periodic unit approach replicated the experiments within 1%, the axisymmetric model under-predicts the leakage by roughly 10% (Recall that the prevailing flow regime at the lowest Reynolds number flow tested in the experiments is uncertain). As indicated in section 2.4, explaining this behavior and the effect of the seal inlet and exit losses was well beyond the scope of the present research. In summary, the 2-D periodic unit approach has been validated and it was sufficient to replicate the experimental observations in the grooved seal of Iwatsubo [38].

Regarding 3-D simulations, a numerical analysis similar to the approach described in section 3.7 of Ref. [19] was performed. The minimum periodic unit based on the honeycomb of Kaneko [37] with the test clearance of 176 μm (~ 6.9 mils) was doubled in the stream wise direction and mirrored along a symmetry plane, to create what is called a double full periodic unit. Figure 34 compares the base minimum periodic unit (M.P.U.) and the double full periodic unit (2 P.U.), including the boundary conditions imposed on the X and Z boundary planes (no slip wall conditions are always imposed on the Y boundary planes).

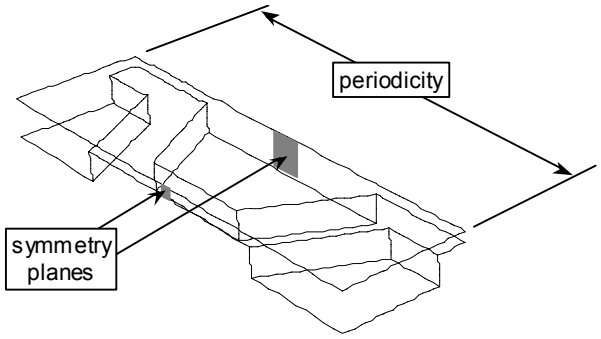


(a) Minimum periodic unit.

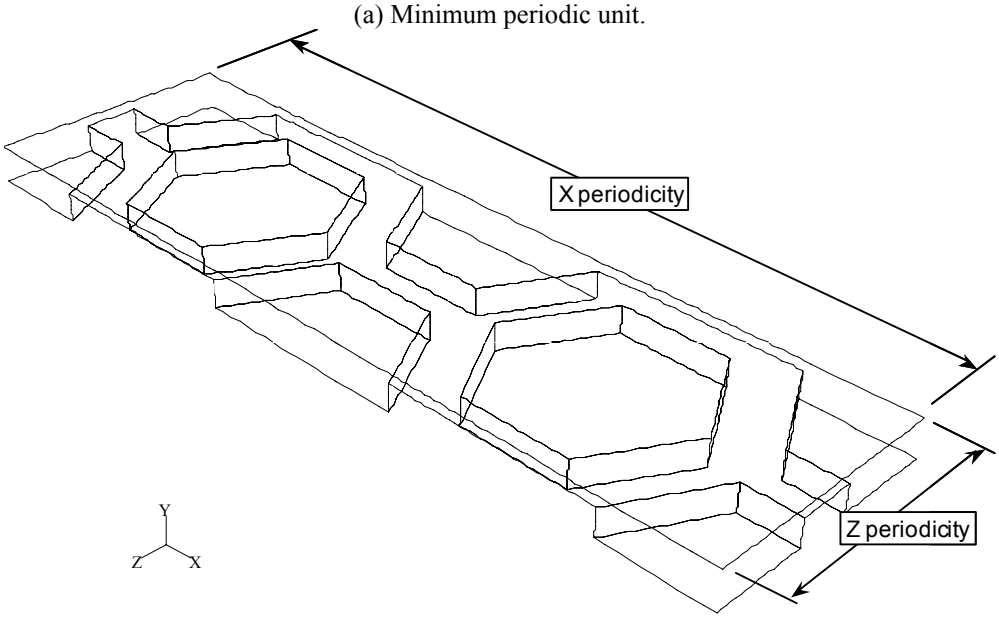


(a) Double full periodic unit.

Figure 34. Numerical domains of the Kaneko's honeycomb geometry, periodicity validation.

Figure 35 compares predictions in the M.P.U. and 2 P.U. honeycomb domains with the

laminar model. Results correspond to the power law discretization scheme for all variables, the PRESTO scheme for pressure, and the PISO option for the pressure-velocity linking algorithm. The performed doubling and mirroring guarantees that meshing is identical in both models.

Deviations in predicted Reynolds number, Figure 35(a), do not exceed 0.06%. When predictions are compared in terms of friction factor, Figure 35(b), maximum deviations do no exceed 0.13%. These results confirm that the numerical model replicates the flow field from roughness pattern to roughness pattern, an indication that periodicity is achieved.

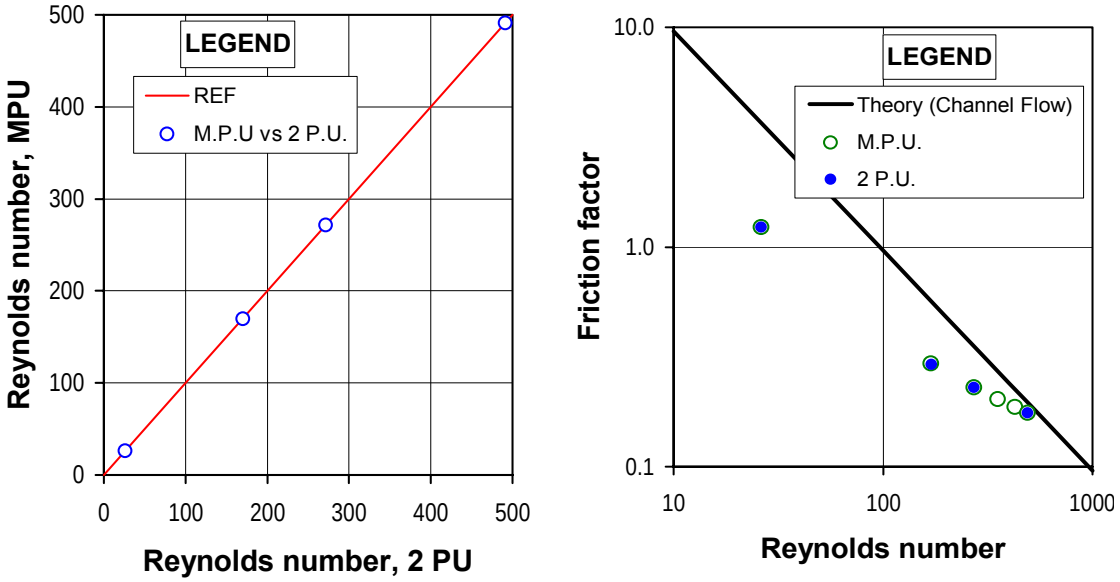


(a) Reynolds numbers (b) Friction Factor

Figure 35. M.P.U. vs. 2 P.U. solutions in the honeycomb geometry, laminar solutions.

Figure 36 compares again predictions in the M.P.U. and 2 P.U. honeycomb domains but now with the turbulent model. Simulation results correspond to the power law discretization scheme for all variables, the PRESTO scheme for pressure, and the PISO option for the pressure-velocity linking algorithm. The RSM model was used in the core flow with the so-called enhanced wall treatment as near-wall treatment, with identical $y^+$ values.

Deviations in predicted Reynolds number, Figure 36(a), do not exceed 0.02%. When predictions are compared in terms of friction factor, Figure 35(b), maximum deviations do no exceed 0.04%. Again, these results confirm that the numerical model replicates the flow field from roughness pattern to roughness pattern, an indication that periodicity is achieved.

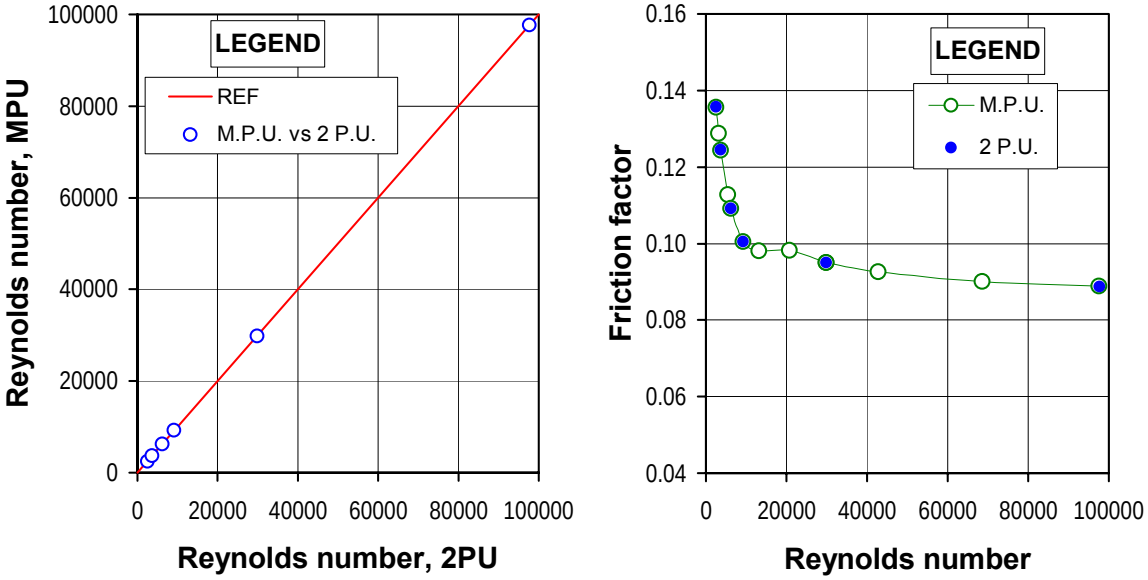


(a) Reynolds numbers (b) Friction Factor

Figure 36. M.P.U. vs. 2 P.U. solutions in the honeycomb geometry, turbulent solutions.

In summary, the 3-D numerical analysis of the periodicity condition confirms the observations of Kaneko[37] that the fully developed condition is achieved. Indeed, his axial pressure distribution measurements indicate that the entry region and actual inlet losses in the honeycomb seal are negligible in comparison to the smooth seal, which showed a significant length for the entry region and a localized pressured drop of roughly 20%.

### *4.2.2. Symmetry*

As introduced in section 3.1, most calculations described herein have been performed using what is called the minimum periodic unit. In contrast, all previous 3-D numerical research in flow over roughened surfaces invoking periodicity have use a domain that contains at least two patterns; one full pattern in the center of the domain and four quarters, one on each corner. To recover the original surface length, the periodic unit would be replicated on either planar direction. Invoking symmetry, the periodic unit can be divided in half to contain just one pattern, the absolute minimum, one half of the pattern in the sided center of the domain, and two quarters, one at either end of the domain oppositely sided to the one half in the center.

The minimum periodic unit approach was validated in selected clearances of all pattern geometries under simulation. Presented here the studies performed on the small recess or round hole pattern of Nava [30] and the honeycomb of Kaneko [37]. Figure 37 compares the classical periodic unit and the minimum periodic unit of the small recess for the clearance of 254 μm (10 mils).

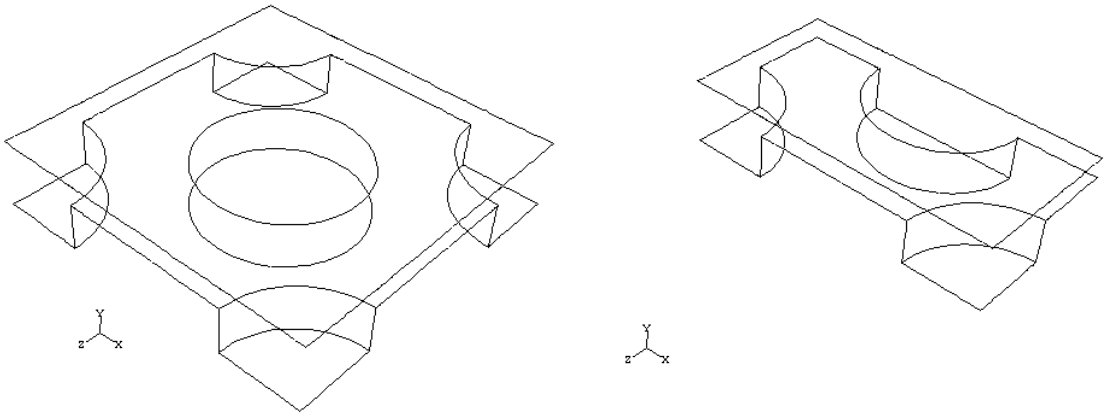

(a) Classical or full periodic unit. Minimum periodic unit.

Figure 37. Numerical domain of the small recess geometry [30], 254 μm (10 mils) clearance.

Figure 38 compares the predicted flow rate of the minimum periodic unit (MPU) with the value obtained in the full periodic unit (PU) of the small recess geometry for a given pressure gradient and in terms of the Reynolds number. Numerical results correspond to the

final grid on each geometry, the power law discretization scheme, and the PISO option for the pressure-velocity linking algorithm. Simulations include results in the laminar regime, and low and high Reynolds number flow range. Low Reynolds number results were obtained with the standard k-ε model and the two-layer zonal approach, $y^+$ equal to 0.15~5.06 (enhanced wall treatment [24]). High Reynolds number results were obtained with the wall function approach for the near-wall treatment of turbulence, $y^+$ equal to 14.8~28.1.

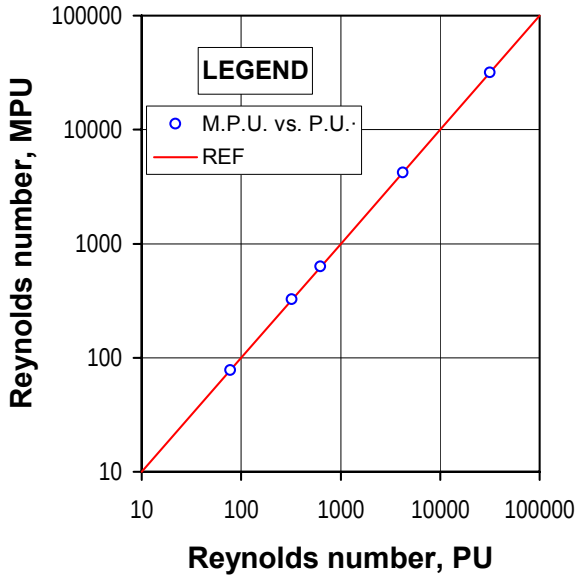


Figure 38. Comparison of flow rate predictions in both small recess periodic units.

Flow predictions in both regimes, laminar and turbulent, and with all turbulence models tested are equal within 0.02%, and deviations barely exceeded 0.05% in one case. Figure 39 compares several profiles along the symmetry plane of both numerical domains for a laminar case with a pressure gradient of $2 \cdot 10^4$ Pa/m. Local X-velocity deviations averaged less than 0.3% and rarely exceeded 1.0%. On the other hand, local Y-velocity and vorticity deviations averaged less than 1.0 % and rarely exceeded 10%. It should be noted that averaged deviations are largely affected by the local absolute value of the variable under scrutiny. Largest deviations were observed in the X1 coordinate Y-velocity profiles where its absolute value is close to zero.

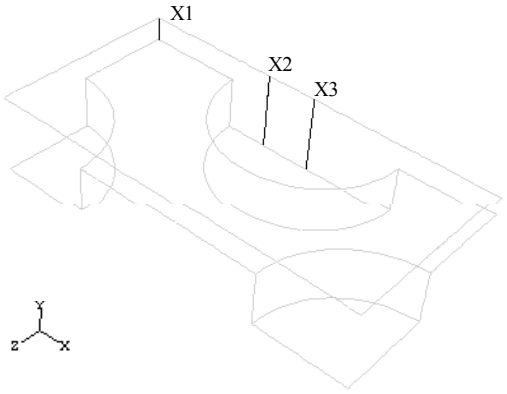


X1 = 0.00 mm
X2 = 1.46 mm
X3 = 2.00 mm (50% of the pattern length)

(a) PU symmetry plane constant X lines, MPU shown.

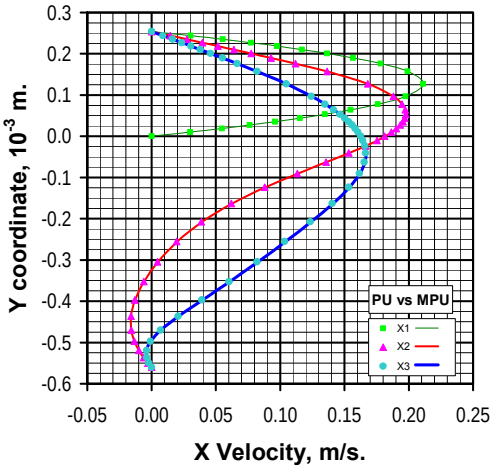


(b) X Velocity profile.

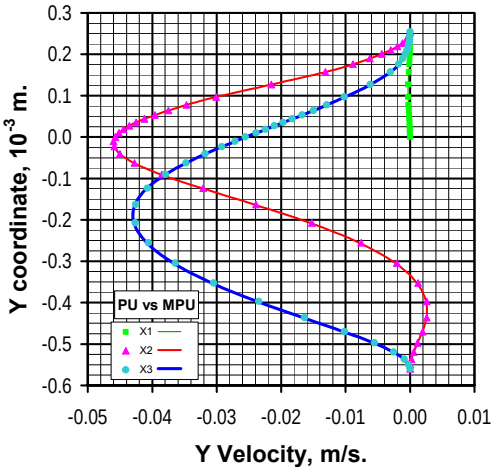


(c) Y velocity profile

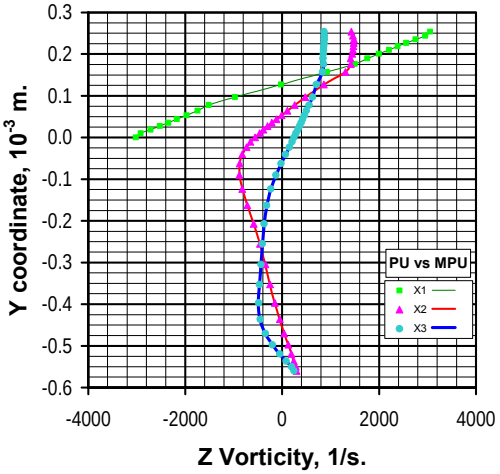


(d) Symmetry plane vorticity

Figure 39. PU and MPU numerical profiles of the small recess geometry at Re~80, 254 μm (10 mils) clearance.

Similarly, Figure 40 compares several profiles along the symmetry plane of both numerical domains for a turbulent case with a pressure gradient of $2 \cdot 10^8$ Pa/m. Local X-velocity deviations averaged less than 0.2% and rarely exceeded 1.0%, while local Y-velocity averaged less than 2.0 % and rarely exceeded 10%. On the other hand, local turbulent kinetic energy deviations averaged less than 0.1 % and rarely exceeded 1%, while local turbulent dissipation deviations averaged less than 0.5 % and rarely exceeded 2%. Again, calculated deviations are largely affected by the local absolute value of the variable under scrutiny.

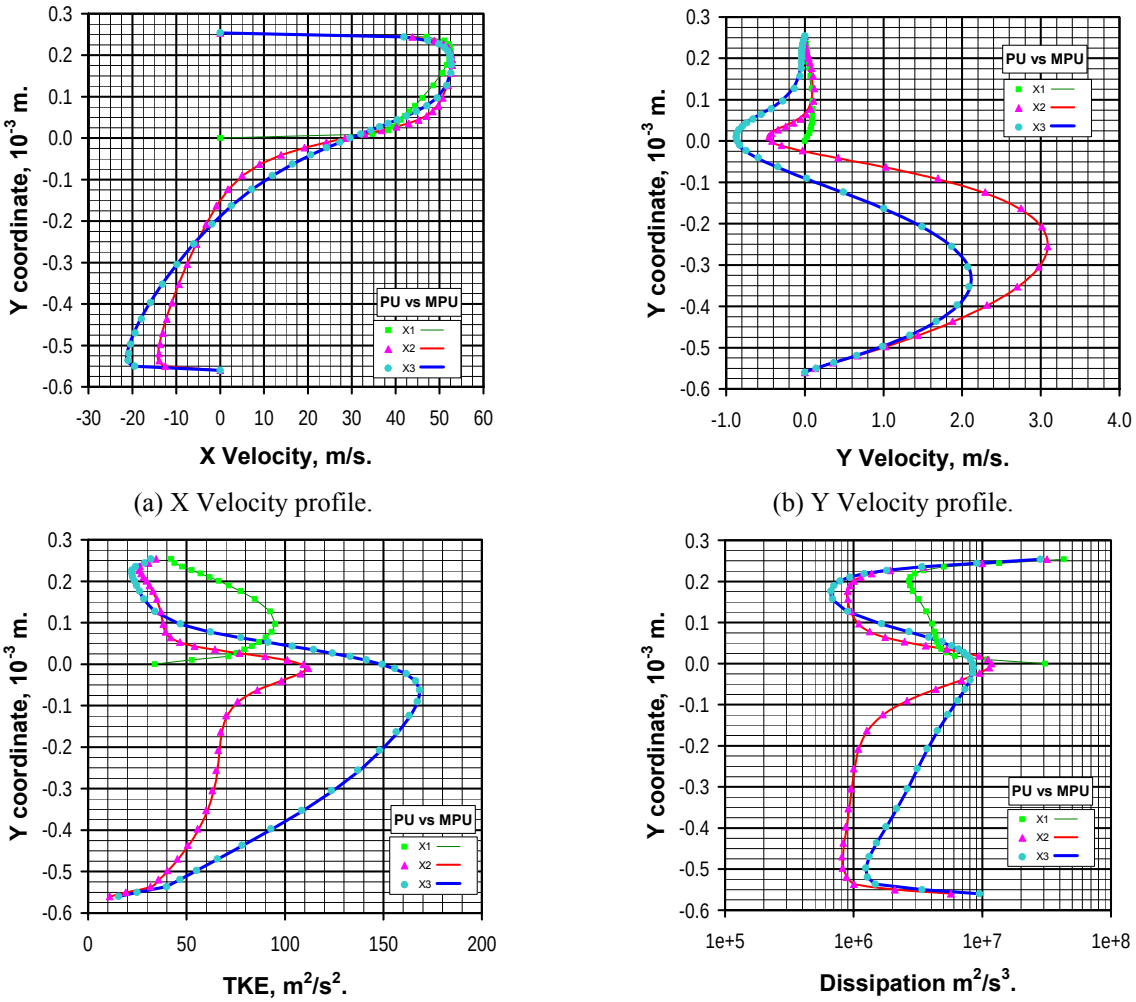


(a) X Velocity profile.

(b) Y Velocity profile.

(c) Turbulent kinetic energy profile.

(d) Turbulent dissipation profile.

Figure 40. PU and MPU numerical profiles of the small recess geometry at Re~$3.2 \cdot 10^4$, 254 μm (10 mils) clearance.

Likewise, Figure 41 compares geometries of the classical periodic unit and the minimum periodic based on the honeycomb of Kaneko [37] for the test clearance of 176 μm (~6.9 mils).

Figure 42 compares the predicted Reynolds number in the MPU versus the value obtained in the PU for a given pressure gradient. Numerical results correspond to the final grid of each geometry, the power law discretization scheme, and the PISO option for the pressure-velocity linking algorithm. Simulations are shown in the laminar and turbulent regime separately. The Reynolds stress model was used in the core flow (locally high Reynolds number), while both two-layer zonal model and wall functions for the near-wall

treatment were used depending on the Reynolds number values. At low Reynolds number results were obtained by maintaining $y^+$ equal to 1.26~23.1, while $y^+$ exceeded 28.8 at high Reynolds number. A complete discussion on the validity of $y^+$ values for each near-wall treatment of turbulence is included in section 4.3. At this point, it is sufficient to mention that both numerical solutions, MPU and PU, have identical $y^+$ values in the common domain in the whole Reynolds number flow range under study.

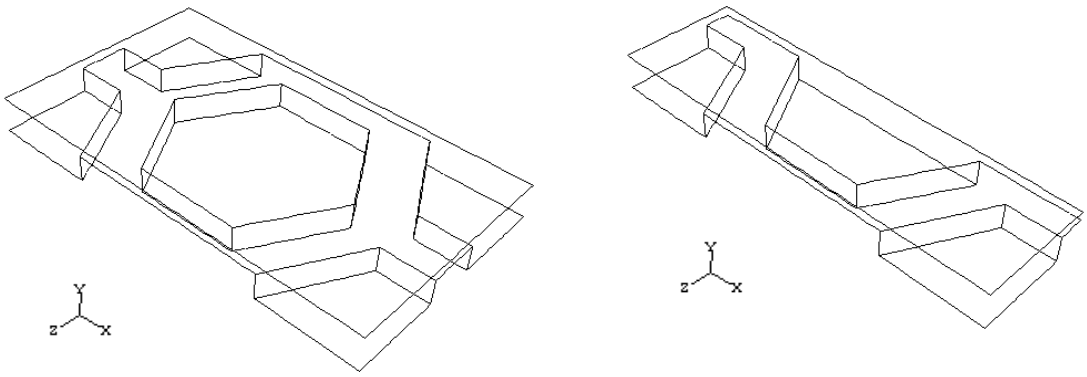

(a) Classical or full periodic unit. Minimum periodic unit.

Figure 41. Numerical domain of the Kaneko's honeycomb geometry, 176 μm (~7 mils) clearance.

Flow predictions in the laminar flow regime are equal within 0.05% and deviations barely exceeded 0.20% in one case. Flow predictions in the turbulence regime with the models tested are equal within 0.02%.

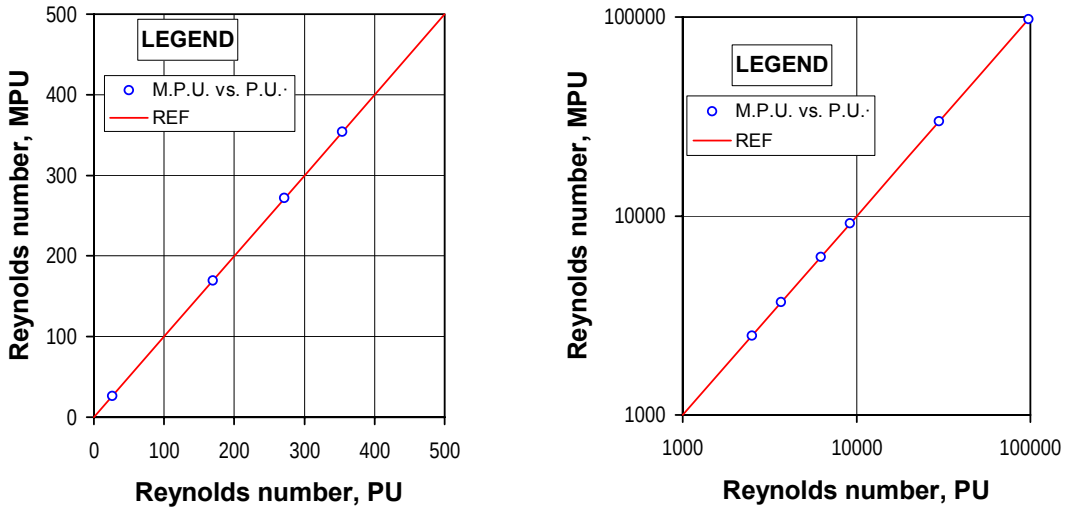


(a) Laminar flow regime (b) Turbulent flow regime

Figure 42. Comparison of flow rate predictions in both periodic units of the honeycomb.

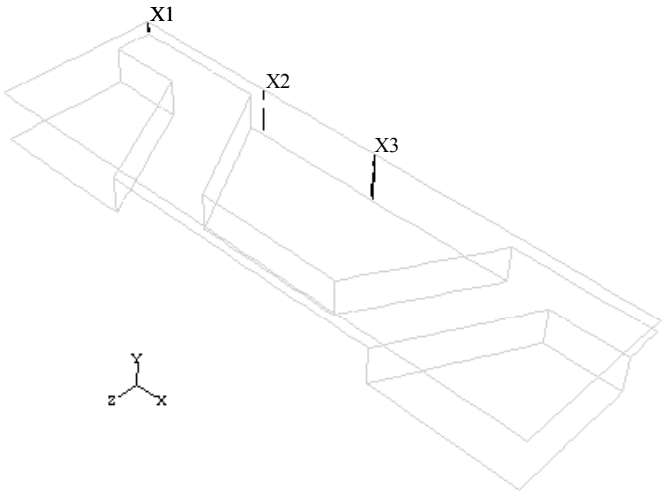


X1 = 0.00 mm
X2 = 2.07 mm
X3 = 3.87 mm (50% of the pattern length)

(a) PU symmetry plane constant X lines, MPU shown

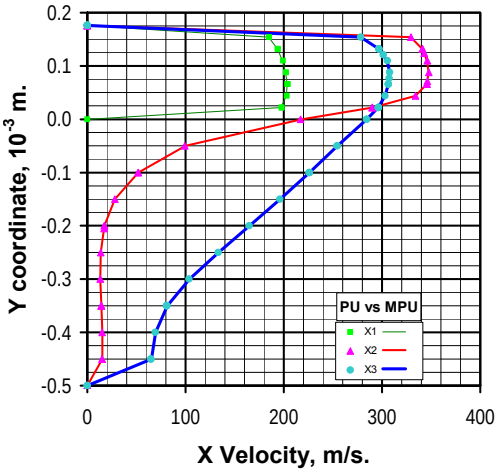


(b) X Velocity profile.

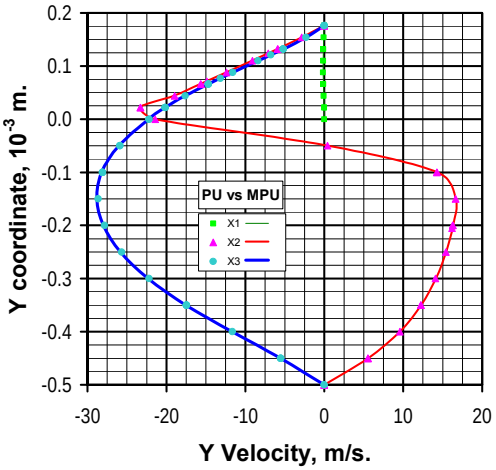


(c) Y Velocity profile.

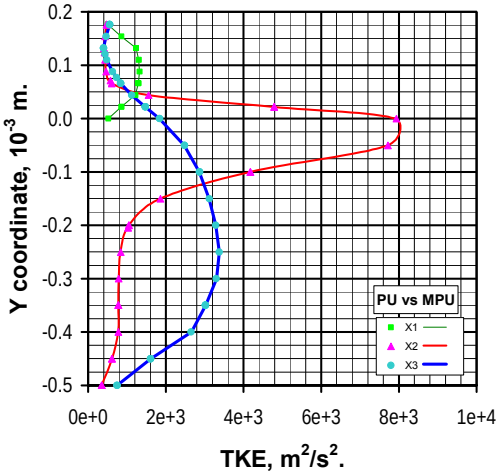


(d) Turbulent kinetic energy profile.

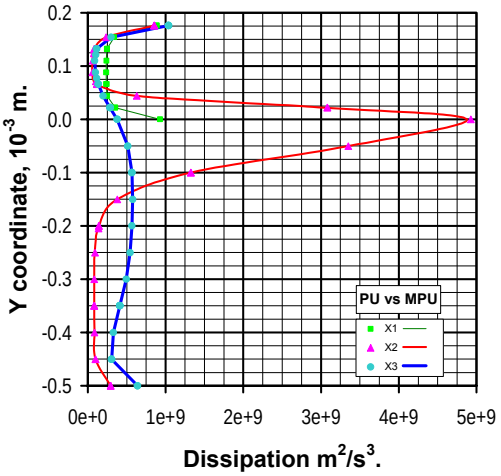


(e) Turbulent dissipation profile.

Figure 43. PU and MPU numerical profiles in the honeycomb geometry at Re~$9.8 \cdot 10^5$, 176 µm (~7 mils) clearance.

Figure 43 compares several profiles along the symmetry plane of both numerical domains for the largest Reynolds number turbulent case, pressure gradient of $1 \cdot 10^{10}$ Pa/m. Local X-velocity deviations averaged less than 0.1% and exceeded 1.0% once. On the other hand, local Y-velocity averaged less than 0.3 % but exceeded 3% in the X1 line where the largest absolute value is 0.15 m/s (less than 0.08% of the local X-velocity values). Similarly, local turbulent kinetic energy deviations averaged less than 0.1 % and did not exceed 0.9%, while local turbulent dissipation deviations averaged less than 0.3 % and rarely exceeded 1%.

Similar results were obtained in the remaining of the pattern geometries under simulation. Mass flow rate and friction factor predictions in the Minimum Periodic Unit and the full Periodic are similar within 0.20%. Similarly, local differences in velocity and other variables profiles rarely exceeded 1%. Deviations exceeding 1% were always associated to local velocity profiles close to zero and several orders of magnitude smaller than the prevailing mean velocity magnitude of the flow. In summary, the minimum periodic unit approach is numerically equivalent to the traditional full periodic unit approach, and the numerical effort to simulate a particular geometry of a repeated pattern in a concentric annular seal is reduced in half.

### *4.2.3. Pressure gradient vs. mass flow rate*

The use of the periodic approach to simulate fully developed turbulent flow requires a slight modification in the pressure gradient term of the traditional Reynolds averaged Navier Stokes equations. While all remaining flow variables are treated as if the domain is repeated infinitely so discretized equations form a closed loop in the stream wise direction, as shown in equation (10):

$$V(\vec{r}) = V(\vec{r} + \vec{L}) = V(\vec{r} + 2 \cdot \vec{L}) = V(\vec{r} + 3 \cdot \vec{L}) = \ldots \qquad V = u, v, w, k, \varepsilon, \overline{u_i' u_j'} \tag{10}$$

the pressure term needs to be modified because the absolute pressure is not repeated. It is the periodic pressure or pressure drop between modules [24], or periodic units, that actually repeats itself in the stream wise direction, equation (11):

$$\Delta P|_{\vec{r}}^{\vec{r}+\vec{L}} = P(\vec{r}) - P(\vec{r} + \vec{L}) = P(\vec{r} + \vec{L}) - P(\vec{r} + 2 \cdot \vec{L}) = P(\vec{r} + 2 \cdot \vec{L}) - P(\vec{r} + 3 \cdot \vec{L}) = \ldots \tag{11}$$

As discussed in section 3.5 of reference [19], the pressure gradient is decomposed into two parts [24], the gradient of a linearly varying component in the mean flow direction, and the gradient of a periodic component, the periodic static pressure gradient:

$$\nabla P(\vec{r}) = \beta \cdot \frac{\vec{L}}{|\vec{L}|} + \nabla \widetilde{P}(\vec{r}) \tag{12}$$

Term $\beta \cdot \vec{L} / |\vec{L}|$ is related to the global mass flow and $\nabla \widetilde{P}(\vec{r})$ is related to the detailed local motions [46]. In the software segregated solver option, the user can either specify the mass flow rate, $\dot{m}$, crossing the periodic boundary or the linear pressure gradient term, $\beta$. Preliminary convergence tests performed in both 2-D and 3-D domains [19] indicated that prescribing $\beta$ instead of $\dot{m}$ resulted in straightforward converged solutions; indeed, no 2-D converged solution was obtained then while prescribing $\dot{m}$.

All numerical solutions obtained and presented herein have been obtained by prescribing the linearly varying pressure gradient, $\beta$. As discussed in sections 2.1, 2.2, and 3.1, preliminary 3-D simulation results based on Nava's [30] experiments seemed to

confirm the constant over prediction of the friction factor obtained with the 2-D numerical approach [19]. In theory, either prescribing $\beta$ or $\dot{m}$ should result in the same numerical solution. In practice, some pilot cases were run to validate that results should not change if $\dot{m}$ is prescribed instead of $\beta$, and to possibly find an explanation to the early difficulty encountered in using such approach.

Figure 44 compares static pressure profiles and contours in the honeycomb MPU for the 176 µm (7 mils) clearance with prescribed $\beta$ versus the solution obtained while prescribing $\dot{m}$. Results correspond to identical grids, the power law discretization scheme, and the PISO option for the pressure-velocity linking algorithm. The standard k-ε model was used in the core flow with wall functions as near-wall treatment, with $y^+$ equal to 11.3~31.1.

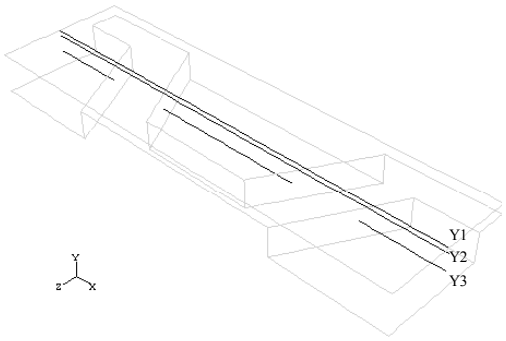


Y1 = 176 µm (top wall)
Y2 = 88 µm (mid-clearance)
Y3 = -200 µm (40% of the pattern depth)

(a) MPU constant Y lines.

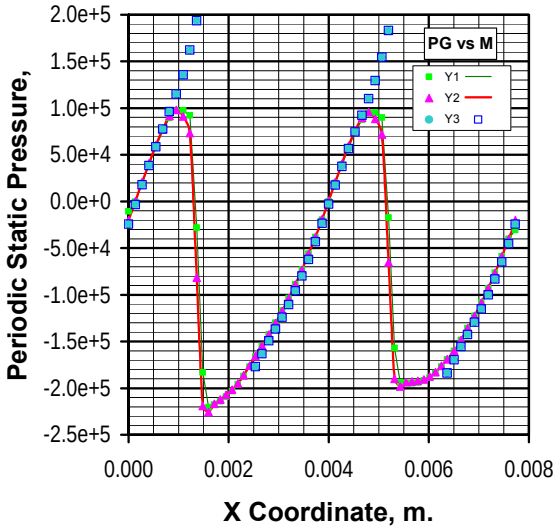


(b) Periodic static pressure profiles.

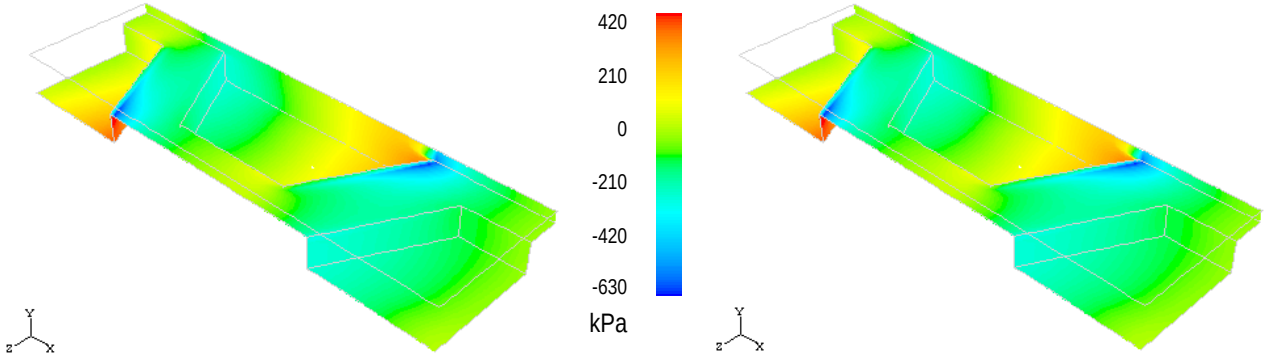


(c) PG solution bottom wall static pressure contour

(d) M solution bottom wall static pressure contour

Figure 44. Prescribed $\beta$ (PG) vs. $\dot{m}$ (M) solution profiles, honeycomb [37] geometry at Re~$10^4$.

Local static pressure deviations averaged less than 0.01%, exceeding 0.10% just once on the Y3 coordinate profile, and 1.0% only twice on the Y1 and Y2 coordinate profiles. Again, largest deviations are associated with absolute values that are actually close to zero. On the other hand, deviations are simply imperceptible when comparing pressure contours on the bottom wall of both solutions.

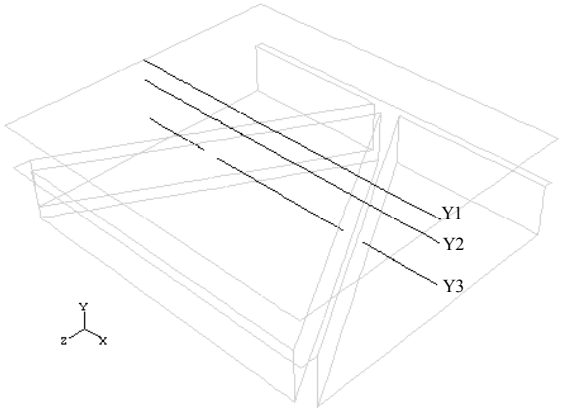


Y1 = 254 µm (top wall)
Y2 = 127 µm (mid-clearance)
Y3 = -112.5 µm (~40% of the pattern depth)

(a) MPU constant Y lines.

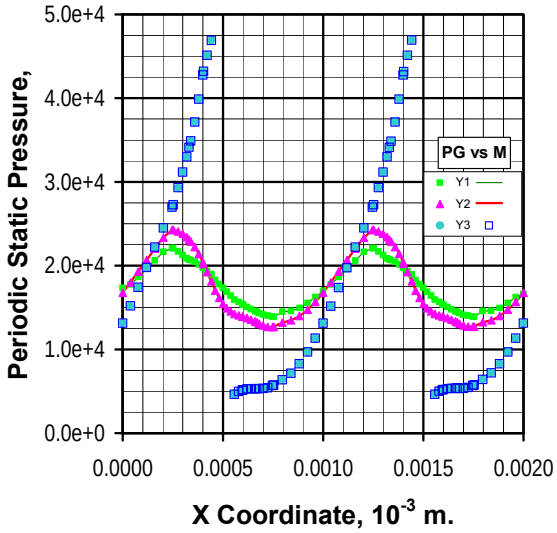


(b) Periodic static pressure profiles.

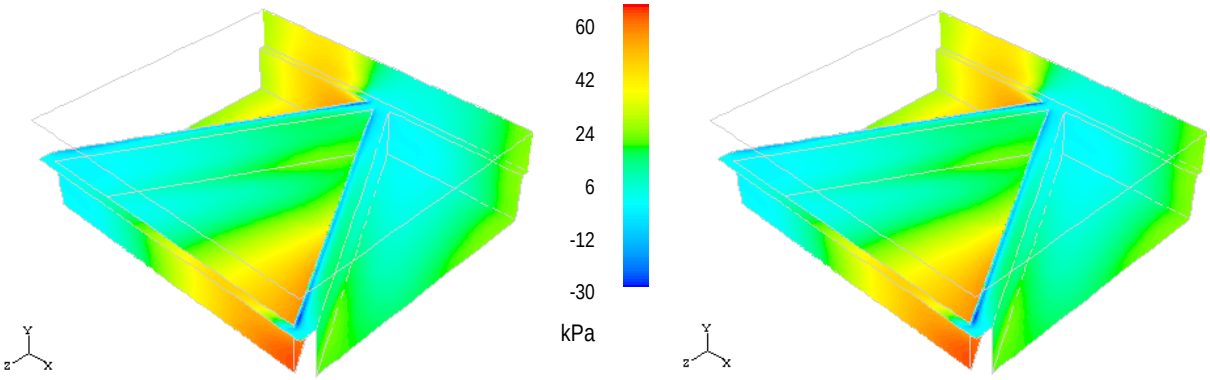


(c) PG solution bottom wall static pressure contour

(d) M solution bottom wall static pressure contour

Figure 45. Prescribed $\beta$ (PG) vs. $\dot{m}$ (M) solution profiles, isogrid [36] geometry at Re~$6 \cdot 10^3$.

Likewise, Figure 45 compares static pressure profiles and contours in the isogrid MPU for the 254 µm (10 mils) clearance with prescribed $\beta$ versus the solution obtained while prescribing $\dot{m}$ instead. Results correspond to identical grids, the power law discretization scheme, and the PISO option for the pressure-velocity linking algorithm. The standard k-ε

model was used in the core flow with the two-layer zonal model as near-wall treatment, with $y^+$ equal to 0.39~14.42.

Local static pressure deviations averaged less than 0.0002% for all cases. Similarly, they are imperceptible when comparing bottom wall pressure contours of both solutions.

Additional tests with the laminar model yielded similar results; there is no difference in the flow field resolution when prescribing either the pressure gradient or the mass flow rate. On the other hand, while performing theses pilot tests it was observed again that the convergence process is more stable when prescribing the pressure gradient. As described in the manual [24], prescribing the mass flow rate, $\dot{m}$, at the periodic boundaries requires an additional loop within the pressure correction algorithm to calculate the linearly-varying pressure gradient, β. Default relaxation factors in this additional iteration loop were adjusted in some cases of the performed pilot tests to achieve convergence, even when the 'exact' mass flow rate was prescribed at the boundaries. No indication is given in the manual [24] on how the term β is estimated when the solver tries to match the calculated mass flow rate with the prescribed value at the boundaries. Given the periodic approach formulation stated in equation (12), it might be inferred that imposing the 'exact' β value in every cell when the user prescribes the linearly-varying pressure gradient, and letting the solver finding a converged flow field, where the mass flow rate is simply an integrated quantity at the boundary, has to be a more stable numerical approach, rather than calculating or extracting a common β value from a 'floating' flow field to be imposed in every cell so the integration process in the boundary yields the prescribed mass flow rate.

In summary, prescribing the linearly-varying pressure gradient β and imposing the mass flow rate $\dot{m}$ at the boundaries in the periodic approach are numerically equivalent. The additional iteration loop within the pressure iteration correction algorithm when the mass flow rate is prescribed is thought to be the reason that prescribing the linearly-varying pressure gradient results in a more stable convergence process.

### *4.2.4. Interface interpolation*

As discussed extensively in the 2-D numerical analysis of Nava's experiments [19,42], the friction-factor-to-clearance proportionality was better captured when using the two-layer zonal approach as near-wall treatment of turbulence. Then, it was apparent that wall functions neglected the effect of the clearance in such 2-D approach, indeed predicting comparable friction factors for the range of Reynolds numbers and clearance values under scrutiny. An updated 3-D review of the performance of each near wall treatment is included in section 4.3. Here, it is simply emphasized that the two-layer zonal approach (updated in [24] as the enhanced wall treatment) requires using extremely fine grid near each wall in the numerical domain. In a smooth surface, refining the wall distance of the first cell in the numerical domain is straightforward. In an artificially roughened surface, refining the distance of the first cell closest to each wall defining the roughness pattern affects the grid of all nearby cells in the numerical domain when using conformal grids.

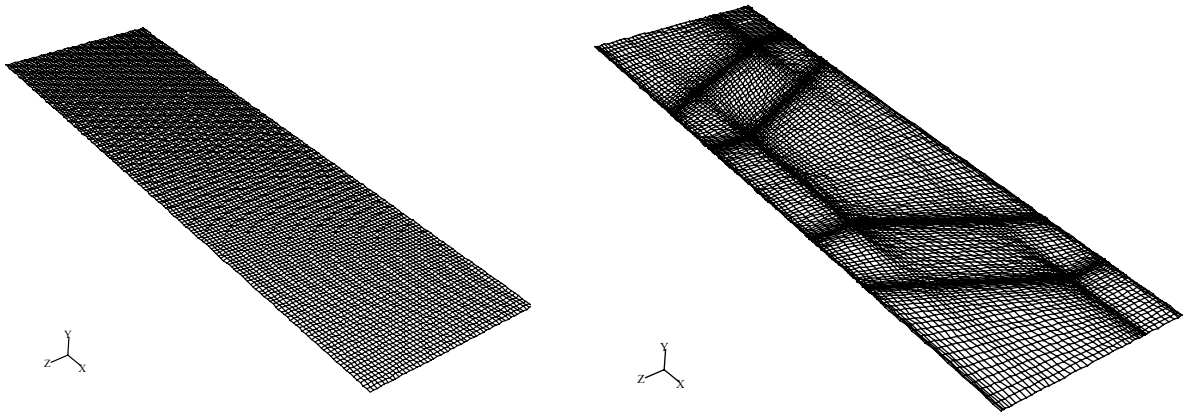

(a) Uniform grid (b) Boundary layer type grid

Figure 46. Honeycomb pattern constant Y coordinate plane grids.

Figure 46 compares the XZ (constant Y coordinate) planes of the finest grids used in modeling the honeycomb pattern of Kaneko[37]. Figure 46(a) shows a uniform mesh in the X and Z directions, while 46(b) shows a non-uniform mesh that is the result of projecting towards the seal clearance the same boundary layer type mesh, clustered to each roughness wall, developed to reproduce the roughness pattern. In this figure, the shape of the honeycomb pattern can easily be inferred noting that near-wall cells create darker and

thicker lines in the low-resolution images.

Creating a seal clearance numerical block by projecting the boundary layer type mesh of the roughness pattern results in grids containing very small cells in locations where high resolution in the numerical model is not required, leading presumably to convergence problems and certainly to grids with additional number of nodes. One of the techniques proposed to overcome this problem [47] is the use of non-connecting multiple blocks in the numerical domain. Contiguous non-connecting blocks share adjacent faces but the grids on those faces do no need to be connected, the numerical information is transferred by interpolation. Simulations in pilot cases were performed to evaluate if using the multiple block technique could result in an advantage when modeling flow over roughened surfaces.

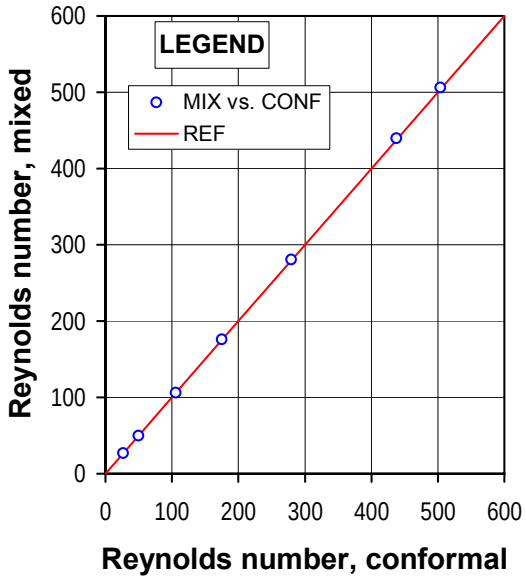


Figure 47. Comparison of flow rate predictions in mixed and conformal grid MPU's, honeycomb geometry.

Figure 47 compares predicted mass flow rates, in terms of Reynolds number, in the minimum periodic units based on the honeycomb geometry, two block mixed grid (mixed) and single block conformal grid (conformal), for a given pressure gradient in the laminar flow regime. The mixed MPU was created projecting the grid shown in Figure 46(a) into the top half of the numerical domain (from half the 176 μm test clearance to the top smooth wall), and the grid shown in Figure 46(b) into the bottom half of the numerical domain including the roughness pattern. The conformal MPU was created projecting the latter the

grid into the whole numerical domain. Numerical results correspond the power law discretization scheme, and the PISO option for the pressure-velocity linking algorithm.

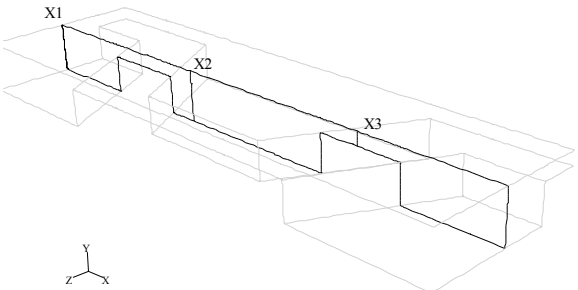


X1 = 0.00 mm
X2 = 2.93 mm
X3 = 5.77 mm

(a) MPU mid Z-coordinate plane constant X lines

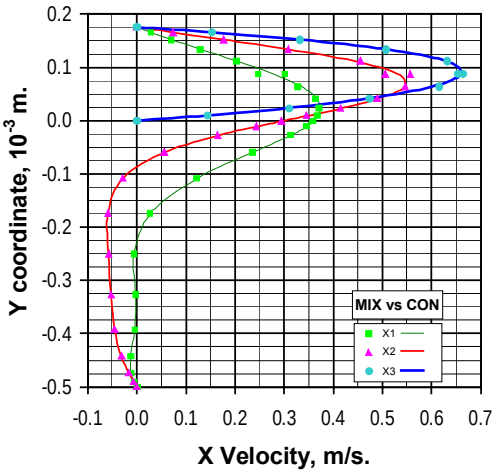


(b) X Velocity profile.

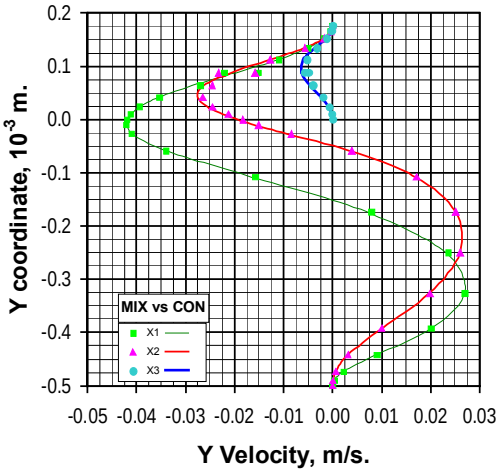


(c) Y velocity profile

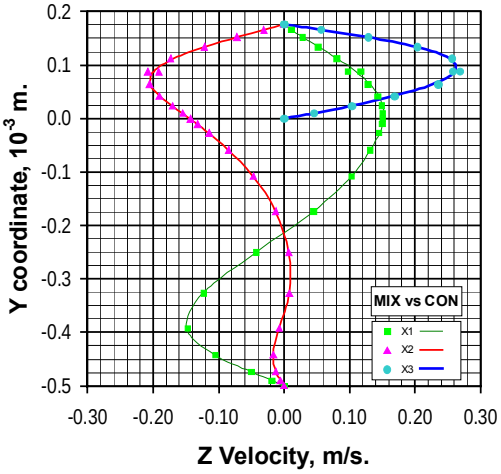


(d) Z velocity profile

Figure 48. Mixed and conformal grid numerical profiles of the Kaneko's honeycomb at Re~175.

Deviations in flow prediction range from 0.15% to 0.47%. Figure 48 compares several profiles along a Z-coordinate plane of both mixed and conformal grid geometries for a laminar case with a pressure gradient of $1 \cdot 10^5$ Pa/m. Local X-velocity deviations averaged 2.30% and 2.22% in the X1 and X2 lines, and 1.38% in the X3 line. Similarly, local Z-velocity deviations averaged from 1.53%to 1.96%. On the other hand, local Y-velocity deviations averaged 2.46% in the X1 line, 4.98% in the X2 line, and 13.7% in the X3 line. It should be noted that averaged deviations are largely affected by the local absolute value of

the variable under scrutiny. In this case, larger deviations were observed in the cells located in the interface of the mixed grid and within the roughness pattern where profile values are close to zero and change sign several times.

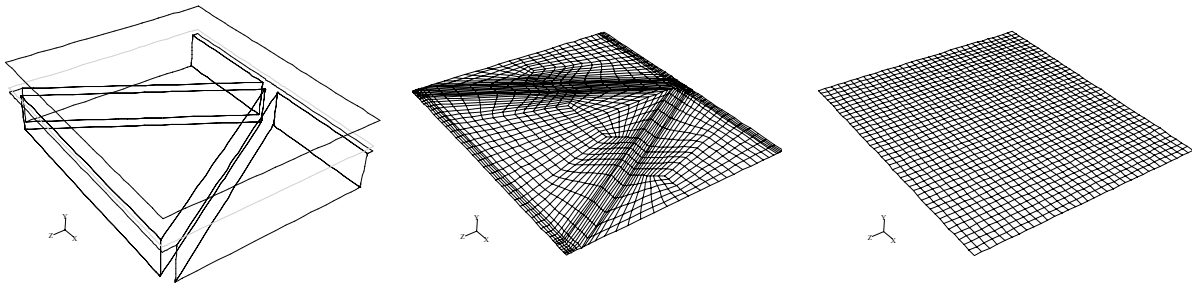

(a)Interface location (b) Non-uniform grid (bottom block) (c) Uniform grid (top block)

Figure 49. Isogrid pattern multi-block geometry and constant Y coordinate plane grids.

Similarly, Figure 49 shows the details of the grids used in modeling the isogrid pattern of Iwatsubo [36] with the multi-block approach for the clearance of 254 μm ( 10 mils).

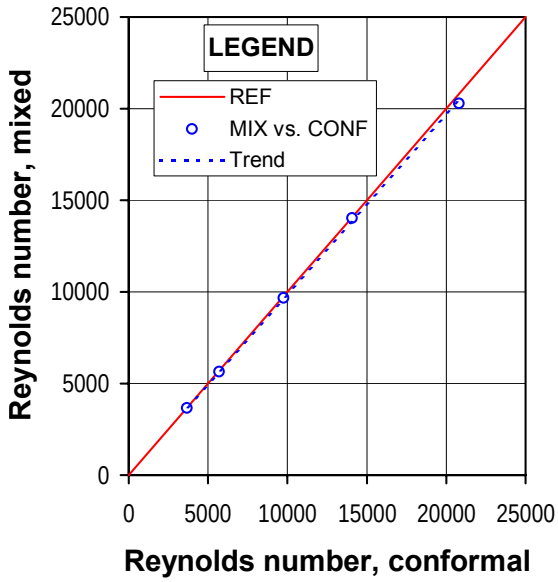


Figure 50. Comparison of flow rate predictions in mixed and conformal grid MPU's, isogrid.

Figure 50 compares predicted flow rates in the isogrid two block mixed grid minimum periodic unit (mixed) and the values obtained in the single block conformal grid minimum periodic unit (conformal) for a given pressure gradient in terms of the Reynolds number in

the turbulent flow regime. Numerical results correspond the power law discretization scheme, and the PISO option for the pressure-velocity linking algorithm. The standard k-ε model was used in the core flow with the two-layer zonal model as near-wall treatment, with $y^+$ equal to 0.15~4.03 for the mixed grid and 0.36~3.17 for the conformal grid.

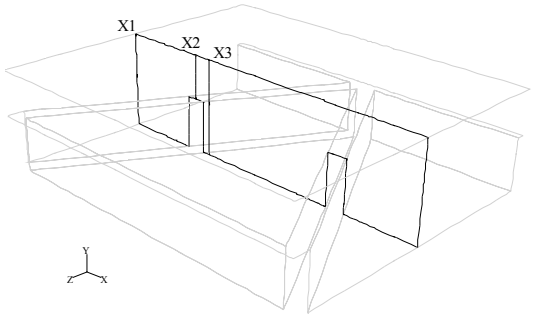


X1 = 0.00 mm
X2 = 0.50 mm
X3 = 0.60 mm

(a) MPU mid Z-coordinate plane constant X lines

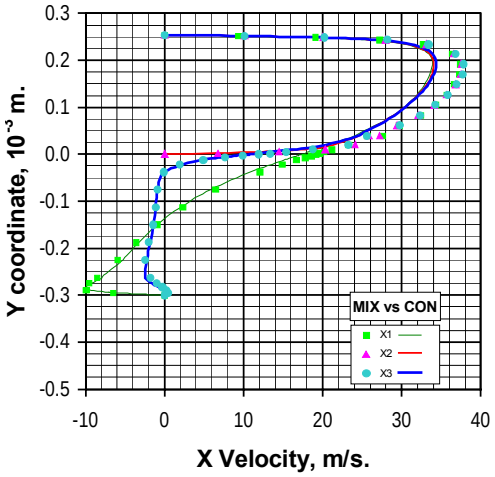


(b) X Velocity profile.

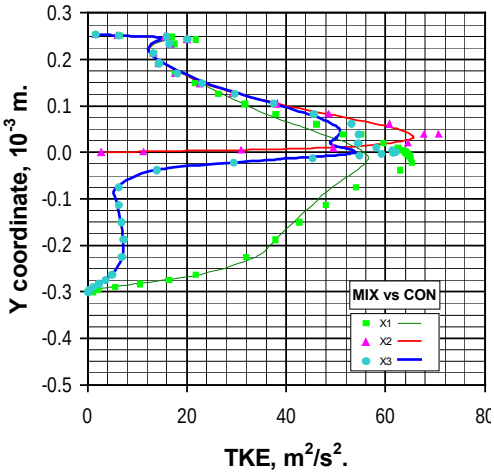


(c) Turbulent kinetic energy profile

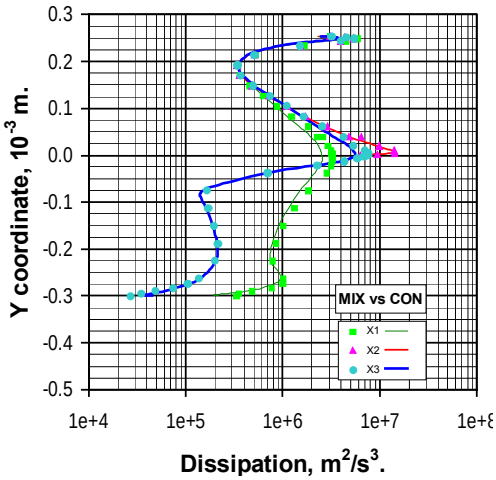


(d) Turbulent dissipation

Figure 51. Mixed and conformal grid numerical profiles of the Iwatsubo's isogrid at Re~$1.4 \cdot 10^4$.

Deviations in flow prediction range from 0.31% to 2.48%. Figure 51 compares several profiles along a Z-coordinate plane of both mixed and conformal grid geometries for a turbulent case with a pressure gradient of $1 \cdot 10^8$ Pa/m. Local X-velocity deviations averaged 8.66% in the X1, 10.5% in the X2 line, and 9.47% in the X3 line. Similarly, local turbulent

kinetic energy deviations averaged from 9.81% to 14.0%. On the other hand, local turbulent dissipation deviations averaged from 24.8% to 30.4%. In this case, deviations are mostly associated with accentuated profile differences in the cells located near the interface of the two block mixed grid minimum periodic unit.

While deviations in mass flow rate predictions in both flow regimes in the geometries tested are reasonable and in most cases below 2%, they are several orders of magnitude larger than the deviations associated with the use of alternative boundary conditions and modeling approaches presented in previous sub-sections. On the other hand, deviations in variable profiles, mixed vs. conformal, are relatively large and are numerically unacceptable in the turbulent regime for both geometries.

Grid refinement studies in both geometries were performed, mixed and conformal grids, to confirm that deviations are associated with the interpolation procedure at the interface. In addition, no significant advantage in terms of improving the convergence rate or reducing the number of cells in a particular geometry was observed when using the multi block grid technique to create the numerical domain.

Unfortunately, the use of single conformal grids did actually lead to convergence problems in several cases depending on the turbulence model used, section 4.3. On the other hand, the magnitude of the errors in the numerical solution introduced by the use of interpolation and the multi block grid technique are significantly larger than those associated with the use of highly distorted grids in the single block approach, section 4.2.4. Therefore, single conformal grids were used for most simulations included in the present research.

## *4.3. Verification of the numerical accuracy*

### *4.3.1. Residual convergence criteria*

In the 2-D modeling of Nava's experiments[19], a detailed analysis on the numerical convergence process indicated that mass flow rate residuals were consistently the driver of the convergence process in the iterative solution of the governing equations. Monitoring two integral variables, mass flow rate and pressure gradient, was sufficient to warrant the achievement of convergence. It was also concluded that a minimum mass flow rate residual in the order of $10^{-4}$ to $10^{-6}$ was required to assure that solutions had stabilized depending on the flow regime and the turbulence model, and that the numerical sensitivity to the actual grid size observed in some cases required further research because performed calculations were even affected by the operating system environment under which the software was run.

For the residual convergence analysis of the 3-D modeling approach, mass flow rate and pressure gradient ratios were initially retained as primary indicators of iterative convergence. These ratios are calculated as follows:

$$\overline{m}_i = \frac{\dot{m}_i}{\dot{m}_{ref}} \qquad i = 0,1,2,\ldots, N \tag{13}$$

$$\overline{P}_i = \frac{\Delta P_i}{\Delta P_X} \qquad i = 0,1,2,\ldots, N \tag{14}$$

whereas the convergence residual level is equivalent to:

$$R_i = \frac{1}{10^i} \tag{15}$$

Figure 52 shows the iterative convergence history of four representative laminar simulations cases based on the geometries of the Kaneko and Iwatsubo experiments. As it was found in the 2-D modeling analysis, the mass flow rate residual, continuity equation, was the driver of the convergence process and a minimum value in the order of $10^{-3}$ to $10^{-4}$ is required to achieve iterative convergence. There was no apparent effect from the actual clearance, the geometry, the Reynolds number, neither the grid size nor the number of nodes. The fact that some cases show low convergence ratios at larger residual levels is associated with simulations that were either started from a zero flow field solution or obtained with a large increase in the prescribed pressure gradient from a previous solution.

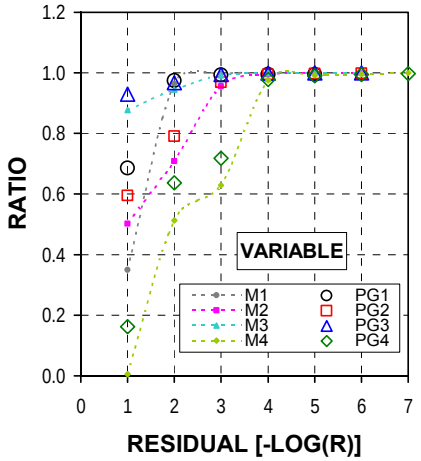


| Case | Geometry | Re | Clearance, μm (mils) |
|---|---|---|---|
| 1 | honeycomb | 26 | 176 (~ 7 ) |
| 2 | honeycomb | 715 | 1270 ( 50 ) |
| 3 | isogrid | 306 | 508 ( 20 ) |
| 4 | isogrid | 88 | 762 ( 50 ) |

In equation(13), $\dot{m}_{ref} = \dot{m}$ at the lowest residual

In equation(14), $\Delta P_X$ = prescribed pressure gradient

Figure 52. Residual convergence history in laminar flow regime cases.
Mass flow rate (M) and pressure gradient (PG) ratios.

Following Roache [31], regarding monitoring integral variables while focusing the analysis in quantities and definitions of interest, tracking the friction factor convergence was included in the residual analysis. Accordingly, friction factor ratio was defined as follows:

$$\bar{f}_i = \frac{f_i}{f_{ref}} \qquad f_{ref} = f \text{ at the lowest residual} \tag{16}$$

Figure 53 shows the convergence history of cases 1 and 2 separately. Again, simulations can be considered fully converged at a residual equivalent to either $10^{-3}$ or $10^{-4}$. On the other hand, it shall be noted that friction factor ratio is more sensitive; therefore it is a convergence criteria stricter than either mass flow rate or pressure gradient ratios.

Similarly, Figure 54 shows the convergence history of cases 3 and 4; and these simulations can again be considered fully converged at a residual equivalent to $10^{-4}$.

As simulations switched to turbulent flow, the three ratios described above were included in the residual convergence analysis.

Figure 55 shows the convergence history of two representative turbulent cases. Both simulations were obtained with the standard k-ε model for the core flow and wall functions as near-wall treatment. In contrast to laminar cases, these simulations can be considered fully converged at a residual equivalent as low as $10^{-2}$, $10^{-3}$ at the most. This low residual

requirement was consistently observed when using wall functions as near-wall treatment. When residual convergence was achieved, it was achieved quickly but it was not unusual to have good grid independent solutions where solution residuals stalled when using this near wall approach. Note that in Figure 55(a), such solution can be considered converged within 1% at the initial residual level of 1 ($10^{-0}$).

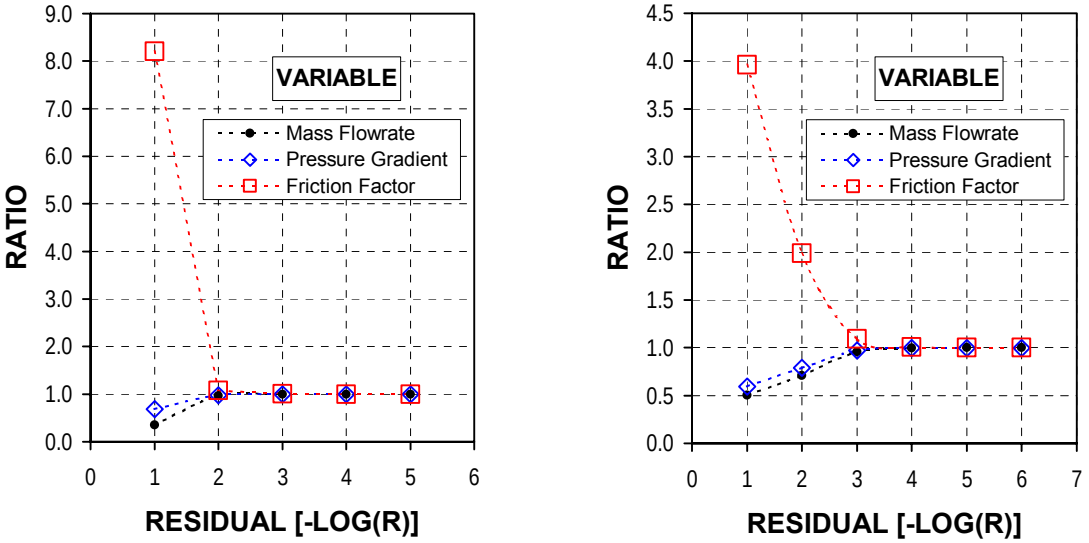


(a) Re ~ 26, clearance 176 µm (~ 7 mils) (b) Re ~ 715, clearance 1270 µm (50 mils)

Figure 53. Residual convergence history in laminar cases, Kaneko honeycomb geometry.

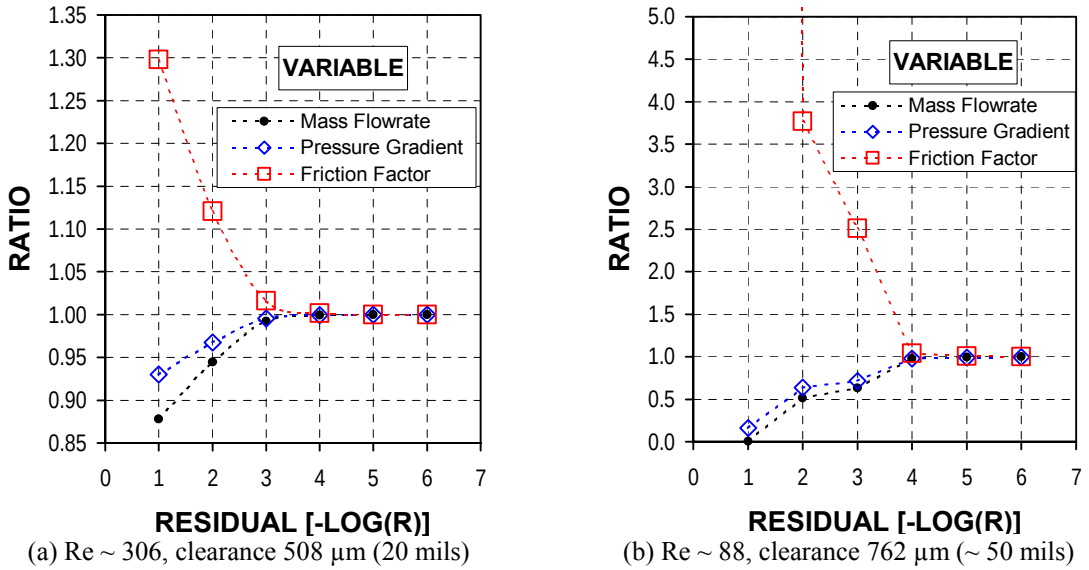


(a) Re ~ 306, clearance 508 µm (20 mils) (b) Re ~ 88, clearance 762 µm (~ 50 mils)

Figure 54. Residual convergence history in laminar cases, Iwatsubo isogrid geometry.

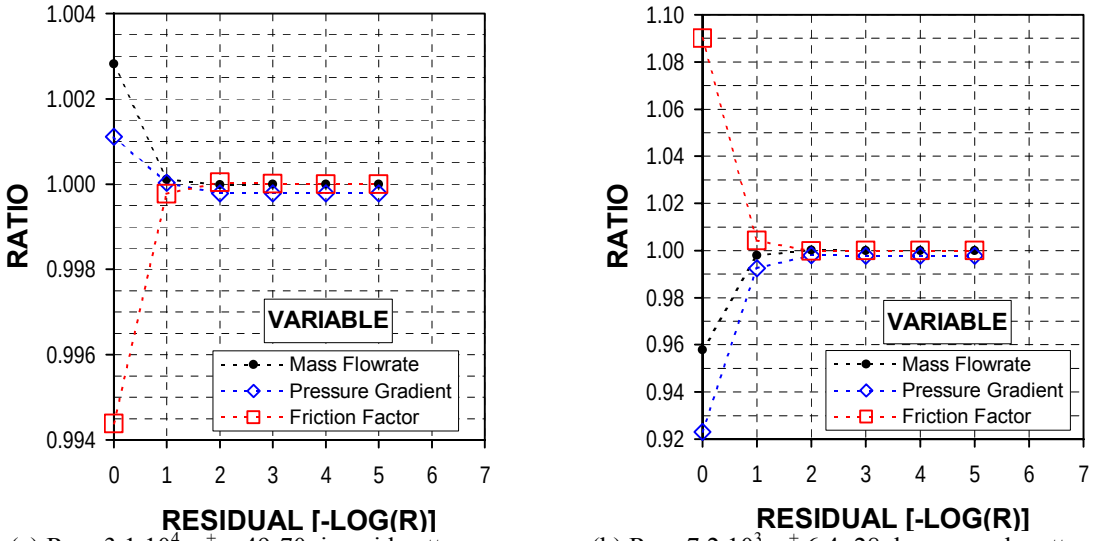


(a) Re ~ $3.1 \cdot 10^4$, $y^+$ ~ 49-70, isogrid pattern, clearance = 254 µm (10 mils).

(b) Re ~ $7.2 \cdot 10^3$, $y^+$ 6.4~28, honeycomb pattern, clearance = 762 µm (30 mils).

Figure 55. Residual convergence history in turbulent cases, wall functions as near wall treatment.

Likewise, Figure 56 shows the convergence history of the same cases with the two-layer zonal model as near-wall treatment of turbulence. In contrast to laminar and wall function cases, these simulations required higher residual levels, in terms of the negative power exponent, and the mass flow rate ceased to be the only convergence driving force (R stands for continuity residual and E for epsilon residual). High residual requirements and epsilon equation residual as convergence driving force were frequently observed when using the two-layer zonal model. When residual convergence was achieved, it was achieved steadily but slowly and sometimes intermediate grid solutions showed diverging residuals.

There are many lessons learned while scrutinizing and comparing the convergence process of the several models used in the present research. In the following paragraphs, the ones considered essential are presented, given the fact that results included in section 3 are based on the enhanced wall treatment (an updated version of the two-layer zonal model approach) because as indicated in ref [19,42] and compare in section 4.3, this model outperforms the use of wall functions in capturing the friction-factor-to-clearance behavior.

First, note that all variable ratios in Figure 56 indicate that numerical solutions were initially diverging, and the residual sequence is not continuous. Grid requirements are extremely demanding when using the two-layer zonal model, even at low Reynolds numbers. Figure 56(a) is a case where an interpolated solution from a coarse grid is

transferred to an intermediate fine grid, and selective local grid refinement is performed to comply with $y^+$ modeling requirements. In contrast, Figure 56(b) is a case where the interpolated solution from the coarse grid is directly transferred to the finest grid already in compliance with $y^+$ modeling requirements. Both approaches were used indistinctively because they performed similarly in terms of execution time and obtaining grid independent solutions. The use of interpolated solutions, local grid refinement, and multiple grids is the major reason these solutions appear to temporarily diverge during the convergence process.

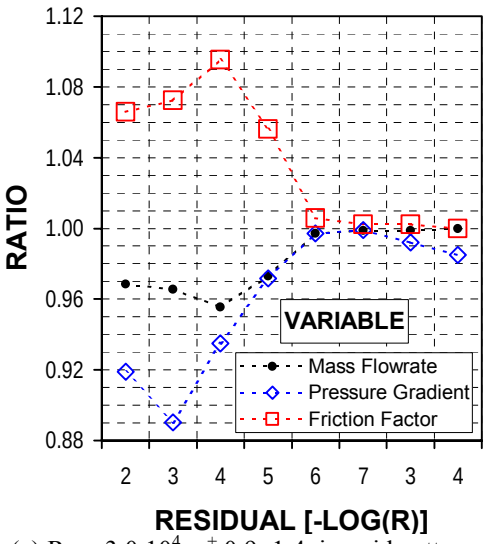


(a) Re ~ $3.0 \cdot 10^4$, $y^+$ 0.9~1.4, isogrid pattern, clearance 254 µm (10 mils)

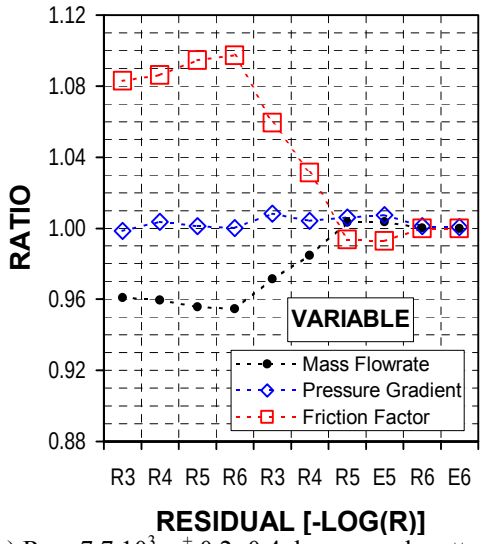


(b) Re ~ $7.7 \cdot 10^3$, $y^+$ 0.2~0.4, honeycomb pattern, clearance 762 µm (30 mils)

Figure 56. Residual convergence history in turbulent cases, two-layer zonal model as near wall treatment.

Secondly, note that fully converged solutions (mass flow rate and friction factor ratios equal to 1.000) have either pressure gradient ratios close but not to equal to 1.000, 0.998 at the last residuals, Figure 55(a) and (b), or slightly diverging pressure gradient ratios, 0.985 at the last residual on Figure 56(a). As described in equation (2), the friction factor is a function of the mass flow rate and the pressure gradient. It turned out that numerical friction factor calculations were performed with the prescribed pressure gradient instead of the numerically integrated pressure gradient, using such values leads to friction factor ratios, as defined in equation (16) above, that are numerically equivalent to the following expression:

$$\bar{f}_i = \frac{1}{\bar{m}_i^2} \tag{17}$$

Actual simulation friction factor ratios based on numerical results are really defined as:

$$\bar{f}_i = \frac{\overline{P}_i}{\overline{m}_i^2} \tag{18}$$

In the limit, the numerical simulation result will be as good as the ability of the model to recover upon integration of the surface forces the prescribed pressure gradient. Because the mass flow ratio is a relative measure of convergence it should be employed with caution. Figure 57 shows the same convergence history presented in Figure 56 but with the correct definition for the friction factor ratio and extended residual convergence history.

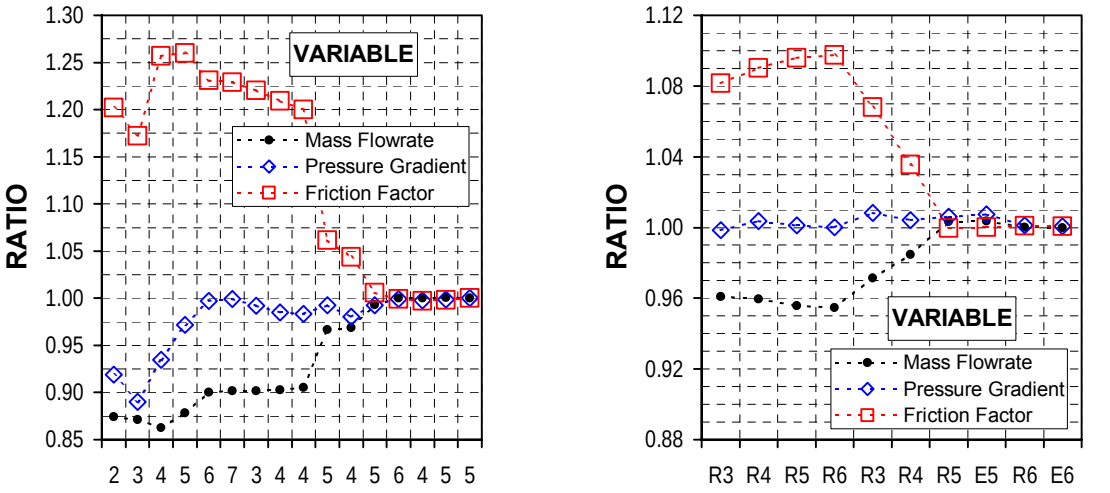


(a) Re ~ $3.4 \cdot 10^4$, $y^+$ 1.0~1.5, isogrid pattern, clearance 254 µm (10 mils)

(b) Re ~ $7.7 \cdot 10^3$, $y^+$ 0.2~0.4, honeycomb pattern, clearance 762 µm (30 mils)

Figure 57. Complete residual convergence history, correct friction factor ratio definition.

Now, note that all variable ratios reach unity at the end of the convergence process. Nevertheless, note that looking solely at friction factor ratios in Figure 57(b) the solution could have prematurely been halted at the second R5 residual. In contrast to all 2-D simulations, 3-D solutions with the laminar model, and 3-D turbulent predictions with wall functions as near-wall treatment; it was consistently found that to obtain fully converged solutions when using the enhanced wall treatment (two-layer zonal model) as near-wall approach, all relevant variables have to be monitored, including the actual $y^+$ of all cells closest to the wall.

### *4.3.2. Strategies to speed convergence (grid independent solution study)*

In a naïve effort to save computational time, the experience gained in developing grid independent results in the 2-D numerical analysis [19] of Nava's experiments was extrapolated into the present research. Then, the numerical grid of pilot cases started with very coarse and uniform spacing and ended with very fine spacing clustered to the wall in a boundary layer style. From a modeling perspective, boundary layer meshing is better suited to account for the flow physics because wall bounded turbulent flows are characterized for larger gradients of mean properties close to the wall. Solving properly the laminar sub-layer (two-layer zonal model) demanded physical spacing so small that most numerical cases, particularly at high Reynolds number, were run in grids with the first point closest to the wall located at 2 μm.

Exploratory grids for the large knurl and small recess geometries of Nava's experiments as described in section 3.1 were created with the first point closest to the wall located at 10 μm. A grid relatively fine for using wall functions as near wall treatment but fine enough that compliance with the two-layer zonal model could be achieved with few ulterior grid refinements. Figure 58 compares the grids used to model the small recess for a clearance of 508 μm (20 mils).

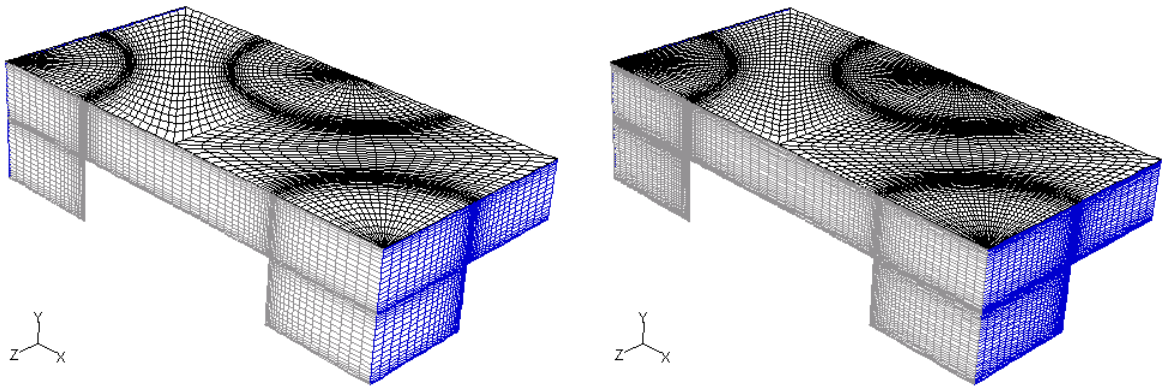


(a) Coarse Grid, Nc = 82308. (b) Fine Grid, Nc = 241200.

Figure 58. Small recess geometry modeling grids.

The grid refinement factor in the XZ plane is 1.26 while it was basically doubled in the Y direction to 1.58. Preliminary running tests showed a stronger sensitivity to the Y coordinate of most flow field variables. The equivalent global grid refinement factor is 1.43.

Literature on numerical accuracy [31, 48] recommends a minimum factor of 1.3.

As in the residual convergence analysis, integral variables were monitored, mass flow rate and pressure gradient, and the primary quantity of interest, the friction factor, to evaluate that solutions were grid independent. Reynolds number is directly proportional to the mass flow rate, therefore results in this section are presented in terms of the Reynolds number to facilitate grasping the flow regime. Figure 59 contrasts the results of the fine grid to the coarse grid of the small recess for a clearance of 508 µm (20 mils). Results correspond to the first order upwind discretization scheme for all variables except pressure, the standard scheme for the latter, and the SIMPLEC option for the pressure-velocity linking algorithm. The standard k-ε model was used in the core flow with wall functions as near-wall treatment, with $y^+$ equal to 1.36~6.32. The Reynolds number flow range corresponds to the experimental pressure gradient range.

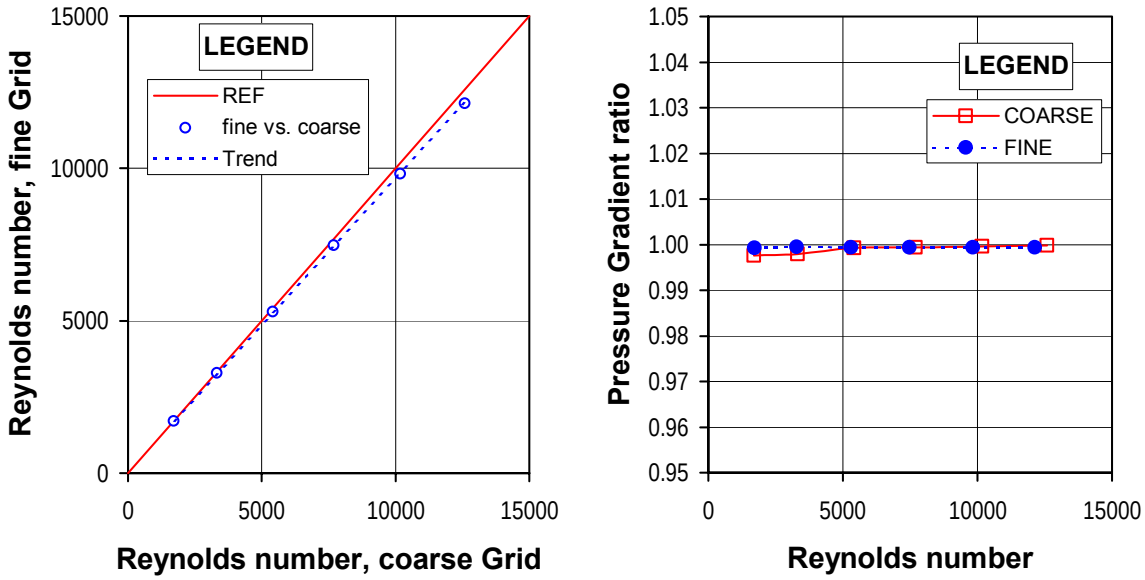


(a) Predicted Reynolds numbers. (b) Pressure gradient ratios.

Figure 59. Comparison of grid solutions in the small recess geometry.

Deviations in predicted Reynolds number among grids range from 0.49% to 3.56%. Contrary to, pressure gradient ratios are similar within 0.02% and the maximum deviation of 0.17% occurs at the lowest Reynolds number case. From a mass flow rate perspective, the numerical results can be considered grid independent although deviations fairly

correlate with Reynolds number indicating that further refinement might be needed at higher flow rates. On the contrary, pressure gradient ratios appeared to be insensitive to grid refinement, provided solutions have achieved iterative convergence; therefore, its usefulness as indicator of grid convergence is questionable.

Figure 60 contrasts friction factor predictions of both grids versus the values registered in the experiments of Nava.

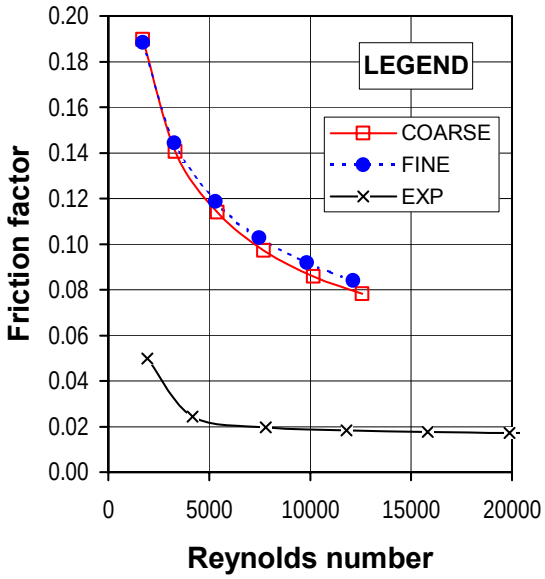


Figure 60. Experiments versus 3-D predictions in the small recess geometry.

As it should be expected, given the discussion on residual convergence about friction factor ratios, predicted friction factor deviations are larger among grids than mass flow rate deviations, and range from 0.47% to 5.83% at equal Reynolds numbers. There is no absolute figure or 'magical' number to define when grid convergence has been established, it is simply problem dependent. A deviation of 5.83% might be considered large if the modeler is seeking results or predictions within 1 to 2 %. But when both grid solutions coarse and fine over predict experimental registered data by 337% and 363% respectively at the experimental Reynolds number of $1.18 \cdot 10^4$; a deviation in predictions of 5.83% is an indication that grid convergence have been relatively achieved. Clearly, there is something fundamentally wrong with either the modeling, the registered experimental data, or both.

From a modeling perspective, the quality of the actual grid nodes layout and the validity

of the near wall treatment was reviewed. Although concentrating a large number of cells in the vicinity of each roughness pattern is required given the nature of the flow, there were two aspects for improvement in the grid layout. First, the grid was defined with constant distance wall cells along the cylindrical surface of the round-hole pattern, resulting in concentric meshing. This concentric meshing guaranteed the equal distance near the wall cells constraint, but concentrated cells in the center on the round-hole pattern, where high resolution is not needed, presumably leading to convergence stiffness. Secondly, the concentric meshing from the round-hole pattern was extended to the rest of the domain, resulting in cells not aligned with the expected mean flow direction in the channel portion of the domain, presumably leading to numerical diffusion. On the near wall treatment side, actual $y^+$ values do not comply with the law of the wall. As discussed in refs [19,42], using the law of the wall with nodes located in the inner layer, leads to reduced mass flow rate predictions (conversely to increased friction factor), mainly associated to the over estimation of turbulence dissipation near the walls. Mass flow rate under predictions in the 2-D modeling [42] of the small recess associated with low $y^+$ values did not exceed 25%.

As the analysis was extended to more experiments with round-hole geometries, the grid layout was improved within the pattern and the annular gap, increasing the actual distance of the near wall cells. In addition, numerical tests in 2-D modeling of turbulent channel flow were executed to quantify the reduction in mass flow rate predictions associated solely with the actual value of $y^+$. In channel flow, mass flow rate under predictions associated with low $y^+$ values did not exceed 45%. In summary, the friction factor over prediction in this particular roughness geometry is not explained by modeling errors. Further details on near wall modeling are discussed in section 4.3.

On the experimental side, this analysis corresponds to the worst case in modeling Nava's [30] experimental testing, and reviewed primarily to illustrate the relevance of validating simulations, what some authors have started to refer to as "numerical experimentation", with actual experimental data of negligible uncertainty. As presented in sections 2.3, 3.1 and 3.2, friction factors were better reproduced in Nava's knurl geometries but over predictions of 50% were still considered excessive. Given the uncertainty in the registered absolute values rather than the relative trends, further modeling in any Nava's' roughness pattern geometry was halted.

Numerical analysis continued on the ‘damper’, round-hole roughness pattern, seal experiments of Fayolle [8]. Exploratory grids for the shallow round hole were created with the first point closest to the wall located at 22 μm. A grid fine enough for using wall functions as near wall treatment but too coarse to comply with the two-layer zonal model even at very low Reynolds, possibly requiring many grid refinements near the wall. Figure 61 compares coarse and fine grids used to model this geometry for a clearance of 130 μm (~5.1 mils). The grid refinement factor in the XZ plane is 1.66. The number of cells along the Y coordinated is similar.

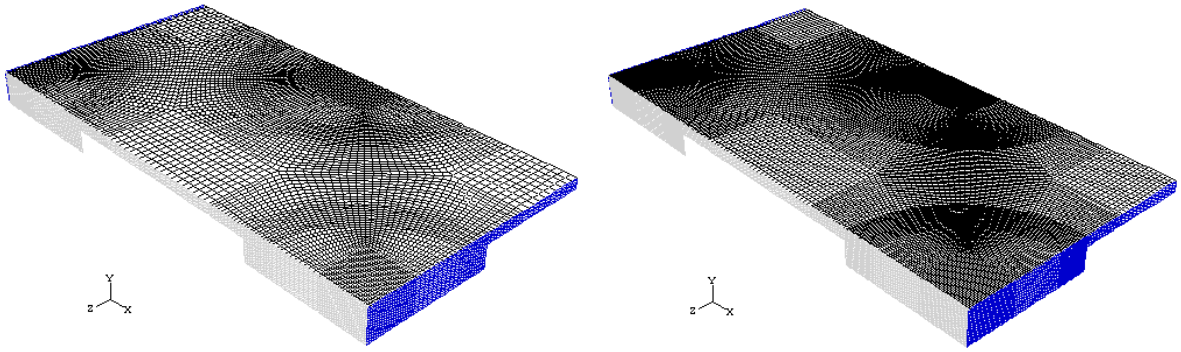

(a) Coarse Grid, Nc = 99360 (b) Fine Grid, Nc = 263160

Figure 61. Shallow round-hole geometry exploratory grids.

Figure 62 contrasts the results of both grids, which correspond to the power law discretization scheme for velocities, the PRESTO scheme for pressure, and the PISO option for the pressure-velocity linking algorithm. The Reynolds number flow range corresponds to the laminar flow regime.

Deviations in predicted Reynolds number among grids range from 0.30% to 0.72%. Instead, pressure gradient ratios are similar within 0.005% and the maximum deviation of 0.011% occurs at the lowest Reynolds number case. From a mass flow rate perspective, the numerical results can be considered grid independent. As in the numerical analysis of the small recess geometry, pressure gradient ratios are insensitive to grid refinement and they were discarded as indication of grid convergence.

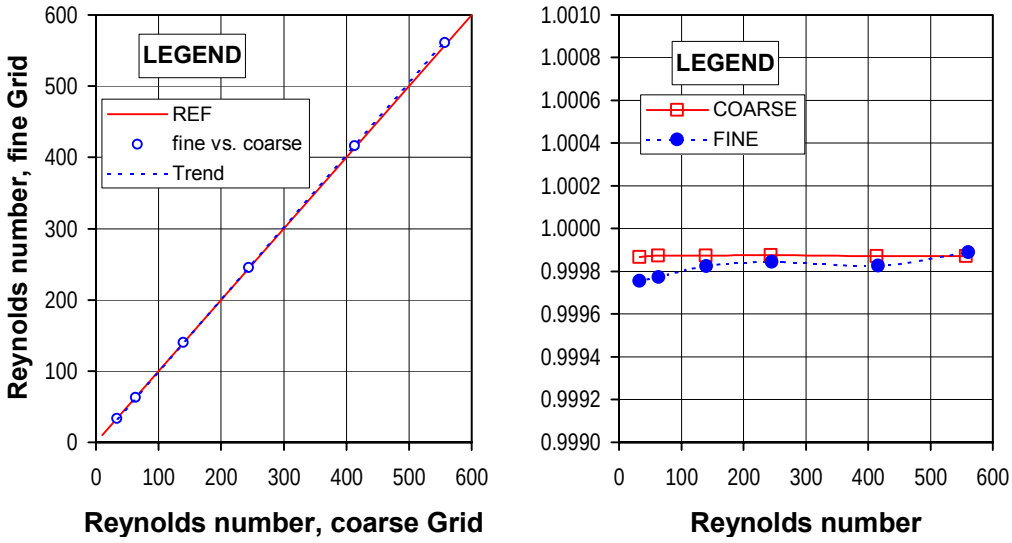


(a) Predicted Reynolds numbers (b) Pressure gradient ratios

Figure 62. Comparison of grid solutions in the shallow round-hole geometry of Fayolle [8], laminar flow.

Figure 63 compares friction factor predictions of both grids versus the theoretical flow on a channel of the same clearance. Deviations between both grid solutions range from 0.60% to 1.42%, an indication that results are clearly grid independent. On the other hand, solution deviations from laminar channel flow theory (96/Re line) vary from 55.8% to 21.2%, reducing as the Reynolds number is increased. These deviations are associated with the fact that the flow reattaches to the bottom wall of the roughness pattern.

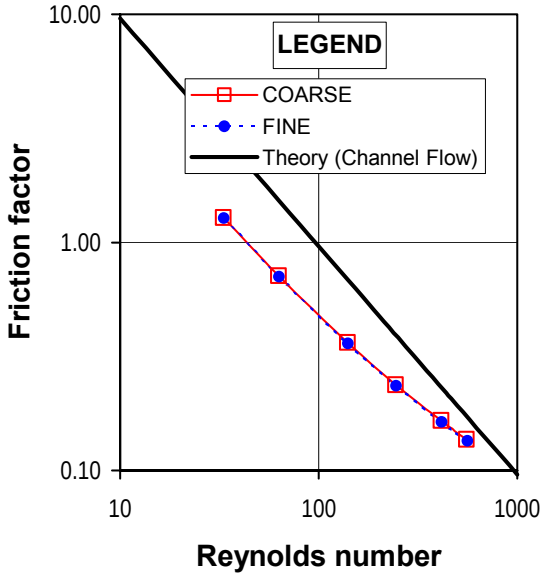


Figure 63. Friction factor predictions in the shallow round-hole geometry of Fayolle [8], laminar flow.

Similarly, Figure 64 compares low-Reynolds turbulent simulations results from both grids, which correspond to the power law discretization scheme for all variables, the PRESTO scheme for pressure, and the PISO option for the pressure-velocity linking algorithm. The RNG k-ε model was used in the core flow with the two-layer zonal model as near-wall treatment, with $y^+$ equal to 0.54~19.7.

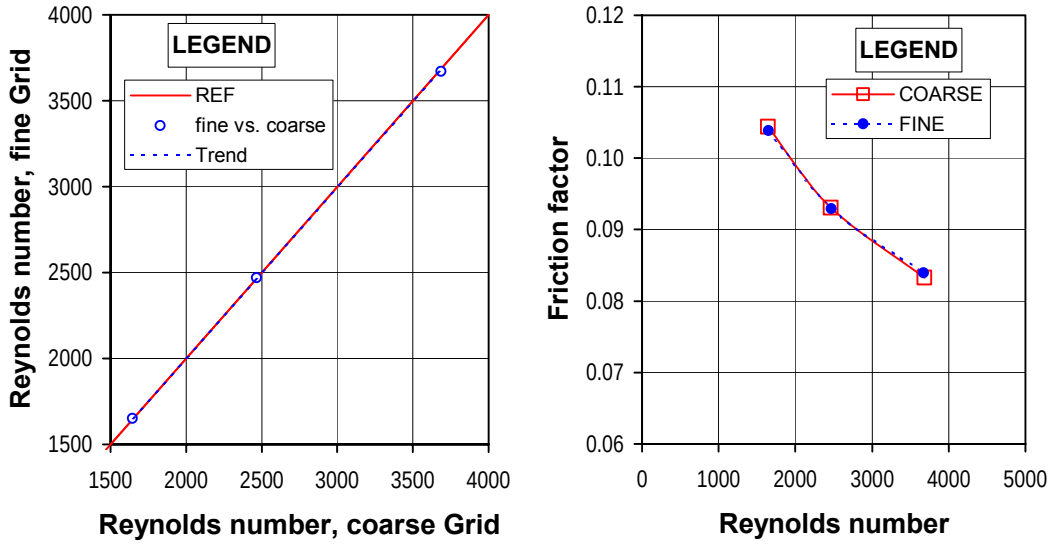


(a) Reynolds numbers (b) Friction Factor

Figure 64. Comparison of grid solutions in the shallow round-hole geometry, turbulent flow.

Deviations in predicted Reynolds number among grids range from 0.08% to 0.40%. In the same way, deviations in friction factors range from 0.17% to 0.79%. These results were clearly independent of the grid size.

Initial attempts to perform turbulent calculations at larger Reynolds numbers did not reach iterative convergence. Although all variable residuals reached very low magnitudes, $<10^{-6}$, continuity residual showed an erratic behavior. Independently of the grid used in modeling Fayolle geometries, continuity residuals either stalled at around $10^{-3}$ to $10^{-4}$ after decreasing monotonically in some cases, or stalled at around $10^{-1}$ to $10^{-2}$ after suddenly increasing when they were also decreasing monotonically. Local grid refinement based on continuity residual magnitudes or $y^+$ wall distance seemed to improve iterative convergence. Nonetheless, as each grid was continuously refined to achieve iterative convergence the number of nodes became prohibitively large.

As discussed in sections 3.1 and 3.2, experiments and simulations agree in indicating that recesses or round-holes provide less resistance to flow than non-symmetrical roughness pattern. Indeed, higher friction factors are observed in honeycomb, isogrid, or knurl patterns. Therefore, further scrutiny in explaining the numerical shortcomings encountered in modeling Fayolle[8] geometries were temporarily halted to examine the two patterns that provide the largest resistance to flow, the isogrid of Iwatsubo[36] and the honeycomb of Kaneko [37].

Initial grids for the experimental clearances of both patterns, isogrid and honeycomb, were created with the first point very close to the wall, maintaining cell aspect ratios as close to unity as possible using low grow expansion rates, resulting in very fine grids with a relatively smooth and close to uniform spacing in all coordinate directions.

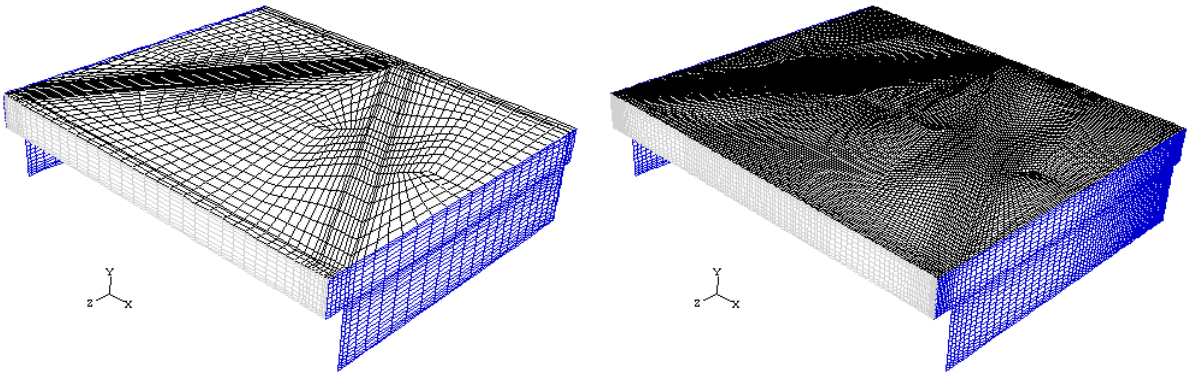

(a) Coarsest Grid (GG04), Nc = 35356 (b) Fine Grid (GG01), Nc = 314528

Figure 65. Isogrid pattern extreme grids.

Figure 65 compares the coarsest and fine preliminary grids used to model the isogrid pattern of Iwatsubo [36] for a clearance of 175 μm (~ 6.9 mils). Grid points near each wall are located at 10 μm; a distance relatively fine for using wall functions as near wall treatment at low Reynolds number flow, but fine enough that compliance with the two-layer zonal model could be achieved with very few localized grid refinements. The equivalent global grid refinement factor is 2.07, well above the minimum recommended of 1.3. Considering intermediate grids, the global refinement factor is split in increments of 1.22 (coarsest to coarser, GG04 to GG01cr), 1.13 (coarser to coarse, GG01cr to GG01c), and 1.50 (coarse to fine, GG01c to GG01).

Figure 66 contrasts the results of all grids in the laminar regime using the power law discretization scheme for all variables except pressure, the PRESTO scheme for the latter, and the PISO option for the pressure-velocity linking algorithm. Deviations in predicted Reynolds number among all grids range from 0.05% to 0.55% showing oscillatory convergence, coarsest grid values are within –0.15% and 0.49% of the fine grid values. Equally, deviations in friction factors range from 0.10% to 1.10%, where maximum deviations correspond to the coarsest grid at the lowest Reynolds number simulated. These results are clearly independent of the grid size, even for the coarsest grid.

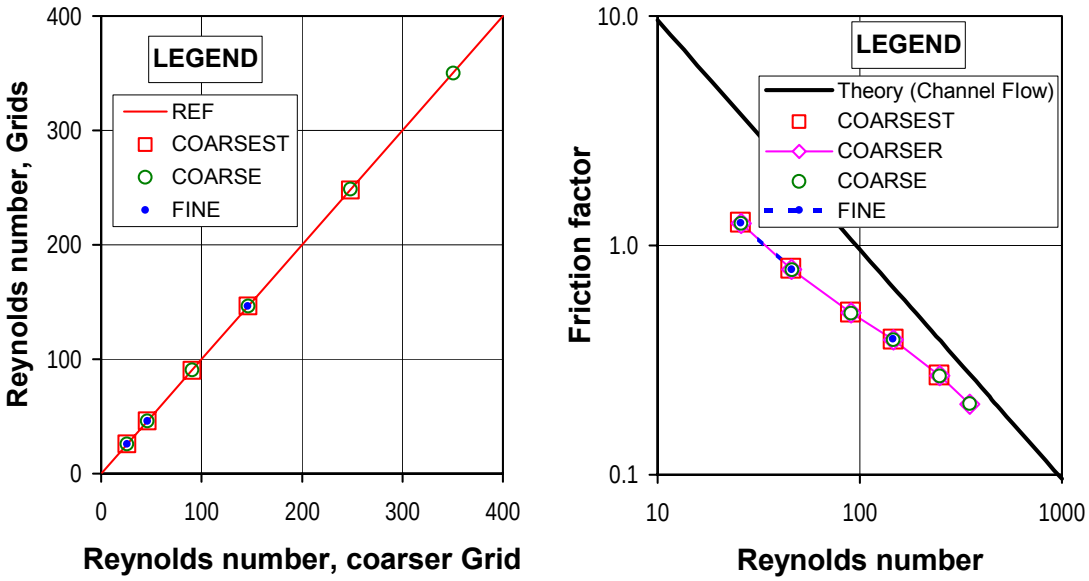


(a) Reynolds numbers (b) Friction Factor

Figure 66. Comparison of grid solutions in the isogrid geometry, laminar flow.

Similarly, Figure 67 compares low-Reynolds turbulent simulations results from all grids, except the coarsest, which correspond to the power law discretization scheme for all variables, the PRESTO scheme for pressure, and the PISO option for the pressure-velocity linking algorithm. The RNG k-ε model was used in the core flow with wall functions as near-wall treatment, with $y^+$ equal to 3.13~17.5. Deviations in predicted Reynolds number values among grids average 0.16% to 0.31% in the overlapping flow range, but increase up to 1.28% at the largest value. Likewise, deviations in friction factors average 0.32% to 0.62%, but increase up to 2.62% at the largest common Reynolds number. These results can

be considered grid independent, even for the coarser grid. Largest deviations are associated with the fact that data of the largest Reynolds number value on each grid solution did not achieve iterative convergence.

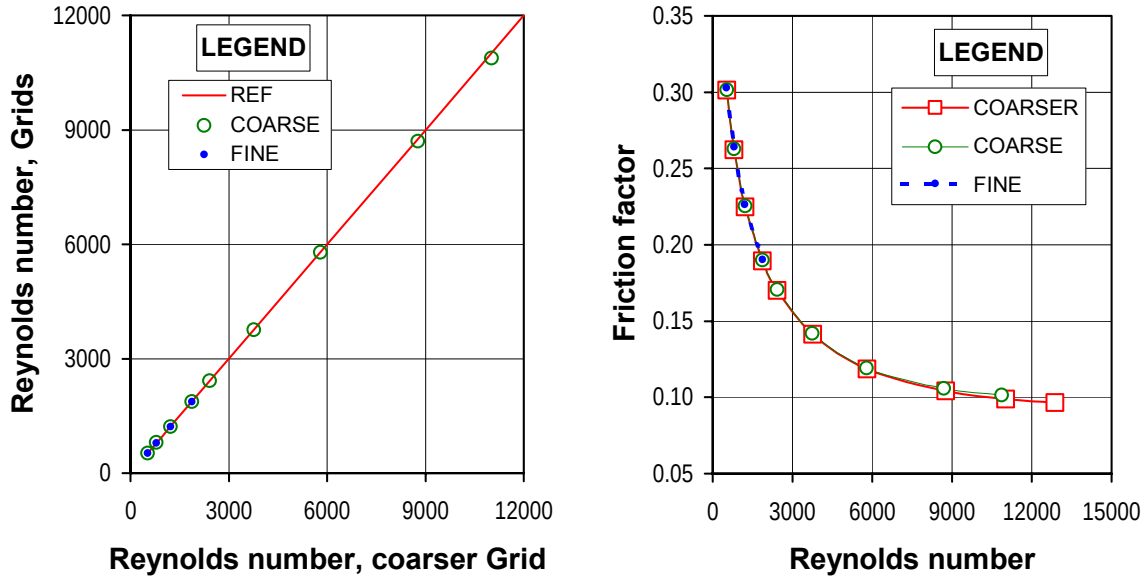


(a) Reynolds numbers (b) Friction Factor

Figure 67. Comparison of grid solutions in the isogrid geometry, turbulent flow.

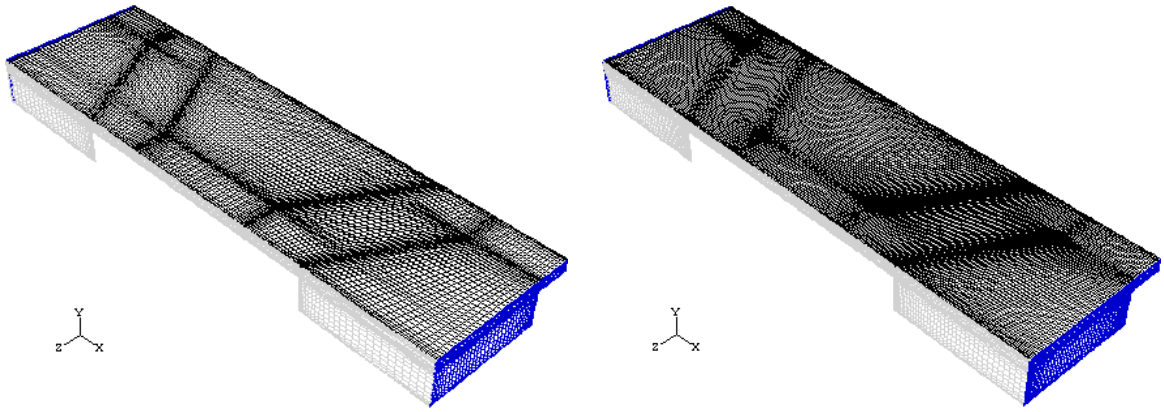

(a) Fine Grid (GG01), Nc = 121820 (b) Refined Grid (GG01r), Nc = 281224

Figure 68. Honeycomb pattern initial grids.

In a similar approach, Figure 68 compares the fine preliminary grid used to model the honeycomb of Kaneko [37] and its refined counterpart for a clearance of 176 μm (~ 6.9 mils). Again, grid points near each wall were located at 10 μm., looking that compliance

with both near wall treatments under study could be achieved with few localized grid refinements. The equivalent global grid refinement factor is 1.32. Figure 69 compares both grid results in the laminar regime using the power law discretization scheme for all variables, the PRESTO scheme for pressure, and the PISO option for the pressure-velocity linking algorithm. Deviations in predicted Reynolds number range from 0.12% to 0.79%. Similarly, deviations in friction factors range from 0.24% to 1.60%, where the maximum deviation corresponds to the largest Reynolds number case when the refined grid solution showed signs of becoming unstable. These results are also clearly grid independent

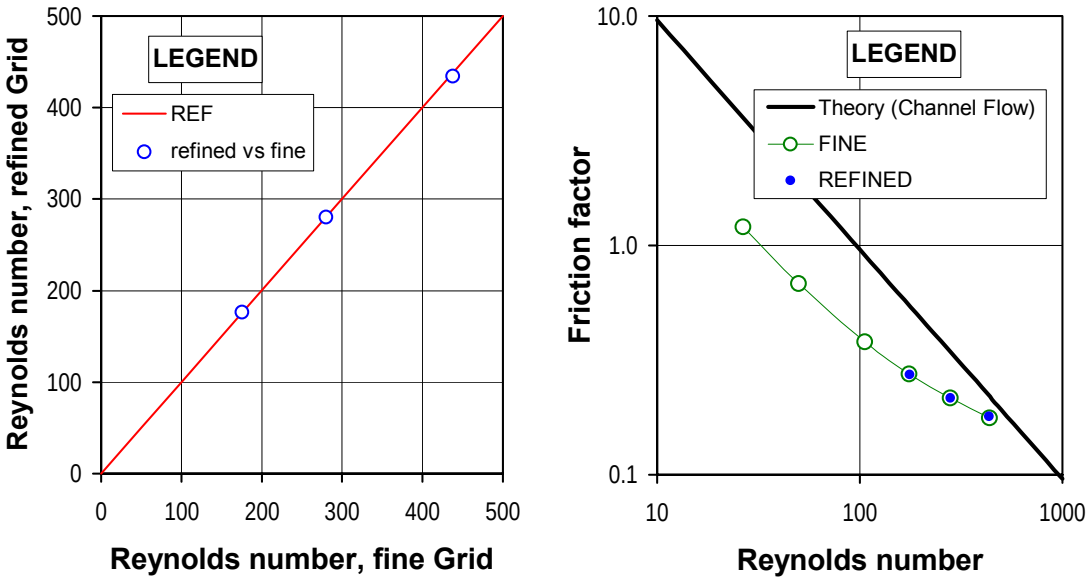


(a) Reynolds numbers (b) Friction Factor

Figure 69. Comparison of grid solutions in the honeycomb geometry, laminar flow.

Similarly, Figure 70 compares low-Reynolds turbulent simulations results, which correspond to the power law discretization scheme for all variables, the PRESTO scheme for pressure, and the PISO option for the pressure-velocity linking algorithm. The RNG k-ε model was used in the core flow with wall functions as near-wall treatment, with $y^+$ equal to 0.41~7.47. It should be noted again that these values are not in compliance with the law of the wall requirements ($y^+ > 11.5$). As recommended in any CFD literature, preliminary solutions should be obtained with the simplest model possible at first and switch to more complex models as the analysis progresses. Such low $y^+$ values are the result of the very

low Reynolds number nature of the flow, and the modeling intention of using the two-layer zonal model as near wall treatment of turbulence at last. Deviations in predicted Reynolds number range from 0.06% to 0.27%. Similarly, deviations in friction factors range from 0.13% to 0.55%. These results are also clearly grid independent. On the other hand, preliminary attempts to perform turbulent calculations at larger Reynolds numbers did not reach iterative convergence just as in almost all previous geometries modeled.

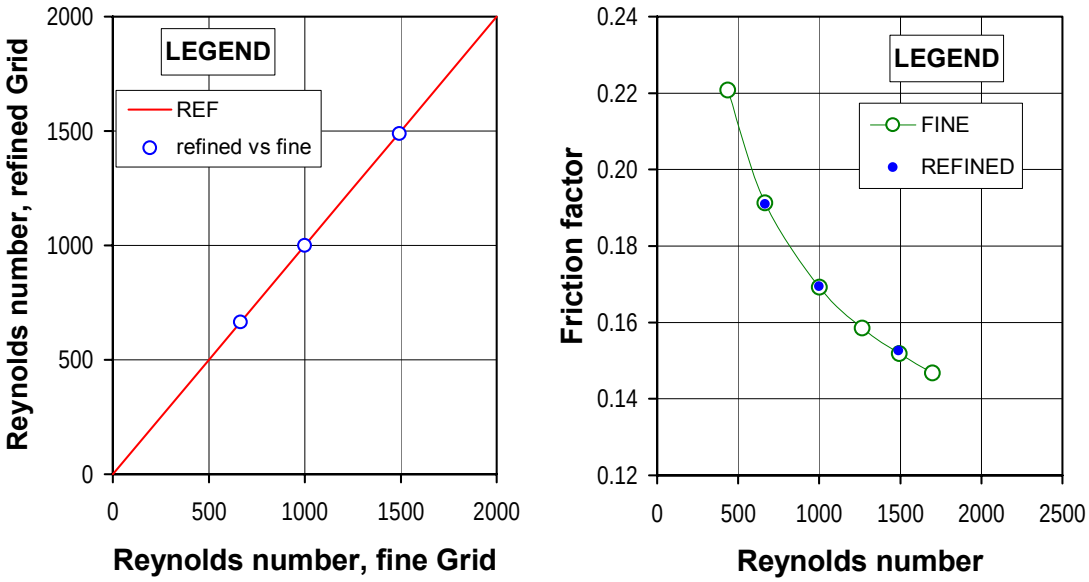


(a) Reynolds numbers (b) Friction Factor

Figure 70. Comparison of grid solutions in the honeycomb geometry, turbulent flow.

Giving the recurrence of failed attempts in obtaining converged solutions sequentially in most of the roughness geometries analyzed, an exhaustive analysis on the effect of grid refinement in achieving iterative convergence was performed. In a typical calculation sequence [19], the flow field is initialized to zero when using the laminar model to obtain the first converged solution at a very low Reynolds number. As the imposed pressure gradient on the domain boundaries is increased, laminar solutions become unstable and the solver is switched to model turbulence with the simplest approach. The previous fully converged solution is always the initial guess to the next pressure gradient case.

Initial grids (GG01) in both geometries, isogrid and honeycomb, were relatively fine as solutions from coarsest grids in each case were accurate within 3%. Actual CPU time to

obtain a converged solution in any of these fine grids was prohibitively large, from several hours to days; therefore; to evaluate the impact of a particular grid refinement on a solution a review of the meshing process was initiated from scratch. The process was aimed at finding the coarsest grid able to replicate the results of these fine grids in the laminar regime and evaluate their performance when switching the modeling to the turbulent regime.

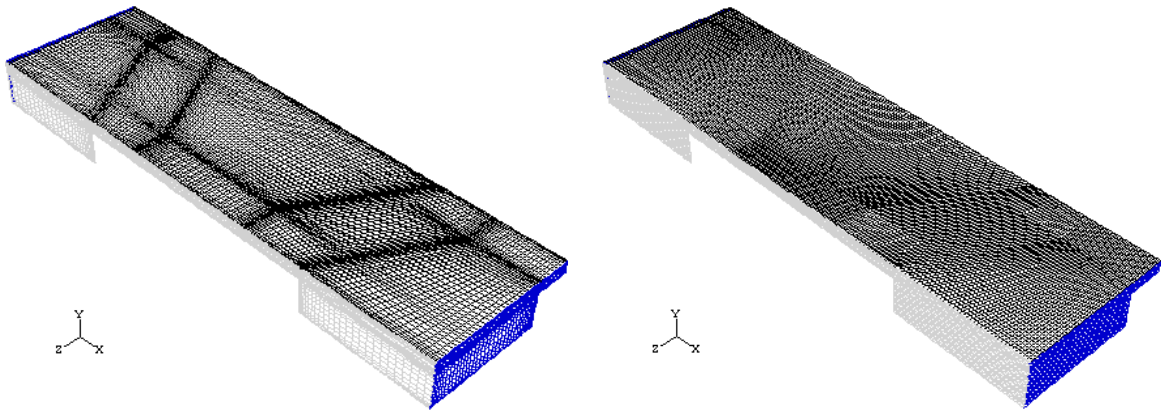

(a) Fine Grid (GG01), Nc = 121820 (b) Base Uniform Grid (GG04U), Nc = 191200

Figure 71. Honeycomb pattern initial grids, boundary layer type vs. Uniform.

Figure 71 compares the boundary layer type fine grid (GG01) versus a uniform type grid (GG04U). In the latter, grid points near each wall were located at 22 µm. and special care was taken to minimize the aspect ratio of each cell. Indeed, the total number of cells in the uniform grid is larger by 57%.

Figure 72 contrasts Reynolds number predictions of these two grids in the laminar regime using the power law discretization scheme for all variables except pressure, the PRESTO scheme for the latter, and the PISO option for the pressure-velocity linking algorithm. Deviations range from 0.12% to 2.90% at the largest Reynolds number.

Then, the base uniform grid was coarsened progressively in the X and Z direction while retaining the original node distribution in the Y direction. In this way, the coarsest grid generated, GG04Ucrxczcyh, contained only 18240 cells, Figure 73. Actual CPU time to obtain a converged solution in this grid was in the order of minutes to few hours.

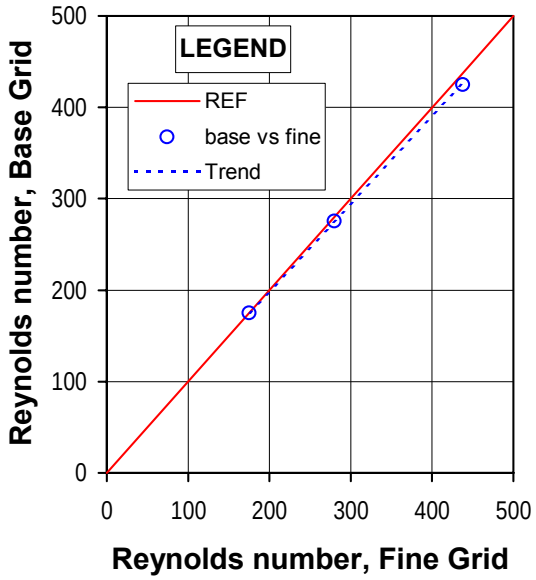


Figure 72. Base (GG04U) vs. Fine (GG01) grid predictions, honeycomb pattern, laminar flow.

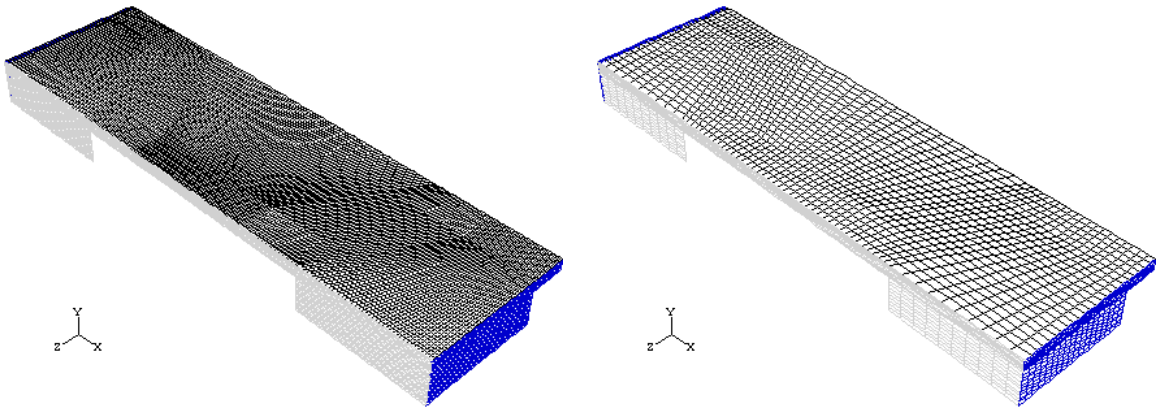

(a) Base Uniform Grid (GG04U), Nc = 191200 (b) Coarsest Grid (GG04Ucrxczcyh), Nc = 18240

Figure 73. Honeycomb pattern base grids.

Figure 74(a) contrasts the results of all GG04U grids in the laminar regime using the same numerical scheme. Deviations in predicted Reynolds number range from 3.17% at the lowest Reynolds number to only 0.14% at the largest value. When all predictions are compared in terms of friction factor, Figure 74(b), maximum deviations range from 0.24% to 6.07%. Considering that the global refinement factor is as large as 2.49 (the recommended minimum value is 1.3) when comparing the refined grid (GG01r) versus the coarsest one (GG04Ucrxczcyh), all results are accurate enough and can be considered grid independent, at least in the flow range analyzed in the laminar regime.

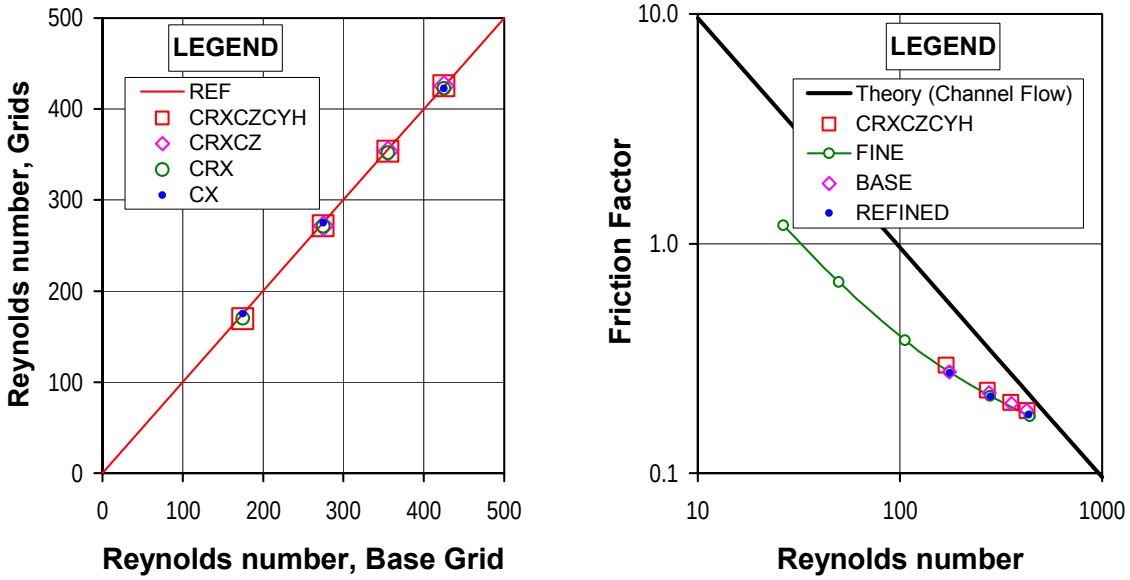


(a) Reynolds number flow (b) Friction factor

Figure 74. Base grids (progressive coarsening of GG04U) predictions, honeycomb pattern, laminar flow.

In addition to reducing the number of nodes, the progressive coarsening of the base grids while controlling the aspect ratio was aimed at reducing the gradient of each velocity component in all three coordinate directions. As already discussed for the round-hole geometries, local grid refinement based on continuity residual magnitudes, $y^+$ wall distance, or pressure gradient, seemed to improve iterative convergence just in few cases. Velocity gradient magnitudes appeared to have a stronger impact in achieving iterative convergence than any of these. Figure 75 present a typical velocity gradient comparison among fine and base grids (for the same pressure gradient and similar numerical modeling at low Reynolds number). It is clear that controlling the aspect ratio and the progressive coarsening reduced drastically the absolute magnitude in seven of the nine velocity gradient components.

As iterative convergence was achieved in the coarsest grid for a full range of Reynolds numbers with a particular turbulence modeling combination of each roughness pattern geometry, grid convergence was spot checked at several Reynolds number values. Using an interpolated flow field of all variables extracted from a coarse grid solution as initial guess, key Reynolds number cases were run in the finer grids to evaluate if solutions were grid independent.

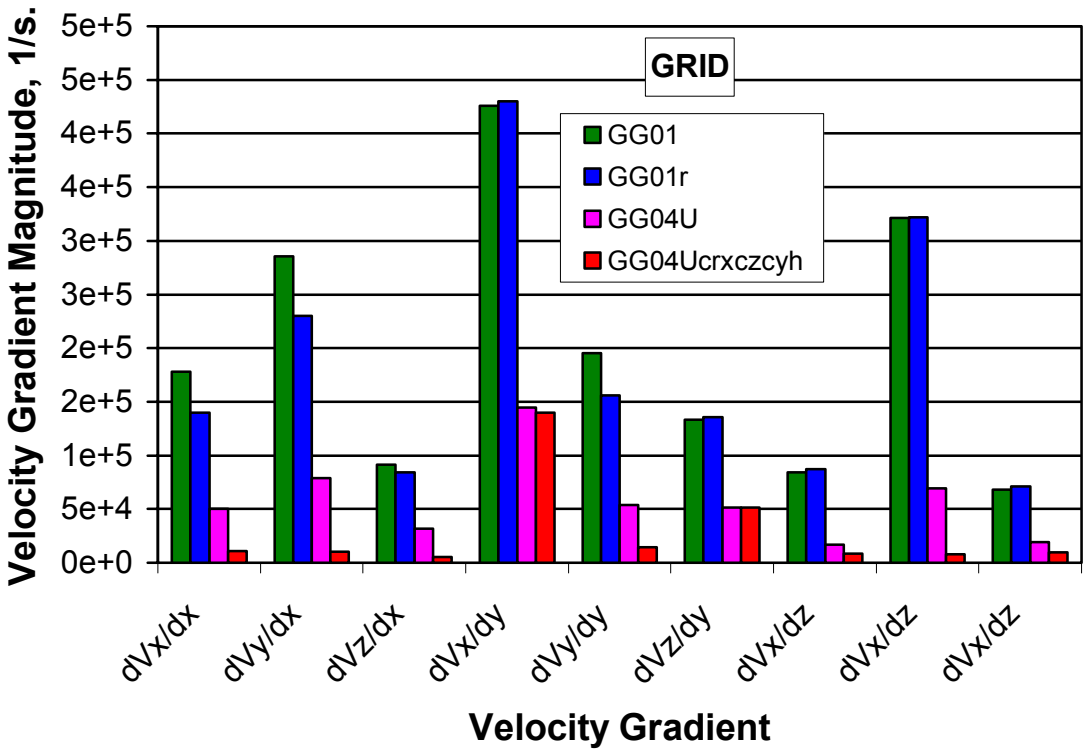


Figure 75. Typical velocity gradient magnitudes, maximum values, honeycomb geometry.

Figure 76 compares turbulent simulation results of the coarsest grid (GG04crxczcyh) versus the fine grid (GG01) in the honeycomb pattern (test clearance of 176 μm) which correspond to the power law discretization scheme for all variables, the PRESTO scheme for pressure, and the PISO option for the pressure-velocity linking algorithm. The RSM model was used in the core flow with the so-called enhanced wall treatment as near-wall treatment, with comparable $y^+$ values, 11.1 vs. 4.14 at low Reynolds number, and 42.3 vs. 89.2 at high Reynolds number.

Deviations in predicted Reynolds number values average 0.97% to 1.50%. Likewise, deviations in friction factors average 1.97% to 3.06%. Recalling that the grid refinement factor for these two grids is 1.88, these deviations indicate that results are grid independent for this particular geometric pattern and the turbulence modeling combination employed.

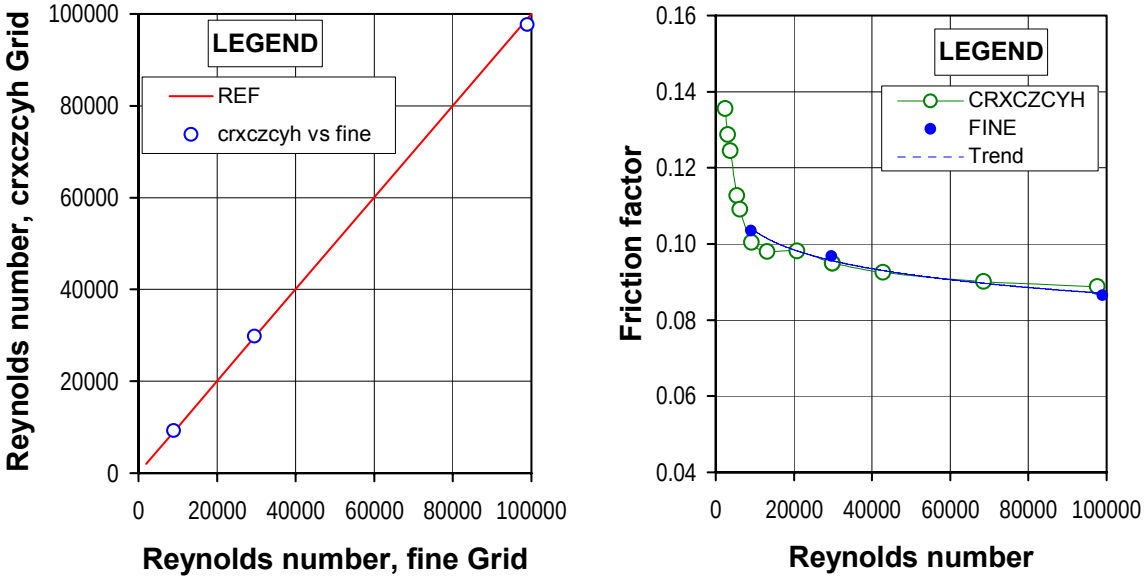


(a) Reynolds number flow (b) Friction factor

Figure 76. Coarsest versus fine grid predictions, honeycomb pattern, turbulent flow.

As the research progressed and the numerical analysis was extended to larger clearances, it was found that controlling the grid cell aspect ratio (i.e. velocity gradient magnitude), although relevant, did not assure achieving iterative convergence in all cases. Commonalities among all cases showing stalled residuals indicated that particular turbulence models were more sensitive than others to the Reynolds number range under study. In particular, the combination of using the RNG k-ε model in the core flow region with any wall function approach as near-wall treatment showed stalled residuals in almost all turbulent cases when the Reynolds number was lower than $10^4$. Indeed, several cases showed stalled residuals in just a small range of Reynolds numbers, around $10^4$, particularly when standard wall functions (the original model of Launder and Spalding [49]) were used as near wall treatment. Figure 77 shows the iterative convergence sequence of the cases ran in the coarsest grid (GG04Ucrxczcyh) of the honeycomb pattern geometry at the test clearance, 176 µm. The Reynolds number range, the core turbulence model, and the near wall treatment of each particular case ran in the sequence are indicated with brackets.

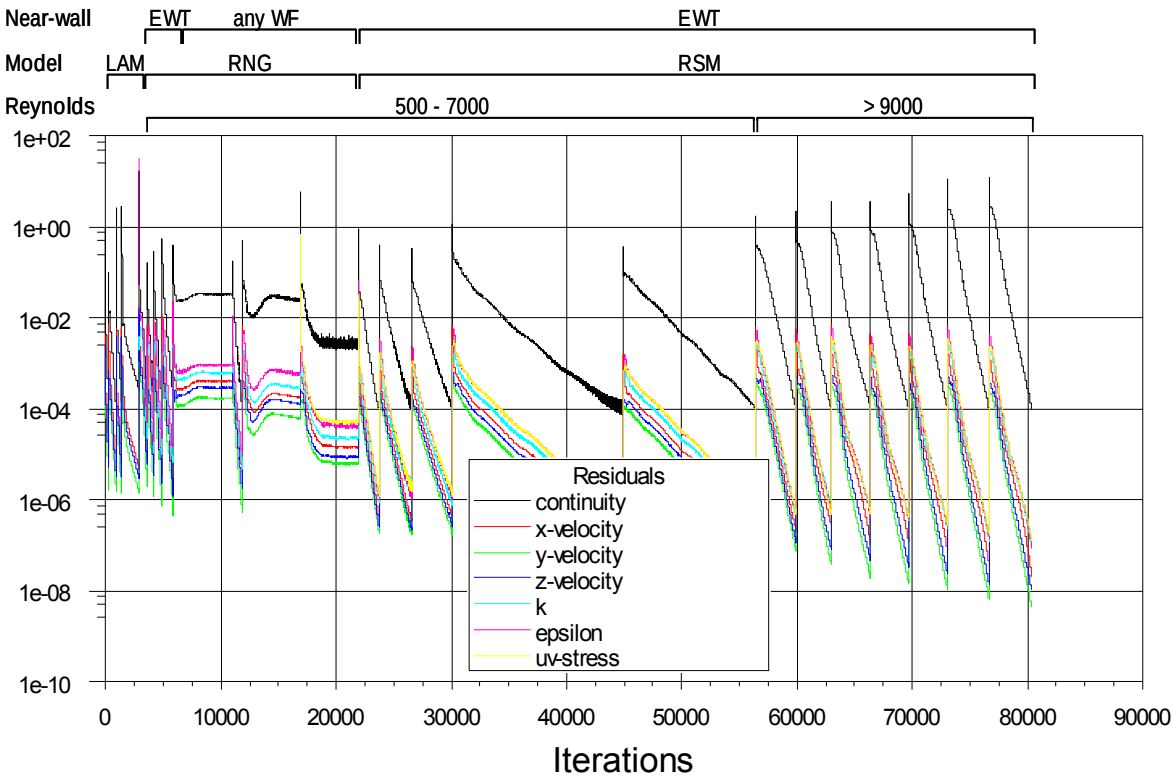


Figure 77. Residual convergence sequence, honeycomb geometry.

The above-discussed behavior was prevalent in most calculations performed. On the other hand, the combination of the standard k-ε model with the enhanced wall treatment (equivalent to the two-layer zonal model when properly resolved) as near-wall treatment appeared to be more stable. As already discussed in Section 3, most calculations included in the present research were performed with this turbulence modeling combination.

Numerical accuracy, grid independent results, in the additional clearances simulated was ensured following a similar approach to the one described herein. Grids identified as GG01cr in the isogrid pattern and GG04Ucrxcyczh in the honeycomb pattern were used as base meshes to extend the numerical domain to larger clearances. Subsequent grid refinement was required depending on the Reynolds number range and local $y^+$ values. Additional lessons learned while validating numerical results are included in the following two sections.

### *4.3.3. The grid convergence index (GCI)*

In 1994, Roache [31] proposed the use of a Grid Convergence Index (GCI) for the uniform reporting of grid convergence studies in Computational Fluid Dynamics. The claim is that the method provides an objective asymptotic approach to quantify uncertainty of grid convergence. It is based on an error estimator derived from the theory of generalized Richardson extrapolation that can be used to improve the accuracy of the predictions.

As already discussed in Section 1, the GCI approach has been used by some authors in analyzing numerical calculations of laminar flow over roughness patterns and in turbulent flow on draft tubes. The GCI is also recommended by the Journal of Fluids Engineering [48] to demonstrate numerical solution accuracy.

The Grid Convergence Index is numerically defined as:

$$GCI = F_S \cdot \frac{|\varepsilon|}{r^p - 1} \tag{19}$$

$|\varepsilon|$ is the relative error of any particular local variable $f$ evaluated at the same domain location or any global quantity $\phi$ change as the grid is refined:

$$|\varepsilon| = \frac{f_2 - f_1}{f_1} = \frac{\phi_2 - \phi_1}{\phi_1} \tag{20}$$

$r$ is grid refinement factor:

$$r = \frac{h_2}{h_1} \tag{21}$$

$p$ is the observed order of convergence:

$$p = \frac{1}{Ln|r|} \cdot Ln\left|\frac{\varepsilon_{32}}{\varepsilon_{21}}\right| \tag{22}$$

$$r = r_{32} = \frac{h_3}{h_2} = r_{21} = \frac{h_2}{h_1} \tag{23}$$

for any given constant grid refinement factor, where $h$ is the representative grid cell size. As hinted by equation (23), at least three different grid solutions are required; $h_1$ defined as the size of the fine grid, to calculate the observed order of convergence of a particular numerical calculation and properly estimate the GCI. As such, the technique can

be then used to estimate the "exact" solution as:

$$f_{exact} \cong f_1 + \frac{f_1 - f_2}{r^p - 1} \tag{24}$$

As defined, the GCI can be calculated locally in any given node common to all grids within the numerical domain. The focus of the present research is mass flow rates and friction factors, so an overall GCI might be sufficient but calculated values shall be look with caution when dealing with locally refined meshes. Ideally, grids shall be uniform and the refinement itself should be uniform, preferably using geometrically similar cells.

The benefits of using the GCI approach were first evaluated in analyzing theoretical channel flow while performing the calculations included in sections 2.4 and 2.5. In the 2-D analysis of the groove experiments, uniform grids were purposely used to double the number of nodes on each direction when refining each grid. (r = 2.0). Figure 78 compares the three grids used in simulating channel flow at the experimental clearance of the Iwatsubo [38] grove seal experiment of 175μm (~ 7 mils). They are the same grids used to simulate the grooved seal experiments with the groove portion removed from the domain.

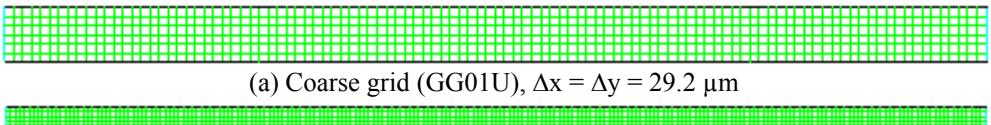

(a) Coarse grid (GG01U), Δx = Δy = 29.2 μm

(b) Medium grid (GG01Ur), Δx = Δy = 14.6 μm

(c) Fine grid (GG01Urr), Δx = Δy = 7.3 μm

Figure 78. Channel flow Grids, clearance = 175μm (~ 7 mils).

Figure 79 present the results of the grid convergence analysis of channel laminar flow. Being redundant, the grid refinement factor in the XY plane is 2.0 and results correspond to the power law discretization scheme for velocities, the PRESTO scheme for pressure, and the PISO option for the pressure-velocity linking algorithm. All variables are normalized by the theoretical values. Although results shown correspond to a particular pressure gradient, they are applicable for any Reynolds number because the mass flow rate is directly proportional to the imposed pressure gradient in the laminar regime:

$$(\dot{m}_l)_{theory} = -\frac{1}{12}\cdot\frac{{C_r}^3}{\nu}\cdot\left(\frac{\partial P}{\partial x}\right) \tag{25}$$

$$(f)_{theory} = \frac{96}{\mathrm{Re}} \qquad \text{[Re from equation (1)]} \tag{26}$$

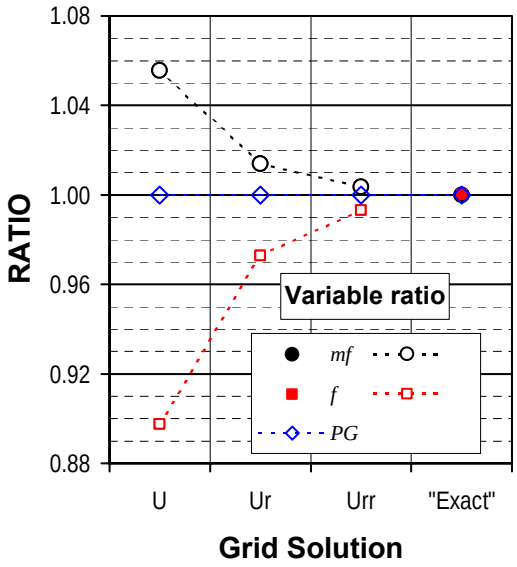


$$mf = \frac{(\dot{m}_l)_{numerical}}{(\dot{m}_l)_{ref}}$$

$$(\dot{m}_l)_{ref} = (\dot{m}_l)_{theory}$$

$$f = \frac{(f)_{numerical}}{(f)_{ref}}$$

$$(f)_{ref} = (f)_{theory}$$

Figure 79. Grid convergence analysis, laminar channel flow, Re = 173.4 ($\Delta P_x$ = -2·10$^5$ Pa).

From Figure 79, it is clearly observed that the numerical solution approaches the theoretical solution as the grid is refined. Deviations in mass flow rate and friction factor for the coarse grid are 5.6% and 10.2% respectively, while reducing to 0.35% and 0.69% in the fine grid. The observed order of convergence is second order accurate ( $p$ = 1.99), and for $F_s$ equal to 1.00, the GCI for the fine grid is equivalent to the observed deviations. The "exact" solution was calculated extrapolating the solutions from the medium and fine grid using equation (24). The "exact" solution is within 0.005% of the theoretical solution. The GCI approach and the Richardson extrapolation performed properly with global variables in this simplified flow case. In addition, note again that pressure gradient ratios are not a reliable indicator of grid convergence.

The performance of the GCI approach in evaluating the local grid order of convergence was also analyzed. The main limitation of this local validation is that the variable under scrutiny must be available (calculated) at the chosen location on each grid solution. Figure 80 compares the stream wise velocity profile of the three grids and the "exact" solution. The "exact" profile is for practical purposes equivalent to the theoretical profile so the latter is

not included. A meticulous observer would notice that markers of each profile do not overlap, as the grid was refined. In other words, the solution is not available at the same location in every grid. This is a consequence of the control volume formulation implemented in the software to solve the governing equations. Discrete variables are computed and stored at cell centers and not in the nodes that define the grid. While nodes of the initial grid remain common to a systematically refined grid, new cell centers are located within the original location of the centers in the previous grid, as shown in Figure 81.

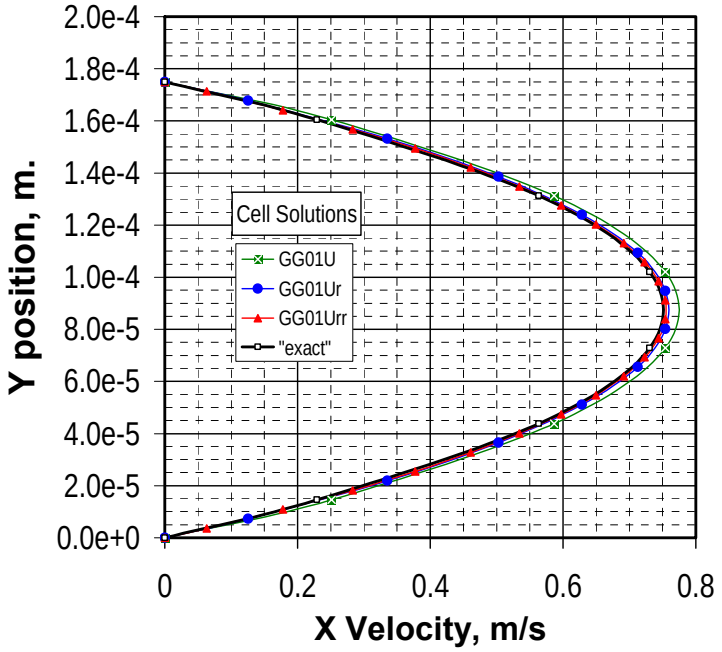


Figure 80. Stream wise velocity profiles, laminar channel flow, cell solutions, Re=173.4 ($\Delta P_x = -2 \cdot 10^5$ Pa).

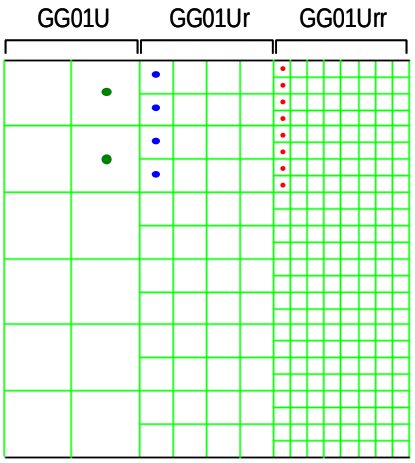


Figure 81. Location of the cell centers, the original uniform grid systematically refined.

As suggested by Roache [31], solutions of the medium and fine grids were interpolated (polynomial regression) to the location of the cell centers in the coarse grid. The observed order of convergence, *p* values, varies from 1.77 in near-center cells to 2.75 in the near-wall cells. Local GCI values for the fine grid vary from 0.25% to 0.19% respectively, for $F_s$ equal to 1.00. Figure 82(a) compares the velocity profiles of the original coarse solution, medium and fine solutions interpolated to the cell centers of the coarse grid, and the "exact" solution derived from the GCI analysis. During this analysis, it was noted that the maximum velocity calculated in each grid, independently of the actual location of the cell center, was similar to the theoretical value within 0.0006%. This observation is better illustrated by showing the new velocity profiles that are obtained by linearly interpolating to the nodes, each original cell solution. Figure 82(b) shows "nodal" velocity profiles of each grid solution as interpolated by the employed software. All "nodal" profiles are within 0.0001% to 0.0006% of the "exact" and theoretical solutions.

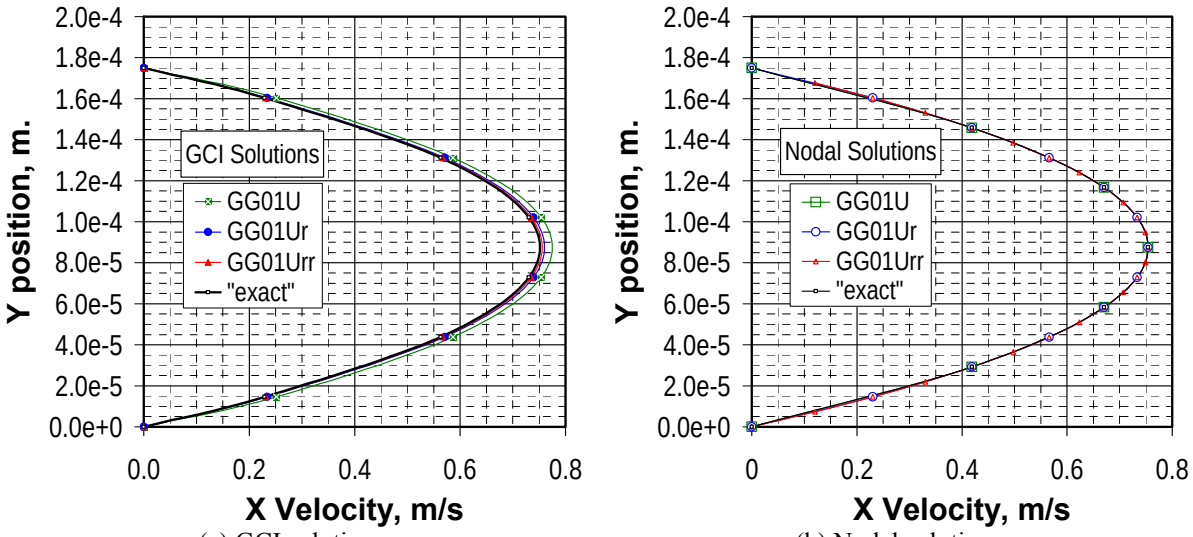


(a) GCI solutions (b) Nodal solutions

Figure 82. Stream wise nodal velocity profiles, laminar channel flow, Re = 173.4 ($\Delta P_x = -2 \cdot 10^5$ Pa/m).

Explaining why linear interpolation of each grid solution from the cells to the nodes result in obtaining the "exact" solution even in the coarse grid is beyond the scope of the present section. Nonetheless, the fact that stream wise velocity values were apparently more accurate in any grid than the mass flow rate, a global variable calculated from such velocity

values, was surprising. Before extending the use of the GCI approach to evaluate the actual numerical analysis of the present research, such apparent contradiction should be explained.

Figure 83 presents the theoretical solution (red line) for Re=173.4, the coarse grid solution (black squares), and compares numerical integration methods. Figure 83(a) presents the well-known trapezoidal integration method (blue line) while Figure 83(b) presents the rectangular integration method (light gray rectangles) on the bottom half of the clearance, the method employed by the CFD software. Figure 83(b) also presents shaded triangles in the top half clearance to show the differences between the two integration methods. In the interior cells of the numerical domain, the rectangular method balances itself out, local over estimations (green triangles) cancel out local under estimations (magenta triangles). On the other hand, the over estimation in the flow rate on the cells adjacent to the walls (black line triangle) does not cancel out and contribute significantly to the apparent discretization error (grid convergence not achieved).

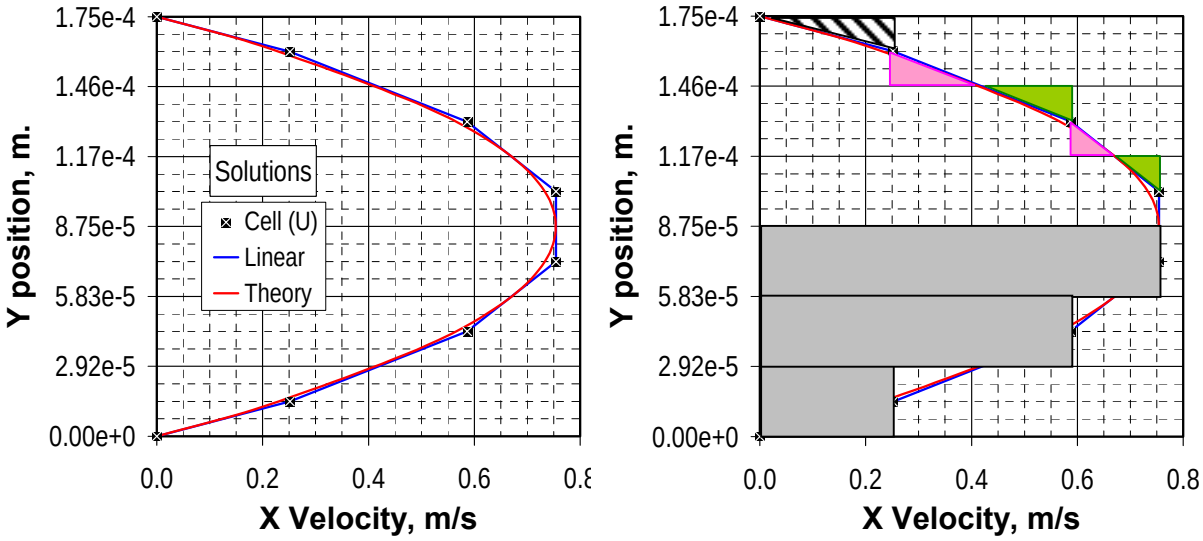


(a) Trapezoidal Integration (b) Rectangular Integration (Fluent)

Figure 83. Trapezoidal vs. rectangular integration, stream wise cell velocity profiles, laminar flow, Re=173.4.

Figure 83(a) also explains why linear interpolation of the cell solutions to the nodes results in replicating the "exact" or theoretical solution. Numerically, linear interpolation is equivalent to use the trapezoidal rule for integration; straight lines 'connecting' velocity values at cell locations are tangent to the theoretical profile exactly at the node locations.

Figure 84 presents again the results of the grid convergence analysis of channel laminar flow but with the mass flow rate (and friction factor) calculated with the trapezoidal integration method. Deviations for the coarse grid reduced to 1.4% and 2.7% respectively, while reducing to 0.09% and 0.17% in the fine grid. The observed order of convergence remained as second order accurate and the GCI for the fine grid is also equivalent to the observed deviations, 0.09%. What is more relevant, it is the fact that the solution from the coarse grid was already accurate within 1.4% (using the trapezoidal rule), and the solution from the medium grid would have been more than accurate enough. Indeed, 75% of the deviations from the theoretical laminar solution are due to the use of the rectangular integration method in calculating the mass flow rate.

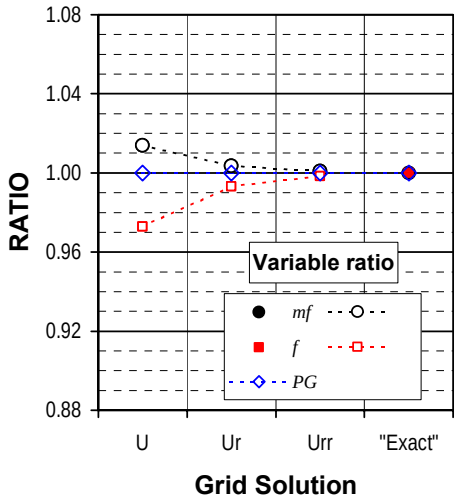


Figure 84. Grid convergence analysis (trapezoidal integration method), laminar flow, Re = 173.4.

Once the GCI effectiveness was confirmed in the analysis of laminar flow, the GCI applicability to turbulent flow without a theoretical solution as a reference was evaluated. Using a similar three-grid sequence as the one shown in Figure 78, turbulent channel flow was simulated at a clearance of 175µm (~ 6.9 mils).

Figure 85 compares the results of the grid convergence analysis that correspond to the power law discretization scheme for all variables, the PRESTO scheme for pressure, and the PISO option for the pressure-velocity linking algorithm. The RNG k-ε model was used in the core flow with wall functions as near-wall treatment, with $y^+$ equal to 16.3 to 65.4 (fine to coarse grid). All variables are normalized by the "exact" values estimated with the

GCI approach and the Richardson extrapolation. Results shown correspond to a particular pressure gradient to generate a medium Reynolds number. Similar analyses were performed at selected values in the range under analysis, up to $Re=10^5$, with comparable results.

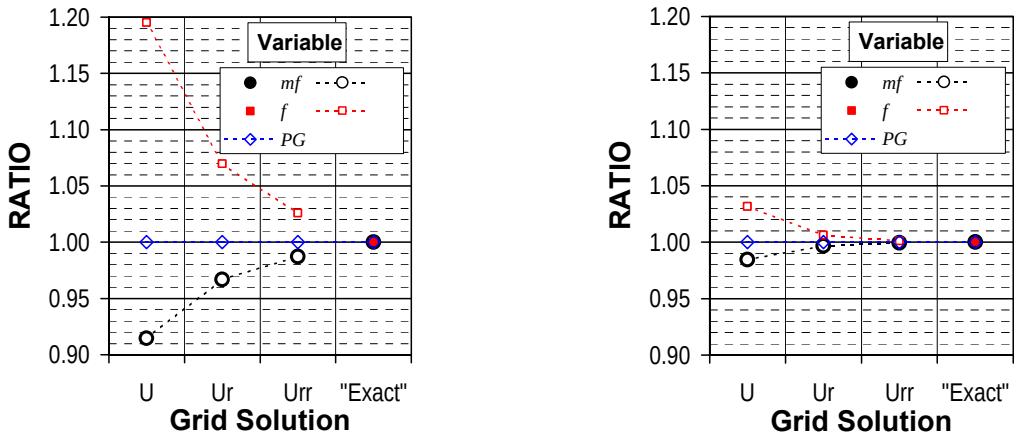


(a) Trapezoidal Integration

(b) Rectangular Integration (Fluent)

Figure 85. Grid convergence analysis, turbulent channel flow, $Re_N = 28680$ ($\Delta P_x = -2.3 \cdot 10^8$ Pa/m).

From Figure 85, it is clearly observed that the numerical solution converges asymptotically towards a limiting value, as the grid is refined. Nevertheless, relative deviations in mass flow rate and friction factor for the coarse grid are 8.53% and 19.5% respectively, reducing to 1.27% and 2.58% in the fine grid, when using the trapezoidal rule to calculate the mass flow rate. The observed order of convergence is first order accurate ( $p$ = 1.39), and for $F_s$ equal to 1.00, the GCI for the fine grid is 1.28%. In contrast, relative deviations for the coarse grid are 1.55% and 3.16% respectively, reducing to 0.06% and 0.13% in the fine grid, when using the rectangular method to calculate the mass flow rate. The observed order of convergence is second order accurate ( $p$ = 2.31), and for $F_s$ equal to 1.00, the GCI for the fine grid is 0.06%. The friction factor predictions are within 1.23% and 0.85% respectively of the actual friction factor value for smooth channel turbulent flow, extracted from the Moody Diagram with twice the clearance as the hydraulic diameter to calculate the numerical Reynolds number, $Re_N$.

In contrast to laminar flow, the default integration method (rectangular) significantly outperforms the use of the trapezoidal rule in calculating the mass flow rate in turbulent flow. While the solution from the medium grid was already within 0.31% of the “exact”

solution (equivalent to a relative increase in mass flow rate of only 1.25% from the coarse grid) with the default integration method; the solution from the fine grid with the trapezoidal rule could have been regarded as not accurate enough with a deviation of 1.27% from the "exact" solution (equivalent to a relative increase in mass flow rate of 2.11% from the medium grid).

Figure 86 present a velocity profile calculated from the DNS data of Moser [35] as the reference solution (red line) for Re=27527, and the best coarse grid solution (black squares) to qualitatively compare again both numerical integration methods. In contrast to laminar flow, the trapezoidal integration method (blue line) considerably underestimate (magenta triangles) the mass flow rate, mainly in the cells near the walls, Figure 86(a). On the other hand, the rectangular integration method (light gray rectangles) balances itself out, local over estimations (green triangles) cancel out local under estimations (magenta triangles), as shown in the bottom half of the clearance in Figure 86(b).

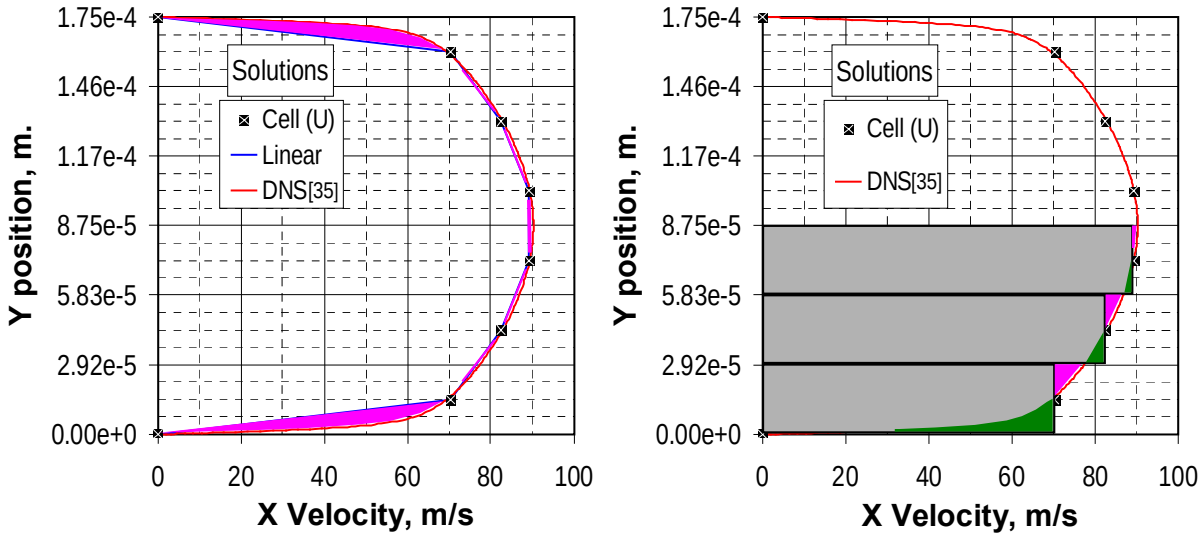


(a) Trapezoidal Integration (b) Rectangular Integration (Fluent)

Figure 86. Trapezoidal versus rectangular integration, stream wise cell velocity profiles.

The GCI approach performed consistently in these simplified flow cases. As the GCI evaluation progressed to analyze results in complicated geometries and grids, its applicability became cumbersome and its consistency was questionable. Figure 87 presents the grid sequence developed to evaluate the GCI methodology while simulating the grooved seal experiments of Iwatsubo [38] described in section 2.4.

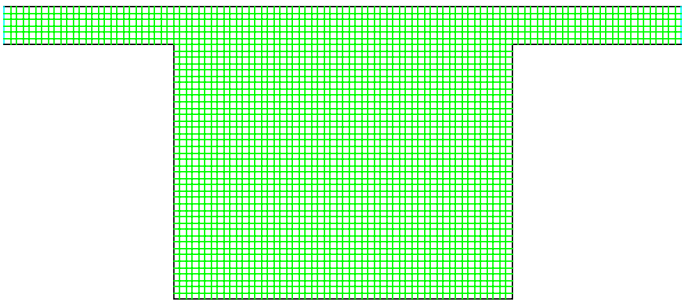

(a) Coarse grid (GG01U), $\Delta x = \Delta y = 29.2$ µm

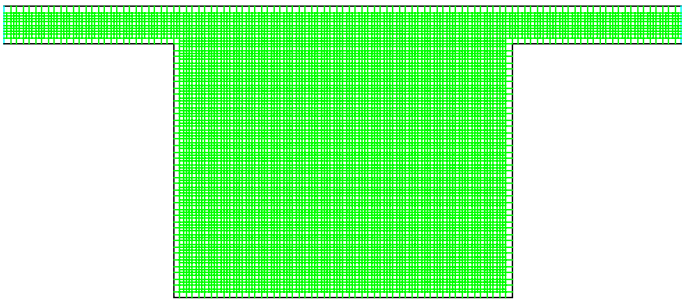

(b) Medium grid (GG01Ue), $\Delta x = \Delta y = 14.6$ µm, $\Delta w = 29.2$ µm

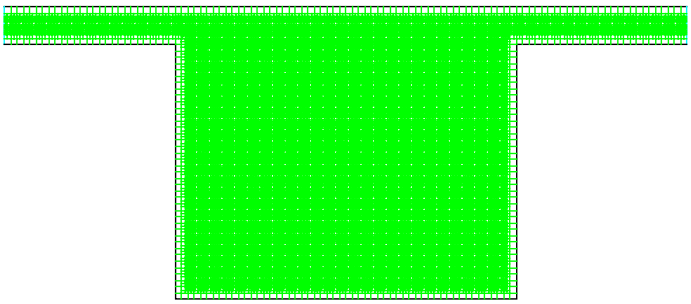

(c) Fine grid (GG01Uee), $\Delta x = \Delta y = 7.3$ µm, $\Delta w = 29.2$ µm

Figure 87. Groove annular seal grids, clearance = 175µm (~ 6.9 mils).

Figure 88 compares the results of the grid convergence analysis that correspond to the power law discretization scheme for all variables, the PRESTO scheme for pressure, and the PISO option for the pressure-velocity linking algorithm. The RNG k-ε model was used in the core flow with wall functions as near-wall treatment, with $y^+$ equal to 12.9 to 16.5 (similar to all grids, note that grid refinement was purposely done on interior cells only to maintain uniform $y^+$ values). In Figure 88(a), variables are normalized by the values estimated with the fine grid, while in Figure 88(b), they are normalized by the actual data extracted from the experiments. Results shown correspond to the medium pressure drop of the experiments, 588 kPa (equivalent to a $1.67 \cdot 10^7$ Pa/m pressure gradient).

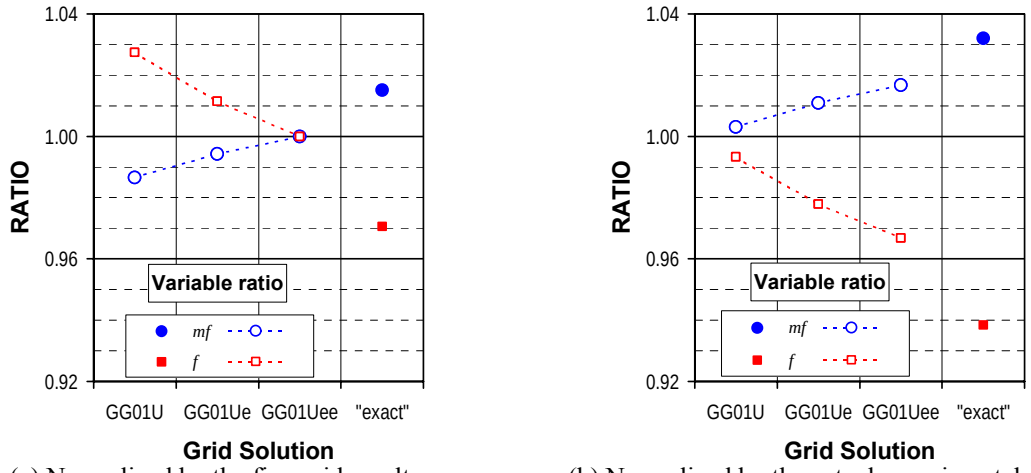


(a) Normalized by the fine grid results (b) Normalized by the actual experimental data

Figure 88. Grid convergence analysis, grooved seal turbulent flow, Re = 4470 ($\Delta P_x = -1.7 \cdot 10^7$ Pa/m).

With surprise, note in Figure 88 that flow predictions that differ by only 0.79%, from coarse to medium grid, and 0.57%, from medium to fine grid, generate an "exact" solution that is larger than the fine grid solution by 1.51%. The discrepancy is a direct consequence of the low observed order of convergence ( $p = 0.46$), worse than first order accurate. This numerical anomaly is better understood when analyzing the local grid order of convergence. Figure 89 compares the velocity profiles on the periodic boundaries of the numerical domain and the "exact" solution determined by the GCI approach when used on either the cell center locations or the grid node locations The observed order of convergence, $p$ values, varies from 2.72 in the cells near the top wall to 0.18 in the cells near the bottom wall. Local GCI values for the fine grid vary from 0.04% to 5.85% respectively, for $F_s$ equal to 1.00. The "hump" on the "exact" velocity profile near the bottom wall, more prominent on the cell solution analysis, is a direct consequence of very small local deviations among grids. As pointed out by Celik [48], the GCI does not work when solution differences among grids are "very close" to zero, an indication of either oscillatory convergence or that the "exact" solution has been attained. As already shown in Figure 88(b), mass flow rate and friction factor predictions in the coarse grid were already within 0.30% and 0.66% of the actual experimental data.

Similar anomalies were observed when the GCI approach was used to analyze the grid independent results of some of the 3-D geometries described in section 4.2.2. The observed order of convergence and consequently "exact" solutions (recalling that they are obtained

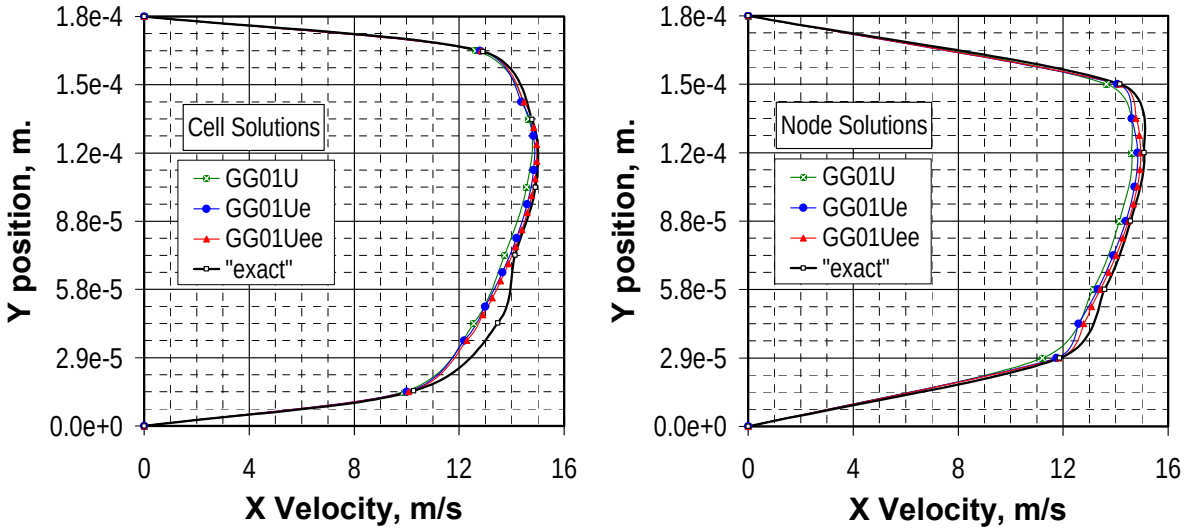


(a) Cell Solutions (b) Nodal Solutions

Figure 89. Stream wise velocity profiles, grooved seal, turbulent flow, Re = 4470 ($\Delta P_x$ = -1.7·10$^7$ Pa/m).

by Richardson extrapolation) vary considerably. As already proven in the cases discussed above, the GCI is numerically equivalent to the relative error when it is calculated without considering the order of convergence and setting $F_s$ equal to unity.

Given the GCI limitations described above, it was only used to estimate convergence and accuracy of the new 2-D predictions, primarily in the 2-D grooved seal parametric analysis included in section 2.5. Instead, the relative error, described as percentage deviations in section 4.2.2, was the main indicator of grid convergence used in the present research. The GCI was only used selectively in some of the 3-D cases to confirm the choosing of the base grid on each geometry, isogrid and honeycomb, and as estimator of numerical uncertainty in selected clearances.

Regarding the effect of the numerical integration in the accuracy of the predictions, most 3-D laminar predictions were estimated with the default integration method, rectangular method. The large overestimation in the mass flow rate observed in the 2-D modeling, up to 10% in coarser grids, is reduced considerably when extending the modeling to 3-D; over prediction due to integration errors in pilot cases were estimated in no more than 2%. All turbulent predictions were estimated with the default integration method. Additional measures to validate the accuracy of the numerical predictions of the present research are included in the following section.

### *4.3.4. Conformal single block grid validation*

As already discussed in previous sections, compliance with the enhanced wall treatment (equivalent to the two-layer zonal when the inner layer is properly resolved) as near-wall modeling of turbulence requires very fine grid near all boundaries defining the roughness pattern geometry. The larger the Reynolds number is, the smaller the distance of each first cell center near all walls must be. When using conformal single blocks grids to avoid interpolation (multiple non-conformal blocks require transferring information in common faces), maintaining actual $y^+$ values around 1.0 result in grids that contain cells with distorted aspect ratio in parts of the domain where high numerical resolution is not required.

Regarding numerical accuracy, the relative error described in section 4.2.2 performed satisfactorily as indicator of grid convergence on these grids with localized distorted aspect ratio cells. Nevertheless, the GCI approach was not consistent in validating the results in such distorted grids. The main concern was that an apparent well-converged grid solution might still include unacceptable discretization errors (numerical diffusion) due to the presence of distorted aspect ratio cells. As the original 2-D modeling of Nava's was validated with a 3-D model, section 2.2, it was reasoned that evaluating the performance of these distorted 3-D grids exactly as they were tailored for each geometry and Reynolds number range in predicting channel flow would give us an indication of the numerical diffusion, if any, introduced by the used of these grids. In addition, these numerical testing could validate the observations about the influence of the aspect ratio in achieving iterative convergence as described in section 4.2.2. In summary, a complementing alternative to the method of the relative error in estimating the numerical uncertainty of the present simulations was sought.

Creating numerical domains to simulate channel flow with the conformal grids developed to analyze the 3-D geometries of each pattern is straightforward. Removing the pattern from each domain leaves only the annular clearance, indeed, the channel geometry. The performance of several grids among the whole Reynolds number range under analysis was evaluated, in laminar flow and in the turbulence regime. Figure 90 compares two channel grids based on the isogrid geometry of Iwatsubo. A base grid used to model laminar and turbulent flow with wall functions, and a base grid refined near walls to comply with $y^+$

requirements of the enhanced wall treatment in a medium Reynolds number flow range.

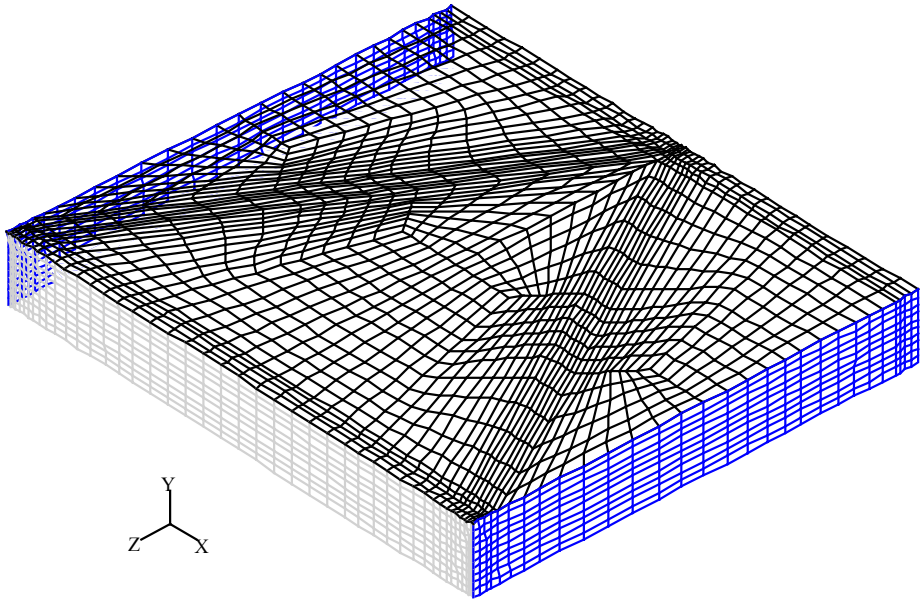


(a) Base grid (GG03), Nc=15000, Clearance = 254µm ( 10 mils).

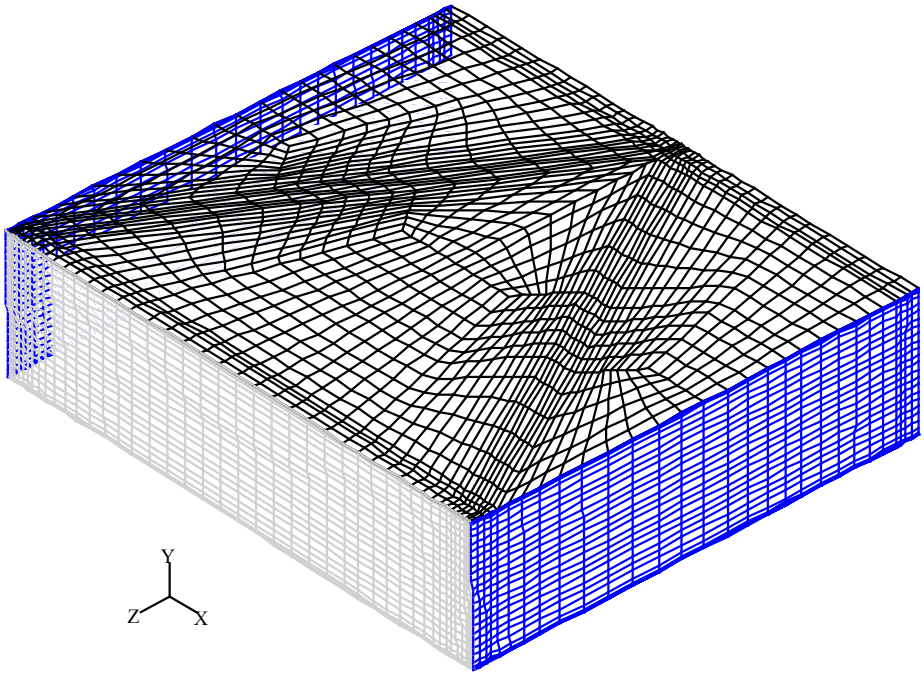


(b) Base grid refined near walls (GG03-1), Nc=42000, Clearance = 508µm ( 20 mils).

Figure 90. Channel flow Grids created from the isogrid geometries of Iwatsubo[36].

Figure 91 compares laminar channel flow predictions in the isogrid based grids with exact theoretical values. The fact that all numerical solutions lie on top of the theoretical 96/Re friction factor line is not enough to assure numerical accuracy because solutions with numerical diffusion (artificial viscosity) would also fall on top the theoretical line. Results shown include 2-D channel flow fine grid predictions, GCI analysis of section 4.2.3.

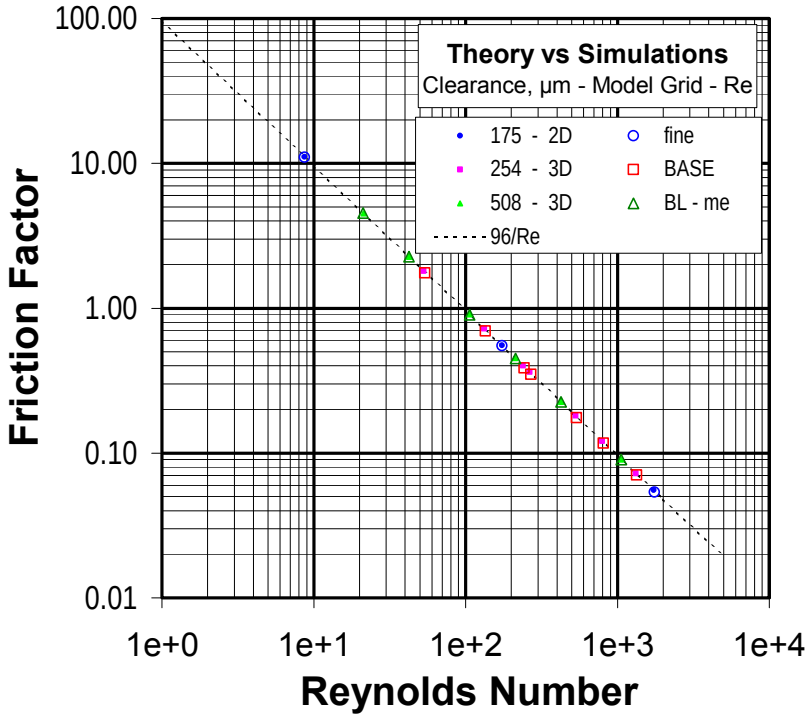


Figure 91. Laminar channel flow vs. numerical simulations from grids based on Iwatsubo[36] geometries.

Deviations from theory in the 2-D numerical solution (175-2D) do not exceed 0.70%. Deviations in the 254 - 3D solutions vary from 3.69% to 2.74%, under predictions associated with the over estimation of mass flow rate due to the default integration method, as deviations in the 508 – 3D solutions only vary from 0.06% to 0.43% as the boundary layer refinement near the walls improve the mass flow rate integration.

Similarly, Figure 92 compares two channel grids based on the honeycomb geometry of Kaneko. A base grid refined near walls to comply with $y^+$ requirements of the enhanced wall treatment in a low Reynolds number flow range, and a base grid used to model laminar and turbulent flow with wall functions. Figure 93 compares 3-D laminar channel flow predictions of honeycomb based grids with the theoretical values in four clearances.

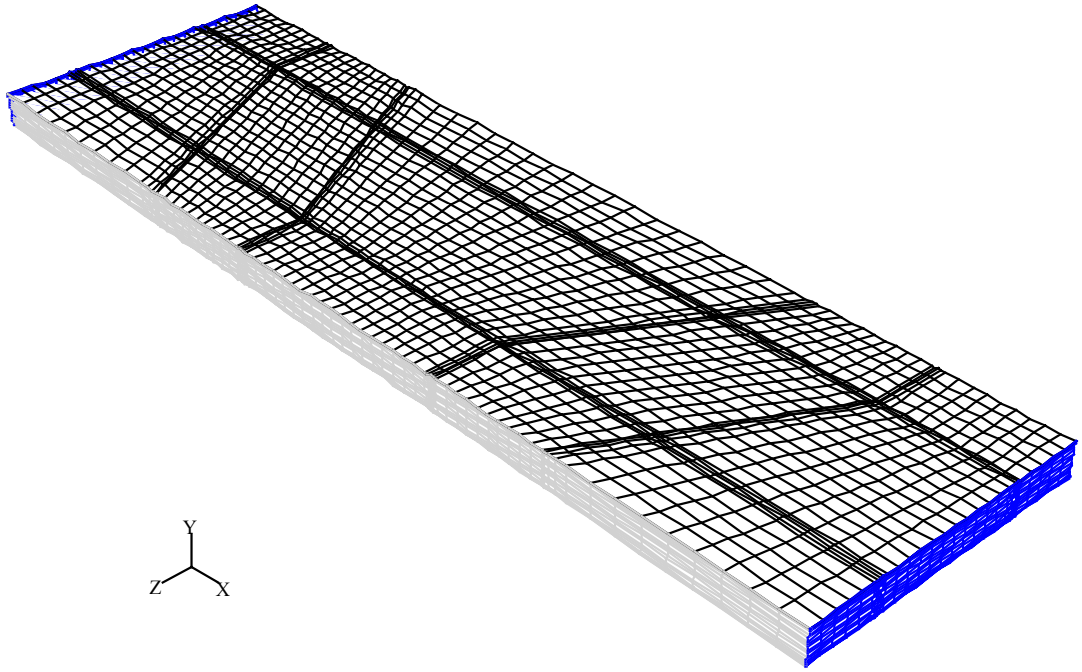


(b) Base grid refined near walls (GG04Ucrxczcyh-1), Nc=37584, Clearance = 254µm ( 10 mils).

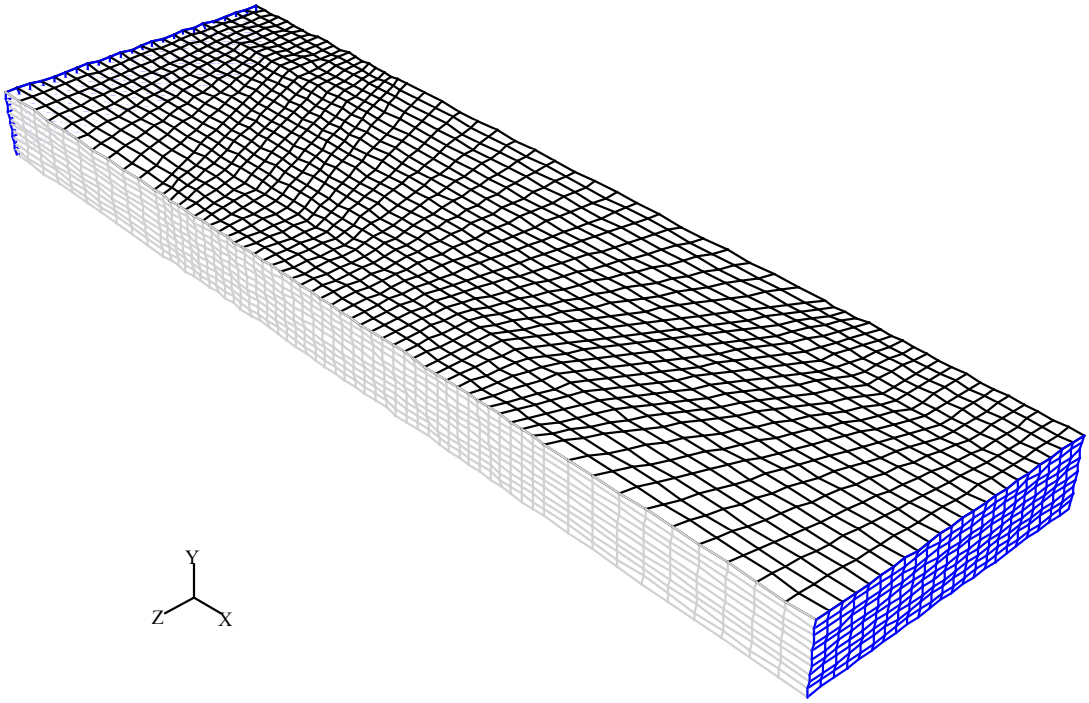


(b) Base grid (GG04Ucrxczcyh), Nc=13800, Clearance = 508µm ( 20 mils).

Figure 92. Channel flow Grids created from the honeycomb geometries of Kaneko [37].

Deviations from theory in the 176 solutions (176 µm clearance) vary from 4.25% to 3.71%. Deviations in the 254 solutions vary from 2.19% to 2.26%. Deviations in the 508 solutions vary from 3.65% to 3.73%. All these deviations are under predictions mainly associated with the over estimation of mass flow rate. On the other hand, deviations in the 762 solutions vary only by 0.93% to 1.81% as the boundary layer refinement near the walls improves the mass flow rate integration.

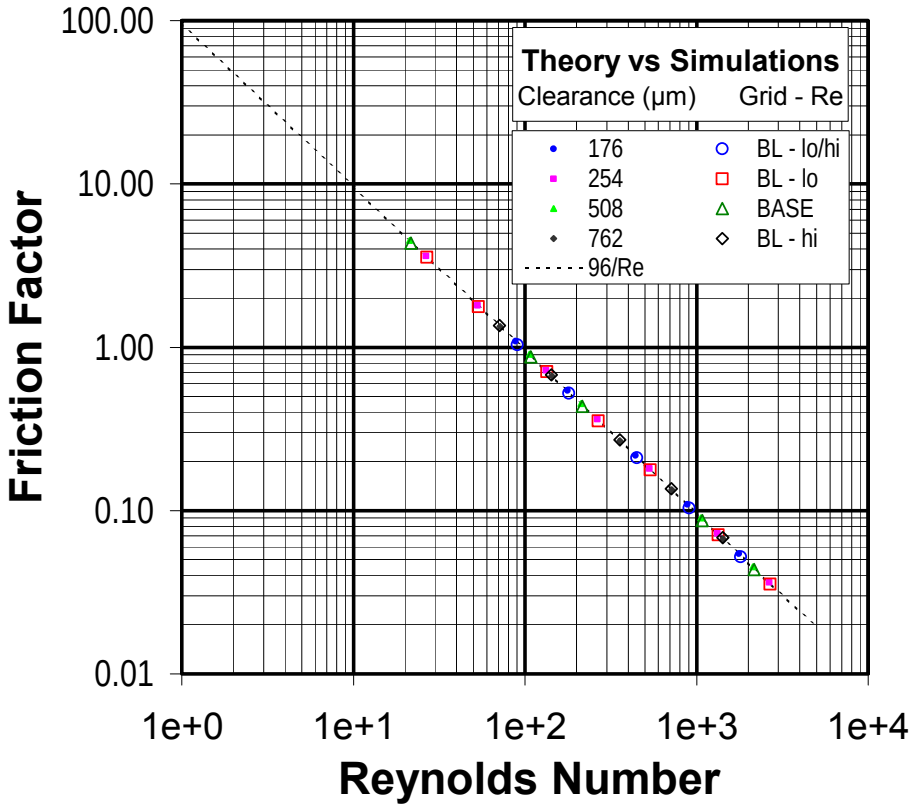


Figure 93. Laminar channel flow vs. numerical simulations from grids based on Kaneko[37] geometries.

In summary, laminar predictions with all channel grids tested replicated satisfactorily the laminar flow solution. When deviations associated with the mass flow rate integration method are removed, all predictions are accurate within 1%. All results correspond to the power law discretization scheme for velocities, the PRESTO scheme for pressure, and the PISO option for the pressure-velocity linking algorithm.

Regarding turbulent channel flow simulations, the performance of the wall function approach as near wall treatment was first evaluated. Although there is no exact theoretical

solution to compare with, the empirical correlation of the friction factor behavior for 'smooth' pipes should provide a good approximation.

Figure 94 compares turbulent channel flow predictions in two base grids with the 'smooth' line of Prandtl. The 'theoretical' friction factor values were calculated with the numerical Reynolds number, $Re_N$, of each discrete simulation, while twice the clearance was used as the equivalent hydraulic diameter to calculate the latter. Results correspond to the power law discretization scheme for all variables, the PRESTO scheme for pressure, the PISO option for the pressure-velocity linking algorithm, and the standard k-ε model was used in the core flow. Results shown include 2-D channel flow calculations, GCI analysis of section 4.2.3 (grid convergence was sought maximizing the flow on each case).

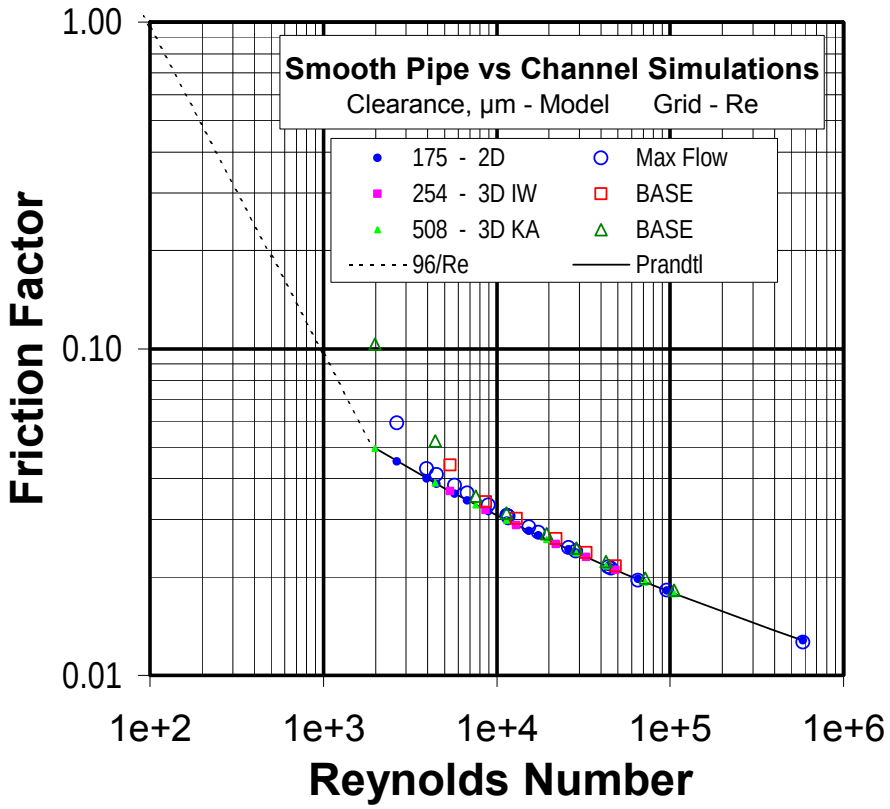


Figure 94. Turbulent channel flow vs. numerical simulations (wall functions).

Deviations from the 'smooth' line in the 2-D numerical solution (175-2D) are as small as 0.12% and do not exceed 1.43% for Reynolds numbers larger than $2.5 \cdot 10^4$. At lower Reynolds number values, deviations increase steadily from 2.42% at Re = $1.7 \cdot 10^4$ to 7.15%

at Re = $4.0 \cdot 10^3$. Deviations in the 254 - 3D IW solutions (base grid from the isogrid pattern) vary from 4.76% to 2.94% for Reynolds numbers larger than $1.3 \cdot 10^4$. Similarly, deviations in the 508 - 3D KA solutions (base grid from the honeycomb pattern) vary from 3.94% to 2.60% for Reynolds numbers larger than $2.0 \cdot 10^4$. Indeed, both 3-D solutions correlate very well with average deviations below 1% in the common Reynolds number flow range.

In summary, turbulent predictions with the wall function approach in all channel grids tested replicated satisfactorily the 'smooth' pipe turbulent flow solution for Reynolds number larger than $2.0 \cdot 10^4$. Deviations within 3-D and 2-D predictions are associated with the selection of a different turbulence model for the core flow. As discussed in references [19,42], using the standard k-ε model results in larger friction factor values. The turbulence model account for up to 1% of the calculated deviations. Larger deviations at lower Reynolds number values are associated with the nature of the near wall treatment. Wall functions are simply not a low Reynolds number model. Instead, deviations only exceed 7% when $y^+$ is below 12.0, as shown by the scattered data in all predictions at very low Reynolds number, where there is also uncertainty in the prevailing flow regime.

Then, the performance of the enhanced wall treatment (two-layer zonal model) as near wall approach was also evaluated. Similarly, it was expected that numerical solutions should correlate well with the empirical friction factor behavior of 'smooth' pipes.

On the contrary, it was found that turbulent predictions with the enhanced wall treatment only matched the 'smooth' pipe solution at the largest Reynolds number under evaluation, Re~$10^5$. Although all clearance and grid solutions correlate fairly within 5%, their deviations from the 'smooth' pipe friction factor line increases monotonically as the Reynolds number is reduced. In fact, numerical solutions blend into the theoretical laminar flow solution for Reynolds number below $10^3$.

To validate that predicted deviations were inherently due to the near-wall turbulence model and not to numerical diffusion levels common to all solutions, a similar 2-D channel flow GCI analysis to the one described in section 4.2.3 was executed, but with the enhanced wall treatment as near-wall turbulence model. Again, grid convergence was sought maximizing the flow on each Reynolds number case. In addition, simulations were also ran with older versions of the CFD software to assure that the original two-layer zonal approach

of Chen[25] is recovered when the newer enhanced wall treatment is properly resolved.

Figure 95 compares turbulent channel flow predictions in one base grid and five near-wall refined grids with the 'smooth' line of Prandtl. Predictions include four clearances and grids derived from the two pattern geometries, isogrid (IW) and honeycomb (KA). Results correspond to the power law discretization scheme for all variables, the PRESTO scheme for pressure, the PISO option for the pressure-velocity linking algorithm, and the standard k-ε model was used in the core flow. With the intent of maximizing flow, the RNG k-ε turbulence model was used in the 2-D channel flow GCI analysis.

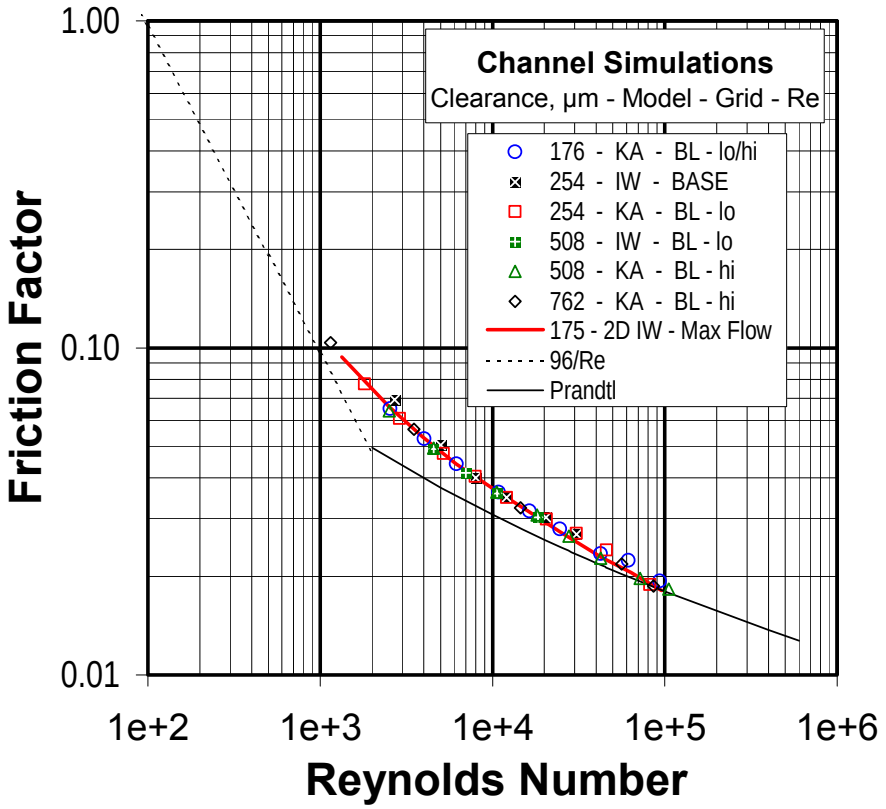


Figure 95. Turbulent channel flow vs. numerical simulations (enhanced wall treatment).

In summary, turbulent predictions with the enhanced wall treatment in all channel grids are consistent but do not replicate the 'smooth' pipe turbulent flow solution. Deviations among 3-D solutions and with the 2-D predictions are associated with the fact that $y^+$ modeling restrictions are not met in the whole Reynolds number flow range simulated in each grid. Recall that each grid was individually tailored for a particular clearance and flow

range when modeling each full 3-D pattern geometry. But even when a base grid designed for wall functions (254 – IW solution) was purposely used to simulate enhanced wall treatment cases, predicted deviations did not exceed 5%, while predictions are consistent within 2% when $y^+$ is below 2.5.

The replication of laminar and turbulent channel flow with meshes identical to the ones used as base and tailored for each pattern geometry on each clearance simulated is an indication that no significance numerical diffusion was introduced with the use of highly distorted grids. Secondly, the consistency of the enhanced wall treatment predictions in deviating for the 'smooth' pipe solution led us to analyze the DNS data of Moser[35]. Such data indicates that enhanced wall treatment solutions (by default the two-layer zonal model) appear to be a better solution to the turbulent channel flow problem than the simplified 'smooth' pipe approximation. Finally, distorted grids affected considerably achieving iterative convergence when using the more elaborated Reynolds stress model for the core flow. These and other modeling considerations are discussed in detail in section 4.3.

A summary of all grids used to model the main patterns under scrutiny, square groove, round-hole, isogrid and honeycomb, is included in the Appendix.

## *4.4. Turbulence modeling*

### *4.4.1. Effect on mass flow rate predictions of the location of the first grid point near the wall when using wall functions*

The effect of locating the first grid point near the wall within the buffer and viscous sub-layer [20] was indirectly addressed in references [19,42] when discussing the grid independent solution study performed in the 2-D numerical analysis of Nava's experiments. Then, an apparent compensating effect made k-ε with wall functions predictions comparable to the results obtained with the Reynolds stress model and the two-layer zonal approach. In the former model combination, turbulence levels predicted in the core region were comparatively lower but dissipation values were clearly larger near the walls. These behavior was thought to be a consequence of law of the wall implementation algorithm. For $y^*$ (equivalent to $y^+$) values below 11.225, the wall friction velocity is adjusted to a laminar profile while the boundary condition in the dissipation equation remains inversely proportional to the wall distance. Therefore, dissipation values at each first cell near the wall always increase as the local grid is refined. Mass flow rate reductions in 2-D simulations based on the small round geometry of Nava [42] did not exceed 25%.

As described in sections 4.2.3 and 4.2.4, the GCI and the use of conformal grids were evaluated while simulating theoretical channel flow. The exact solution to the governing equations was the reference in the laminar regime. In the analysis of turbulent predictions, the 'smooth' pipe solution and the DNS work of Moser [35] were used. All DNS references included herein relate to this work. Using the grids already presented in Figure 78, the effect of the actual $y^+$ value in the mass flow rate prediction for turbulent channel flow was explored. Figure 96 present mass flow rates extracted from the fine and medium grid calculations divided by the flow rate extracted from the coarse grid. Results correspond to the power law discretization scheme for all variables, the PRESTO scheme for pressure, and the PISO option for the pressure-velocity linking algorithm. The RNG k-ε model was used in the core flow with wall functions as near-wall treatment, with $y^+$ equal to 12.0 to 134 for the coarse grid in the whole Reynolds number flow range simulated.

From Figure 96, it can be easily inferred that there is no significant effect in the mass flow rate prediction when the actual value of $y^+$ is larger than 12.0. Indeed, when the law of

the wall criteria (as implemented in the software) is met in all grids, the mass flow rate ratio is simply an indication of grid convergence as described in sections 4.2.2 and 4.2.3. Nevertheless, when the actual value of $y^+$ is below 12.0, the mass flow rate predicted in both grids is significantly reduced. A regression analysis indicate that the mass flow rate reduction is linearly dependent to the decreasing in actual $y^+$ values ( r = 0.9995 ). At $y^+$ equal to 5.0, the mass flow rate prediction is reduced by roughly 30%. These reduction levels are comparable to those observed in references [19] and [42].

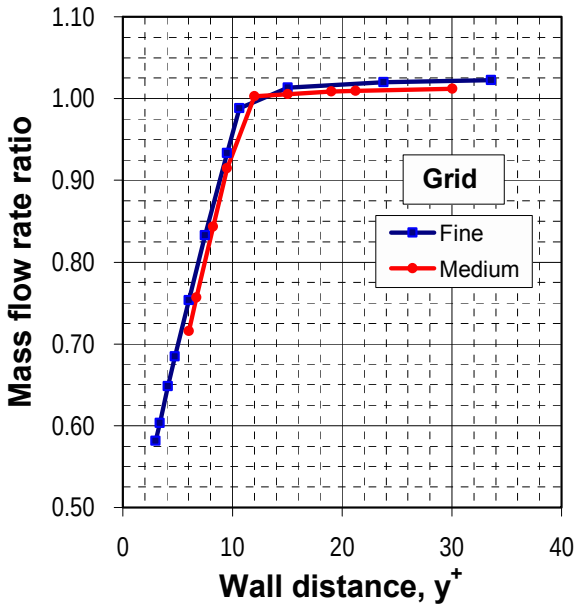


Figure 96. Mass flow rate ratios, Fine and Medium grid solutions, turbulent channel flow, Cr = 175 μm.

Upon confirmation that locating grid points inside the buffer layer when using the wall function approach leads to reduced mass flow rate predictions, the hypothesis that such reduction is due to the numerically enhanced turbulence activity near the walls [42] was analyzed further. Normalized profiles of turbulent dissipation along the channel clearance were compared, Reynolds numbers ranging from $2.6 \cdot 10^3$ to $6.5 \cdot 10^4$, to find no significant difference in predictions for this variable beyond the expected discretization error. Certainly, dissipation values near the walls increase as the grid is refined but predictions remain consistent even when all grid solutions have the first grid point located inside the buffer layer, as shown in Figure 97(a). A consistent behavior of the normalized profiles is predicted (as expected given the model assumptions) at all Reynolds number, Figure 97(b).

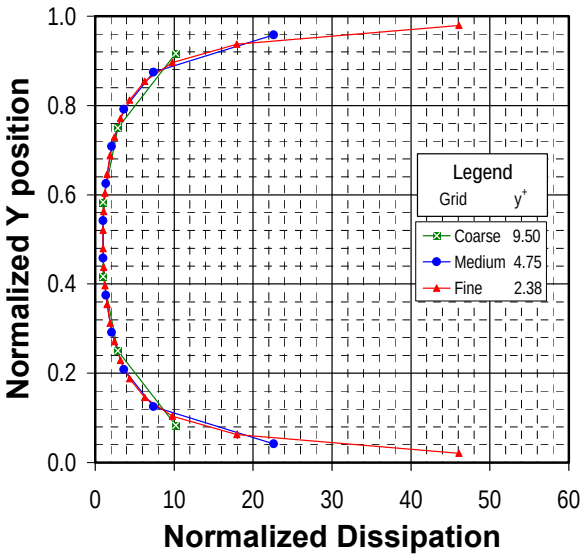


(a) $\Delta P_X$ = 5e6 Pa/m, Re ~ $2.6 \cdot 10^3$, $\varepsilon_0 \sim 4 \cdot 10^3$ $m^2/s^3$

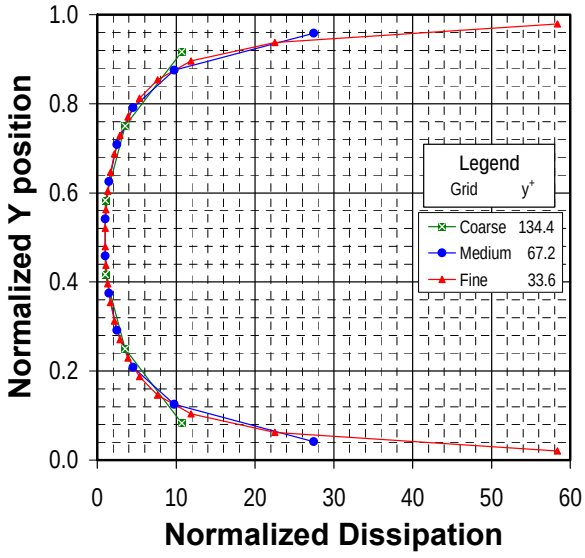


(b) $\Delta P_X$ = 1e9 Pa/m, Re ~ $6.5 \cdot 10^4$, , $\varepsilon_0 \sim 1 \cdot 10^7$ $m^2/s^3$

Figure 97. Normalized dissipation profiles, turbulent channel flow predictions, clearance = 175 µm.

Similarly, normalized profiles of the turbulent kinetic energy were also compared to find that predictions are also consistent, for the fine and medium grid solutions (the coarse solution is too "coarse" for k), but in contrast to dissipation, kinetic energy values near the walls are numerically equivalent, and it is near the centerline where the kinetic energy appear to be slightly under predicted in the coarse grid, Figure 98.

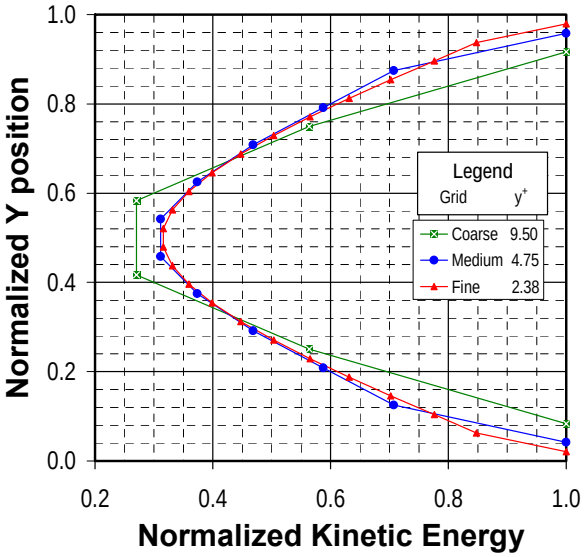


(a) $\Delta P_X$ = 5e6 Pa/m, Re ~ $2.6 \cdot 10^3$, $k_0 \sim 1.4$ $m^2/s^2$

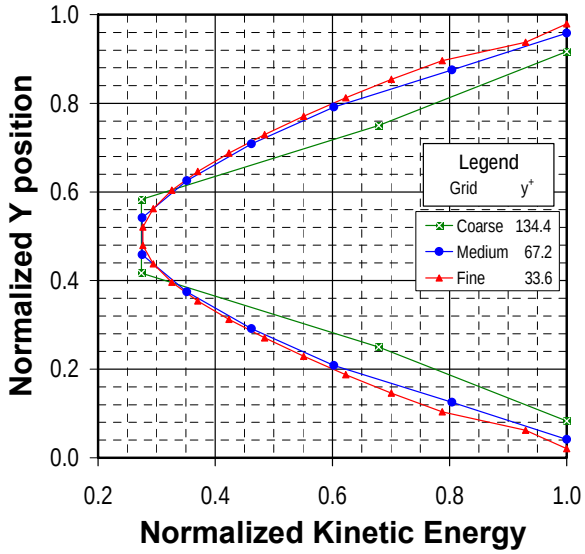


(b) $\Delta P_X$ = 1e9 Pa/m, Re ~ $6.5 \cdot 10^4$, $k_0 \sim 290$ $m^2/s^2$

Figure 98. Normalized turbulent kinetic energy profiles, channel flow predictions, clearance = 175 µm.

The fact that turbulent profiles appear to be barely affected by the actual location of the first cell near the wall is more evident when predictions in those cells are normalized by the values estimated in the coarse grid and plotted as functions of the wall distance, Figure 99.

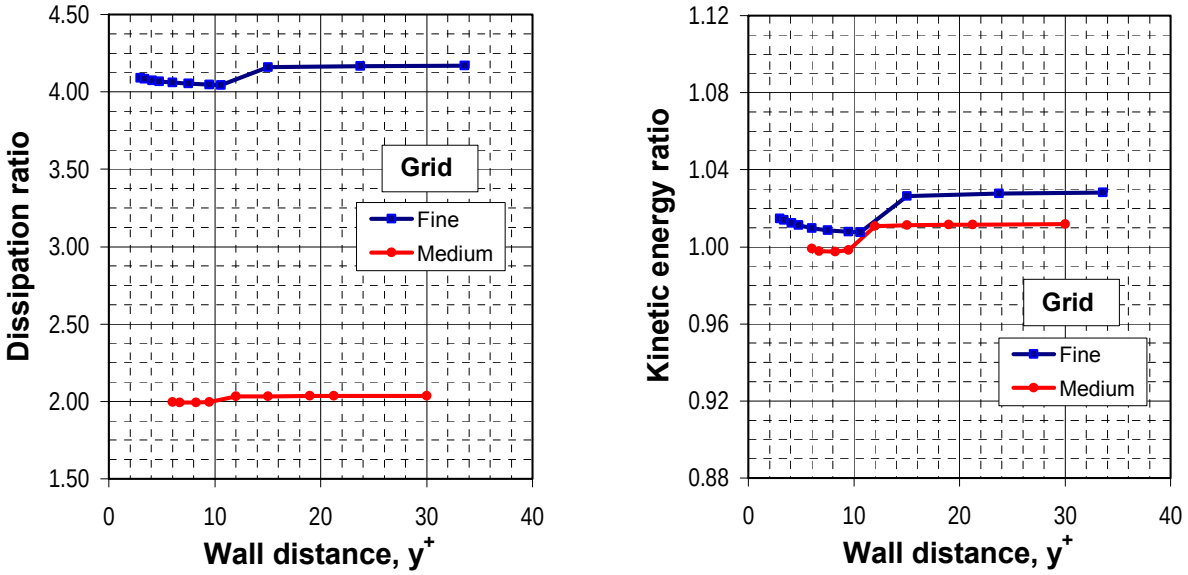


(a) Dissipation (b) Turbulent kinetic energy.

Figure 99. Turbulence profiles ratios, channel flow predictions, clearance = 175 μm.

Dissipation ratio in all fine grid solutions is roughly 4.2 for $y^+$ values larger than 12.0, and varies from 4.05 to 4.09 for $y^+$ values lower than 12.0. Likewise, dissipation ratio in all medium grid solutions is roughly 2.03 for $y^+$ values larger than 12.0, and exactly 2.00 for $y^+$ lower than 12.0. Recalling that the grid refinement factors of both meshes fine and coarse are 4.0 and 2.0 respectively, predicted dissipation values are consistent with the formulation (dissipation in the cells at the walls is inversely proportional to the distance from the cell center to the wall), and no significant deviation can be attributed to locating grid points inside the buffer layer. Similarly, turbulent kinetic energy ratios are consistent within 3% in compliance with the formulation; turbulent kinetic energy in wall cells is proportional to the friction velocity, so grid refinement should not alter the boundary condition for the turbulent kinetic energy.

In summary, moderate deviations predicted in turbulent kinetic energy levels are consistent and they are not affected by the actual $y^+$ value. The numerically exaggerated dissipation value at the wall has a similar behavior. Therefore, they do not explain the sharp

reduction in mass flow rate predictions when the grid have cells with $y^+$ values below 12.0.

As discussed extensively in previous sections, mass flow rate is simply the integration of the predicted velocity profile. Therefore, the attention shifted to the velocity profile. As done for the dissipation and turbulent kinetic energy, the behavior of the velocity in the first cell near the wall was tracked as the grid was refined. Figure 100 shows the velocity of the first cell near the wall in the fine and coarse grid solutions normalized by the corresponding value in the coarse grid solution.

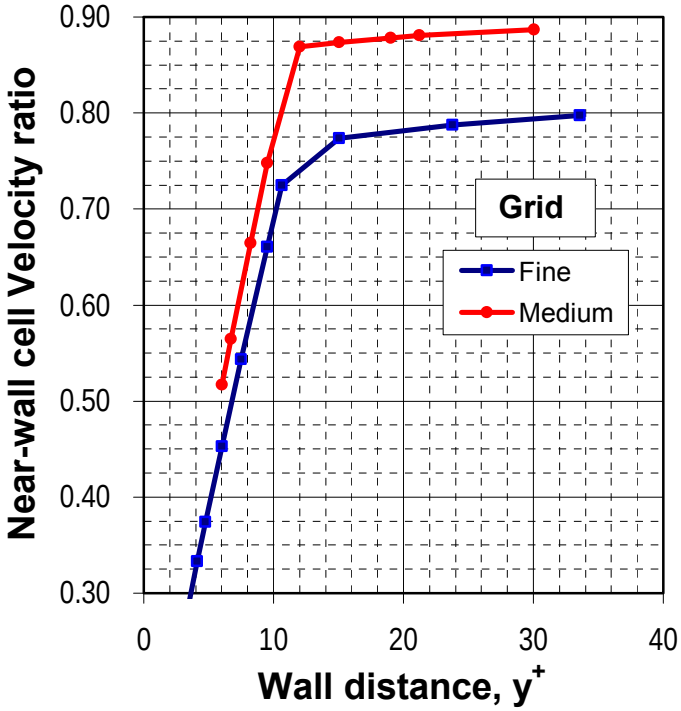


Figure 100. Near-wall cell velocity ratios, Fine and Medium grid solutions, channel flow, Cr = 175 µm.

From Figure 100, it is easily inferred that the velocity of the first cell near the wall is drastically affected by the actual $y^+$ value. For $y^+$ values below 12.0, the velocity ratios are linearly dependent on $y^+$, and as expected, velocity ratios are logarithmically dependent on $y^+$, for values above 12.0. Further scrutiny and derivation of the boundary conditions from the governing equations for all variables indicate that the only constrain at the boundary when using wall functions, as implemented in the software, is the calculation of the friction velocity, $(\tau_w/\rho)^{1/2}$. Both, turbulent kinetic energy and dissipation are proportional to such velocity. Figure 101 shows non-dimensional wall velocities versus the wall distance.

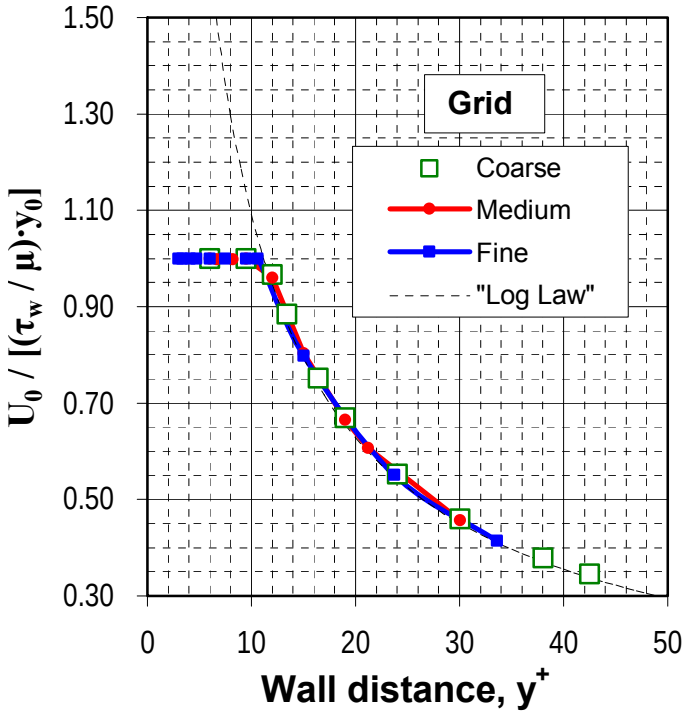


Figure 101. Near-wall non-dimensional velocity, all grid solutions, channel flow, Cr = 175 μm.

Figure 101 presents the non-dimensional velocity of the near-wall cells of all grids as a function of the wall distance. Note that the drastic reduction predicted in mass flow rate in grids with the first point located inside the buffer layer is a consequence of enforcing the laminar relationship $U^* = y^*$, valid only in the laminar sub-layer, in cells with actual $y^*$ values below 11.225 (it was verified that $y^+$ and $y^*$ are equivalent [24]).

In summary, locating grid points inside the buffer layer when the wall function approach is used as near-wall treatment of turbulence leads to under prediction in the mass flow rate due to the enforcing of the laminar relationship $U^* = y^*$. The reduction in mass flow rate is linearly dependent on the actual $y^+$ value. A reduction of 50% in the mass flow rate is expected when the value of $y^+$ is 2.0. A reduction predicted in turbulent channel flow is the maximum expected when extending the use of the wall function approach to the analysis of 3-D models. In 3-D flows, $y^+$ values vary from cell to cell (for grids with equal distance to the wall) due to the presence of the roughness pattern; and strictly speaking, the law of the wall is not valid within them because of flow separation. The main advantage of using wall functions is the relatively easiness in achieving convergence with simple grids.

### *4.4.2. Channel flow.*

As discussed in the conformal single block grid validation, section 4.2.4, turbulent channel flow predictions with the wall function approach reproduced satisfactorily the 'smooth' pipe turbulent flow solution. In contrast, predictions based on the enhanced wall treatment consistently deviated from the 'smooth' pipe solution, particularly at lower Reynolds number, where turbulent predictions appear to blend into the laminar predictions.

Regarding the 'exact' flow behavior in turbulent channel flow, the direct numerical simulation data of Moser [35] is referenced by many researchers [20] as extremely valuable in providing insight into the statistical and structural characteristics of wall-bounded turbulence. DNS predictions are for Reynolds number values of $1.12 \cdot 10^4$, $2.75 \cdot 10^4$, and $4.38 \cdot 10^4$, using equation (1), well within the range being analyzed in the present research, $10^4$ to $10^5$. Figure 102 combines selected wall functions and enhanced wall treatment predictions from Figures 94 and 95, zooming into the Reynolds number range of interest, and adding the DNS and its trend. The smooth seal reference data extracted from the low Reynolds number experiments of Iwatsubo[36] and Kaneko[37] was also added.

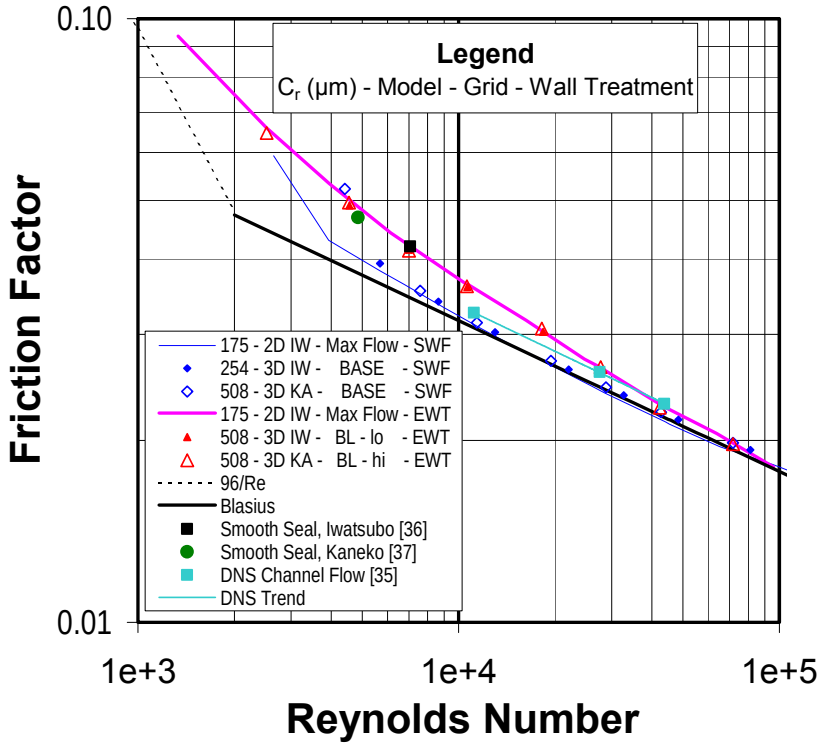


Figure 102. Turbulence modeling channel flow predictions vs. direct numerical simulations [35].

Enhanced wall treatment (EWT) predictions, equivalent to the two-layer zonal model, agree very well with DNS for the medium and large Reynolds number cases. At the lower DNS Reynolds number, DNS predictions lay between standard wall functions (SWF) predictions and the former. Indeed, DNS friction factor data correlates very well with Reynolds number as a power function. Unequivocally, EWT predictions are in better agreement with the smooth seals experiments at low Reynolds number, within 1% to 4%, than the trend indicated by the DNS predictions. To evaluate why the enhanced wall treatment outperforms wall functions in predicting medium range Reynolds number turbulent channel flow, velocity and turbulence profiles at those Reynolds numbers of the 2-D maximum flow predictions were compared to DNS (reverting the non-dimensional approach used to create the original data files [50]). Figure 103 compares velocity profiles at the corresponding pressure gradients extracted from the DNS. Both numerical modeling predictions correspond to the RNG k-ε model for the core flow; standard and RNG k-ε model predictions agree within 0.50% in the DNS Reynolds number data flow range.

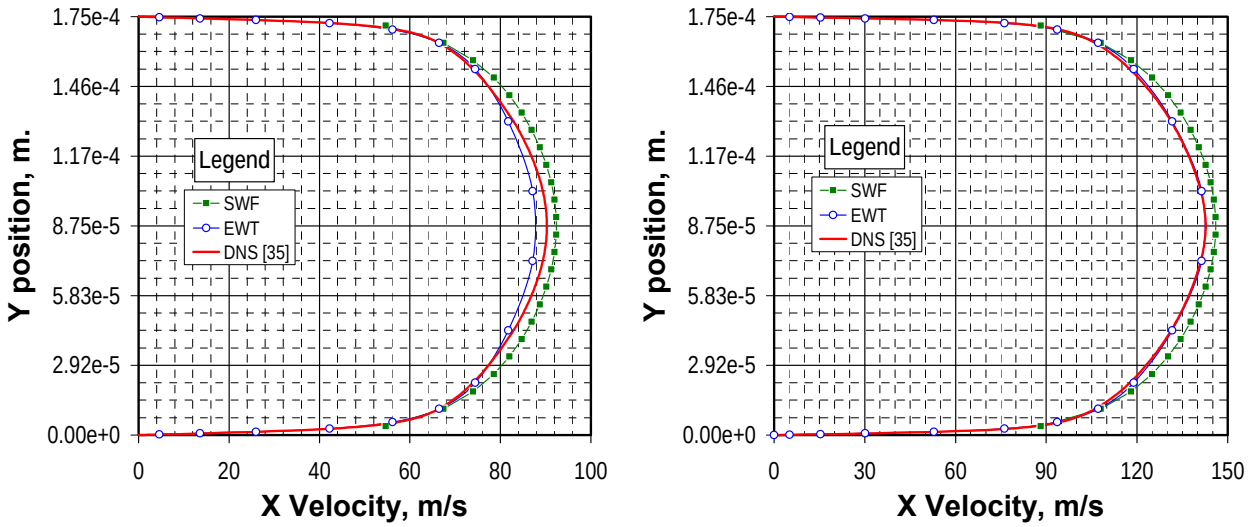


(a) $\Delta P_X = -4.74 \cdot 10^7$, Re ~2.72-2.87·10$^4$, $y^+_{EWT} \sim 1.02$. (b) $\Delta P_X = -5.15 \cdot 10^8$, Re ~4.38-4.55·10$^4$, $y^+_{SWF} \sim 24.5$.

Figure 103. Stream wise velocity profiles, EWT and SWF vs. DNS[35], channel flow, $C_r$ = 175 µm (~6.9 mils).

With the exception of a small deviation (2.5%) near the channel center in Figure 103(a), EWT velocity profiles reproduce DNS predictions within 1.0%. On the other hand, SWF velocity profiles are consistently larger than DNS between 2.4% and 10.0%. The accuracy of the calculated wall friction velocity, defining the value in the first cell near the wall, does

not appear to influence the over prediction level in the wall function approach.

Similarly, Figure 104 compares turbulent kinetic energy profiles of both numerical RNG k-ε modeling predictions and the DNS. Both approaches over estimate turbulent kinetic energy levels near the channel center. At the medium Reynolds number value, Figure 104(a), the SWF approach predicts 30% larger values while the EWT model predicts even larger values by as much as 60%. Instead, the EWT profile is within 1% of the DNS predictions near the wall, while the SWF approach under estimate the level in the first cell by 26%. At the largest Reynolds number value, Figure 104(b), there is a comparable behavior; both approaches over estimate turbulent kinetic energy levels near the channel center by roughly 35%, but the EWT profile is within 2% of the DNS predictions near the wall, while the SWF approach under estimate the level in the first cell by 25%.

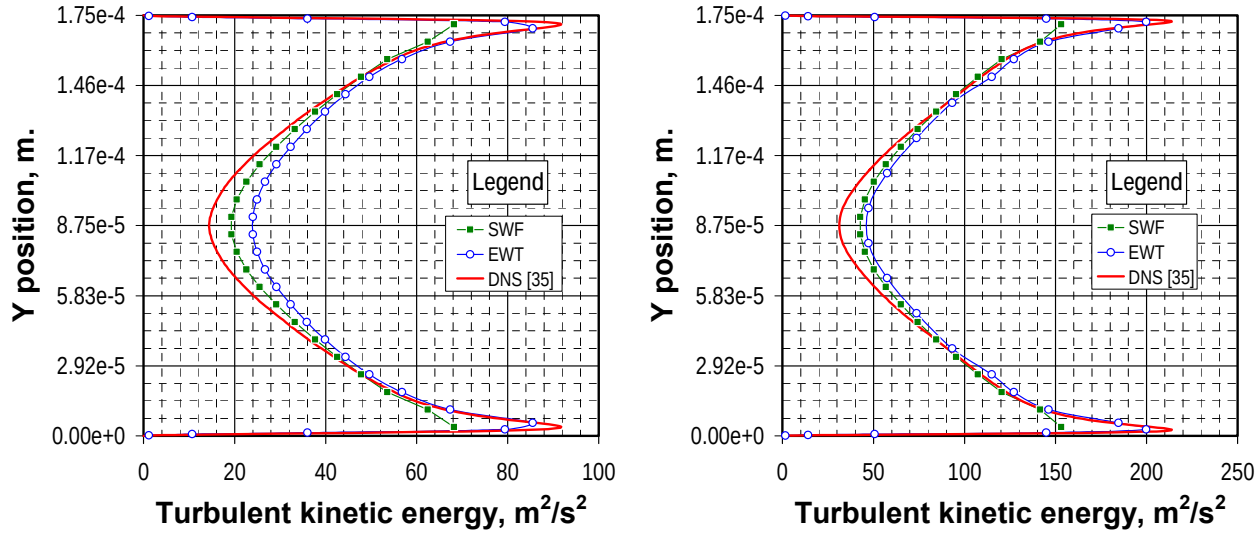


(a) $\Delta P_X = -4.74 \cdot 10^7$, Re ~2.72-2.87·10$^4$, $y^+_{SWF} \sim 16.3$. (b) $\Delta P_X = -5.15 \cdot 10^8$, Re ~4.38-4.55·10$^4$, $y^+_{EWT} \sim 0.76$.

Figure 104. Turbulent kinetic energy profiles, EWT and SWF vs. DNS[35], channel flow, $C_r$ = 175 μm (~6.9 mils).

Lastly, Figure 105 compares dissipation profiles of both numerical RNG k-ε modeling predictions and DNS. At the medium Reynolds number value, Figure 105(a), the SWF approach predicts 4.4% lower values than DNS predictions near the channel center, while the EWT model over estimates dissipation by 5.1%. In the intermediate channel zone (not the center nor the wall), the SWF profile is within 0.4% and 4.5% of the DNS predictions, while the EWT approach underestimate DNS predictions by 0.7% to 25.2%. In contrast, the

EWT profile is within 1% of the DNS predictions near the wall, while the SWF approach over estimate the level in the first cell by 20%. At the largest Reynolds number value, Figure 105(b), the SWF approach predicts between 0.7 to 3.7% lower values than DNS near the channel center, while the EWT model over estimates dissipation by 4.3%. In the intermediate channel zone, the SWF approach over predicts dissipation by 6.3% to 22.6%, while the EWT approach is within 2.3% of the DNS predictions. On the other hand, the SWF approach prediction in the first cell is within 0.7% of the DNS, while the EWT approach over predicts dissipation by 7.9%. It should be noted that while DNS predictions show the maximum dissipation value at the wall, the EWT approach predicts the maximum dissipation slightly off the wall (within the buffer sub-layer).

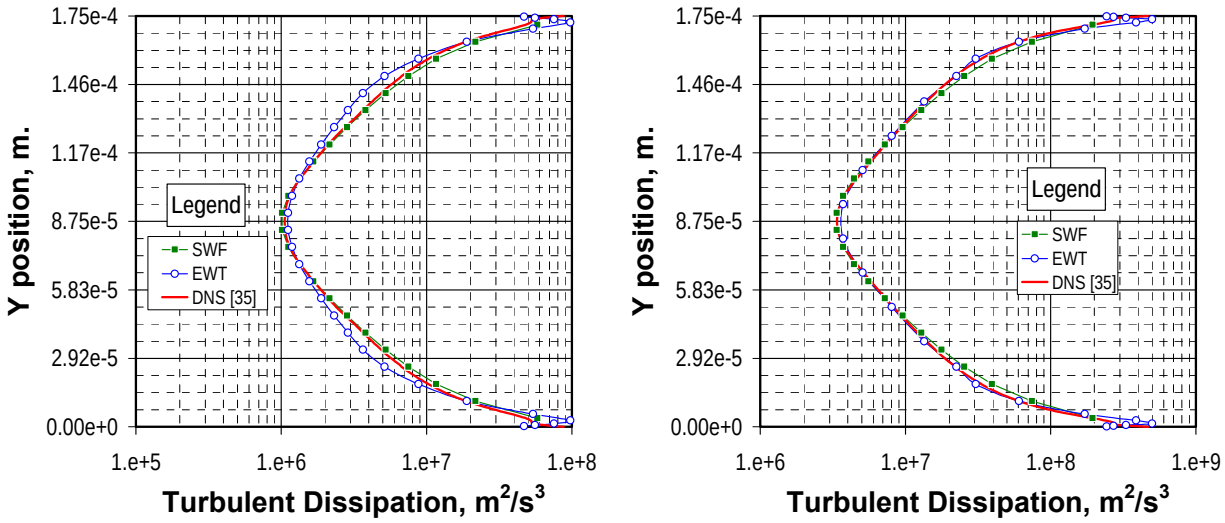


(a) $\Delta P_X = -4.74 \cdot 10^7$, Re ~2.72-2.87·10$^4$ (b) $\Delta P_X = -5.15 \cdot 10^8$, Re ~4.38-4.55·10$^4$

Figure 105. Dissipation profiles, EWT and SWF vs. DNS, channel flow, $C_r$ = 175 µm (~6.9 mils).

In summary, it is apparent that the better resolution of mean velocity and turbulent kinetic energy profiles near the wall is the reason the enhanced wall treatment outperforms the wall function approach in predicting the actual mass flow rate in turbulent channel flow at medium range Reynolds numbers. Indeed, it is apparent that mass flow rate predictions in both approaches are consistent even when turbulent kinetic energy and dissipation profiles are not fully converged (grid dependent), provided velocity profiles are fully converged and the location of the first cell near the wall meet the modeling criteria.

Another issue addressed when performing the conformal single block grid validation described in section 4.2.4, was reviewing why the used of either distorted grids or locally refined grids affected considerably achieving iterative convergence when using the more elaborated Reynolds stress model for the core flow.

As presented in section 4.2.2, fully converged turbulent simulations in the whole Reynolds number under study (up to $10^5$) were first obtained in the coarsest grid developed to model the honeycomb pattern of Kaneko [37] in the test clearance of 176 μm when using Reynolds stress model (RSM) in the core flow and the enhanced wall treatment as near-wall approach. Results were grid independent, but modeling restrictions on $y^+$ values were not met in the high Reynolds number cases. When comparable grids were refined near all walls in a boundary layer style to comply with modeling restrictions, the iterative convergence process was compromised and in most cases residuals either stalled or diverged. Similarly, using local refinement based on actual $y^+$ values in the final grids of the isogrid pattern of Iwatsubo[36] led to slow convergence and stalled residuals.

As found in the 2-D numerical analysis of Nava's experiments [19], simulations based in the RSM modeling resulted in larger friction factors but overall predictions did not improve in comparison with the experiments. When the numerical analysis was extended to larger clearances, iterative convergence remained an issue when refining grids to comply with $y^+$ modeling restrictions. Given the difficulty in achieving iterative convergence and the fact that predictions did not improve in terms of absolute values at the test clearances, simulations using the RSM model were not pursued in further detail.

With the turbulent channel flow numerical data developed for the conformal single block grid validation as reference, the performance of the RSM model was evaluated when used in grids that were refined near the pattern walls. Figure 106 combines 3-D results in selected clearances from both near-wall treatments, standard wall functions (SWF, from Figure 94) and enhanced wall treatment (EWT, from Figure 95). Both 2-D 'maximizing flow' approaches developed for the test clearance in the groove seal of Iwatsubo [38] are also added. Recalling that 'BASE' grids were developed to model laminar and turbulent flow with wall functions, and 'BL / hi' grids were developed to comply with $y^+$ requirements of the enhanced wall treatment in high Reynolds number flow, calculations with both RSMSWF and RSMEWT turbulence modeling combination are included.

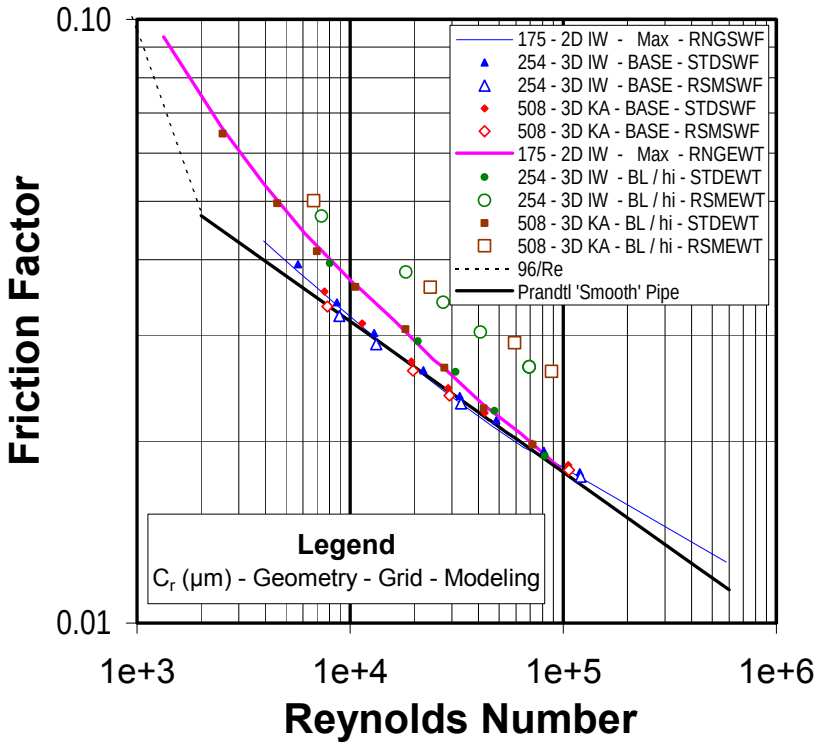


Figure 106. Second vs. First order closure models performance in turbulent channel flow.

Following are the more relevant observations:

- RGNSWF and STDSWF solutions are comparable within 2.0% and they slightly deviate from the Prandtl 'Smooth' pipe solution for Reynolds numbers larger than $2.5 \cdot 10^4$, as already discussed in section 4.2.4.
- RSMSWF solutions are comparable within 0.1% and they both are larger than the Prandtl 'Smooth' pipe solution by 0.8 to1.3 %.
- RGNEWT and STDEWT solutions are consistent within 2.0% but they deviate from the Prandtl 'Smooth' pipe solution in better agreement with DNS predictions at medium Reynolds number flow as discussed above.
- RSMEWT solutions are comparable within 2.4% to 4.6% but they both are consistently larger than the Prandtl 'Smooth' pipe solution by as much as 46%.

In summary, all SWF solutions are comparable within 1 to 4 % independently of the turbulence model selected for the core flow, while EWT solutions differs as much as 46% when the RSM model is used in the core flow. Besides the turbulence model, the only difference in the numerical approach is the use of grids refined near the walls in a boundary

layer manner. Fully converged solutions were obtained in the grid identified as '254 – 3D IW – BL / hi', a grid that was originally refined near the bottom and top walls but not inside the isogrid pattern. In opposition to, solutions obtained in the grid identified as '508 – 3D KA – BL / hi', a grid that was originally refined near all walls including the honeycomb pattern, did not fully converge as most residuals stalled. Figure 107 shows the latter grid and the principal Reynolds stresses distribution along the mid-clearance horizontal plane.

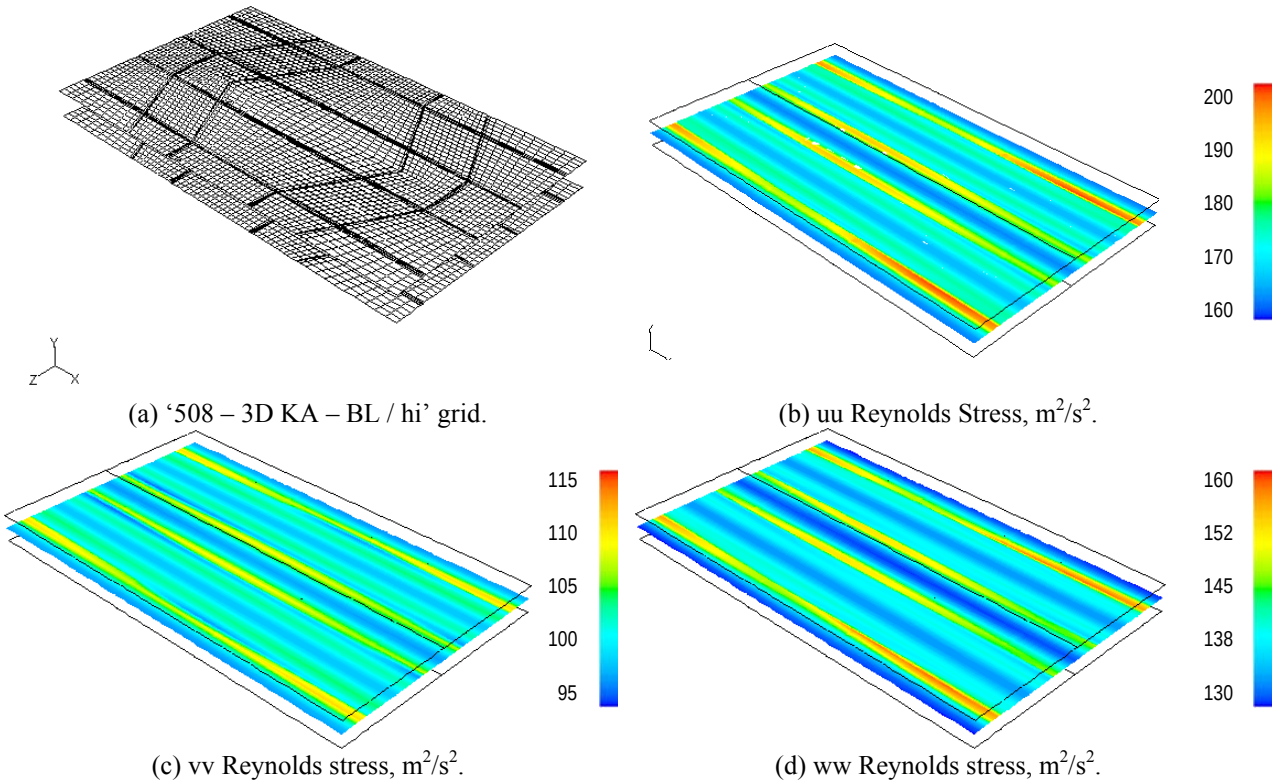


(a) '508 – 3D KA – BL / hi' grid.

(b) uu Reynolds Stress, $m^2/s^2$.

(c) vv Reynolds stress, $m^2/s^2$.

(d) ww Reynolds stress, $m^2/s^2$.

Figure 107. Turbulent channel flow, Reynolds stress predictions at $Re \sim 8.8 \cdot 10^4$, 508 μm (20 mils) clearance.

Reynolds stress variations in the mid-clearance horizontal plane are as large as 25%, where no deviations are expected given the 1-D nature of the mean turbulent flow. As it can be inferred from the contours plots, the variations are predominantly spread in the span wise direction (Z coordinate axis), and the maximum values correspond to the cells that are highly distorted to fit the removed honeycomb pattern with a boundary layer type mesh.

The artificial variations of Reynolds stresses in the span wise direction creates small but not negligible secondary flows in the vicinity of the distorted cells that certainly affect the

convergence process and compromise any numerical prediction. Figure 108 shows contours of the mean velocity components and the Y-vorticity.

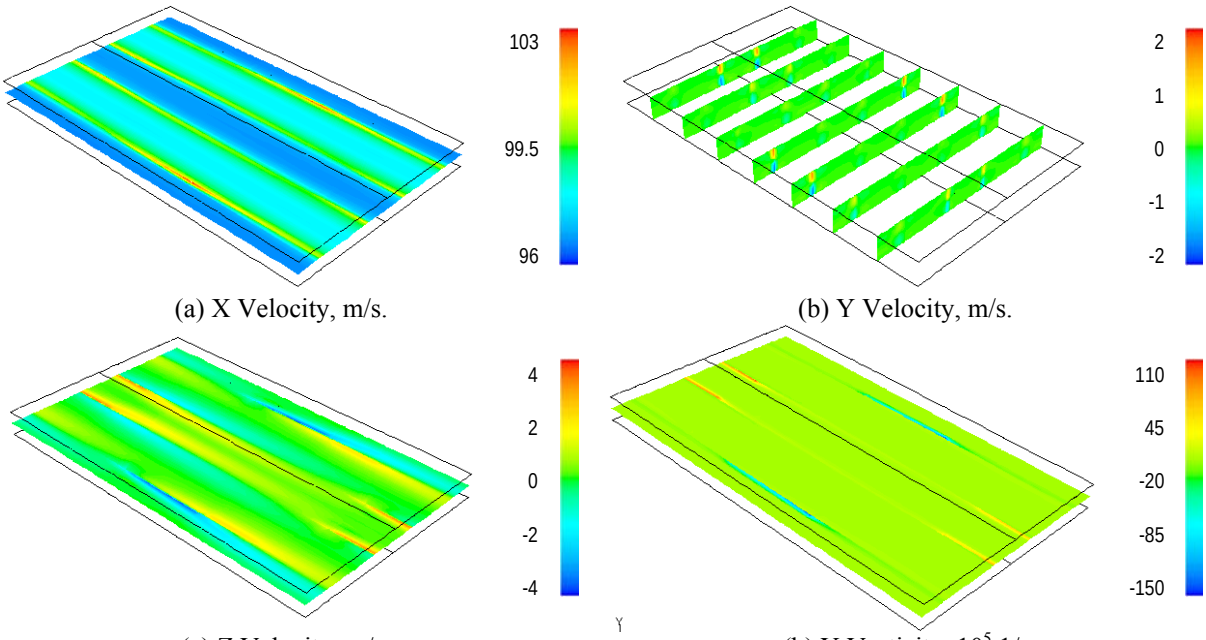


(a) X Velocity, m/s.

(b) Y Velocity, m/s.

(c) Z Velocity, m/s.

(b) Y Vorticity, $10^5 \cdot 1/s$.

Figure 108. Turbulent channel flow, mean velocity predictions at Re~$8.8 \cdot 10^4$, 508 μm (20 mils) clearance.

In contrast, RSMEWT solutions obtained in the '254 – 3D IW – BL / hi' grid did not reflect this localized distortion of Reynolds stresses but the over prediction in the friction factor is associated with larger turbulent kinetic energy levels when compared to DNS and the '254 – 3D IW – BASE' grid solution. The larger levels of turbulent kinetic energy are mostly associated with over prediction of the vv and ww Reynolds stress components.

In summary, the iterative convergence process when using the Reynolds stress model is negatively impacted by the use of distorted grids. On the other hand, using locally refined grids (just near the wall without propagation into other portions of the domain) does not affect iterative convergence when using the Reynolds stress model, but it is apparent that when used in combination with the enhanced wall treatment, larger friction factors are predicted, even in well controlled simplified 2-D grids. Given this limitations, simulations using second order turbulence closure models were not pursued further.

### *4.4.3. Grooved seal of Iwatsubo [38].*

In section 2.4, parallel grooved seal experiments by Iwatsubo [38] were modeled, reproducing the measured leakage within 2% in the 'Seal 1' configuration while using wall functions as near wall treatment, and the RNG *k*-ε turbulence model for the core flow. Figure 109 compares again leakage measurements from 'Seal 1' experiments and numerical predictions obtained with the RNG *k*-ε turbulence model for the core flow but adding the results when using the enhanced wall treatment as near wall approach.

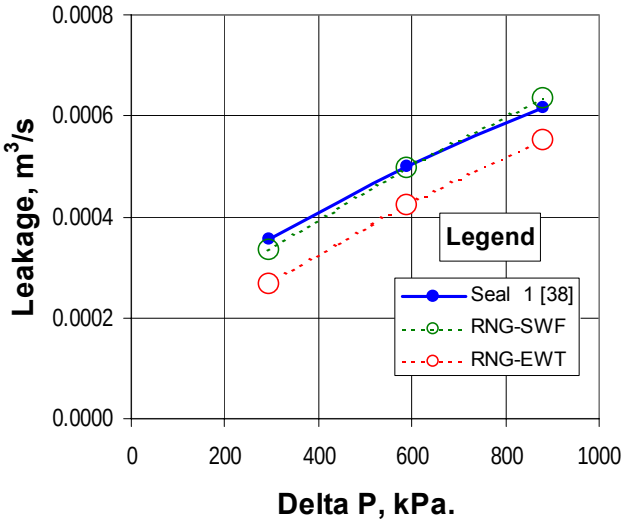


Figure 109. Leakage predictions vs. experiment, 'Seal 1' [38], effect of the near wall treatment.

Wall function predictions are within 2% of the experiments with the exception of the lowest pressure differential case, where the actual Reynolds number was $3.2 \cdot 10^4$, and $y^+$ values in the simulation vary from 9.67 to 11.1 in the top wall and from 0.48 to 11.5 in the bottom wall (including the wall defining the groove). Instead, enhanced wall treatment simulations under predict the mass flow rate ranging from 24.9% to 10.6%. Actual $y^+$ values for this modeling are well within the laminar sub-layer, varying from 0.46 to 1.36 in the top wall and from 0.01 to 3.40 in the bottom wall.

It is worth mentioning that wall functions under prediction at the lowest pressure differential is 6.3%, and that such deviation is mostly associated with actual $y^+$ values which are below the software threshold described in section 4.2.1. A better prediction can be estimated by adjusting the mass flow rate according to the linear regression described in

Figure 96. The wall-velocity-magnitude-weighted-average value for $y^+$ is 9.61, at which expected reduction in mass flow rate for turbulent channel flow is between 6.0% and 7.8%. The actual under prediction in the groove seal, 6.3%, is within this range confirming that mass flow rate predictions are reduced linearly when the calculations with wall functions are performed in grids that have cells near the wall resulting in low $y^+$ values.

To evaluate why wall functions performed apparently better than the enhanced wall treatment in replicating the leakage of the groove seal of Iwatsubo [38], velocity and turbulence profiles were compared at the Reynolds number corresponding to the medium pressure differential in the experiment, 588 kPa. At this value, wall function prediction is within 0.36% of the experimental leakage, but the pressure gradient in the enhanced wall treatment must be adjusted to an equivalent pressure differential of 735 kPa, roughly 25% larger than the experimental value, to have a comparable leakage. Figure 110(a) redraws the numerical periodic unit, and Figure 110(b) compares velocity profiles.

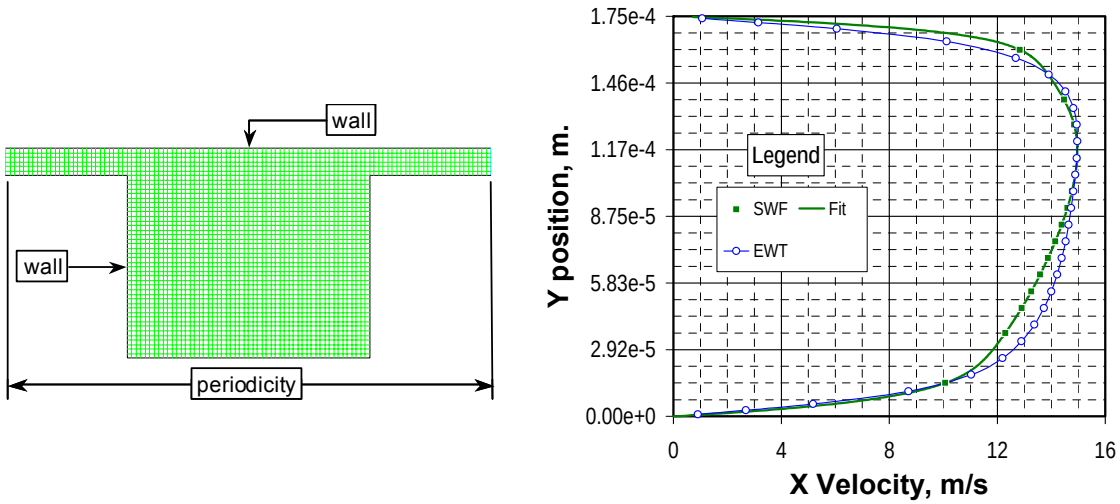


(a) Periodic unit (b) Stream wise velocity profiles in the periodic boundary

Figure 110. Numerical modeling of the grooved seal of Iwatsubo [38], Re ~ $4.4 \cdot 10^3$, $C_r$ = 175 µm (~6.9 mils).

Velocity profiles from both near-wall models are comparable within 1% in the top center portion of the clearance (a polynomial fit was added to the SWF profile to facilitate the comparison). In contrast, enhanced wall treatment (EWT) velocity values are larger than those predicted in the wall function approach (SWF) by 1.8% to 6.4% in the bottom center portion of the clearance. Mass flow rates in both approaches are comparable within 0.55%

because SWF velocity profile near the top wall is larger than the EWT profile by 9.7%.

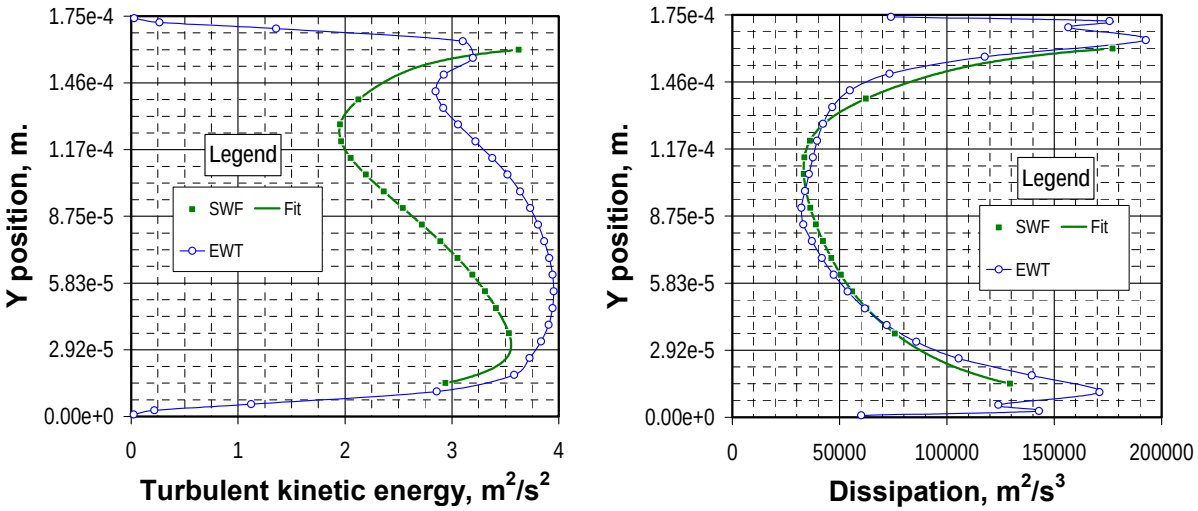


(a) Turbulent kinetic energy (b) Turbulence dissipation

Figure 111. Numerical modeling of the grooved seal of Iwatsubo [38], turbulent properties profiles.

Figure 111 compare turbulent properties profiles. EWT turbulent kinetic energy values, Figure 111(a), are larger that SWF predictions by 15.5% to as much as 64.5% in the whole annular clearance, with the exception of the value at the cell near the top wall, where the SWF prediction is 9.7% larger than the EWT value. In contrast, dissipation profiles, Figure 111(b), are comparable within 10% in most of the annular clearance, with both approaches predicting alternatively larger and lower values from the top wall to the bottom wall.

From the analysis, it is inferred that the larger turbulent kinetic energy levels predicted with the enhanced wall treatment, by an average of 41% when compared to wall function predictions, are responsible for the 25% larger pressure differential required to reproduce the experimental leakage, numerically equivalent to a 25% larger friction factor.

In summary, the wall function approach performed better than the enhanced wall treatment in replicating the groove seal experiments of Iwatsubo [38] in the ‘Seal 1’ configuration. Nevertheless, recall that when results of both seal configurations in the experiments were scrutinized to improve the predictions by refining the pressure gradient values to be used in the simulations, inconsistencies aroused regarding seal inlet and exit pressure losses and the prevailing flow regime at low Reynolds number within the annular clearance, particularly in the Seal ‘2’ configuration, as extensively discussed in section 2.4.

### *4.4.4. Isogrid pattern of Iwatsubo [36].*

In section 3.3, the isogrid seal experiments by Iwatsubo [36] were modeled, and the measured leakage was under predicted by roughly 25%, but the Reynolds-number dependence was reproduced within 8% in the test clearance of the 'Seal 2' configuration while using the enhanced wall treatment (equivalent to the two-layer zonal model) as near-wall approach, and the standard *k*-ε turbulence model for the core flow. The analysis from the test clearance was extended to the four larger clearances of Nava's experiments [30] and used the enhanced wall treatment for the simulations based on the premise [19] that the two-layer zonal model outperformed the use of wall functions when the modeling was focused on capturing the friction-factor-to-clearance proportionality behavior [42].

Figure 112 compares friction factor predictions obtained with the enhanced wall treatment (EWT), section 3.3, to the results obtained while using standard wall functions (SWF) as near-wall treatment. Both results correspond to the power law discretization scheme for all variables, the PRESTO scheme for pressure, the PISO option for the pressure-velocity linking algorithm, and the standard *k*-ε model for the core flow. Each EWT data point was individually scrutinized as multiple grids and local refinement were required to comply with $y^+$ modeling restrictions in every clearance. SWF solutions are generated in the base grid of each clearance, as described in sections 4.2.2 and 4.2.4. SWF, and also in refined grids created by doubling the number of cells on each direction (grid refinement factor of 2.0; minimum recommended, 1.3, section 4.2.2) with the exception of the near-wall cells (to maintain $y^+$ compliance), as an indication of numerical uncertainty for the base grid solutions. The analysis was focused in the Reynolds number range of interest, $10^4$ to $10^5$, and following are the most relevant observations:

- As found in EWT simulations, SWF friction factor predictions are inversely proportional to the clearance for all clearance values simulated.
- At $Re \sim 8 \cdot 10^4$, SWF predicted value at the largest clearance of 1270 μm is smaller than the one predicted at the 175 μm test clearance by roughly 32%. This difference is significant and larger than the numerical uncertainty. A trend that is consistent in the whole Reynolds number range.
- As found in EWT simulations, SWF friction factor dependence on Reynolds number

increases with clearance, although such dependence becomes asymptotic only at the test clearance,175 μm, for Re > $10^5$.

- Numerical uncertainties of the SWF calculations are in the order of 12% for the test clearance, 175 μm, and in the order of 7% to 11% in the rest of clearances, with the lower values at the largest clearance. Indeed, numerical uncertainty levels are comparable to the predicted change in friction factor as the clearance is increased for each base grid calculation.
- SWF trend calculations result in friction factor predictions slightly above EWT simulations. In truth, SWF trends and EWT predictions are comparable within 1.4% and 7.5% in all clearances.

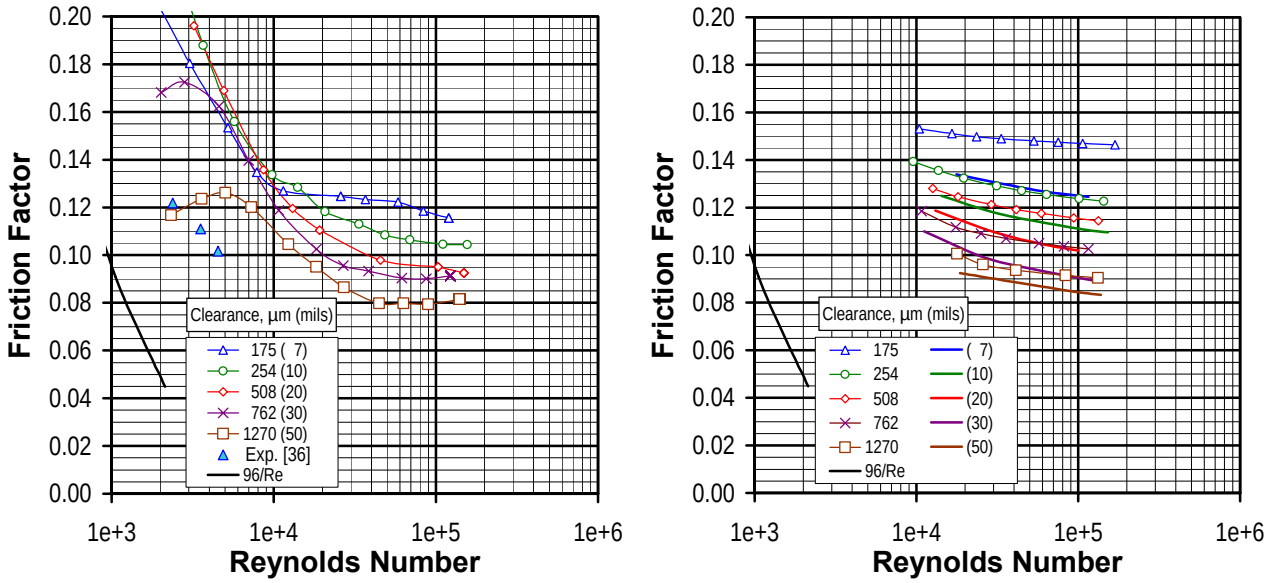


(a) EWT modeling (b) SWF modeling

Figure 112. Friction factor predictions, 'Seal 2' isogrid pattern [36], effect of the near wall treatment.

Figure 113 presents the friction-factor-to-clearance dependence predicted with both near-wall treatments at two Reynolds numbers. SWF and EWT predictions have a similar trend in the friction factor as the clearance is increased, and as already mentioned, they are comparable within 1.4% to 6.2% at Re = $2 \cdot 10^4$, and within 1.6% to 7.5% at Re = $8 \cdot 10^4$.

Regarding compliance with modeling restrictions, table VII summarizes $y^+$ values of both EWT and SWF simulations at every clearance in the comparable flow range. In this

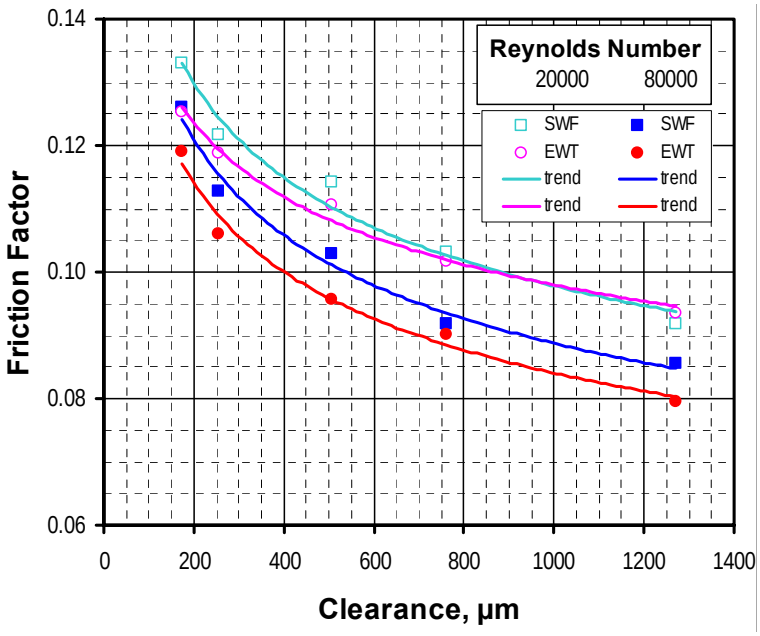


Figure 113. Friction-factor-to-clearance behavior, SWF and EWT predictions, 'Seal 2' isogrid pattern [36].

table, the most significant figure for the local wall distance $y^+$ is the mean value. Mean values shown are obtained by cell-volume weighted averaging, although several others alternatives were explored with comparable results. With very few exceptions, EWT values are within the viscous sub-layer ($y^+ < 5$), and SWF values lay outside the buffer layer ($y^+ > 11.225$) avoiding the 'mass flow rate reduction effect' described in section 4.3.1.

Table VII. Typical y+ values, numerical analysis of the isogrid pattern of Iwatsubo[36]

| MODEL | EWT | | | | SWF | | | |
|---|---|---|---|---|---|---|---|---|
| Clearance, µm | 175 | | | | | | | |
| Pressure drop, Pa/m | $Re \cdot 10^4$ | $y^+$ | | | $Re \cdot 10^4$ | $y^+$ | | |
| | | min | mean | max | | min | mean | max |
| $1 \cdot 10^9$ | 2.6 | 0.00 | 1.33 | 2.60 | 2.4 | 0.36 | 15.04 | 30.9 |
| $1 \cdot 10^{10}$ | 8.4 | 0.00 | 3.50 | 6.54 | 7.5 | 1.04 | 43.38 | 90.6 |
| | 254 | | | | | | | |
| $2 \cdot 10^8$ | 2.1 | 0.09 | 3.46 | 7.88 | 2.0 | 1.55 | 24.59 | 45.4 |
| $5 \cdot 10^8$ | 3.4 | 0.11 | 4.63 | 6.99 | 3.3 | 2.40 | 38.49 | 77.2 |
| | 508 | | | | | | | |
| $1 \cdot 10^8$ | 4.6 | 0.02 | 2.70 | 7.53 | 4.1 | 1.33 | 23.96 | 42.9 |
| $5 \cdot 10^8$ | 10.3 | 0.11 | 6.96 | 15.45 | 10.0 | 2.68 | 52.33 | 104 |
| | 762 | | | | | | | |
| $1 \cdot 10^7$ | 2.7 | 0.03 | 4.93 | 10.74 | 2.6 | 0.89 | 14.60 | 27.6 |
| $5 \cdot 10^7$ | 6.2 | 0.05 | 3.31 | 6.67 | 6.1 | 1.30 | 30.76 | 59.5 |
| | 1270 | | | | | | | |
| $1 \cdot 10^6$ | 1.8 | 0.06 | 3.02 | 5.57 | 1.8 | 0.09 | 6.66 | 10.5 |
| $5 \cdot 10^7$ | 14.0 | 0.23 | 3.16 | 5.69 | 13.8 | 0.76 | 39.94 | 70.0 |

The large difference among maximum and minimum $y^+$ values predicted in every case common to both modeling approaches is an indication of how much variation in the mean flow velocity of every first cell (near the wall) is calculated. Consistently, these extreme values were located within the roughness pattern, where there are zones of stagnant flow with separation and localized high velocity in the roughness pattern edges. Figure 114 shows typical $y^+$ values distribution in the bottom wall of the isogrid pattern for both modeling approaches. In the Figure, extreme values are clearly seen in the SWF modeling because base grids have first cells separated uniformly from the walls, while EWT grids have variable separation in those cells to comply with modeling restrictions. Sharp discontinuities in the EWT color contour are associated with the method used to refine the grid near the lateral walls of the isogrid pattern. While a boundary layer approach was used near all horizontal walls to create cells that would result in $y^+$ values close to 1.0, local refinement was used in the lateral walls based on actual $y^+$ values extracted from each run, given the preliminary large difference among maximum and minimum $y^+$ values observed in the base grids on such locations.

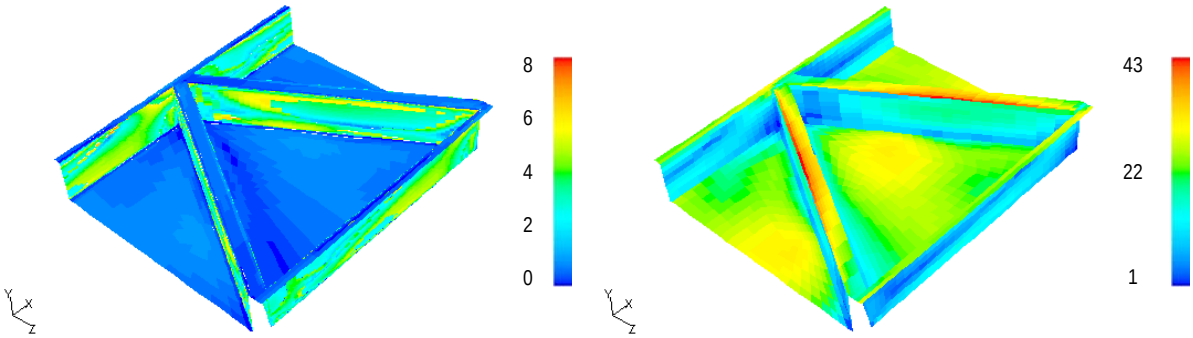


(a) EWT modeling (b) SWF modeling

Figure 114. Typical $y^+$ values distribution, isogrid pattern bottom wall, clearance = 508 μm, PG = $1 \cdot 10^8$ Pa/m.

As implemented, the EWT approach is equivalent to the two-layer zonal model [25] provided there are several cells within the viscosity affected near-wall region ($Re_y < 200$). The boundary layer refinement approach described above was done following this requirement leading to the creation of at least two additional grids per clearance. Subsequently, each grid was locally refined several times for every case ran, resulting in many grids as cases generated. The use of successive local refinements resulted in final

grids that were comparatively large in terms of the actual numbers of cells. In addition, several tests performed indicate that the actual number of successive local refinements is limited; several solutions did not converge after a particular grid was locally refined three to five times. In such testing, mean $y^+$ values were tracked including their histogram distribution to confirm the fact that EWT predictions appear to be consistent provided actual $y^+$ values are below 10.0 [19,42] as found when using the two-layer zonal model.

Figures 115 and 116 compare flow field profiles of both EWT and SWF predictions in the periodic boundary of the isogrid pattern at the test clearance, 175 μm (~6.9 mils). Results correspond to a pressure gradient in which both models agree within 2% in mass flow rate and 4% in friction factor predictions. Following are the more relevant observations:

- Stream wise component or x-velocity:
  - Deviations are more noticeable within the annular clearance, where EWT profiles are larger than SWF predictions by 12.2% to 20.2% in the gap region (Z1 and Z5 locations). In contrast, EWT values are consistently smaller in the center of the pattern (Z2, Z3, Y1, Y2, and Y3 locations) by 5.6% to 5.8%.
  - Inside the pattern, both profiles are comparable within 5% (Z2, Z3, and Y4 locations) in the pattern center, but EWT values are consistently larger up to 20.2% near the lateral walls (Z4 and Y5 locations).
  - A localized sudden variation is predicted atop the vicinity of the pattern corners (Y3 location within a circle) by the EWT model. This variation that is barely captured by the SWF model.
- Vertical component or y-velocity:
  - Y-velocity profiles have a similar trend but deviations are noticeable inside the pattern, where SWF profiles are larger than EWT predictions by 7% to 29% (Z2, Z3, and Z4 locations). Recall than percentages are affected by the local value.
  - As with the x-velocity profiles, a localized sudden variation is predicted atop the vicinity of the pattern corners (Y2 and Y3 locations within a circle) by the EWT model. This variation that is mildly captured by the SWF model.

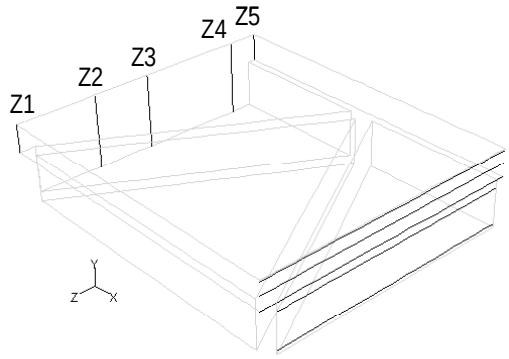


Z1 = 1.73 mm  Z4 = 0.19 mm
Z2 = 1.21 mm  Z5 = 0.00 mm
Z3 = 0.84 mm

(a) Periodic unit, $C_r$ = 175 µm (~6.9 mils)

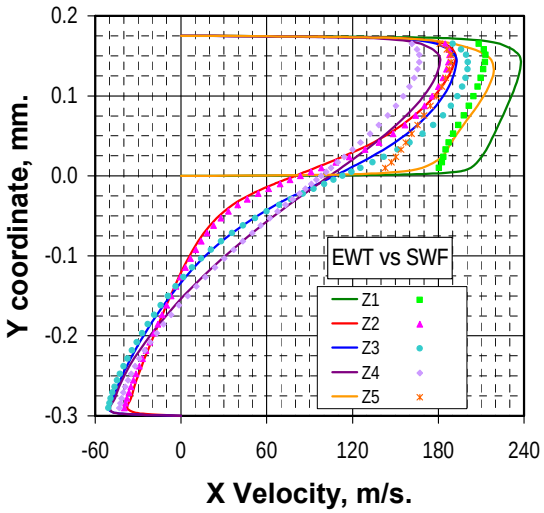


(b) Stream wise velocities

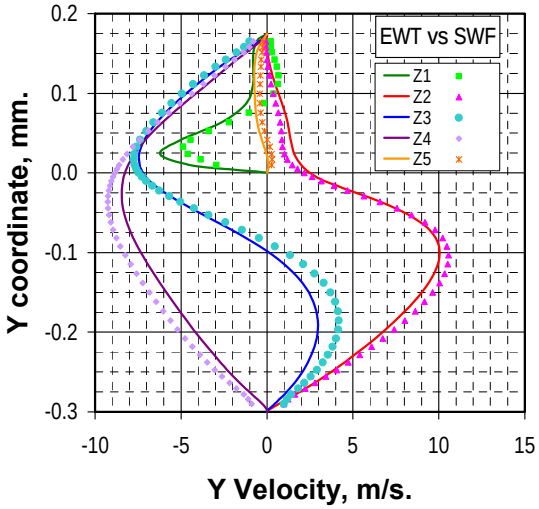


(c) Vertical velocities

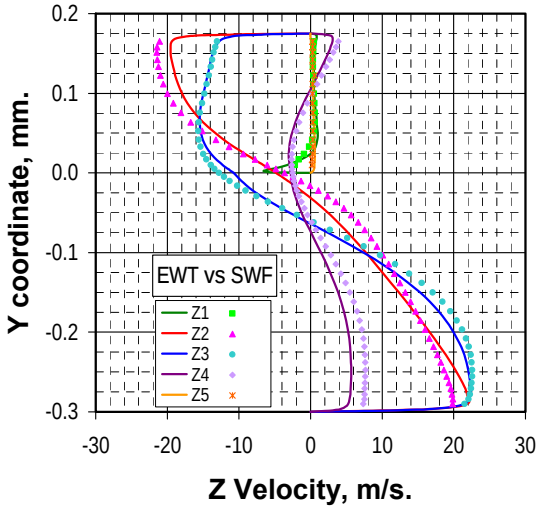


(d) Span wise velocities

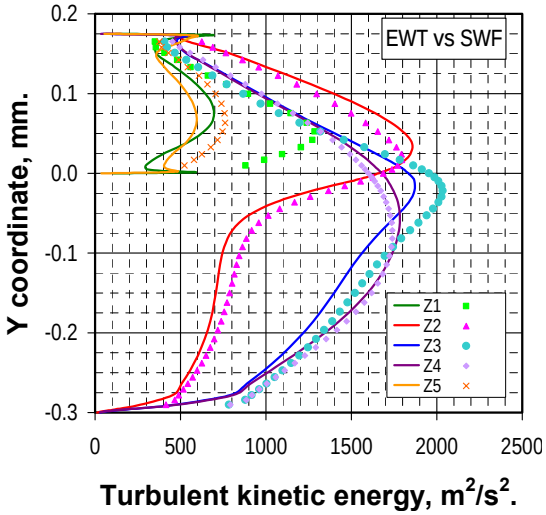


(e) Turbulent kinetic energy

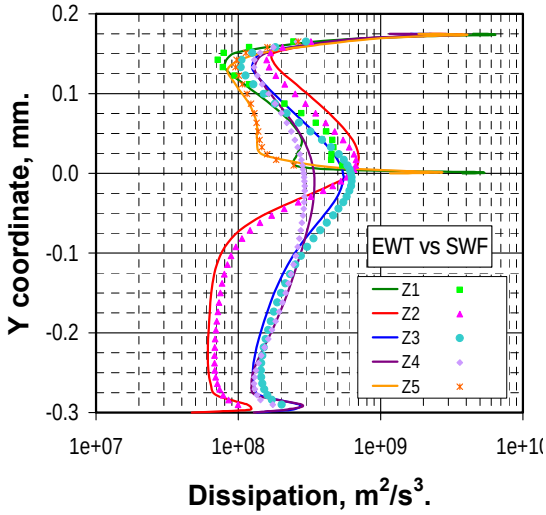


(f) Dissipation

Figure 115. Vertical line profiles, 'Seal 2' isogrid pattern [36], near-wall treatment effect, PG = $5 \cdot 10^9$ Pa/m.

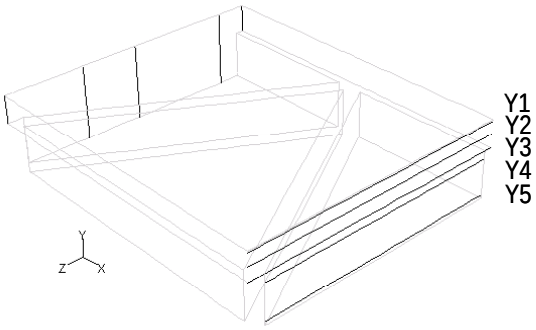


Y1 = 165 µm  Y4 = -52.7 µm (18% depth)
Y2 = 87.5 µm (half the clearance)
Y3 = 10 µm  Y5 = -278 µm (93% depth)

(a) Periodic unit, $C_r$ = 175 µm (~6.9 mils)

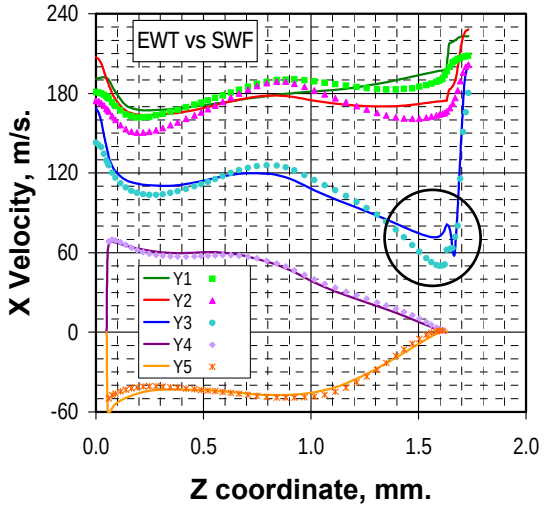


(b) Stream wise velocities

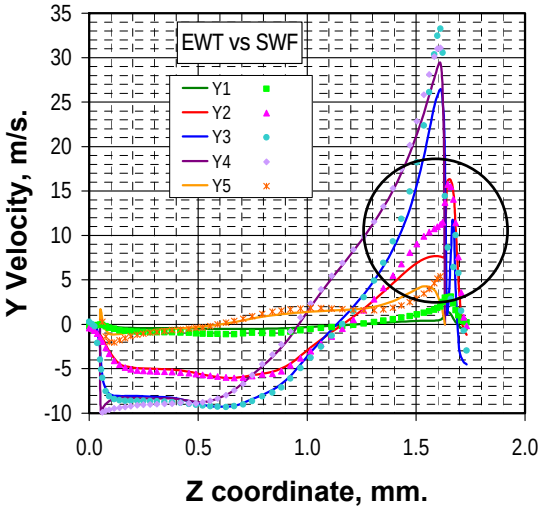


(c) Vertical velocities

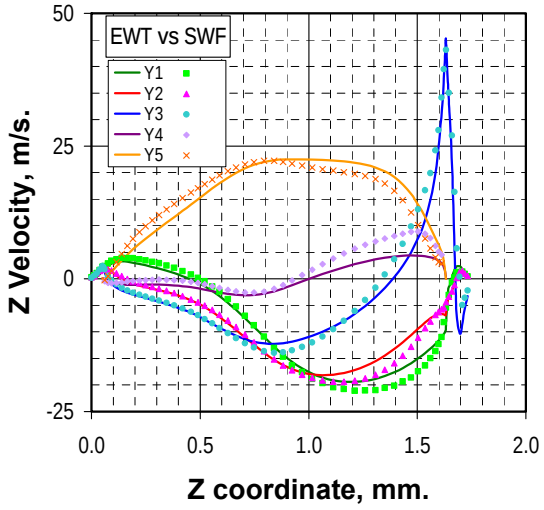


(d) Span wise velocities

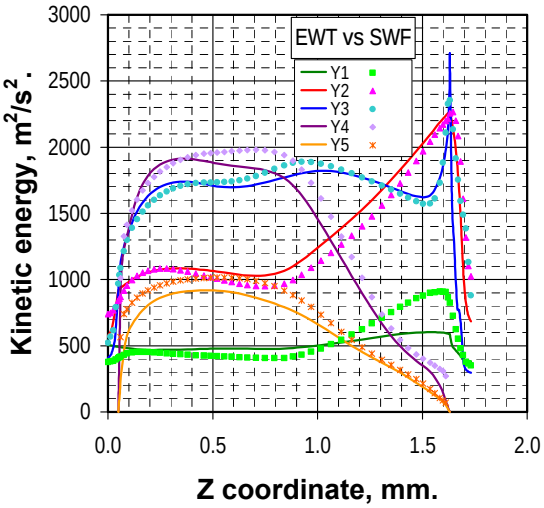


(e) Turbulent kinetic energy

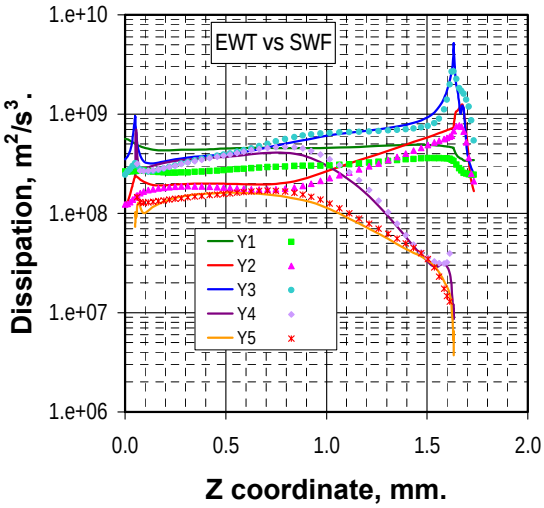


(f) Dissipation

Figure 116. Horizontal line profiles, 'Seal 2' isogrid pattern [36], near-wall treatment effect, PG = $5 \cdot 10^9$ Pa/m.

- Span wise component or z-velocity:
  - EWT and SWF profiles are comparable within 4% in the mid-clearance and the pattern center (Y2 and Z3 locations).
  - Deviations are more noticeable in the vicinities of the corners and lateral walls of the pattern, in both within the annular clearance and inside the pattern, where SWF profiles are larger than SWF predictions by 10% to 25% and as large as 50% (Z2, Z4, and Y4 locations).
  - A localized sudden variation is predicted atop the vicinity of the pattern corners (Y3 location) by the EWT model which is barely captured by the SWF model.
- Turbulent kinetic energy:
  - SWF profiles are consistently larger than EWT values in most regions, particularly in the clearance gap (Z1 and Z5 locations) where deviations range from 16% to 64%. Inside the pattern, SWF profiles are also larger by 9% to 12% and more significantly near the bottom wall (Y5 location) where deviations exceed 28%.
  - Both models agree in predicting that larger kinetic energy values occur in the shear layer (vicinity of the interface of the clearance and the roughness pattern) with peaks atop the pattern corners (Z3 and Y3 locations).
- Turbulence Dissipation:
  - EWT profiles are consistently larger than SWF values in the annular clearance, particularly in the upper mid-clearance (Z2, Z3, Z4, Y1, and Y2 locations) where deviations range from 0.8% to 43%. In contrast, SWF profiles are larger by an average of 10% to 16% inside the pattern (Z2, Z3, Y4, and Y5 locations).
  - Both models agree in predicting that larger dissipation occurs near the top and bottom walls (defining the annular clearance) and in the shear layer (vicinity of the interface of the clearance and the roughness pattern) with peaks atop the pattern corners (Z3 and Y3 locations).

Similarly, Figures 117 and 118 compare flow field profiles of both predictions at a clearance of 762 μm (30 mils). Although final predictions agree within 1.4% in mass flow rate and 2.8% in friction factor, SWF profiles correspond to the base grid, so any observed differences are uniquely associated to the near-wall treatment (recalling that EWT results

correspond to the base grid with local refinement). Following are the more relevant observations:

- Stream wise component or x-velocity:
  - All EWT profiles are consistently larger than SWF predictions by 6.6% to 12.1% in the annular clearance. Indeed, SWF profiles are similar within 3% when scaled up to compensate the Reynolds number deficit (SWF mass flow rate is 7.1% lower than the EWT prediction).
  - Inside the pattern, EWT values are also consistently larger than SWF predictions, particularly near the pattern walls (Y4 and Y5 locations) where deviations progressively increase from 10% to 48%.
- Vertical component or y-velocity:
  - Y-velocity profiles have a similar trend but deviations are noticeable inside the pattern, where SWF profiles are larger than EWT predictions by 8%, 13%, up to 23% (Z4, Y4, and Y5 locations). Recall than percentages are affected by the local magnitude of the velocity which is comparatively small.
- Span wise component or z-velocity:
  - Z-velocity profiles have also similar trends with noticeable deviations inside the pattern. Some values in the SWF profiles are larger than EWT predictions by 10%, 20%, up to 38% (Y3 and Y5 locations) but EWT values can be the larger values in other locations from 11% to 90% (Z4 and Y4 locations). Recall than percentages are affected by the local magnitude of the velocity which is comparatively small.
- Turbulent kinetic energy:
  - SWF profiles are consistently larger than EWT values in most regions, particularly in the clearance gap (Z1 and Z5 locations) where deviations range from 3.3% to 14%. Inside the pattern, SWF profiles are also larger and more significantly near the bottom wall (Y5 location) where deviations exceed ranges from 15% to 64%.
  - Both models agree in predicting larger kinetic energy values occur in the shear layer with peaks atop the pattern corners (Z3, Z4, Y3 and Y4 locations).

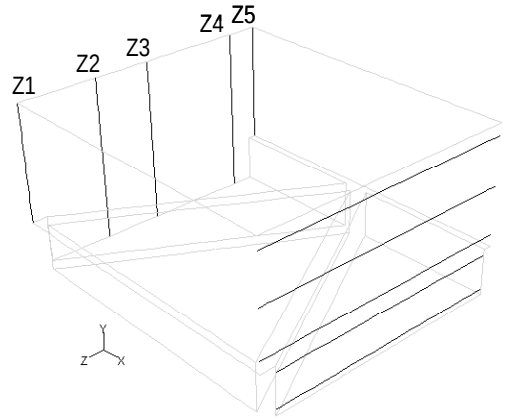


Z1 = 1.73 mm  Z4 = 0.19 mm
Z2 = 1.21 mm  Z5 = 0.00 mm
Z3 = 0.84 mm

(a) Periodic unit, $C_r$ = 762 µm ( 30 mils)

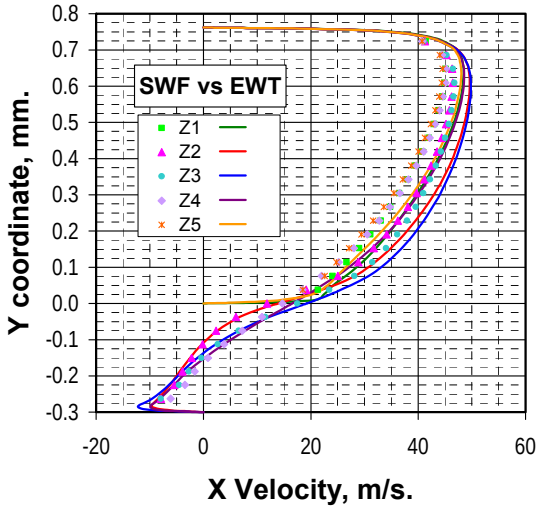


(b) Stream wise velocities

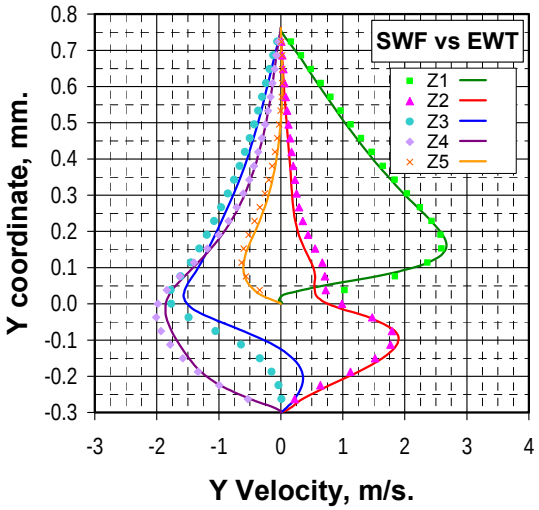


(c) Vertical velocities

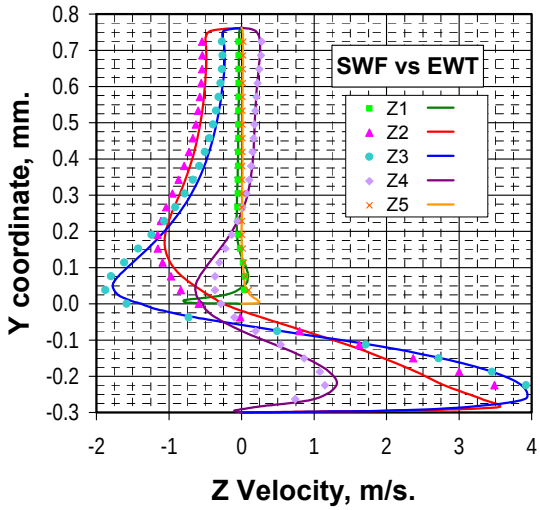


(d) Span wise velocities

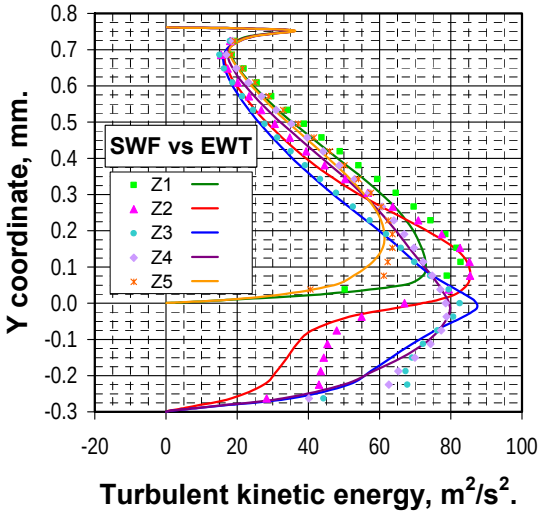


(e) Turbulent kinetic energy

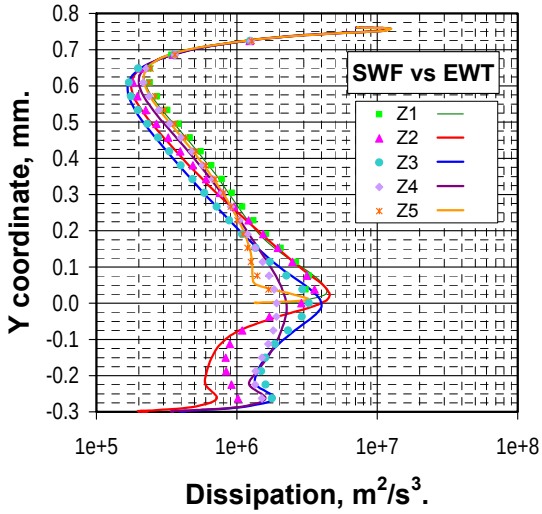


(f) Dissipation

Figure 117. Vertical line profiles, isogrid pattern, near-wall treatment effect, PG = $5 \cdot 10^7$ Pa/m.

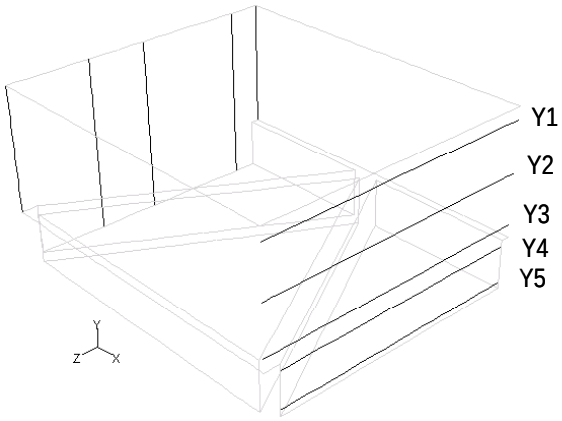


Y1 = 686 µm  Y4 = -38 µm (13% depth)
Y2 = 381 µm (half the clearance)
Y3 = 76 µm  Y5 = -263 µm (88% depth)

(a) Periodic unit, $C_r$ = 762 µm ( 30 mils)

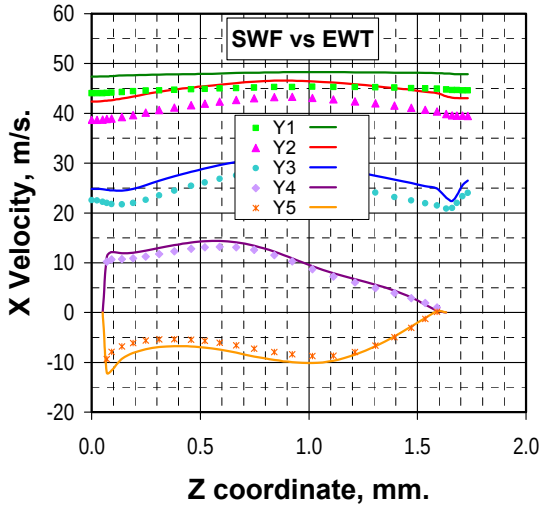


(b) Stream wise velocities

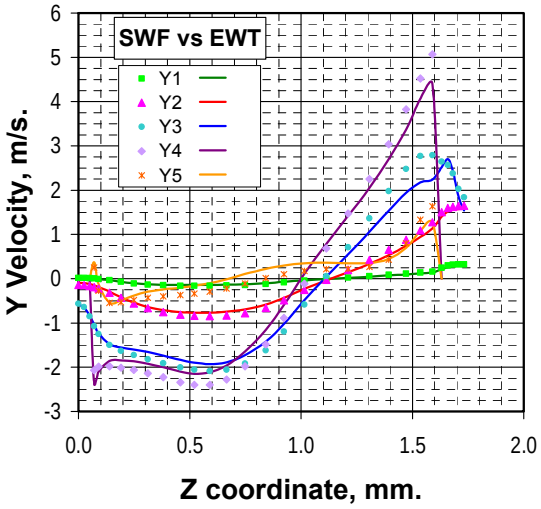


(c) Vertical velocities

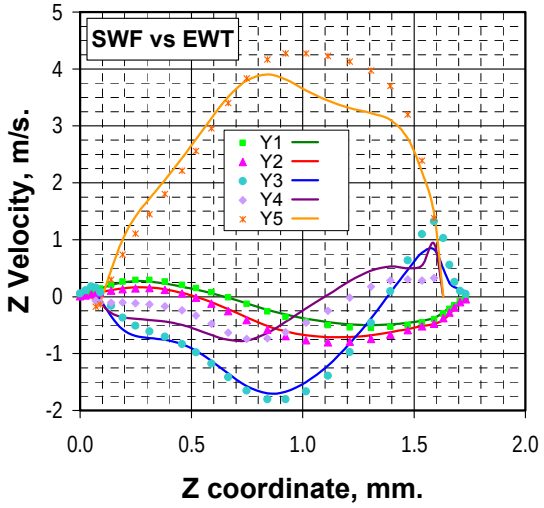


(d) Span wise velocities

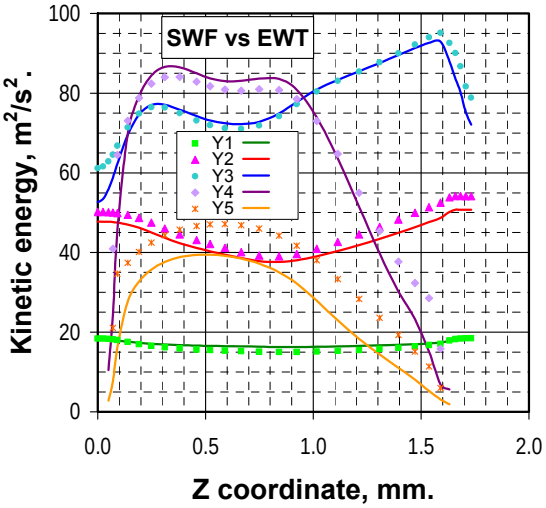


(e) Turbulent kinetic energy

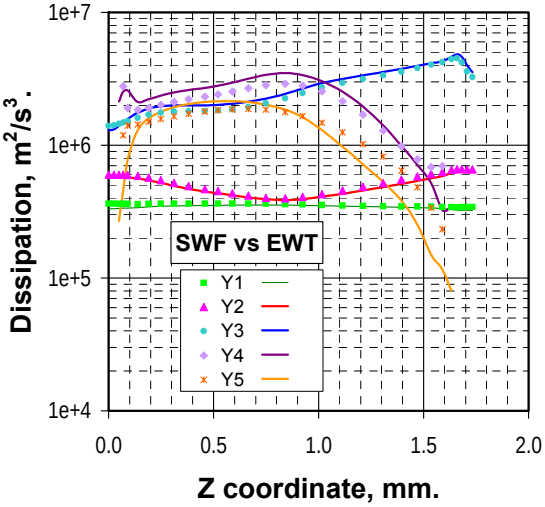


(f) Dissipation

Figure 118. Horizontal line profiles, isogrid pattern, near-wall treatment effect, PG = $5 \cdot 10^7$ Pa/m.

- Turbulence Dissipation:
  - EWT and SWF profiles are comparable within 5% in the annular clearance, while EWT values are larger in the shear layer by 10% to 20% (Y3 and Y4 locations). In contrast, SWF profiles are larger up to 50% inside the pattern (Z2, Y4, and Y5 locations), particularly near the lateral walls.
  - Both models agree in predicting that larger dissipation occurs near the top wall and in the shear layer, with peaks atop the pattern corners (Z2 and Y3 locations).

In summary:

- SWF friction factor predictions are slightly larger than those obtained with the EWT modeling. Depending on the clearance, differences vary from to 1.1% to 7.5%.
- Both models predict a similar friction-factor-to-clearance-behavior. For a Reynolds number flow range of $10^4$-$10^5$, simulations indicate that the traditional behavior is expected in the isogrid pattern of Iwatsubo [36], with the friction factor decreasing as the clearance is increased.
- Local refinement used for EWT compliance resulted in comparatively large grids, with a large concentration of cells inside the pattern edges where achieving low $y^+$ values is extremely difficult. In addition, successive local refinements are limited, introduces the use of interpolation within refined cells, see section 4.1.4, and each grid is suitable for only a single Reynolds number case.
- Most differences in flow field predictions among the two near-wall models are observed inside the roughness pattern, particularly in the turbulent kinetic energy and dissipation levels, which SWF estimates are significantly larger that EWT values. In addition, EWT velocities are also consistently larger, particularly near the pattern walls.

### *4.4.5. Honeycomb pattern of Kaneko [37].*

In section 3.4, the honeycomb experiment by Kaneko[37] was modeled, over predicting the measured leakage by only 14% when using the enhanced wall treatment as near-wall approach and the standard *k*-ε turbulence model for the core flow. As in the isogrid pattern, the analysis in the honeycomb pattern was extended to the four larger clearances of Nava's experiments [30] and used this wall treatment given its apparent modeling advantage[42].

Figure 119 compares EWT and SWF friction factor predictions. The numerical scheme is similar to the one described in section 4.3.4. Likewise, multiple grids and local refinement were required to comply with $y^+$ modeling restrictions in every clearance for the EWT simulations. On the other hand, SWF solutions are generated on the base grid of each clearance, and the trend of calculations obtained while doubling the number of cells on each direction (with the exception of the near-wall cells in selected clearances to maintain $y^+$ compliance) are also included, as an indication of the numerical uncertainty. Following are the most relevant observations:

- As found in EWT simulations, SWF friction factor predictions are directly proportional to the clearance up to the 508 μm value. And the trend is reversed for larger clearances, friction factor predictions are directly proportional to the clearance from the former value up to the 1270 μm clearance.
- At $Re \sim 8 \cdot 10^4$, SWF predicted value at the clearance of 508 μm is larger than the one predicted at the 175 μm test clearance by roughly 20%. This difference is significant and larger than the numerical uncertainty. A trend that is consistent in the whole Reynolds number range.
- In contrast to EWT predictions where each clearance has a particular Reynolds number dependence, SWF friction factor predictions indicate that such dependence is comparable in all clearances. Nonetheless, the Reynolds number dependence is still present for $Re > 10^5$, in agreement with EWT predictions.
- Numerical uncertainties of the SWF calculations are in the order of 2.7% to 4.8% for the original clearance, 175 μm; exceptionally low from 0.2 to 0.8% in the 508 μm clearance; and in the order of 1.5% to 8.5% in the rest of clearances, with the larger values at the largest clearance value. Indeed, numerical uncertainty levels are lower

than predicted change in friction factor as the clearance is varied for each base grid.

- SWF trend calculations result in friction factor predictions larger than EWT simulation values by 7.8% to 15.4%, depending on the actual clearance value.
- Both SWF trends and EWT simulations agree in predicting that the clearance value of 508 µm is likely a plateau for the honeycomb pattern of Kaneko[37].

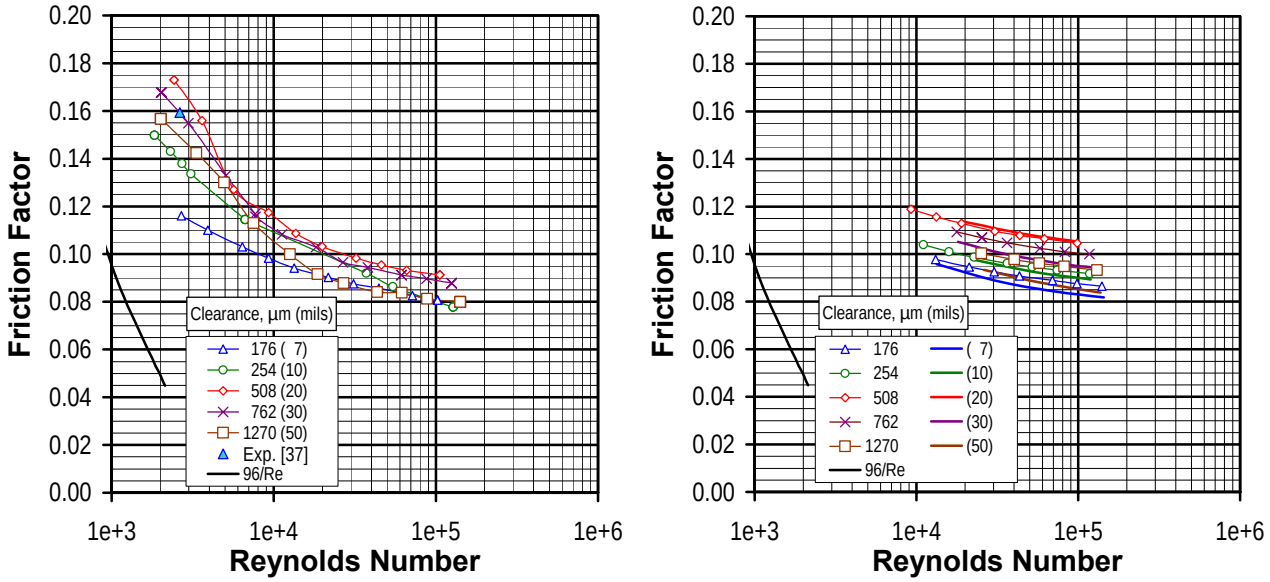


(a) EWT modeling (b) SWF modeling

Figure 119. Friction factor predictions, honeycomb pattern [37], effect of the near wall treatment.

Figure 120 presents the friction-factor-to-clearance dependence predicted with both near wall treatments at two Reynolds numbers. SWF and EWT predictions have a comparable trend in the friction factor as the clearance is increased, pointing to a plateau at around the 508 µm clearance value, and as already mentioned, SWF trends are above EWT predictions by 0.4% to 12.4% at $Re = 2 \cdot 10^4$, and by 7.8% to 15.4% at $Re = 8 \cdot 10^4$.

Regarding compliance with modeling restrictions, table VIII summarizes $y^+$ values of both EWT and SWF simulations at every clearance in the comparable flow range. As in the previous section, the most significant figure is the mean value for the local wall distance $y^+$, obtained by cell-volume weighted averaging. With the exception of the 175 and 254 µm clearance values, all EWT values are well inside the viscous sub-layer ($y^+ < 2$). Equally important, all SWF values lay outside the buffer layer ($y^+ > 11.225$).

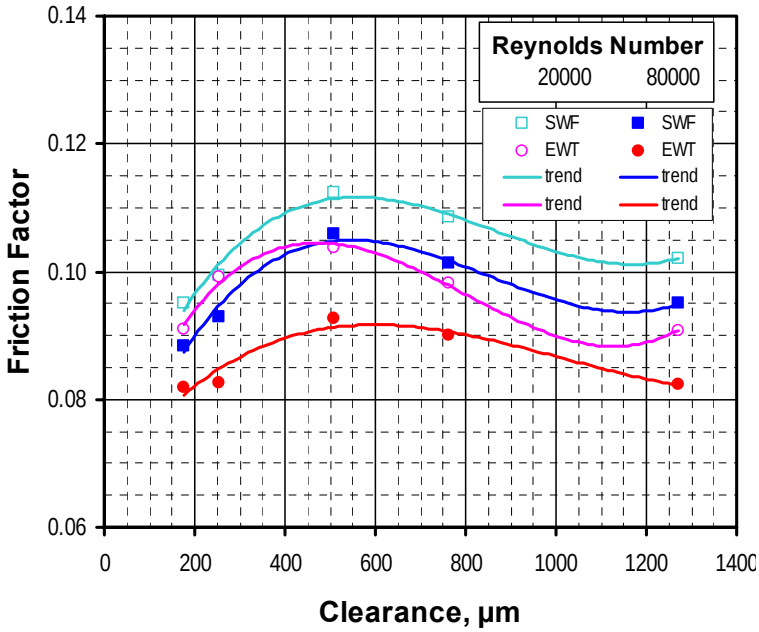


Figure 120. Friction-factor-to-clearance behavior, SWF and EWT predictions, honeycomb pattern [37].

As found in the modeling of the isogrid pattern, extreme $y^+$ values were consistently located within the honeycomb roughness pattern, lowest values in zones of stagnant flow with separation at the bottom wall and corners, and largest values in zones of localized high velocity in the roughness pattern edges. Figure 121 shows typical $y^+$ values distribution in the bottom wall of the honeycomb pattern for both modeling approaches.

Table VIII. Typical y+ values, numerical analysis of the honeycomb pattern of Kaneko[37].

| MODEL | EWT | | | | SWF | | | |
|---|---|---|---|---|---|---|---|---|
| Clearance, µm | 175 | | | | | | | |
| Pressure drop, Pa/m | $Re\cdot10^4$ | $y^+$ | | | $Re\cdot10^4$ | $y^+$ | | |
| | | min | mean | max | | min | mean | max |
| $2\cdot10^8$ | 1.3 | 0.21 | 3.38 | 14.88 | 1.3 | 1.96 | 21.9 | 126 |
| $5\cdot10^9$ | 7.2 | 0.21 | 3.87 | 15.27 | 7.1 | 11.5 | 86.5 | 602 |
| | 254 | | | | | | | |
| $5\cdot10^8$ | 3.7 | 0.20 | 3.40 | 7.18 | 3.6 | 7.63 | 70.6 | 335 |
| $5\cdot10^9$ | 12.8 | 0.20 | 9.39 | 19.69 | 11.9 | 2.30 | 97.2 | 697 |
| | 508 | | | | | | | |
| $1\cdot10^7$ | 1.4 | 0.11 | 0.51 | 3.17 | 1.3 | 2.21 | 19.6 | 73.7 |
| $5\cdot10^8$ | 10.6 | 0.03 | 1.71 | 5.22 | 9.8 | 10.1 | 122 | 475 |
| | 762 | | | | | | | |
| $5\cdot10^6$ | 1.8 | 0.00 | 0.39 | 1.44 | 1.8 | 1.55 | 13.9 | 64.4 |
| $2\cdot10^8$ | 12.5 | 0.02 | 1.37 | 4.10 | 12.1 | 7.44 | 79.5 | 366 |
| | 1270 | | | | | | | |
| $2\cdot10^6$ | 2.7 | 0.00 | 0.28 | 0.88 | 2.6 | 1.41 | 12.3 | 52.8 |
| $5\cdot10^7$ | 14.1 | 0.02 | 0.93 | 2.90 | 13.8 | 5.62 | 55.9 | 244 |

Extreme $y^+$ values are clearly seen in the SWF modeling because base grids have first cells separated uniformly from the walls, while EWT grids have variable separation in those cells to comply with modeling restrictions. In contrast to the isogrid modeling, there are no sharp discontinuities in the EWT color contour within a particular wall surface because a boundary layer approach was used to create near-wall cells that would result in $y^+$ values close to 1.0 in all wall surfaces.

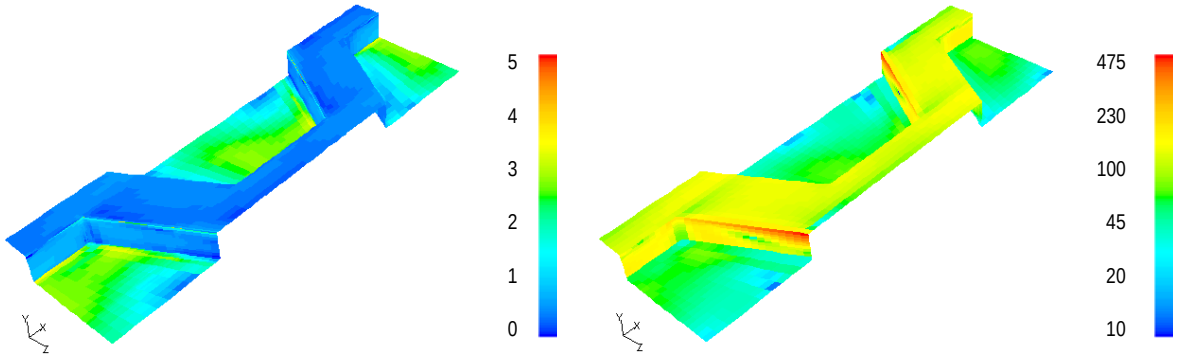


(a) EWT modeling (b) SWF modeling (log scale)

Figure 121. Typical $y^+$ values distribution, honeycomb bottom wall, clearance = 508 μm, PG = $5 \cdot 10^8$ Pa/m.

The boundary layer refinement approach described above was done following the requirement of having several cells within the viscosity affected near-wall region ($Re_y$ < 200) leading to the creation of at least three additional grids per clearance. Preliminary solutions in the base grids of each clearance were scrutinized in terms of actual $y^+$ values to calculate the required cell size near the wall on each surface to generate a new grid in compliance with modeling restrictions in a given Reynolds number flow range. Then, preliminary solutions of the base grids were used as initial solutions for each newly created grid and actual $y^+$ values and their histogram distribution were tracked while achieving iterative convergence to verify that modeling restrictions were fulfilled. Finally, each fully converged solution was again scrutinized in terms of $y^+$ values but also for grid convergence, and the whole process was repeated as required for modeling compliance and grid convergence. There are several advantages of this approach when compared to the local refinement used in the previous section. First, a final grid created with the boundary layer approach with full modeling compliance in all surfaces is good for several Reynolds number cases while relying in local refinement resulted in as many grids as cases generated.

Secondly, the final grid thus created has a specific cell size on each wall surface to match a particular $y^+$ target, while local refinement relies on halving the near-wall cells with $y^+$ values above the specified target without specific control on the wall distance and resulting in eight new cells per each original cell being refined (the halving is performed on each coordinate direction). Thirdly, although comparable in sizes (actual number of cells), final grids created with full boundary layers are conformal while local refinement results in grids that require interpolation at the boundaries of all refined cells. On the other hand, full boundary layer conformal grids contain highly distorted cells in regions that refinement is not needed, as discussed in section 4.2.4, requiring more iterations to meet the convergence criteria. Finally, tracking $y^+$ values and their histogram distribution in this pattern indicates also that EWT predictions appear to be consistent provided actual $y^+$ values are below 10.0.

Figures 122 and 123 compare flow field profiles of both EWT and SWF predictions in the periodic boundary of the honeycomb pattern at the test clearance, 176 μm (~6.9 mils). Results correspond to a pressure gradient in which both models agree within 0.8% in mass flow rate and 1.7% in friction factor predictions. Following are the more relevant observations:

- Stream wise component or x-velocity:
  - EWT and SWF profiles are comparable within ±5% in most regions of the annular clearance. Deviations are more noticeable in the gap region (Z1, Y1, Y2, and Y3 locations), where EWT profiles are larger than SWF predictions by 11.8% to 27.7%.
  - Inside the pattern, both profiles are also comparable within ±4% (Z3 and Y4 locations), but EWT values are consistently larger by 5.8 to 23.2% in the pattern center and up to 31.3% near the bottom wall (Z1, Z2, and Y5 locations).
- Vertical component or y-velocity:
  - Y-velocity profiles have also a similar trend in most regions but deviations are noticeable inside the pattern, particular near the lateral and bottom walls, where EWT profiles are larger than SWF predictions up to 64% (Z3 and Y5 locations). Recall than percentages are affected by the local magnitude of the velocity which is comparatively small.
- Span wise component or z-velocity:

- Z-velocity profiles have also similar trends. EWT and SWF profiles are comparable within ±5% in most of the annular clearance, although SWF profiles are consistently larger up to 6% in the mid-clearance of the pattern center (Z2 location), but EWT values are larger up to 17.5% in the shear layer near the lateral wall (Z3 location).
- Inside the pattern, deviations are more noticeable where EWT profiles are consistently larger than SWF predictions by 14%, 17%, 18%, up to 21% (Z1, Z2, Z3, and Y5 locations) near the bottom wall.

- Turbulent kinetic energy:
  - EWT and SWF profiles are comparable but there are significant deviations in several locations within the domain. Within the annular clearance, EWT and SWF profiles alternate large values, with SWF profiles being larger in the annular gap region atop the lateral wall up to 38.1% (Z3 and Z4 locations), while EWT values are larger by 1.8% and up to 40% in the pattern center and in the annular gap region close to the symmetry boundary (Z1, Z2, and Z5 locations). SWF profile near the top wall (Y1 location) has also a distinctive behavior, while values are lower than EWT prediction up to 31.4% in the pattern center, the maximum value is larger than the EWT counterpart by 38.1% atop the vicinity of the lateral wall.
  - Inside the pattern, SWF values are consistently larger than EWT predictions in most regions including the pattern center up to 29% and 36% (Z1 and Z3 locations), and particularly near lateral and bottom walls (Y4 and Y5 locations) up to 71.5% and 134%, respectively.
  - Both models agree in predicting larger kinetic energy values occur in the shear layer with peaks atop the lateral walls (Z3, Y2 and Y3 locations).
- Turbulence Dissipation:
  - Both predictions are comparable, but EWT profiles are consistently larger by an average of 5.4% to 35.5% in the annular clearance (Z1, Z2, Z3, Z4, Z5, Y1, and Y2 locations). In contrast, both profiles are comparable within ±4% in most of the shear layer (Y3 and Y4 locations), while SWF values are larger inside the pattern, particularly in the pattern center up to 34.6% (Z1 location) and near the lateral walls up to 45.3% and 80.5% (Z3, Y4, and Y5 locations).

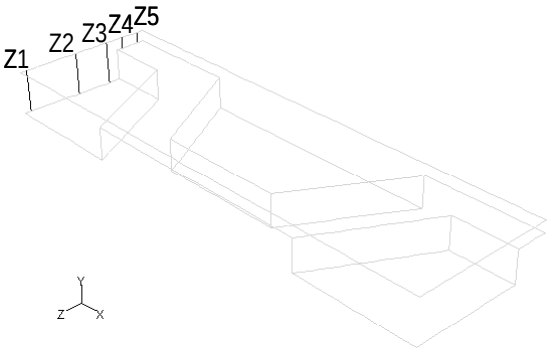


Z1 = 2.13 mm  Z4 = 0.40 mm
Z2 = 1.26 mm  Z5 = 0.10 mm
Z3 = 0.69 mm

(a) Periodic unit, $C_r$ = 176 µm (~6.9 mils)

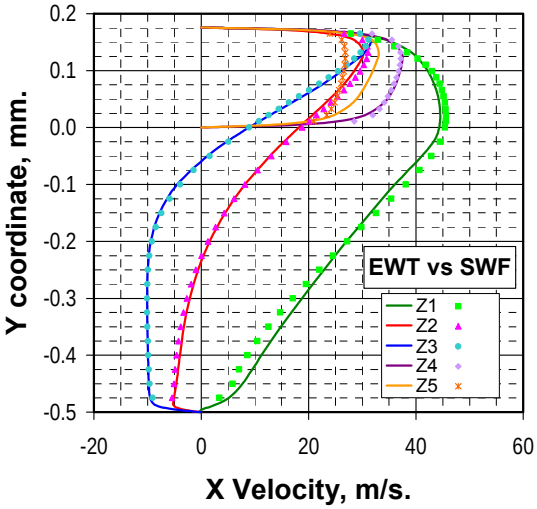


(b) Stream wise velocities

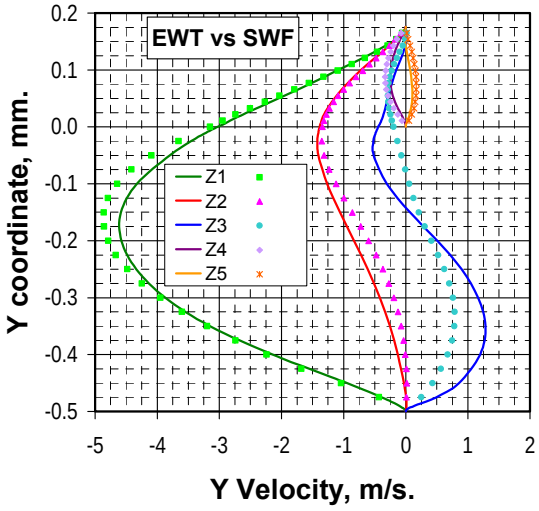


(c) Vertical velocities

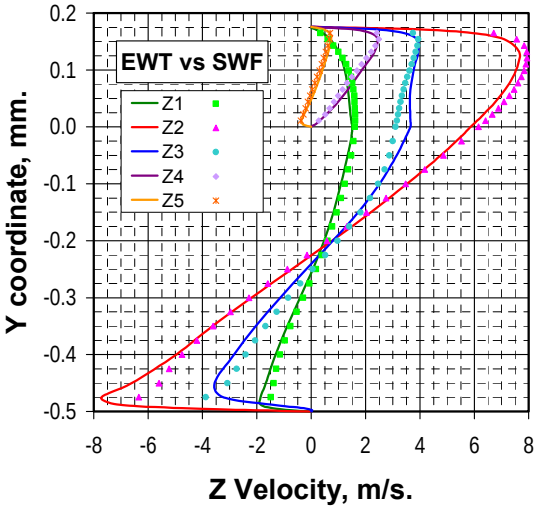


(d) Span wise velocities

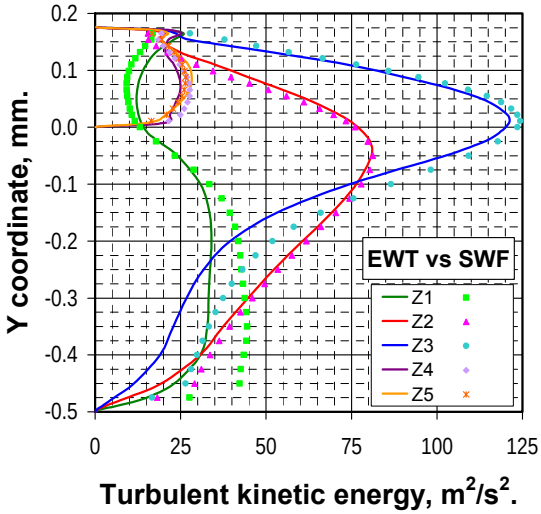


(e) Turbulent kinetic energy

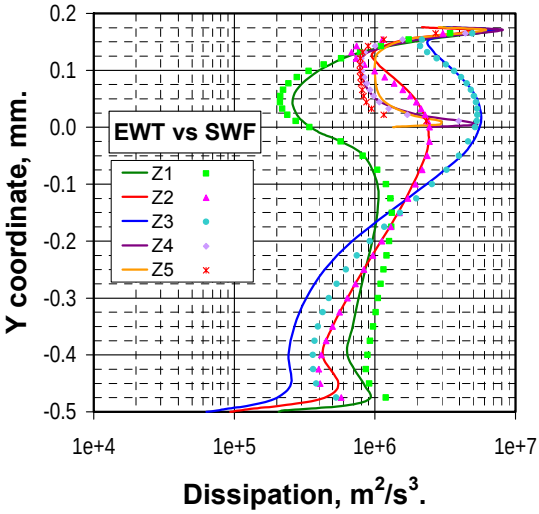


(f) Dissipation

Figure 122. Vertical line profiles, honeycomb pattern [37], near-wall treatment effect, PG = $2 \cdot 10^8$ Pa/m.

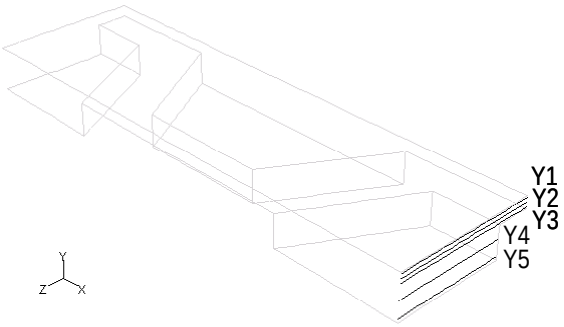


Y1 = 154 µm  Y4 = -200 µm (40% depth)
Y2 = 88 µm (half the clearance)
Y3 = 22 µm  Y5 = -450 µm (90% depth)

(a) Periodic unit, $C_r$ = 176 µm (~6.9 mils)

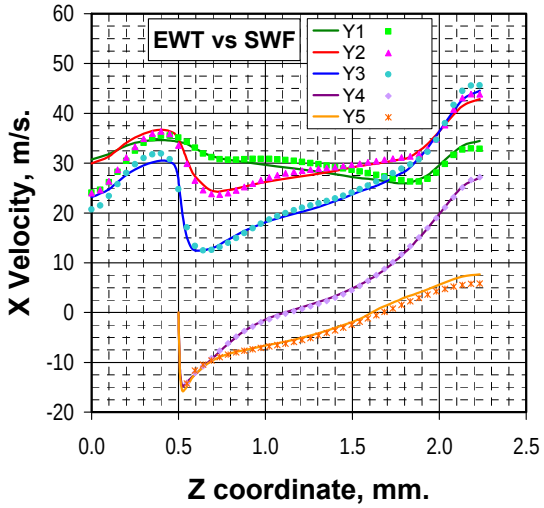


(b) Stream wise velocities

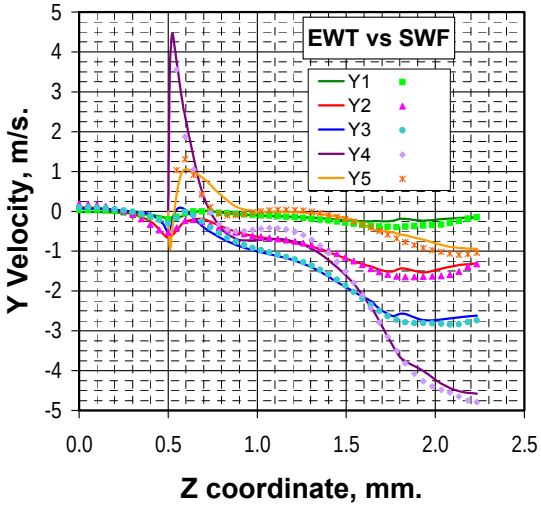


(c) Vertical velocities

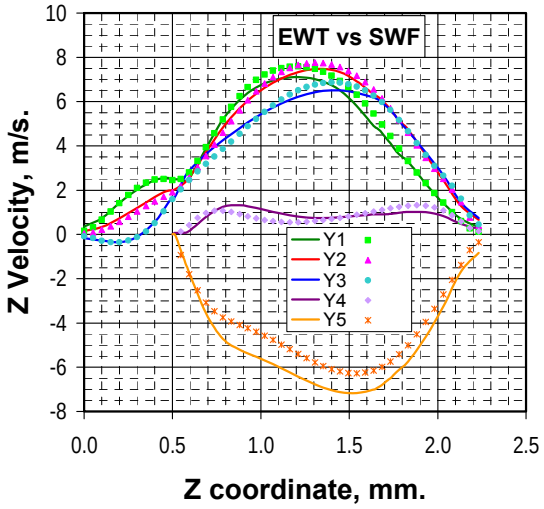


(d) Span wise velocities

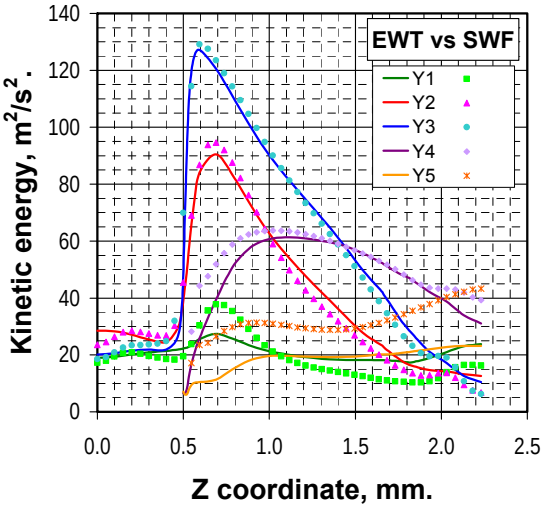


(e) Turbulent kinetic energy

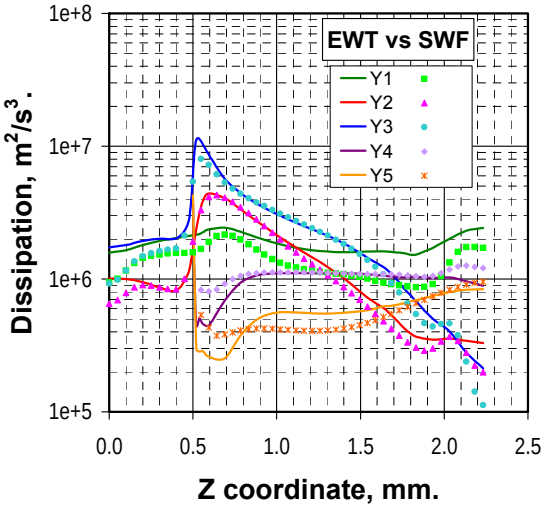


(f) Dissipation

Figure 123. Horizontal line profiles, honeycomb pattern [37], near-wall treatment effect, PG = $2 \cdot 10^8$ Pa/m.

- Both models agree in predicting that larger dissipation occurs primarily in the shear layer with peaks atop the lateral walls (Y2 and Y3 locations), and near the top wall.

Similarly, Figures 124 and 125 compare flow field profiles of both predictions at a clearance of 508 μm (20 mils). Results correspond to a pressure gradient in which the SWF model predicts 6.3% less mass flow rate and 13.8% more friction factor. Following are the more relevant observations:

- Stream wise component or x-velocity:
  - All EWT profiles are consistently larger than SWF predictions by 7.6% to 17.3% in the annular clearance.
  - Inside the pattern, EWT values are comparable within 1% to SWF predictions in the shear layer affected zone (Y4 location), but EWT values are consistently larger near the bottom wall up to 13.3% (Y5 location), and particularly near the lateral wall by 11% to 120% (Z3 and Y4 locations).
- Vertical component or y-velocity:
  - Y-velocity profiles have a similar trend but deviations are noticeable inside the pattern, where SWF profiles are larger than EWT predictions by 8.7% up to 29% (Z1 and Z2 locations). In contrast, a significant reverse trend is observed near the lateral walls, where EWT profiles indicate changes in the direction of the velocity that are not captured by the SWF model (Z3 and Y4 locations).
- Span wise component or z-velocity:
  - Z-velocity profiles are also similar. Both model profiles are comparable within ±4% in most of the annular clearance, although EWT values are consistently larger up to 11% and 80% in the shear layer near the lateral walls (Z2 and Z3 locations).
  - Inside the pattern, deviations are more noticeable where EWT profiles are consistently larger than SWF predictions by 26%, 34%, 21%, up to 26% (Z1, Z2, Z3, and Y5 locations) near the bottom wall.

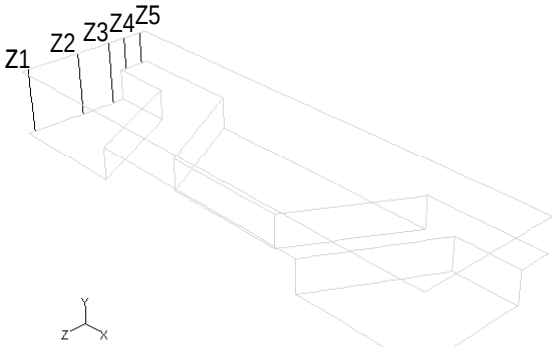


Z1 = 2.13 mm  Z4 = 0.40 mm
Z2 = 1.26 mm  Z5 = 0.10 mm
Z3 = 0.69 mm

(a) Periodic unit, $C_r$ = 508 µm ( 20 mils)

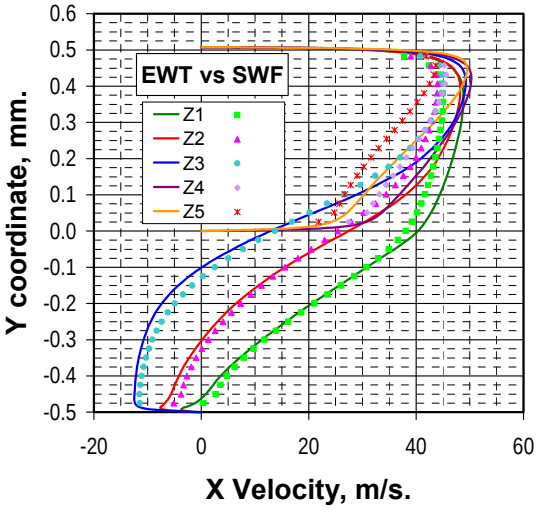


(b) Stream wise velocities

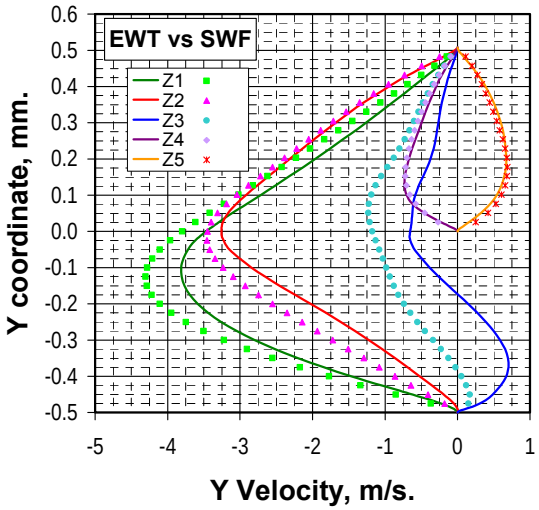


(c) Vertical velocities

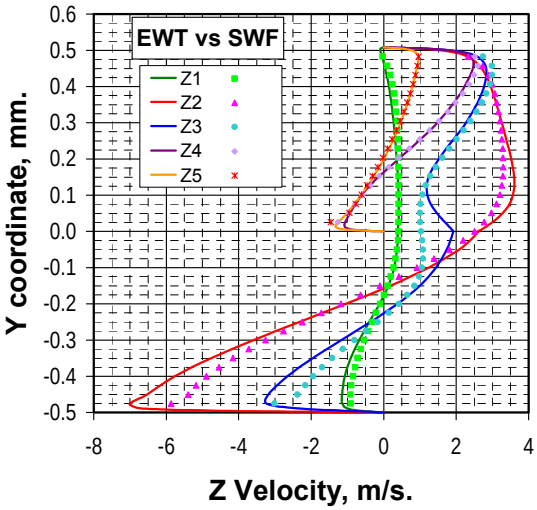


(d) Span wise velocities

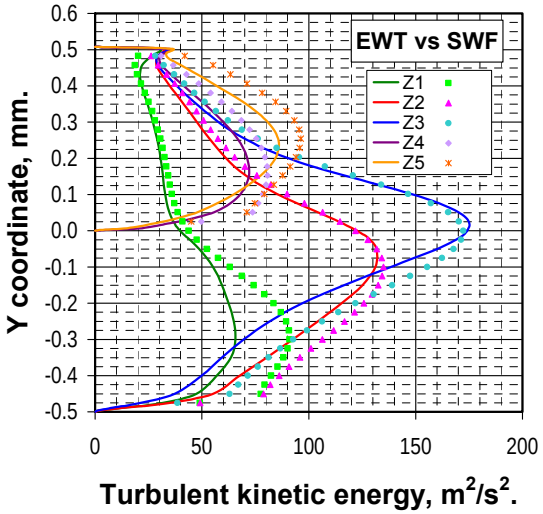


(e) Turbulent kinetic energy

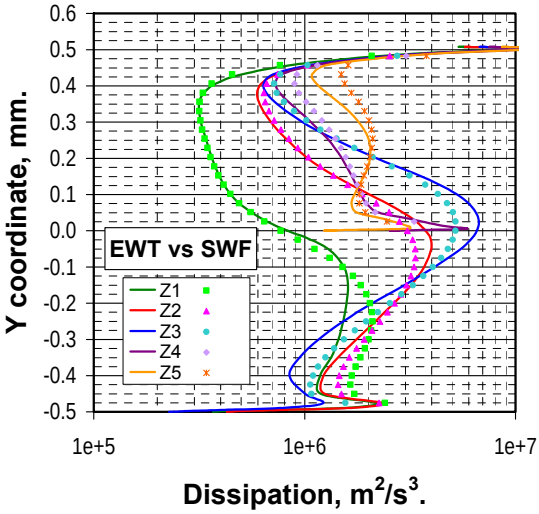


(f) Dissipation

Figure 124. Vertical line profiles, honeycomb pattern [37], near-wall treatment effect, PG = $1 \cdot 10^8$ Pa/m.

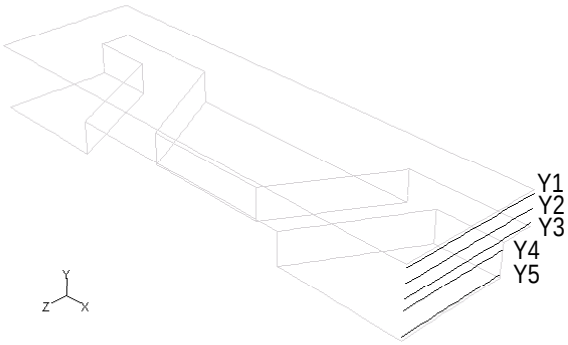


Y1 = 457 µm  Y4 = -100 µm (20% depth)
Y2 = 254 µm (half the clearance)
Y3 = 50.8 µm  Y5 = -450 µm (90% depth)

(a) Periodic unit, $C_r$ = 508 µm ( 20 mils)

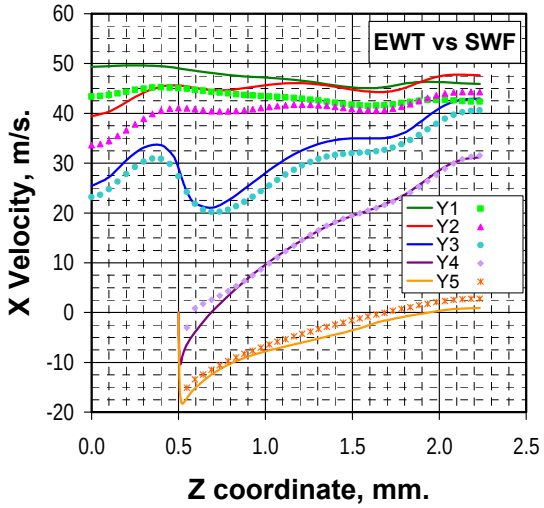


(b) Stream wise velocities

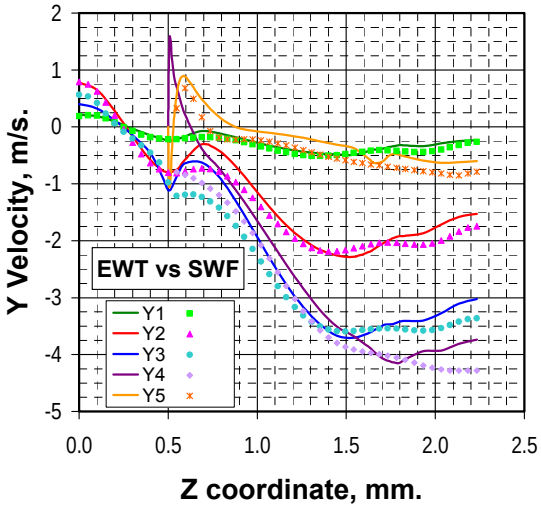


(c) Vertical velocities

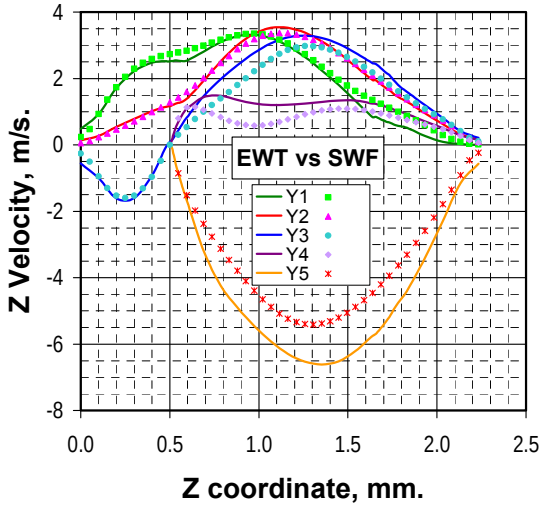


(d) Span wise velocities

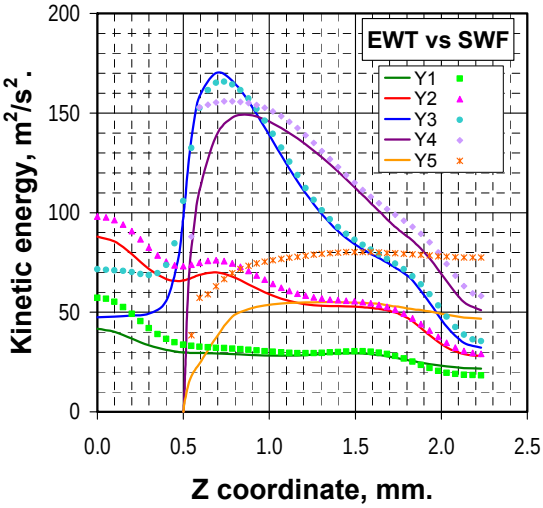


(e) Turbulent kinetic energy

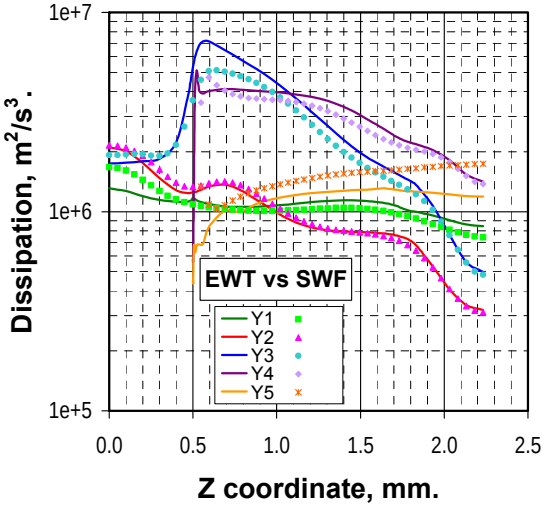


(f) Dissipation

Figure 125. Horizontal line profiles, honeycomb pattern [37], near-wall treatment effect, PG = $1 \cdot 10^8$ Pa/m.

- Turbulent kinetic energy:
  - SWF values are consistently larger than EWT prediction in most regions. Within the annular clearance, SWF profiles are larger by 11.2% and 48.5% up to 37.5% and 50.9%, particularly in the annular gap region close to the symmetry boundary (Z4, Z5, Y1, and Y3 locations).
  - Inside the pattern, SWF values are also consistently larger than EWT predictions up to 43%, 64% and 70% (Z1, Z2, and Z3 locations) near the bottom wall, and particularly near the lateral walls (Y4 and Y5 locations) up to 37.4% and 70%.
  - Both models agree in predicting larger kinetic energy values occur in the shear layer with peaks atop the lateral walls (Z3, Y2 and Y3 locations).
- Turbulence Dissipation:
  - Both predictions are comparable, but EWT profiles are consistently larger by an average of 9.8% and 17.6% up to 28.4% in the shear layer (Y3, Y4, and Z3). In contrast, both profiles are comparable within ±5% near the top wall and the pattern center (Y1 and Z1 locations), while SWF values are larger inside the pattern, particularly near the bottom walls up to 19.7%, 32.3%, 44%, and 46.5% (Z2, Z3, Z1, and Y5 locations).
  - Both models agree in predicting that larger dissipation occurs primarily in the shear layer with peaks atop the lateral walls (Y3 and Y4 locations), and near the top wall.

In summary:

- SWF friction factor predictions are larger than those obtained with the EWT modeling. Depending on the clearance, differences vary from to 7.8% to 15.4%.
- Both models predict a similar friction-factor-to-clearance-behavior. For a Reynolds number flow range of $10^4$-$10^5$, simulations indicate that a plateau is likely to occur at a clearance value of 508 μm (20 mils) in the honeycomb pattern of Kaneko [37]. Indeed, both predictions indicate that the friction factor is directly proportional to the clearance for values lower than the plateau, while the traditional behavior is expected for larger clearance values in this pattern, with the friction factor decreasing as the clearance is increased.
- Boundary layer refinement also resulted in comparatively large grids when used for

EWT compliance. On the other hand, a grid created with specific cell sizes in all surfaces with the boundary layer approach is suitable for several Reynolds number cases, and with the conformal approach does not require grid cell interpolation. On the downside, full boundary layer conformal grids contain highly distorted cells requiring more iterations to meet the convergence criteria.

- Most differences in flow field predictions among the two near-wall models are observed inside the roughness pattern, particularly in the turbulent kinetic energy and dissipation levels, which SWF estimates are significantly larger that EWT values. In addition, EWT velocities are also consistently larger, particularly near the pattern walls.

# 5. DISCUSSION

This section summarizes the more relevant observations regarding the predicted friction factor behavior in liquid annular seals with deliberately roughened surfaces. First, a review is presented on laminar flow predictions to analyze the effect of the clearance, identify the losses mechanism in this flow regime, and compare initial recirculation patterns inside the different roughness under study. Secondly, a similar review is presented for turbulent flow predictions in the Reynolds number flow range of interest, closing with a comparison to the parametric analysis, section 2.5, emphasizing the relevance of the surface roughened area and the length-to-clearance ratios in determining the flow resistance of roughened seals.

## *5.1. Laminar solutions*

As already discussed briefly in sections 3.3, 3.4, and 4.2.2, laminar flow predictions deviate from the theoretical solution for laminar channel flow. In this section, predictions based on the hole-pattern geometry of Fayolle [8] are compared to evaluate the effect of the hole depth in the friction factor and recirculation flow patterns. Similarly, predictions based on the patterns of Iwatsubo [36] and Kaneko [37] are compared to evaluate the effect of the clearance in the friction factor and recirculation flow patterns.

### *5.1.1. The round-hole pattern of Fayolle [8].*

In a traditional friction factor versus Reynolds number diagram, Figure 126(a), predictions in both deep and shallow patterns are significantly lower than the theoretical solution for an infinite width channel, (96/Re) equation (26) in section 4.2.3, but they appear to be comparable in the common flow range. Indeed, predictions are similar within 0.38% at the lowest Reynolds number simulated. In contrast, friction factors predicted in the deep pattern are larger than the corresponding values in the shallow pattern by up to 10%, as the Reynolds number is increased. These differences can be better appreciated if friction characteristics of the surfaces are expressed in terms of the product ($f \cdot Re$) rather than the friction factor itself. In this way, predictions can be directly compared to the infinite width channel solution for which ($f \cdot Re$) product is equivalent to 96, while the differences among patterns are emphasized. Figure 126(b) compares ($f \cdot Re$) products of both patterns.

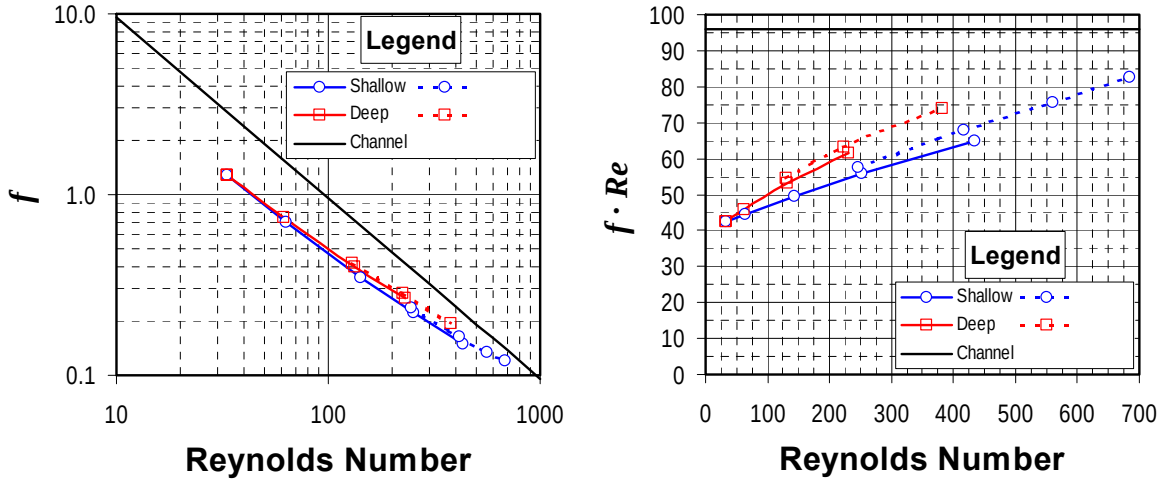


(a) Friction factor versus Reynolds number (b) *f·Re* product versus Reynolds number

Figure 126. Predicted friction factor behavior in the round-hole pattern of Fayolle [8], laminar flow regime.

Following are the more relevant observations derived from Figure 126(b):

- For Reynolds number below 75, there is no significant difference in the predicted friction behavior of the shallow and the deep round-hole patterns.
- For Reynolds number above 75, differences among friction characteristics of both patterns are significantly larger than the numerical uncertainty (dotted lines). Indeed, the deep pattern provides larger resistance to flow in this Reynolds number range.
- In both patterns, flow resistance increases with Reynolds number. The product (*f·Re*) increases asymptotically with Reynolds number, as the infinite width channel behavior appears to be the limiting solution.

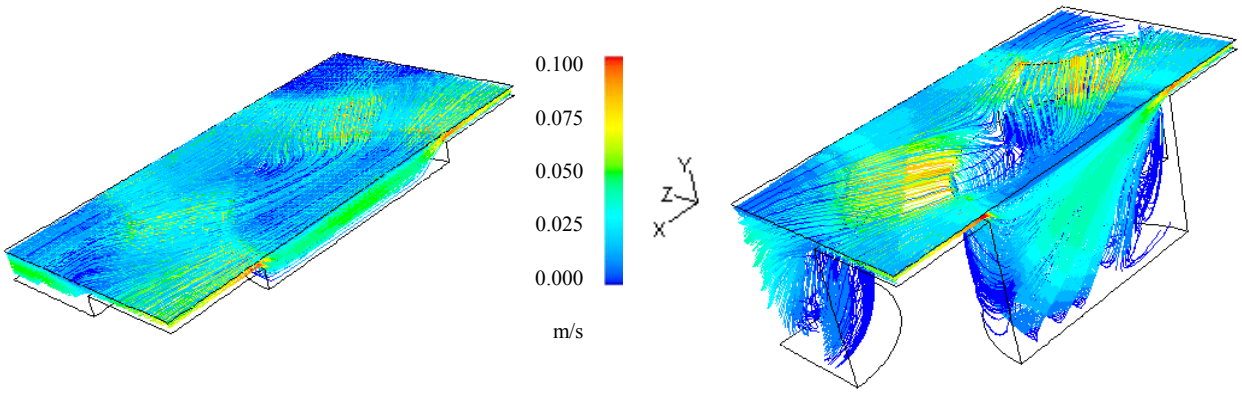


(a) Shallow round-hole. Flow Direction, X (b) Deep round-hole.

Figure 127. Flow path in the round-hole patterns of Fayolle [8], Re~33, PG = $1 \cdot 10^4$ Pa/m.

Figure 127 compares flow path lines in both patterns for an equal pressure gradient at the lowest common Reynolds number. Path lines are colored by the actual velocity magnitude in the flow. In both cases, flow velocities are considerably reduced as the flow enters the round-hole. While the flow reattaches quickly to the bottom wall in the shallow pattern, it is 'channeled' towards the pattern center in the case of the deep pattern. Flow reattachment to the hole walls in the shallow pattern is easily visualized in the wall shear stress contours included in Figure 128. The contours include only positive values in the stream-wise flow direction (X coordinate axis). With the exception of a small zone in the leading edge of the hole, wall shear stresses are positive in most of the bottom wall of the shallow pattern, Figure 128(a). On the contrary, there are almost no positive shear stresses values in the deep pattern, Figure 128(b). Note that shear stresses distribution on the wall defining the clearance is similar among the two patterns.

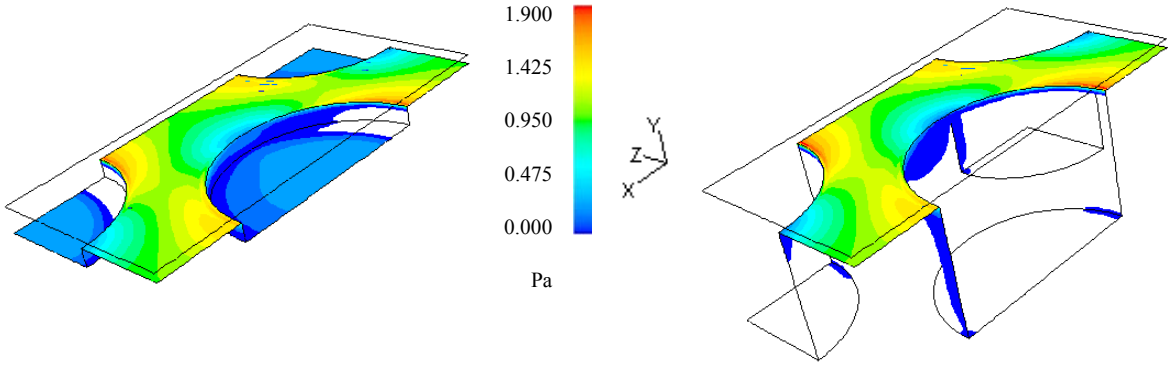


(a) Shallow round-hole. Flow Direction, X (b) Deep round-hole.

Figure 128. Bottom wall shear stresses (X direction) in the round-hole patterns, Re~33.

Regarding recirculation paths within the hole pattern, the quick reattachment to the hole walls prevents the creation of secondary flows in the shallow pattern. The channeling effect of the flow in the deep pattern promotes the creation of two pairs of counter rotating vortices in the horizontal and span-wise vertical planes, as shown in Figure 129, recalling that only half the deep pattern was actually solved (minimum periodic unit). Note the channeling flow reattaches to the bottom wall of the deep pattern at much lower Reynolds numbers, when XZ plane vortices disappear and YZ planes vortices remain.

As the Reynolds number increases, the flow path in the shallow pattern geometry does not change significantly but the flow now reattaches only to the bottom wall of the hole, Figure 130(a). An interesting feature observed in the wall shear stress distribution of this pattern, Figure 130(b), is the prediction of a small stagnant flow region immediately after the trailing edge of the hole. This region is better predicted when higher order discretization schemes are used for simulation purposes.

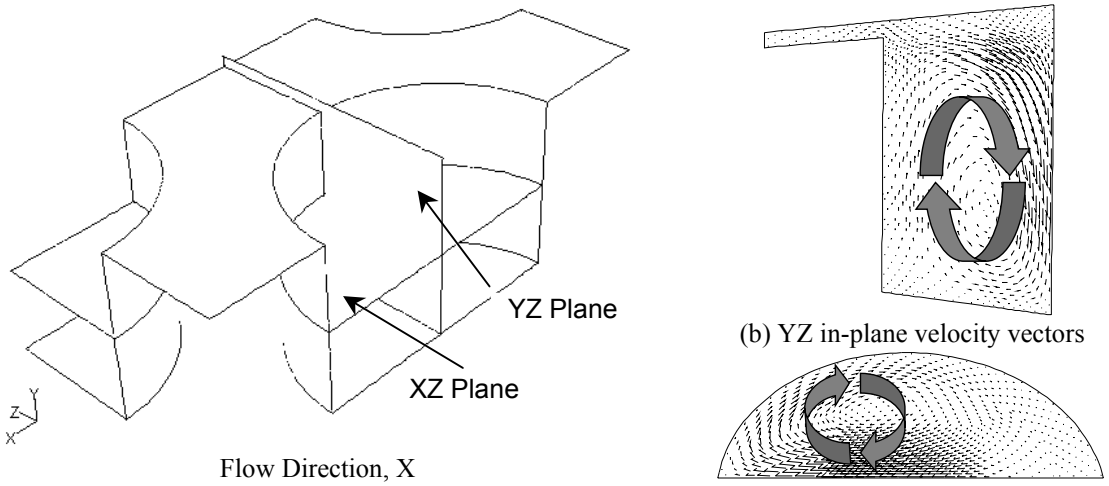


Flow Direction, X

(a) Deep hole geometry plane locations

(b) YZ in-plane velocity vectors

(c) XZ in-plane velocity vectors

Figure 129. Initial recirculation paths in the deep round-hole pattern, Re~33.

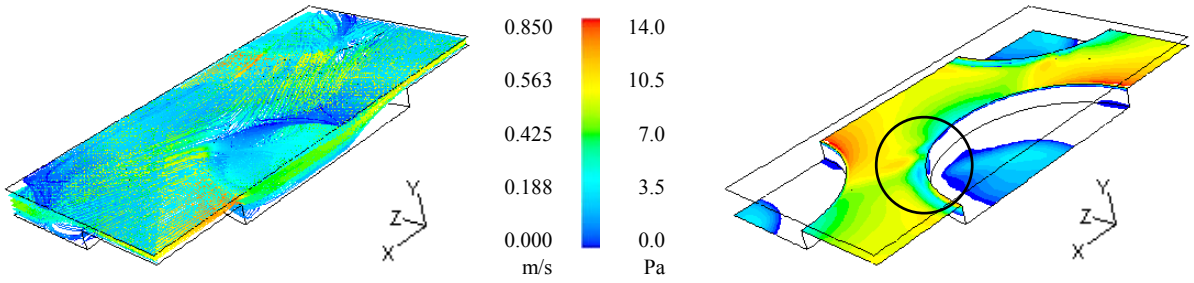


(a) Path lines.

Flow Direction,

(b) X-wall shear stresses.

Figure 130. Flow path and shear stress in the shallow hole pattern, Re~250, PG = $1 \cdot 10^5$ Pa/m.

Likewise, the channeling of the flow in the deep pattern intensifies towards the top of the pattern, as the 'traditional' strong, stream-wise recirculation path is established, Figure 131(a). As with the shallow pattern, a stagnant flow region is predicted after the hole trailing edge; see the wall shear stress distribution in Figure 131(b). Note that shear stresses distribution on the clearance bottom wall are comparable among the two patterns.

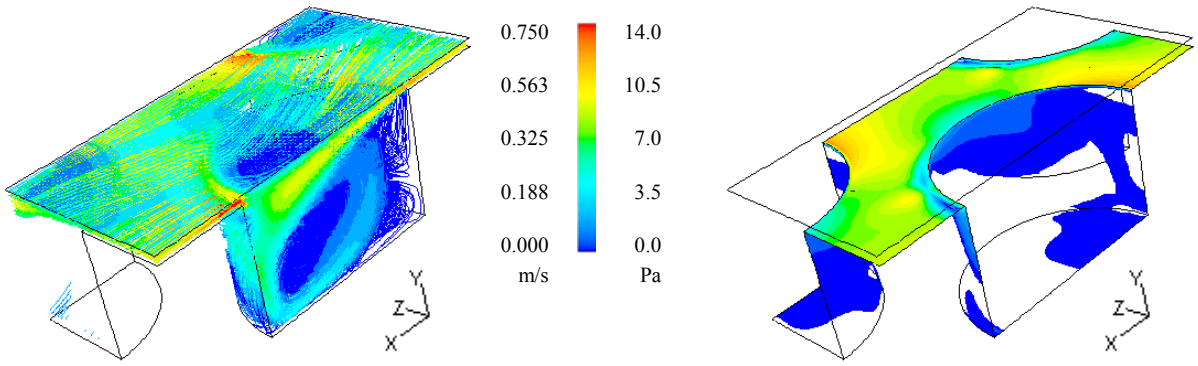


(a) Path lines. Flow Direction, X (b) X-wall shear stresses.

Figure 131. Flow path and shear stress in the deep hole pattern, Re~230, PG = $1 \cdot 10^5$ Pa/m.

Regarding recirculation paths at this larger Reynolds number, the reattachment to the hole bottom wall still prevents the creation of significant secondary flows in the shallow pattern. Instead, the intensified channeling effect of the flow in the deep pattern promotes recirculation in several ways. The stronger vortex now lies in the stream-wise plane (symmetry or XY plane), Figure 132(b). This vortex is the traditional recirculation path observed in square grooves or holes and what is known as 'cavity' flow. In contrast, there are at least six pairs of counter rotating vortices that can be identified in the horizontal and span-wise vertical planes, as shown in Figure 132(c) and (a), respectively.

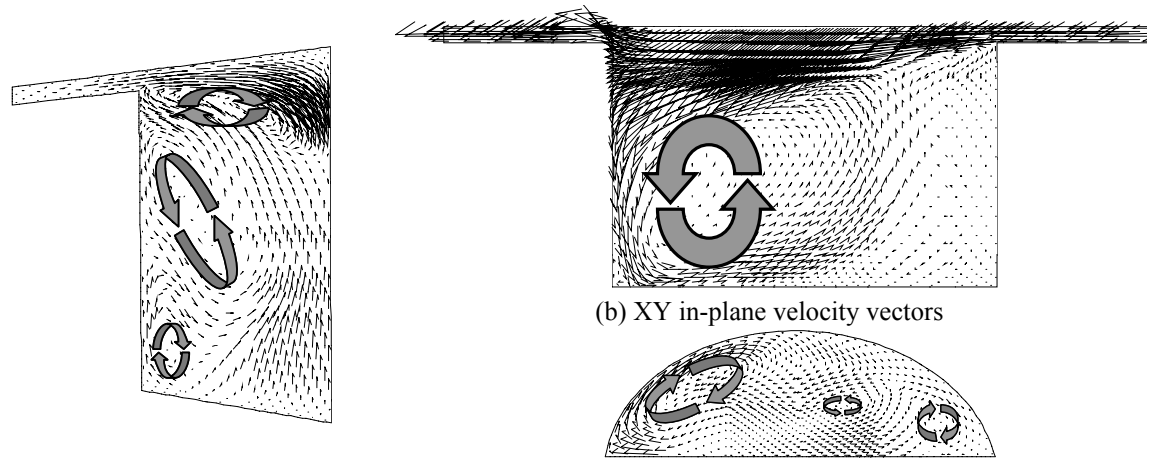

(b) XY in-plane velocity vectors

(a) YZ in-plane velocity vectors (c) XZ in-plane velocity vectors

Figure 132. Recirculation paths in the deep round-hole pattern, Re~230.

Lastly, the proportion of the friction factor that is due to the static pressure forces acting

on the lateral walls of the hole pattern is analyzed. Figure 133 presents the ratio of the static pressure force and the total force (numerically equivalent to the pressure gradient times the periodic unit length) acting in the flow direction as a function of the Reynolds number for both round-holes, shallow and deep.

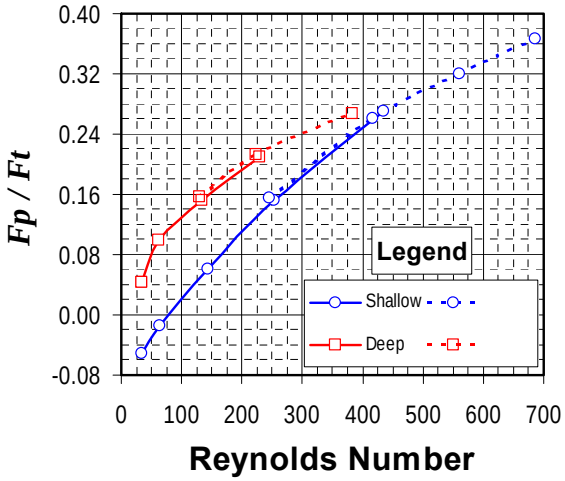


Figure 133. Stream-wise forces predicted proportion in the round-hole pattern, laminar flow regime.

Following are the more relevant observations:

- At low Reynolds numbers, the static pressure force does not contribute significantly to the overall pressure gradient in the shallow pattern, and even becomes negative (static pressure force acting in the same direction of the pressure gradient). In other words, most of the losses come from shear stresses at the walls defining the clearance.
- Static pressure force ratios are always positive in the deep pattern, oppose the pressure gradient, and are larger than the shallow-pattern values at all Reynolds numbers.
- In both patterns, static pressure force ratios increase with Reynolds number.

Figure 134 compares periodic static pressure distributions in both patterns at the largest common pressure differential. The local static pressure is considerably larger in the trailing side of the deep pattern. Conversely, the local static pressure is lower in the leading side of the shallow pattern. The fact that the actual pressure force in the deep pattern is roughly 40% larger than the corresponding value in the shallow pattern at this Reynolds number is a combination of two factors. First, the static pressure differential within the hole is slightly larger in the deep pattern. Secondly, the integration area for that static pressure differential

within the hole is considerably larger in the deep pattern.

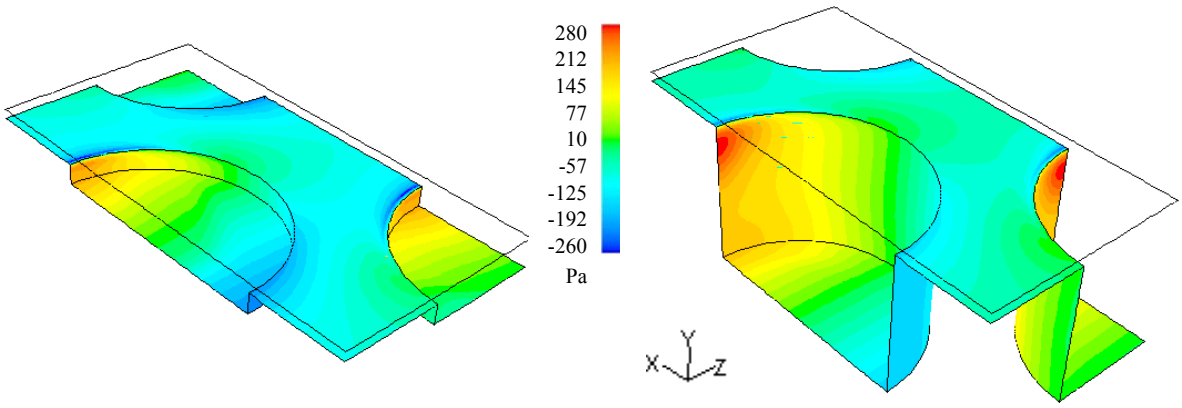


(a) Shallow pattern. Flow Direction, ⅄ (b) Deep pattern.

Figure 134. Periodic static pressure contours, round-hole patterns, Re~230, PG = $1 \cdot 10^5$ Pa/m.

### *5.1.2. The isogrid pattern of Iwatsubo[36].*

Figure 135 summarizes the friction-factor-to-clearance behavior predicted for the isogrid pattern of Iwatsubo[36] in the laminar flow regime, and includes both, the traditional friction factor versus Reynolds number diagram, and the *f·Re* product versus the Reynolds number. As with the previous section, the 'Channel' curves refer to the theoretical solution for an infinite width channel.

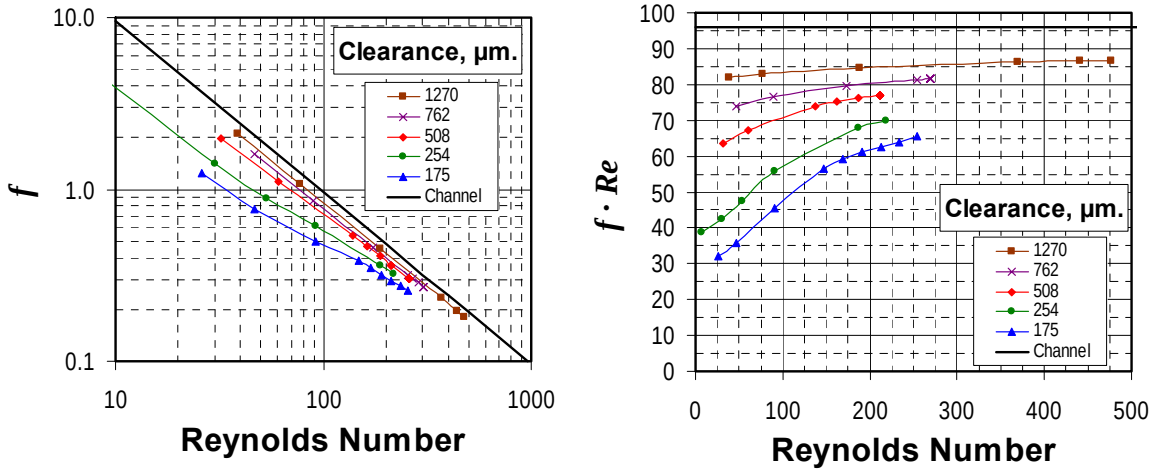


(a) Friction factor versus Reynolds number (prelim) (b) *f·Re* product versus Reynolds number (prelim)

Figure 135. Predicted friction factor behavior, isogrid pattern of Iwatsubo [36], laminar flow regime.

Following are the more relevant observations derived from Figure 135:

- The friction factor is directly proportional to the clearance in the whole Reynolds number flow range simulated.
- Differences among friction factor predictions are reduced considerably for Reynolds numbers above 100, although flow resistance remains proportional to the clearance as indicated by the product ($f \cdot Re$) that remains increasing with clearance.
- Although barely noticeable in the traditional diagram for the larger clearances, flow resistance increases with Reynolds number. The product ($f \cdot Re$) increases asymptotically with Reynolds number in all clearances, but linearly in the smaller values (176 µm, r=0.999; 254 µm, r=0.998) at lower Reynolds numbers.
- As the clearance or the Reynolds numbers is increased, the infinite width channel behavior appears to be the limiting solution in all cases.

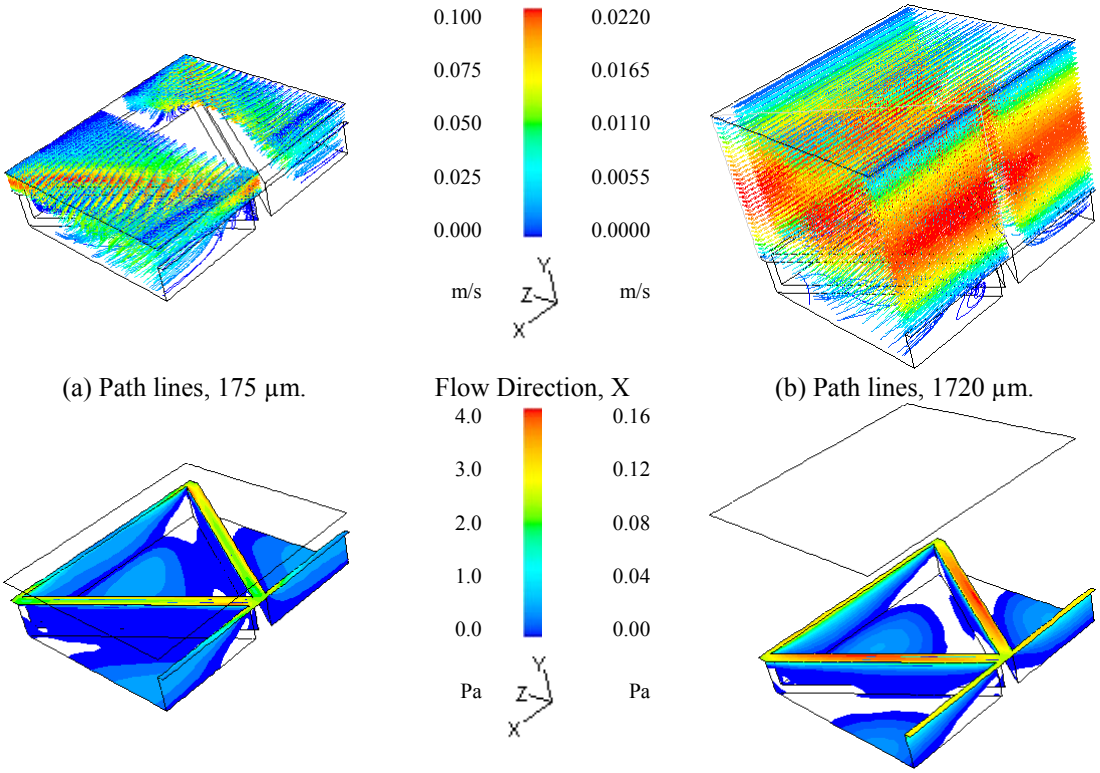


(a) Path lines, 175 µm.

(b) Path lines, 1720 µm.

(c) X-wall shear stresses, Re~26.

(d) X-wall shear stresses, Re~39.

Figure 136. Flow path and shear stress in the isogrid pattern; PG = $1 \cdot 10^4$, $1 \cdot 10^2$ Pa/m.

Figures 136(a) and (b) compare flow path lines in the smallest and largest clearances of

the isogrid pattern at the lowest Reynolds number of each case. Path lines are colored by the actual velocity magnitude in the flow. In both cases, the flow reattaches quickly to the bottom wall of the pattern. While flow velocities are considerably reduced as the flow enters the pattern in the smallest clearance, they are unchanged in the largest clearance case. Flow reattachment to the pattern walls is easily visualized in the wall shear stress contours included in Figure 136(c) and (d). The contours only include positive values in the flow direction. There are small recirculation zones (blank zones) in the leading and middle corners of the pattern in the smallest clearance, while the same zone extends to the whole leading bottom edge of the pattern in the largest clearance case.

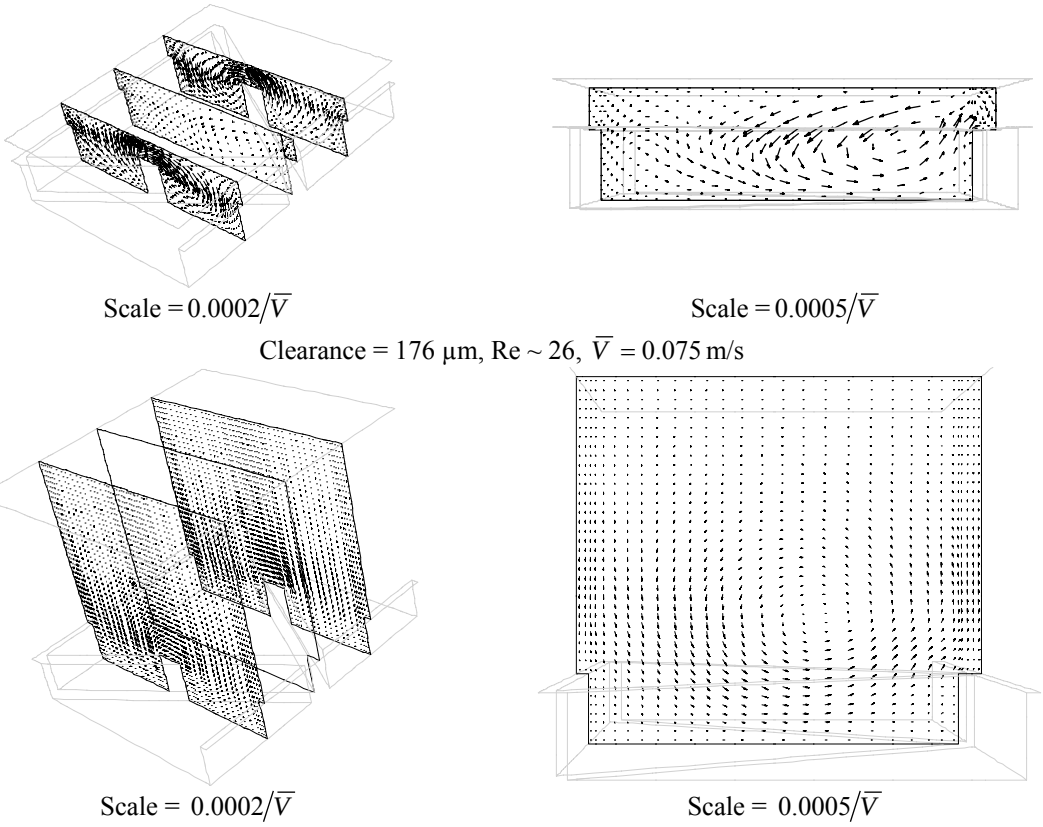


(a) YZ in-planes velocity vectors. (b) Mid YZ plane velocity vectors.

Figure 137. Initial recirculation paths in the isogrid pattern at low Reynolds number.

Regarding recirculation paths inside the isogrid, the reattachment to the pattern walls in all clearances at low Reynolds number prevents the creation of strong secondary flows in

either stream-wise or horizontal planes within the pattern. Nonetheless, there are spam-wise vortices created by the 'converging' or 'zigzag' effect of the flow towards the lateral wall vicinities of each pattern. While these vortexes appear localized inside the pattern in the smallest clearance, they seem to weakly fill the whole clearance in the largest clearance case; see Figure 137. The normalization allows a direct comparison of vectors ($|\vec{V}| \approx \overline{V}$ ).

As the Reynolds number increases, the converging effect of the flow towards the lateral wall vicinities of each pattern effect appears to fade, with the flow only slightly dipping in this region in the smallest clearance, Figure 138(a), as flow separation at the pattern leading edge intensifies and becomes prevalent. This behavior is more evident at the largest clearance, Figure 138(b). Flow separation is easily visualized in the wall shear stress contours included in Figure 138(c) and (d). There are no positive values in the flow direction inside the pattern, an indication that recirculation zones (blank zones) fill most of the pattern in every clearance.

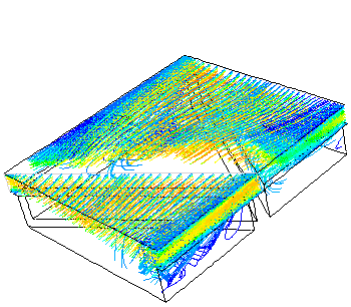

(a) Path lines, 175 µm.

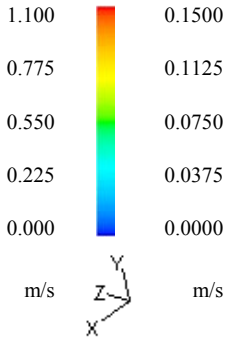


Flow Direction, X

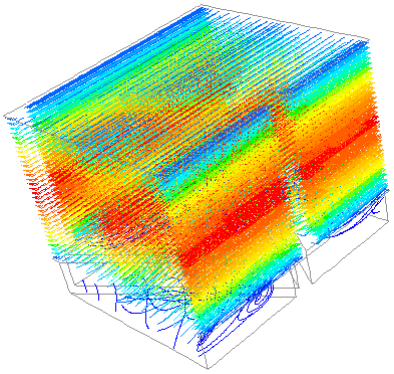

(b) Path lines, 1270 µm.

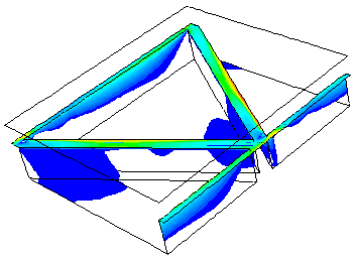

(c) X-wall shear stresses.

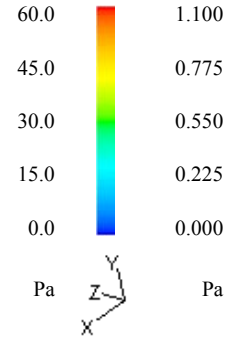


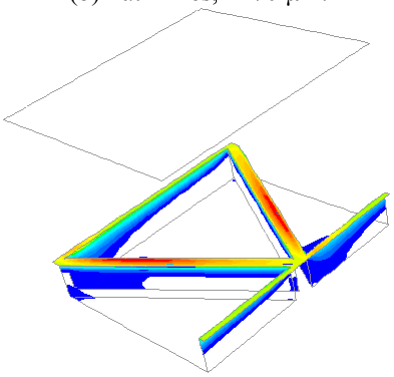

(d) X-wall shear stresses.

Figure 138. Flow path and shear stress in the isogrid pattern; PG = $1 \cdot 10^5$, $6.8 \cdot 10^2$ Pa/m, Re~250.

Regarding recirculation paths at these larger Reynolds numbers, the flow separation at each pattern leading edge in all clearances promotes secondary flows in each plane inside the pattern. Figure 139 presents in-plane velocity vectors of several sections of the isogrid pattern at the smallest clearance. The traditional forward recirculation path, typical of cavity flow, is clearly depicted in Figure 139(a). The low Reynolds number localized vortex is now filling diagonally the mid plane of the pattern, Figure 139(b). This vortex is concentrated in the widest portion of the pattern, as Figure 139(c) shows no evidence of it as the flow moves downstream. Finally, Figure 139(d) shows the strong recirculation prevalent in the mid-depth horizontal plane of the pattern.

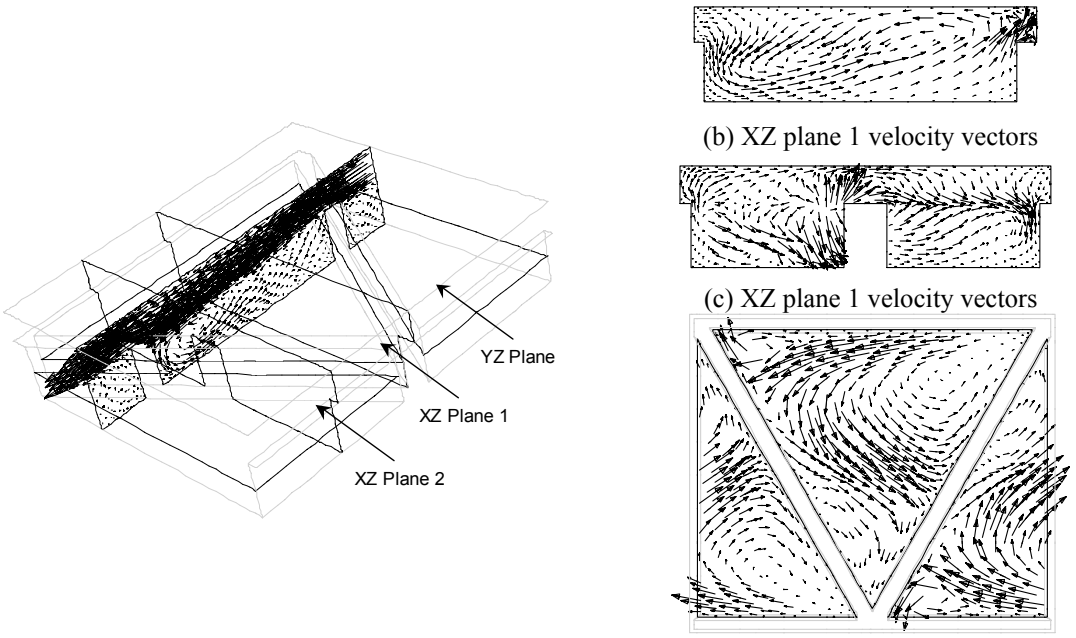


(a) Stream-wise plane velocity vectors
Scale = $0.0002/\overline{V}$

(b) XZ plane 1 velocity vectors

(c) XZ plane 1 velocity vectors

(d) YZ plane velocity vectors
Scale = $0.0005/\overline{V}$

Figure 139. Recirculation paths in the isogrid pattern, clearance = 175μm, Re~250, $\overline{V}$ = 0.736 m/s.

As the clearance is increased, the vortices become weaker. The stream-wise vortex is considerably reduced, and is shifted to the back of the pattern, Figure 140(a). Likewise, the mid-depth horizontal plane strong vortex has disappeared, Figure 140(b). Finally, the localized vortex that filled the whole clearance at low Reynolds number is still present but confined to the widest portion of the pattern, Figure 140(c), as Figure 140(d) shows no

evidence of it as the flow moves downstream.

As with the round-hole pattern of Fayolle[8], Figure 141 presents the static pressure force ratio predicted in the isogrid pattern in the test flow direction as a function of the Reynolds number for all clearances simulated. Following are the more relevant observations:

- At low Reynolds numbers, static pressure force ratios increase with clearance.
- At low Reynolds numbers, the static pressure force does not contribute significantly to the overall pressure gradient in the smaller clearances (175 and 254 μm). Indeed, static pressure force ratios are roughly the same for these two clearance values in the whole Reynolds number flow range simulated.
- As the Reynolds number is increased, above Re~80, static pressure force ratios become inversely proportional to the clearance; i.e., the proportion of the friction factor due to the static pressure forces increases as the clearance is reduced.

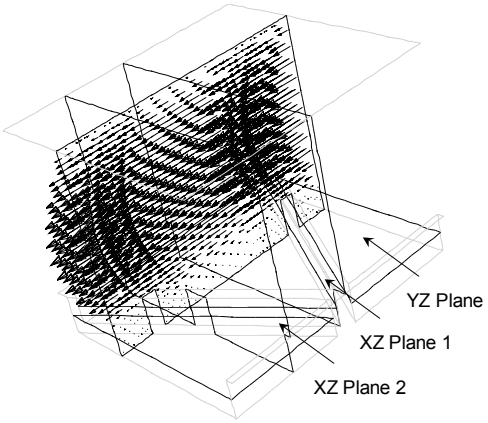


(a) Stream-wise plane velocity vectors, $0.0002/\overline{V}$

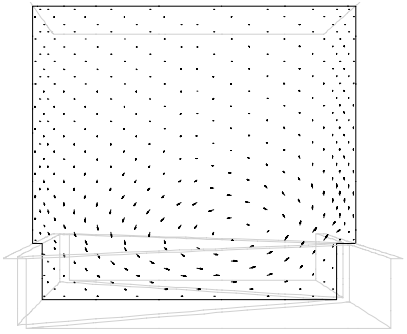

(c) XZ plane 1 velocity vectors, $0.0005/\overline{V}$

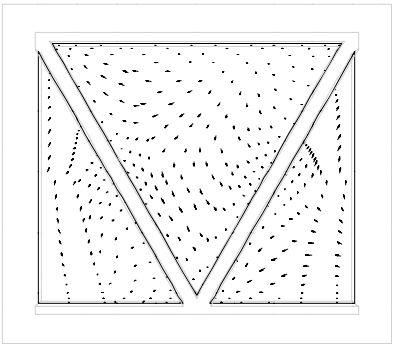

(b) YZ plane velocity vectors, $0.0005/\overline{V}$

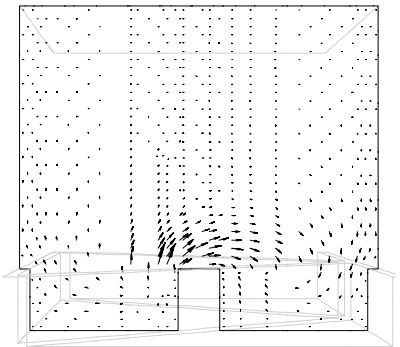

(d) XZ plane 1 velocity vectors, $0.0005/\overline{V}$

Figure 140. Recirculation paths in the isogrid pattern, clearance = 1270μm, Re~250, $\overline{V}$ = 0.098 m/s.

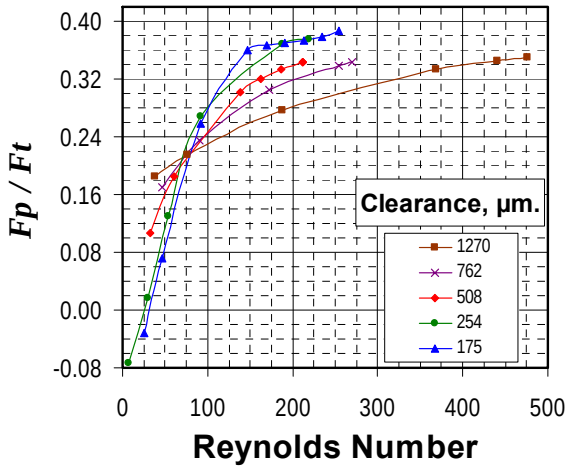


Figure 141. Stream-wise forces predicted proportion in the isogrid pattern, laminar flow regime.

### *5.1.3. The honeycomb pattern of Kaneko[37].*

Figure 142 summarizes the friction-factor-to-clearance behavior predicted for the honeycomb pattern of Kaneko[37] in the laminar flow regime, and includes both, *f* versus Reynolds number diagram, and the *f·Re* product versus the Reynolds number. The 'Channel' curve is also added as a reference.

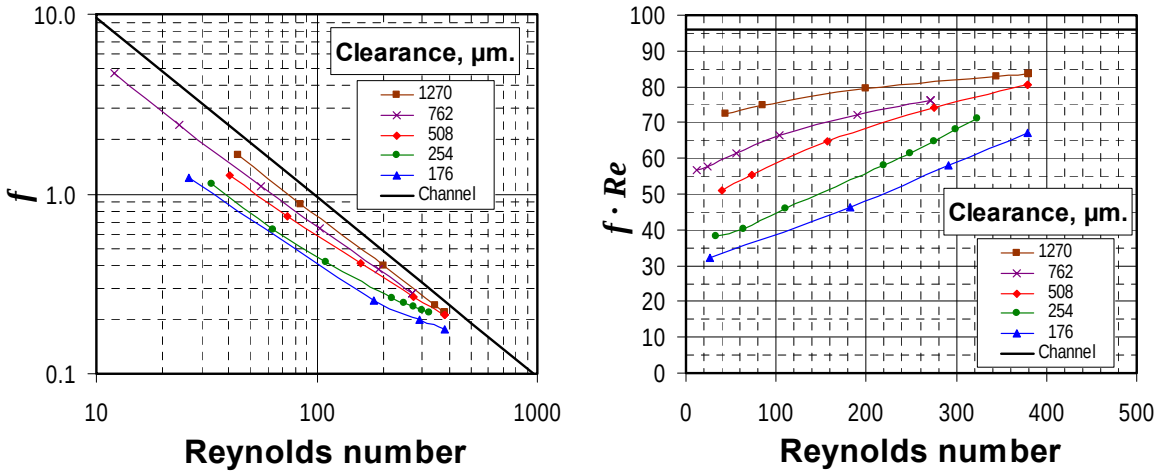


(a) Friction factor versus Reynolds number (b) *f·Re* product versus Reynolds number

Figure 142. Predicted friction factor behavior, honeycomb pattern of Kaneko [37], laminar flow regime.

Following are the more relevant observations derived from Figure 142:

- For Reynolds numbers below 200, the friction factor is directly proportional to the

clearance.

- For Reynolds numbers above 200, differences among friction factor predictions for the larger clearances decrease significantly, although flow resistance remains proportional to the clearance as indicated by the product ($f \cdot Re$) that increases with clearance.
- Although barely noticeable in the traditional diagram, flow resistance increases with Reynolds number. The product ($f \cdot Re$) increases asymptotically with Reynolds number in the larger clearances (508 µm to 1270 µm), but linearly in the smaller values ones (176 µm, r=0.9993; 254 µm, r=0.9991).
- As the clearance or the Reynolds numbers is increased, the infinite width channel behavior appears to be the limiting solution in all cases.

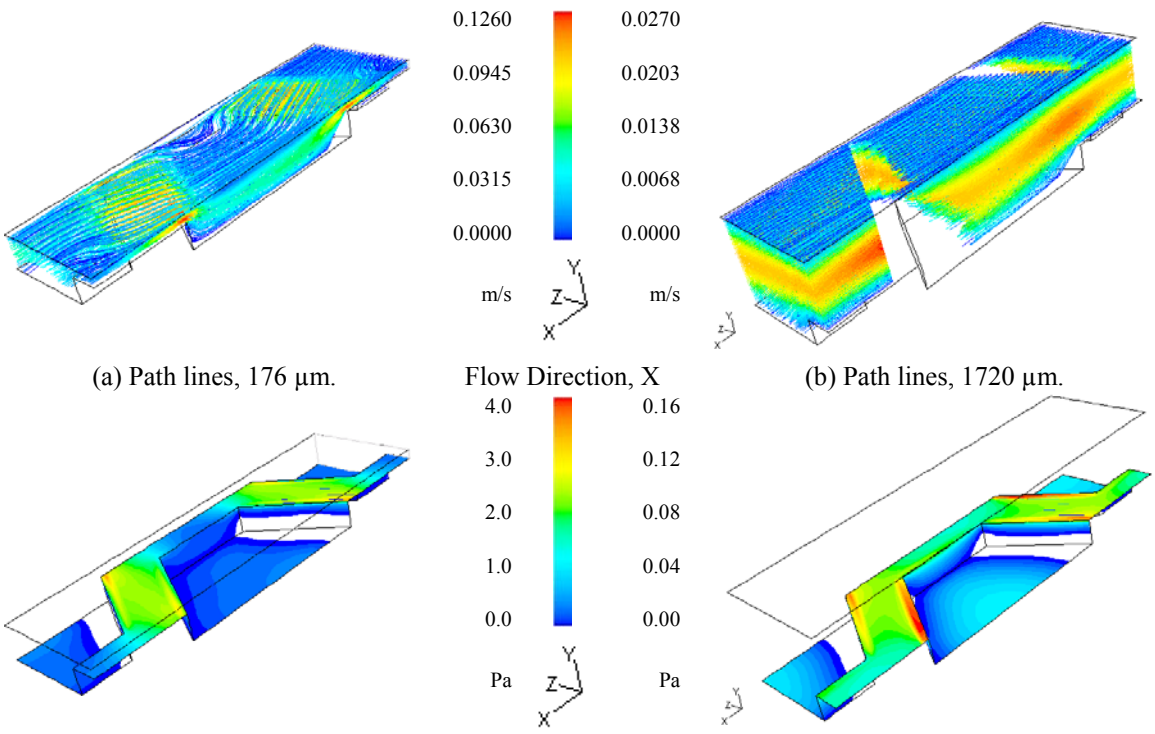


(a) Path lines, 176 µm. Flow Direction, X (b) Path lines, 1720 µm.

(c) X-wall shear stresses, Re~26. (d) X-wall shear stresses, Re~44.

Figure 143. Flow path and shear stress in the honeycomb pattern; PG = $1 \cdot 10^4$, $1 \cdot 10^2$ Pa/m.

Figures 143(a) and (b) compare flow path lines in the smallest and largest clearance simulated for the lowest Reynolds number on each case. Path lines are colored by the actual velocity magnitude in the flow. In both cases, the flow reattaches quickly to the bottom wall

of the honeycomb pattern. While flow velocities are considerably reduced as the flow enters the honeycomb in the smallest clearance, they are just moderately reduced in the largest clearance case. Flow reattachment to the pattern walls is easily visualized in the wall shear stress contours included in Figure 143(c) and (d). The contours only include positive values in the flow direction. With the exception of a small recirculation zone in the leading edge of the pattern (blank zones), wall shear stresses are positive in most of the pattern walls in both cases.

Regarding recirculation paths within the honeycomb, the quick reattachment to the pattern walls in all clearances at low Reynolds number prevents the creation of strong secondary flows in stream-wise and horizontal planes inside the pattern. There are some span-wise vortices created by the converging effect of the flow towards the center of the pattern. While there are clearly two vortices in the smallest clearance, there is a single one in the largest clearance, see Figure 144.

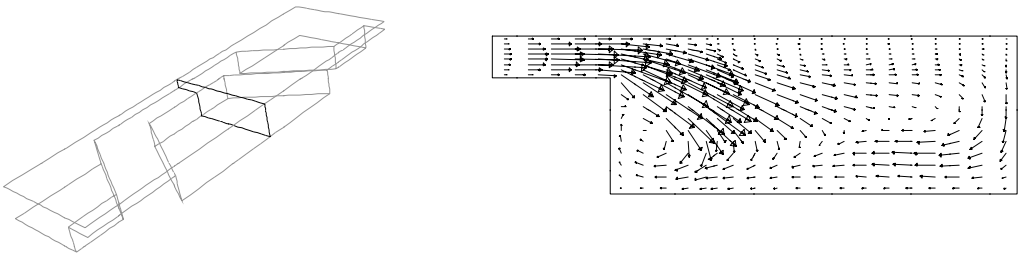

Clearance = 176 μm, Re ~ 26

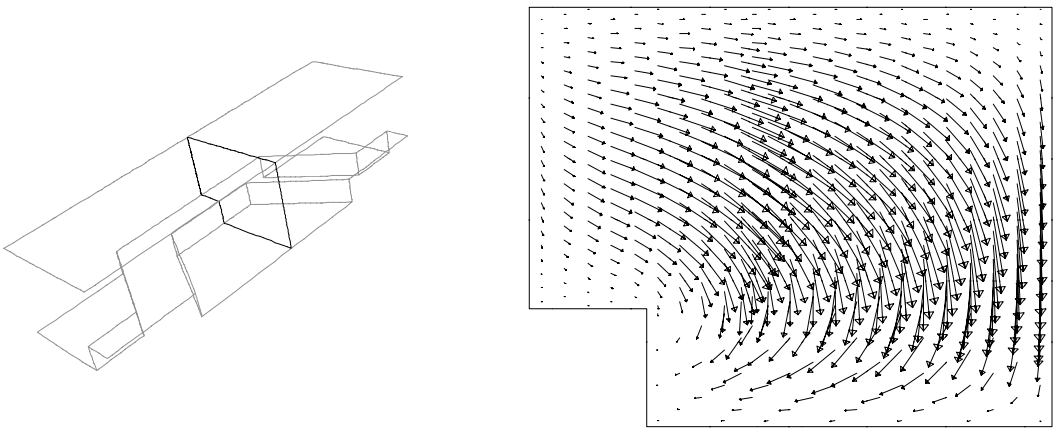

Clearance = 1270 μm, Re ~ 44

(a) Honeycomb spam-wise (YZ) plane location. (b) YZ in-plane velocity vectors, Scale $0.002/\overline{V}$

Figure 144. Initial recirculation paths in the honeycomb pattern at low Reynolds number.

As the Reynolds number increases, the converging effect of the flow towards the center of the pattern increases in intensity becoming a channeling effect in the smaller clearances, with the flow reattaching only towards the center portion of the pattern bottom wall, Figure 145(a). An interesting feature observed in the wall shear stress distribution, Figure 145(b), is the prediction of a large stagnant flow region immediately after the trailing edge of the pattern. The channeling effect appears to fade as the clearance is increased, but the flow still reattaches to the bottom wall at the largest clearance simulated, Figure 145(c). This reattachment is better seen in the wall shear distribution, Figure 145(d), where the region immediately after the trailing edge of the pattern still remains a low stream-wise velocity flow zone.

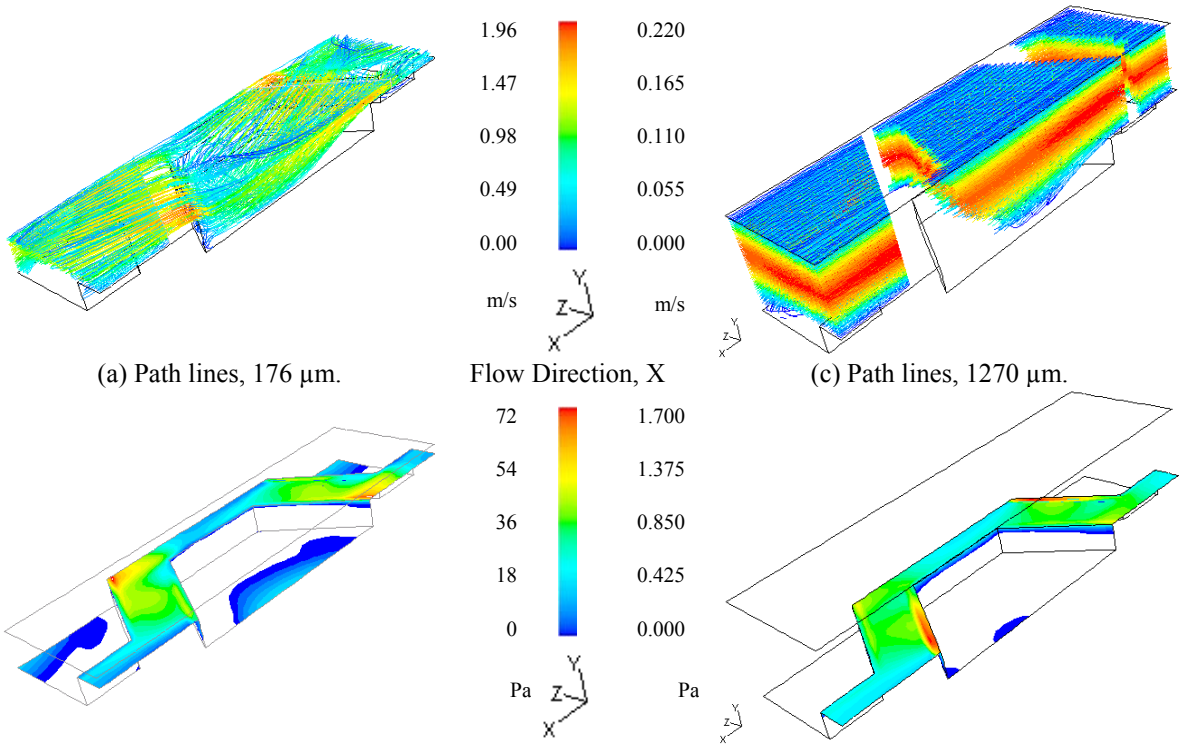


(a) Path lines, 176 µm. Flow Direction, X (c) Path lines, 1270 µm.

(b) X-wall shear stresses, Re~380. (d) X-wall shear stresses, Re~380.

Figure 145. Flow path and shear stress in the honeycomb pattern; PG = $3 \cdot 10^5$, $1 \cdot 10^3$ Pa/m.

Regarding recirculation paths at this larger Reynolds number, the reattachment to the hole bottom wall still prevents the creation of significant secondary flows in the stream-wise plane of the pattern at the smaller clearances. On the other hand, the intensified channeling effect of the flow promotes recirculation in several locations. There are at least

three pairs of counter rotating vortices in the horizontal plane, as shown in Figure 146(b), and a single pair that occupies the whole pattern in the horizontal plane, Figure 146(c).

As the clearance is increased, the counter rotating vortices become weaker but they are still present at the largest clearance. A single vortex is clearly identifiable in the spam-wise plane located closer to the lateral walls of the pattern, Figure 147(b), while a single pair still occupies the whole pattern in the horizontal plane, Figure 147(c).

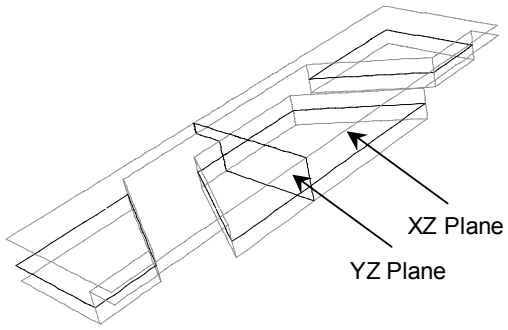


(a) Pattern plane locations

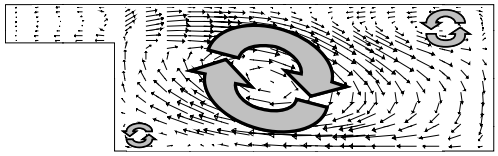

(b) YZ in-plane velocity vectors, Scale $0.0005/\overline{V}$

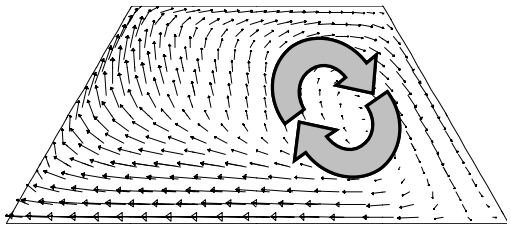

(c) XZ in-plane velocity vectors, Scale $0.0005/\overline{V}$

Figure 146. Recirculation paths in the honeycomb pattern, clearance = 176 μm, Re~380.

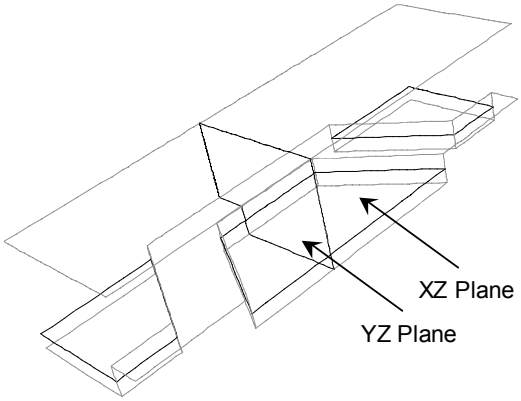


(a) Pattern plane locations

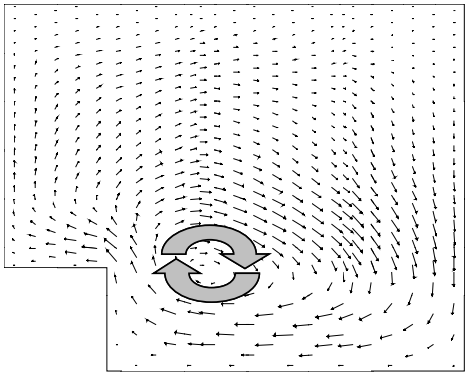

(b) YZ in-plane velocity vectors, Scale $0.0005/\overline{V}$

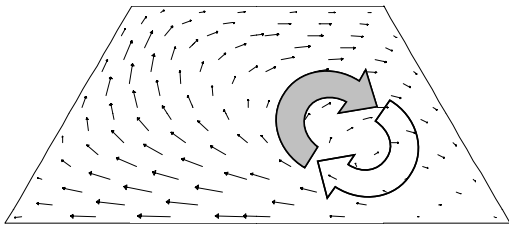

(c) XZ in-plane velocity vectors, Scale $0.0005/\overline{V}$

Figure 147. Recirculation paths in the honeycomb pattern, clearance = 1270 μm, Re~380.

As with previous patterns, Figure 148 presents the static pressure force ratio for the honeycomb pattern as a function of the Reynolds number for all clearances simulated. Following are the more relevant observations:

- At low Reynolds numbers, the static pressure force does not contribute significantly to the overall pressure gradient. Static pressure force ratios are roughly the same in all clearances with the exception of the 1270 µm value, becoming even negative at the lowest Reynolds number simulated.
- Static pressure force ratios increase with Reynolds number at any clearance.
- As the Reynolds number is increased, static pressure force ratios remain comparable in the smaller clearances, 176 and 254 µm, but they become significantly larger than the values of the remaining clearances. In other words, the proportion of the friction factor due to the static pressure forces factor increases as the clearance is reduced.

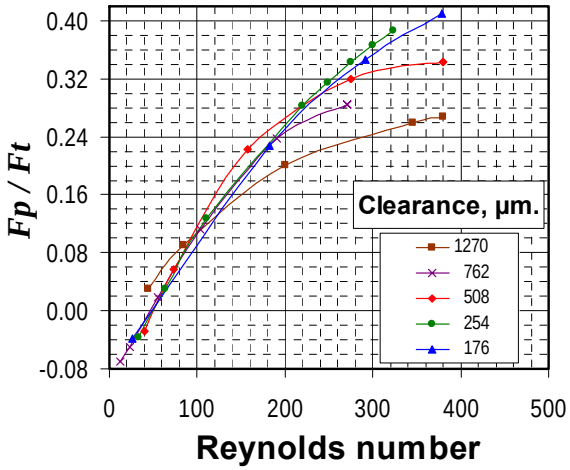


Figure 148. Stream-wise forces predicted proportion in the honeycomb pattern, laminar flow regime.

*5.1.4. Summary, cross pattern geometry discussion.*

The more relevant observations derived by comparing main flow features predicted in each pattern for laminar flow are the following:

- The flow moves sideways in the larger patterns, both round-holes and the honeycomb. This zigzag effect is stronger in the shallow round-hole, Figures 127(a) and (b), and the test clearance in the honeycomb, Figure 143(a). The effect is lessened by the round-hole depth, Figure 131(a), and by the increase in clearance in the honeycomb, Figure 143(b).
- The flow reattaches to all pattern walls in the shallow round-hole and all clearances in the honeycomb at low Reynolds number (below 100). Actually, a very small recirculation zone is predicted in the bottom corners of the leading face of each pattern, Figure 128(a) for the shallow round-hole, and Figure 143(c) and (d) for the honeycomb.
- Increasing Reynolds number and clearance lead to flow separation in all patterns. The effect is better depicted in the shallow round-hole, Figure 130(b), and the honeycomb, Figures 145(b) and (d). Although, separation per se is stronger in the deep round-hole, Figure 131 versus 127(b), and the isogrid, Figure 138 versus Figure 136.
- Predicted static pressure force ratios (Figure 133, round-hole; Figure 148, honeycomb; Figure 141, isogrid) reveal the following trends:
  - Ratios increase with Γ. Predictions in the isogrid (83%) are larger than in the honeycomb (60%). While predictions in the honeycomb are larger that those in the round hole (44%). In the round hole, the deep has larger ratios than the shallow.
  - Ratios increase more rapidly with Reynolds number in the isogrid pattern.
  - Ratios are similar in the smaller clearances of the isogrid and the honeycomb.
  - Ratios are below 50% in all cases, and they are particularly low at low Reynolds number (below 100). Therefore, the primary losses mechanism in all patterns under scrutiny is wall friction for the simulated range of Reynolds number.
- The friction factor is directly proportional to the clearance in the isogrid, Figure 135, and in the honeycomb, Figure 142.

In summary, friction factor predictions in pressure driven laminar flow (Poiseuille) in liquid annular seals or channels where one of the walls has been deliberately roughened with a periodic pattern indicate that either increasing the clearance or the Reynolds number in a particular pattern geometry leads lo larger friction factors. Indeed, the limiting solution in all cases appears to be the smooth channel flow solution. The concept of the limiting solution was studied by Adachi and Uehara [51] in a linear stability analysis of flow in a periodically grooved channel. Although the aspect ratio of the groove they analyzed is large compared to the aspect ratio of the isogrid and honeycomb patterns, their analysis reflects a similar flow behavior. As Reynolds increases, the flow 'dips' less into the groove. And in the limit of instability, the solution to the grooved channel is the plain channel itself.

In perspective, the presence of the roughness pattern in Poiseuille laminar flow leads to a significant reduction in friction factor. In contrast, several studies [32] on Couette laminar flow indicate that the drag on the flat moving wall increases by the presence of a deliberately roughened stationary wall. The most significant difference in the roughness patterns under consideration is the aspect ratio and the actual length. While the present research concentrated in shallow patterns that are very large in terms of the pattern depth and length to clearance ratio; the analysis by Arghir et al [32] concentrated in roughly square roughness with all dimensions comparable to the clearance of the channel. In author's opinion, it is worth exploring how very large patterns would affect drag and lift in shear driven flow.

## *5.2. Turbulent solutions*

Friction factor characteristics and numerical predictions for several roughness patterns in the turbulent regime are the core of the present research and have been discussed in detail in previous sections. In this section, predictions based on the hole-pattern geometry of Fayolle [8], for the largest clearance, are reviewed to evaluate how the hole depth influences the recirculation paths inside the round-hole and the proportion of the friction factor that is due to the static pressure force. Similarly, the predictions based on the patterns of Iwatsubo [36] and Kaneko [37] are analyzed to evaluate the effect of the clearance and orientation in both recirculation flow paths inside the patterns and the static pressure force ratio. The section ends with a summary reviewing how current 3-D results and original 2-D predictions [19] fit in the parametric analysis of grooved seals included in section 2.5.

### *5.2.1. The round-hole pattern of Fayolle [8].*

Figure 149 compares flow path lines in both patterns for a comparable Reynolds number. Path lines are colored by the actual velocity magnitude in the flow. In the shallow pattern case, flow velocities are considerably reduced as the flow enters the round-hole and reattaches to the bottom wall. The flow does not enter or dip significantly into the pattern hole as it flows by the deep hole, and velocities are somewhat reduced but not as much as in the shallow pattern. Indeed, the traditional strong cavity vortex fills the whole pattern; see Figure 149(b). In this Figure, path lines were created releasing particles from the periodic unit mid-plane, and all particles released inside the hole remain trapped in the pattern (note that the quarter holes located on the corners of the periodic unit do not have a single path line).

Flow reattachment to the round-hole walls is easily visualized in the wall shear stress predictions for the bottom wall of the periodic unit, Figure 150. In the shallow pattern case, the flow clearly reattaches to the forward region of the hole bottom wall, Figure 150(a). The contours only include positive values in the stream-wise flow direction and blank or non-colored zones indicate backflow, and there are no positive shear stresses values in the hole bottom wall of the deep pattern. Positive values on lateral walls are due to the recirculation in the pattern and not to the main flow reattaching to them.

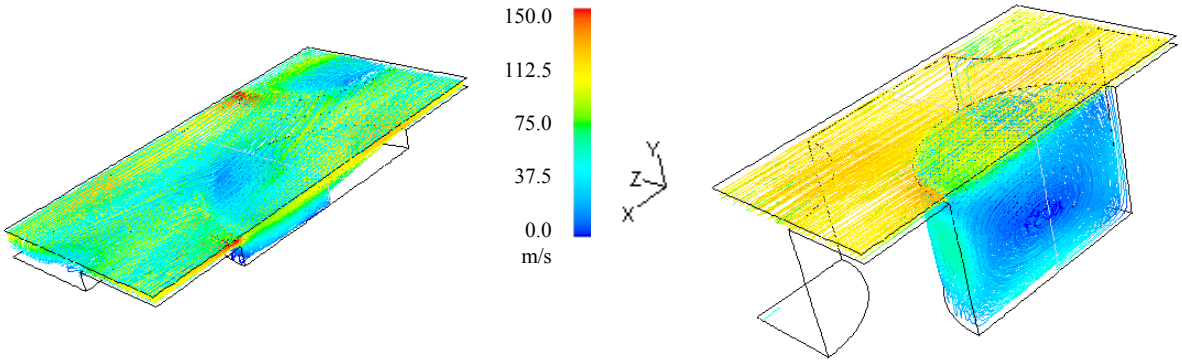


(a) Shallow round-hole. Flow Direction, X (b) Deep round-hole.

Figure 149. Flow path in the round-hole patterns of Fayolle [8], Re~$5.6 \cdot 10^4$, PG = $1.5 \cdot 10^9$, $1.0 \cdot 10^9$ Pa/m.

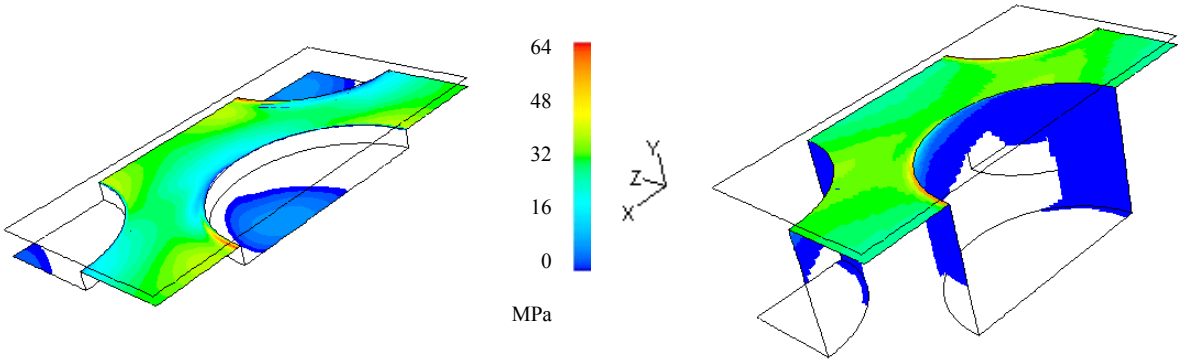


(a) Shallow round-hole. Flow Direction, X (b) Deep round-hole.

Figure 150. Bottom wall shear stresses (X direction) in the round-hole patterns, Re~$5.6 \cdot 10^4$.

The variability in the stream-wise velocity is more evident in Figure 151. Figures 151(a) and (b) compare stream-wise velocity contours in span-wise planes equally spaced along each periodic unit. In the shallow pattern, the flow appears to be channeled towards the center of the hole as it is being decelerated and reattaches to the bottom wall, Figure 151(c). While in the deep pattern, the stream-wise velocity is only affected significantly near the trailing edge, Figure 151(d), where the mean flow barely dips into the hole. A significant portion of the flow in the shallow pattern moves in a zigzag path as indicated by the span-wise velocity contours include in Figure 152(a). Span-wise velocities in this pattern are more than three times larger than the corresponding values in the deep pattern.

Regarding recirculation paths within the hole pattern, the partial reattachment to the bottom hole wall in the shallow pattern prevents the creation of the traditional strong stream-wise vortex typical of deeper cavities, Figure 153(b), although a small vortex still

exist in the leading edge of the hole, promoted by the mean flow separation on that hole edge. The partial reattachment of the flow promotes a strong vortex pair in the horizontal plane of the hole, Figure 153(c). Similarly, the zigzag effect also creates a strong vortex pair in the span-wise planes of the wider portion of the pattern, Figure 153(d).

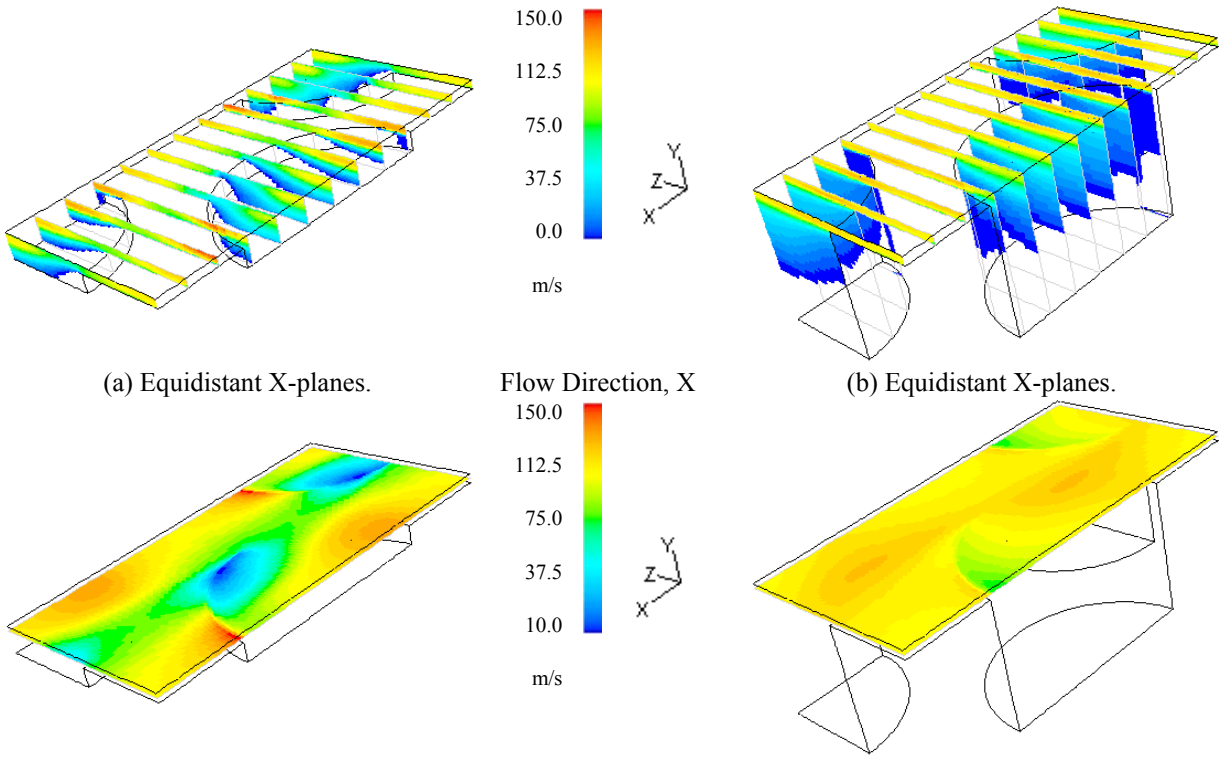


(a) Equidistant X-planes.

Flow Direction, X

(b) Equidistant X-planes.

(c) Mid-clearance plane. Shallow round-hole.

(d) Mid-clearance plane. Deep round-hole.

Figure 151. Stream-wise velocity in the round-hole patterns, Re~$5.6 \cdot 10^4$.

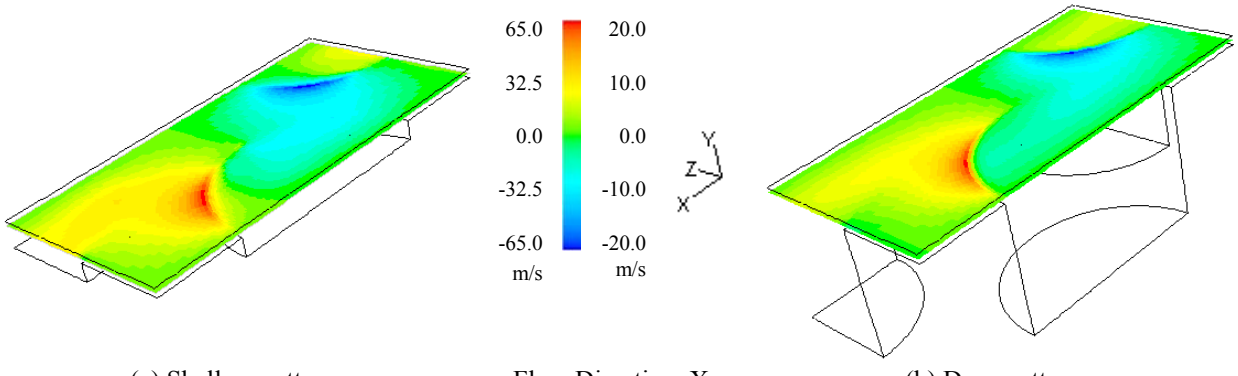


(a) Shallow pattern.

Flow Direction, X

(b) Deep pattern.

Figure 152. Span-wise velocity contours in the mid-clearance plane of round-hole pattern, Re~$5.6 \cdot 10^4$.

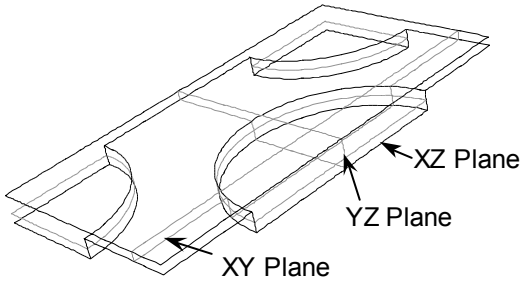


(a) Shallow geometry plane locations

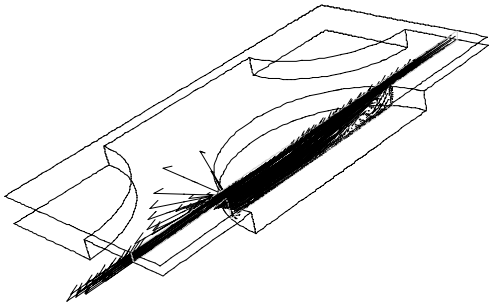

(b) XY in-plane velocity vectors, Scale $0.001/\overline{V}$

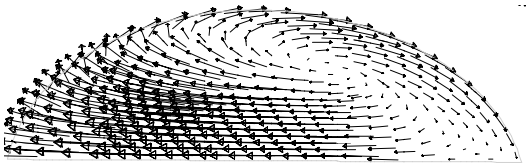

(c) XZ in-plane velocity vectors, Scale $0.001/\overline{V}$

(d) YZ in-plane velocity vectors, Scale $0.001/\overline{V}$

Figure 153. Recirculation paths in the shallow round-hole pattern, Re~$5.6 \cdot 10^4$.

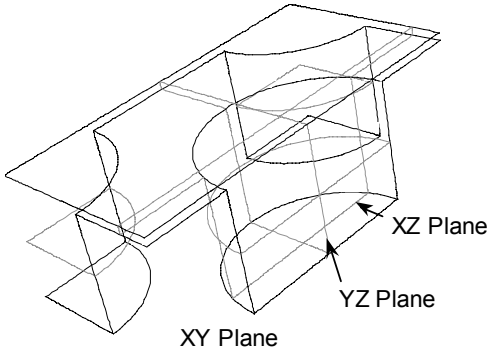


(a) Deep geometry plane locations

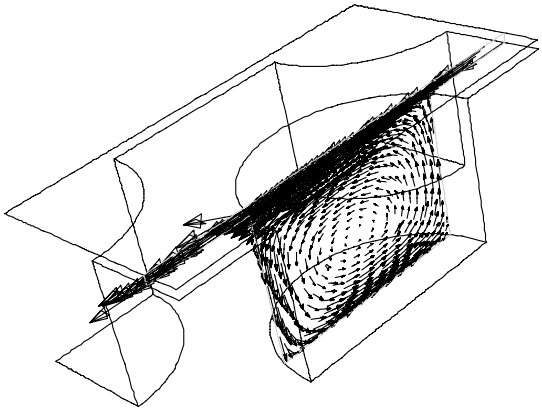

(b) XY in-plane velocity vectors, Scale $0.001/\overline{V}$

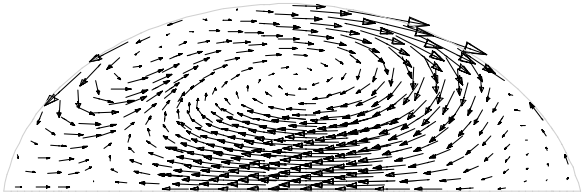

(c) XZ in-plane velocity vectors, Scale $0.005/\overline{V}$

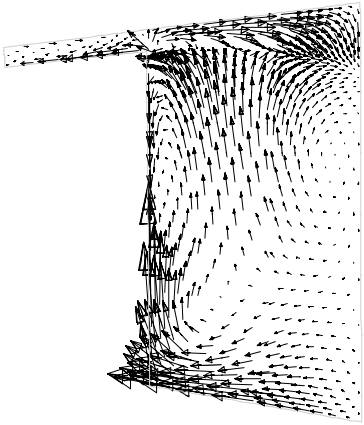

(d) YZ in-plane velocity vectors, Scale $0.005/\overline{V}$

Figure 154. Recirculation paths in the deep round-hole pattern, Re~$5.6 \cdot 10^4$.

In the deep pattern, the strongest vortex is the traditional cavity flow prevalent in all stream-wise planes, Figure 154(b). This strong vortex has 'embedded' several mild counter rotating pairs as shown in Figures 154(c) and (d) (Note that the scale is five time larger).

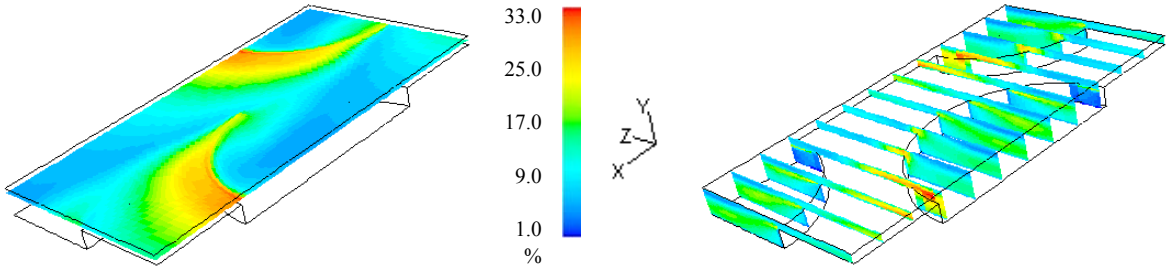


(a) Shallow geometry.

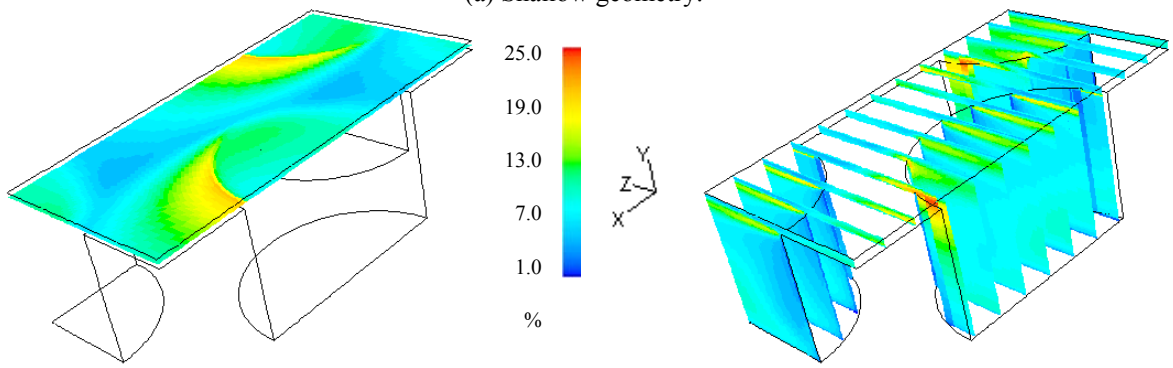


(b) Deep geometry.

Figure 155. Turbulence intensity levels in the round-hole patterns, X is the flow direction, Re~$5.6 \cdot 10^4$.

In Figure 155, turbulence intensity levels are compared in the mid-clearance plane and along several stream-wise planes in both patterns. Turbulence intensity levels in the shallow pattern are roughly 30% larger than those predicted in the deep pattern. The mass-weighted average intensity level is 55% larger (12.27% vs. 7.90%).

Lastly, Figure 156 presents the static pressure force ratio versus the Reynolds number for both shallow and deep patterns. In both cases, static pressure force ratios are above 50%, indicating that most of the friction factor is generated by the static pressure force imbalance in the hole pattern. Values in the shallow pattern are consistently larger than those in the deep pattern up to 23.4% in the Reynolds number flow range simulated.

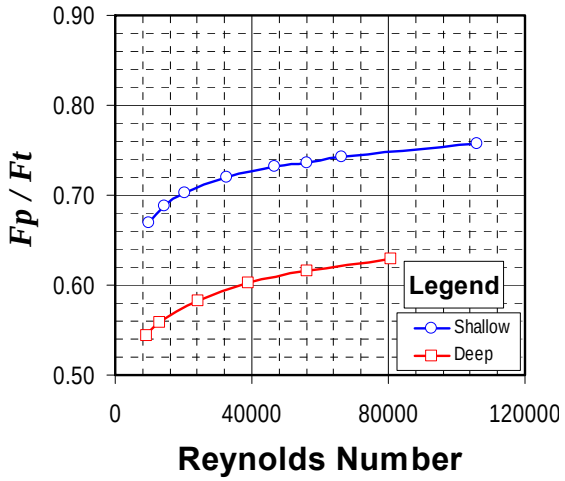


Figure 156. Stream-wise forces predicted proportion in the round-hole pattern, turbulent flow regime.

Figure 157 compares periodic static pressure distributions in both patterns. The local static pressure is roughly the same in the trailing side of both hole patterns. On the other hand, the local static pressure is considerably lower in the leading side of the shallow pattern. In spite of a considerably smaller integration area, the pressure difference among the two patterns results in a predicted pressure force for the shallow pattern roughly 70% larger than the corresponding value in the deep pattern.

Contrary to laminar results, the shallow round-hole pattern is predicted to consistently provide larger friction factors than the deep pattern in the single clearance under scrutiny (130 μm). The present analysis indicate that larger static pressure force ratios and turbulence intensity levels are responsible for this behavior.

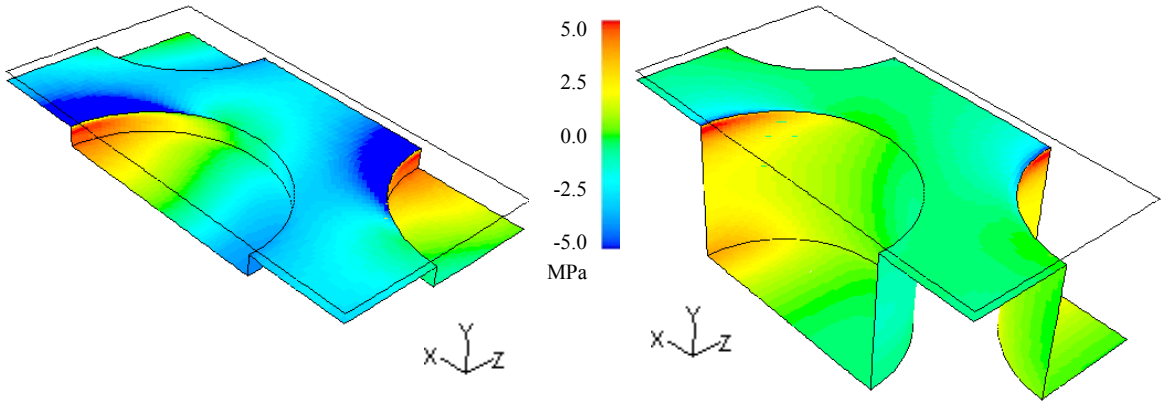


(a) Shallow pattern. Flow Direction, X (b) Deep pattern.

Figure 157. Periodic static pressure contours, round-hole patterns, Re~$5.6 \cdot 10^4$.

### *5.2.2. The isogrid pattern of Iwatsubo[36].*

Figure 158 compares flow path lines and stream-wise velocity contours in the test clearance (175 µm), the intermediate clearance (508 µm), and the largest clearance simulated (1270 µm), for the isogrid pattern at a comparable Reynolds number. Path lines are colored by the actual velocity magnitude in the flow. In all clearances, flow velocities are reduced by the presence of the pattern but the flow does not enter or dip significantly into the pattern as it flows by it. Path lines were created releasing particles from span-wise planes located atop the walls separating each pattern. There are only few lines inside the pattern in every case, an indication that the flow does not dip significantly into the pattern.

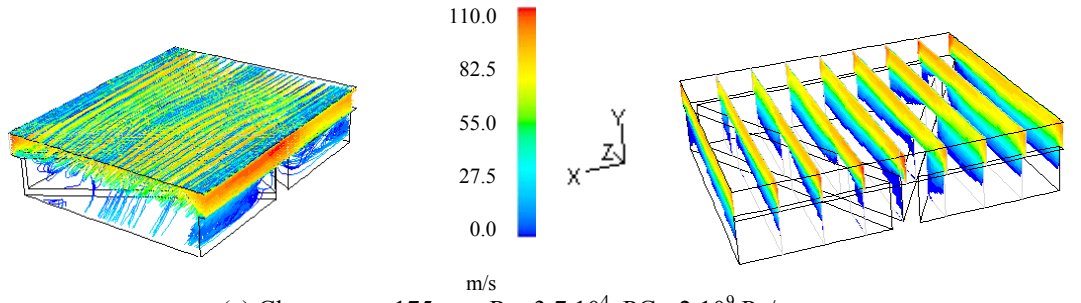


(a) Clearance = 175 µm, Re~$3.7 \cdot 10^4$, PG= $2 \cdot 10^9$ Pa/m.

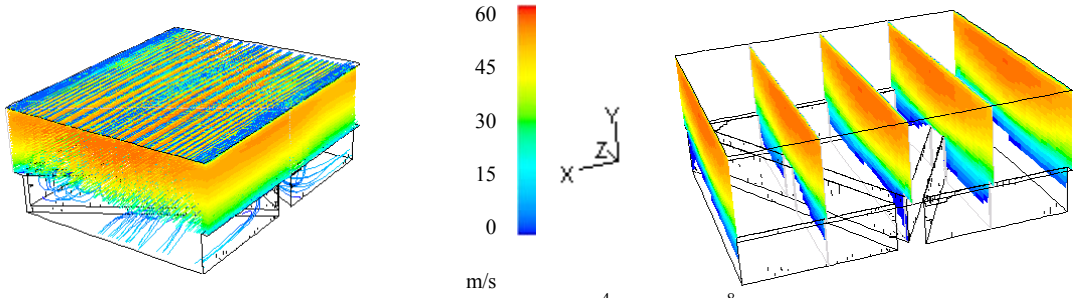


(b) Clearance = 508 µm, Re~$4.6 \cdot 10^4$, PG= $1 \cdot 10^8$ Pa/m.

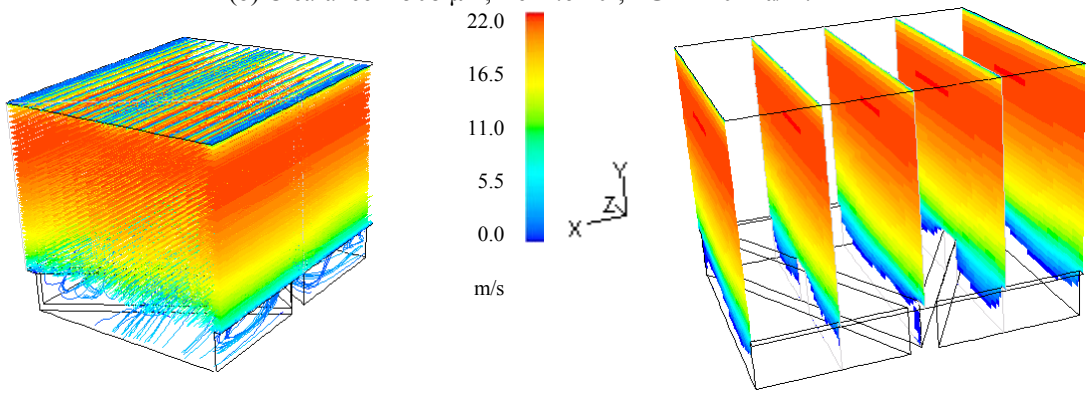


(c) Clearance = 1270 µm, Re~$4.5 \cdot 10^4$, PG= $5 \cdot 10^6$ Pa/m.

Path Lines Flow Direction, X Stream-wise velocity

Figure 158. Path lines and X-velocity contours, effect of the clearance, isogrid pattern, turbulent flow.

In the largest clearance, stream-wise velocity contours along the periodic unit are similar, there is a strong core flow in the upper mid-clearance that is basically two dimensional (no span-wise component). In the intermediate clearance, contours are also similar along stream-wise planes but the flow appears to be channeled towards the upper center of the clearance. In the test clearance (the smallest value simulated), contours are no longer similar along stream-wise planes as predictions indicate that larger flow velocities exist atop pattern corners.

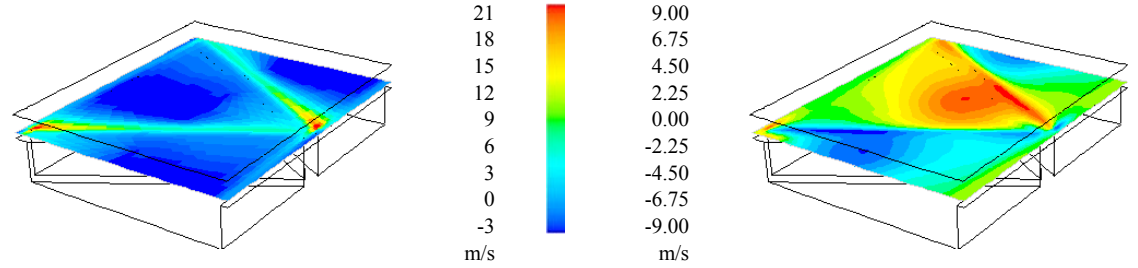


(a) Clearance = 175 µm, Re~$3.7 \cdot 10^4$, PG= $2 \cdot 10^9$ Pa/m.

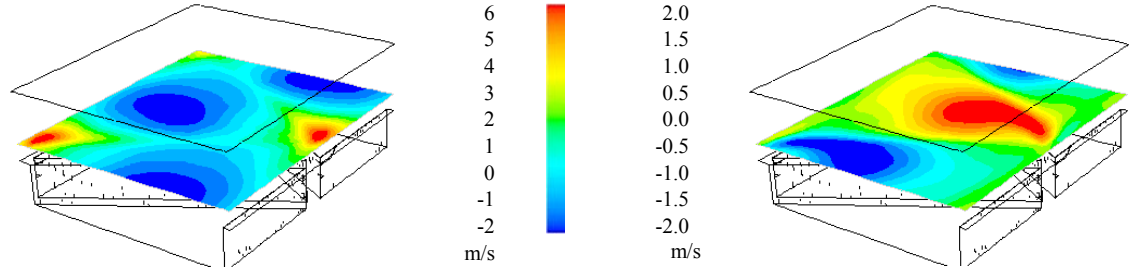


(b) Clearance = 508 µm, Re~$4.6 \cdot 10^4$, PG= $1 \cdot 10^8$ Pa/m.

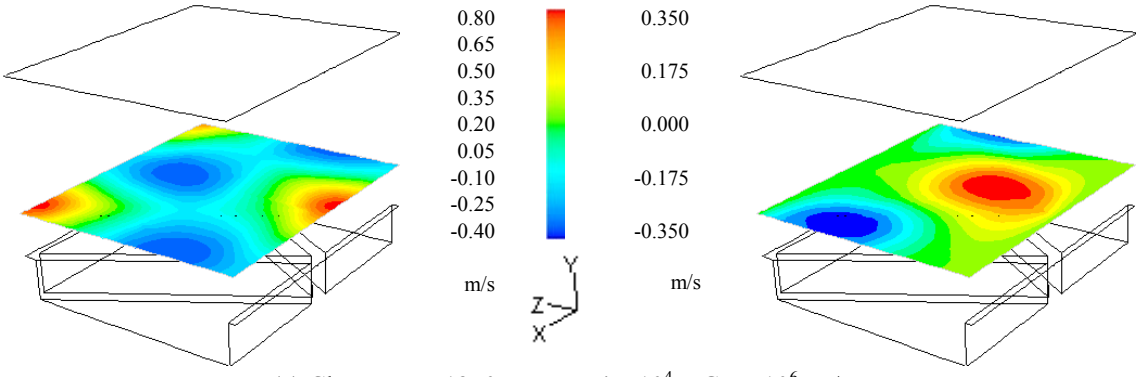


(c) Clearance = 1270 µm, Re~$4.5 \cdot 10^4$, PG= $5 \cdot 10^6$ Pa/m.

Vertical velocity at y=1/4·$C_r$ Flow Direction, X Span-wise velocity at y=1/4·$C_r$

Figure 159. Y and Z velocity contours, effect of the clearance, isogrid pattern, turbulent flow.

Similarly, Figure 159 compares vertical and span-wise velocity contours at horizontal planes located near the bottom clearance wall at a distance equivalent to 25% of the

clearance. Predicted vertical velocities exhibit a common behavior, downward velocity magnitude values (flow dipping slowly into the pattern) are much smaller than upward velocity magnitude values (flow 'accelerating' up in the trailing corner of each pattern). The span-wise contours shows that the flow going up in the trailing edge of each pattern, near the corners, promotes a zigzag path just as it was predicted for the shallow round-hole of Fayolle[8]. The effect appears to intensify as the clearance is reduced, contributing to the channeling effect observed in the stream-wise velocity components.

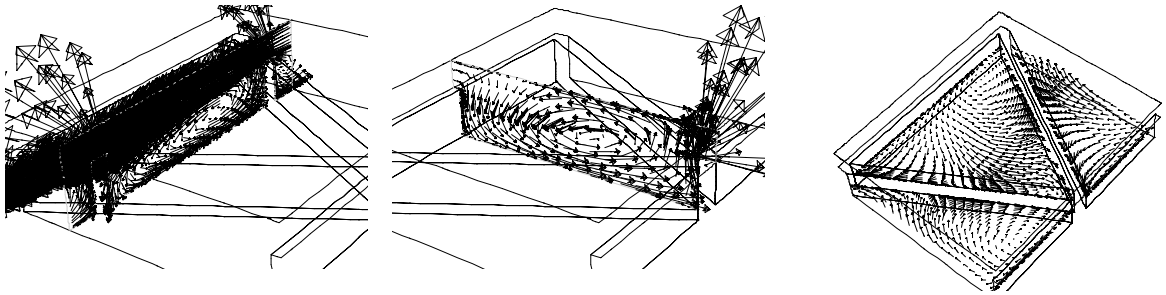

(a) Clearance = 175 μm, Re~$3.7 \cdot 10^4$ ($\overline{V}$ = 106.6 m/s), PG= $2 \cdot 10^9$ Pa/m.

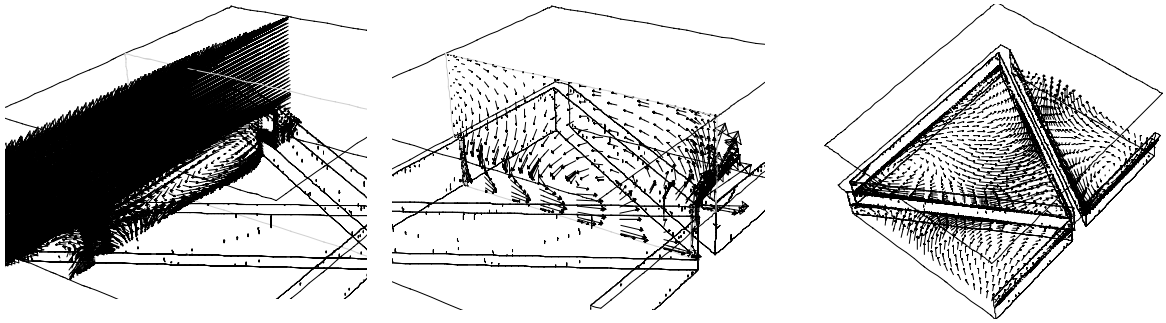

(b) Clearance = 508 μm, Re~$4.6 \cdot 10^4$ ($\overline{V}$ = 45.6 m/s), PG= $1 \cdot 10^8$ Pa/m.

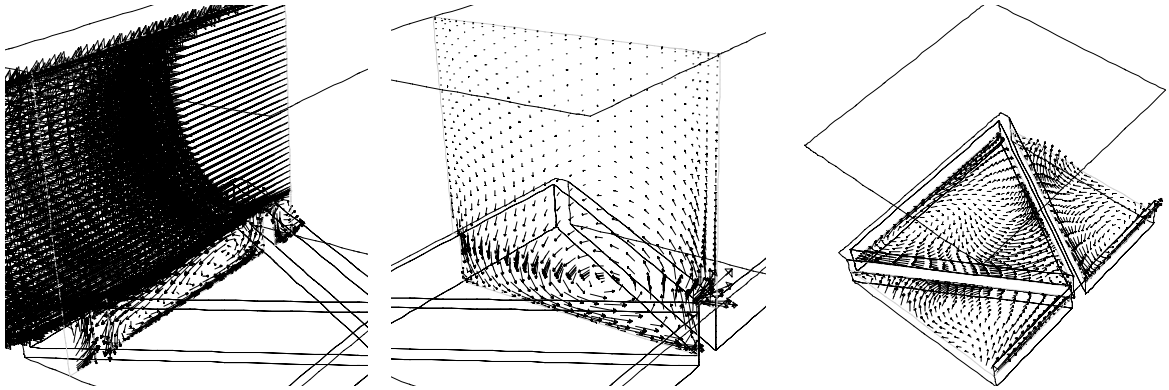

(c) Clearance = 1270 μm, Re~$4.5 \cdot 10^4$ ($\overline{V}$ = 17.8 m/s),, PG= $5 \cdot 10^6$ Pa/m.

Stream-wise plane (z=0.75·width), Scale $0.001/\overline{V}$ | Mid-length span-wise plane, Scale $0.002/\overline{V}$ | Mid-depth horizontal plane, Scale $0.001/\overline{V}$

Figure 160. Periodic unit velocity vectors, isogrid pattern, turbulent flow.

Regarding recirculation paths within the pattern, Figure 160 compares velocity vectors in three planes located at the same coordinates on each periodic unit. In the stream-wise plane, the traditional vortex or cavity flow is prevalent in all clearances, although is somewhat skewed in the smallest clearance, due to the dipping of the flow. Similarly, a counter clock wise single vortex is observed on the span-wise plane located at the widest portion of the pattern in all clearances. This vortex gets stronger as the clearance is reduced (the zigzag effect). Flow in the horizontal planes does not appear to have a consistent vortex path, most of the flow moves sideways toward the middle corner of the pattern as indicated by the span-wise vortexes. Nevertheless, a small clockwise vortex present in the trailing corner of the pattern at the larger clearances, disappears in the smallest clearance where a small counter clockwise is present in the leading corner of the pattern (vortex direction is established looking at the complete pattern in the center of each periodic unit).

Figure 161 compares turbulence intensity levels along several stream-wise planes and in the 25% clearance horizontal plane at the same three clearance values an Reynolds numbers. Turbulence intensity levels are comparable in the smaller clearances but reduce significantly at the largest clearance. Variability in turbulence levels increases as the clearance is reduced, and larger values are observed where the flow goes upward in the trailing edge of each pattern. Similarly, the mass-weighted average turbulence intensity level increases as the clearance is reduced (12.09% at 1270 μm, 13.64% at 508 μm, and 15.53% at 175 μm.)

Now, Figure 162 presents the static pressure force ratio versus the Reynolds number for all clearances simulated. In all cases the static pressure force ratio is well above 50%, indicating that most of the friction factor is generated by the static pressure force imbalance in the pattern. On the other hand, it is clear that the static pressure force ratio increases as the clearance is reduced, but values at the smaller clearances (175 and 254 μm) are comparable within 1%, while intermediate clearance (508 μm) values are consistently larger up to 6% than those predicted in the largest clearance (1270 μm).

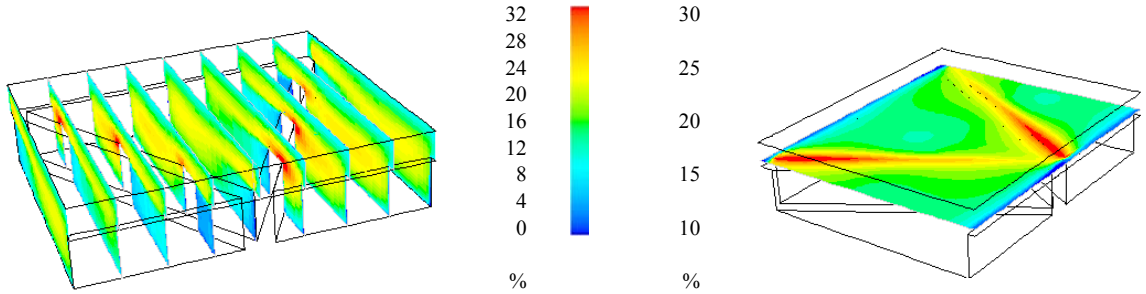


(a) Clearance = 175 µm, Re~$3.7 \cdot 10^4$, PG= $2 \cdot 10^9$ Pa/m.

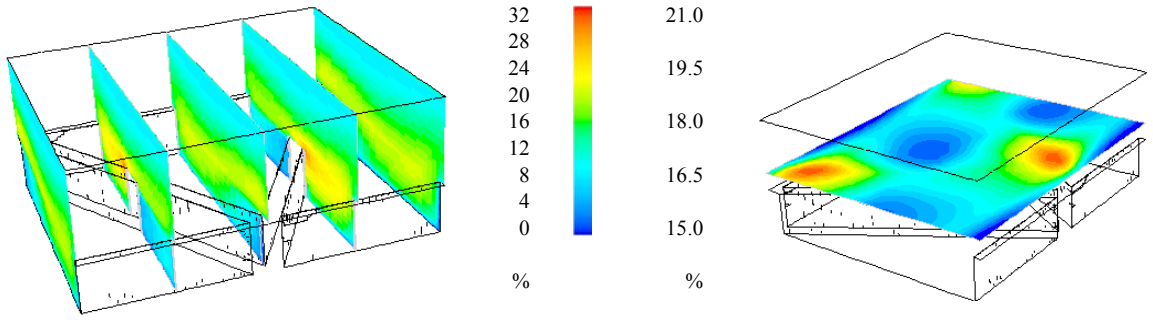


(b) Clearance = 508 µm, Re~$4.6 \cdot 10^4$, PG= $1 \cdot 10^8$ Pa/m.

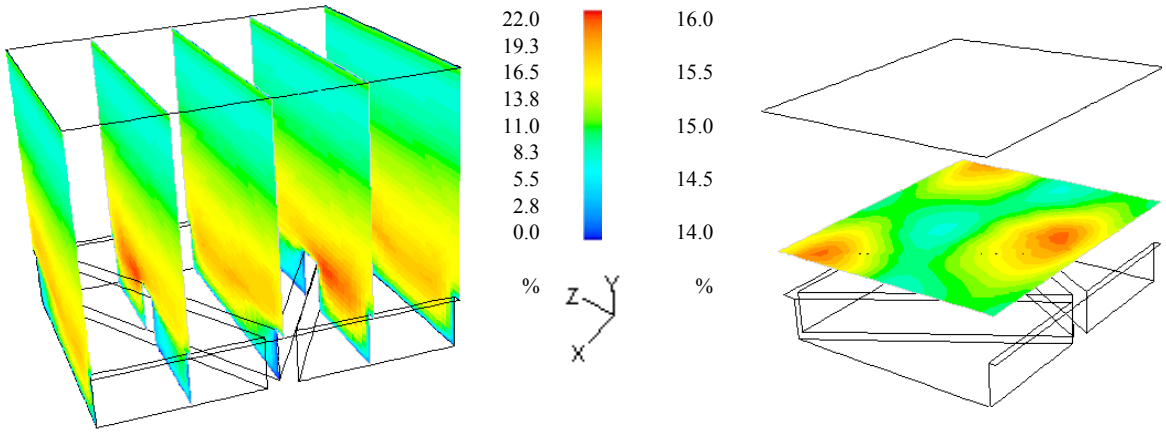


(c) Clearance = 1270 µm, Re~$4.5 \cdot 10^4$, PG= $5 \cdot 10^6$ Pa/m.

Equidistant X-planes  Flow Direction, X  Horizontal plane at y=1/4·$C_r$

Figure 161. Turbulence intensity, effect of the clearance, isogrid pattern, turbulent flow.

Lastly, Figure 163 compares wall shear stresses and periodic static pressure contours. Regardless of the actual magnitude, contours are relatively similar in all clearances. From the wall shear stresses distribution, it is clearly observed that the flow does not reattaches to the pattern walls (no positive values), and a small separation zone with recirculation exist in the horizontal walls near the corner of each pattern. Separation zones are also observed clearly in the pressure contours where the largest negative periodic static pressure is

predicted near corners in the trailing edge of each patter On the other hand, the ‘stagnation’ point (highest static pressure point on the trailing wall of the pattern) shifts slightly from the trailing wall upper center towards the upper vicinity of the trailing corner, as the clearance is reduced.

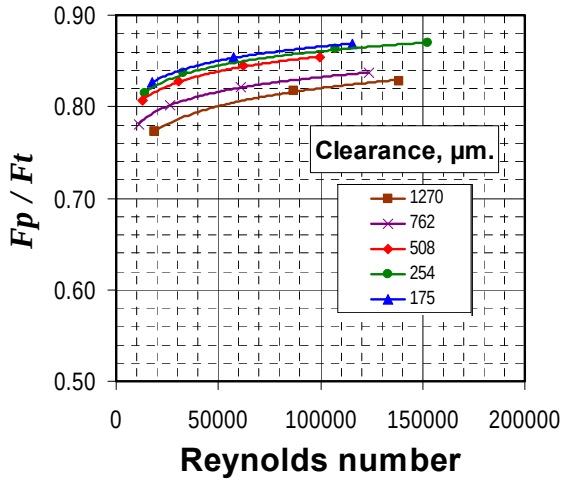


Figure 162. Stream-wise forces predicted proportion in the isogrid pattern, turbulent flow regime.

Contrary to laminar results, friction factor predictions in the turbulent regime indicate that the smallest clearance provide the largest resistance to flow, in other words, the traditional behavior is predicted, the friction factor reduces when the clearance is increased for Reynolds number larger than 10000, see section 3.3. The present analysis indicate that larger turbulence intensity levels and static pressure force ratios are responsible for this behavior.

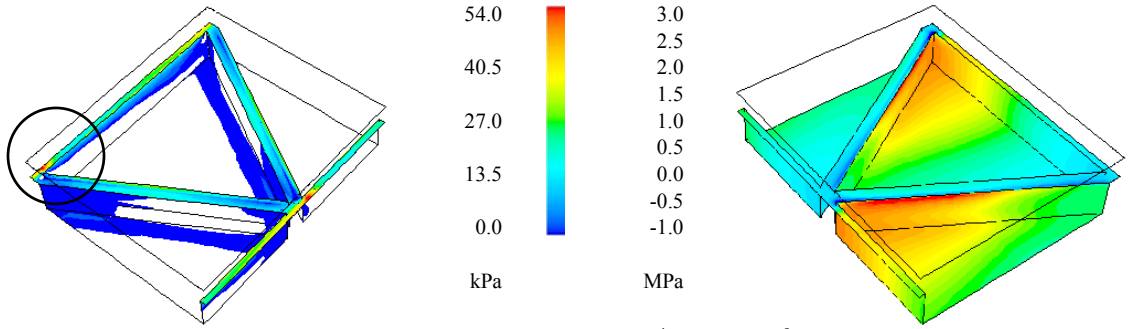


(a) Clearance = 175 µm, Re~$3.7 \cdot 10^4$, PG= $2 \cdot 10^9$ Pa/m.

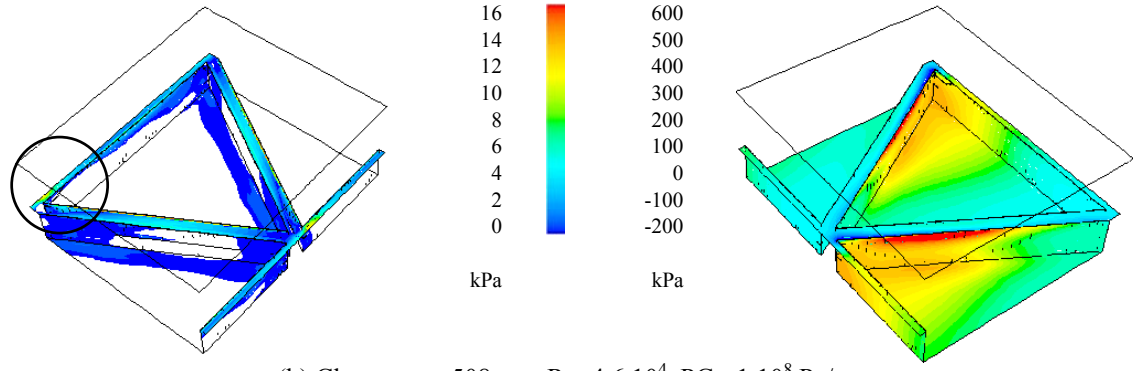


(b) Clearance = 508 µm, Re~$4.6 \cdot 10^4$, PG= $1 \cdot 10^8$ Pa/m.

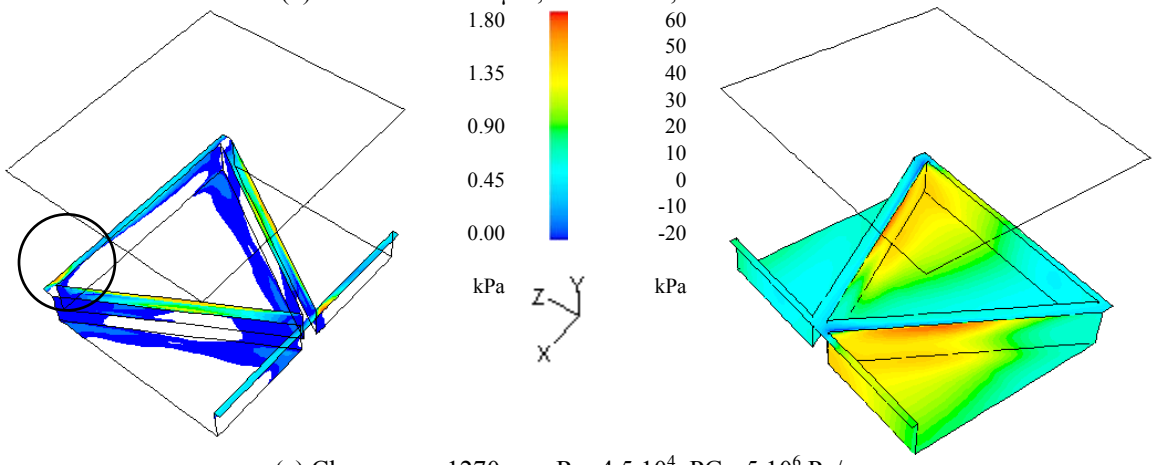


(c) Clearance = 1270 µm, Re~$4.5 \cdot 10^4$, PG= $5 \cdot 10^6$ Pa/m.

Wall shear stress (x-direction) Flow Direction, X Periodic static pressure

Figure 163. Bottom wall shear stresses and pressure contours, isogrid pattern, turbulent flow.

### *5.2.3. The honeycomb pattern of Kaneko[37].*

Figure 164 compares flow path lines and stream-wise velocity contours in the test clearance (176 µm), the intermediate clearance (508 µm), and the largest clearance simulated (1270 µm), for the honeycomb pattern at a comparable Reynolds number. Path lines are colored by the actual velocity magnitude in the flow.

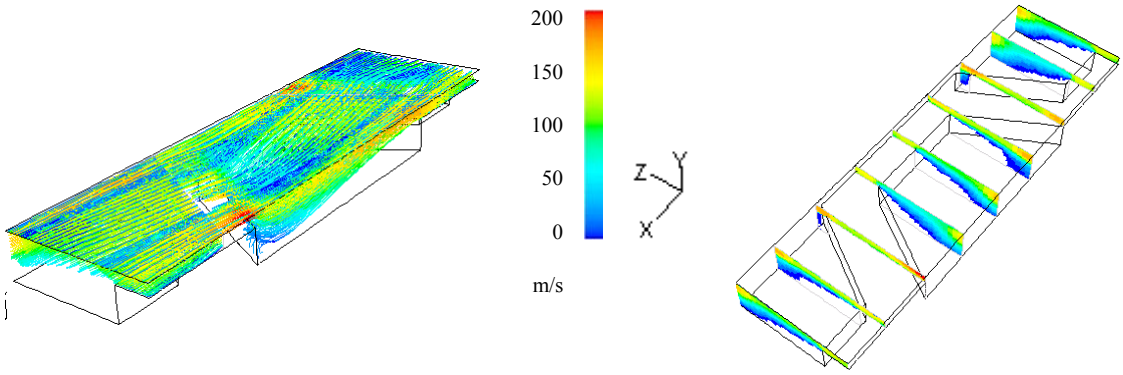


(a) Clearance = 176 µm, Re~$4.4 \cdot 10^4$, PG= $2 \cdot 10^9$ Pa/m.

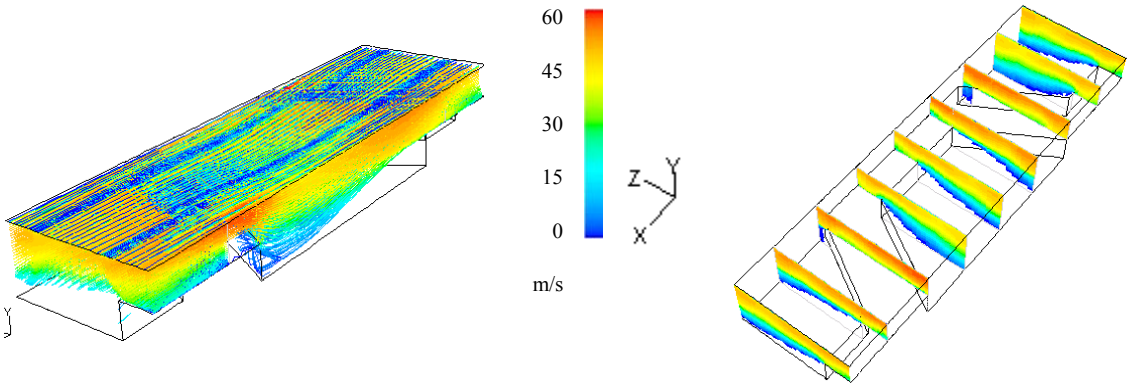


(b) Clearance = 508 µm, Re~$4.6 \cdot 10^4$, PG= $1 \cdot 10^8$ Pa/m.

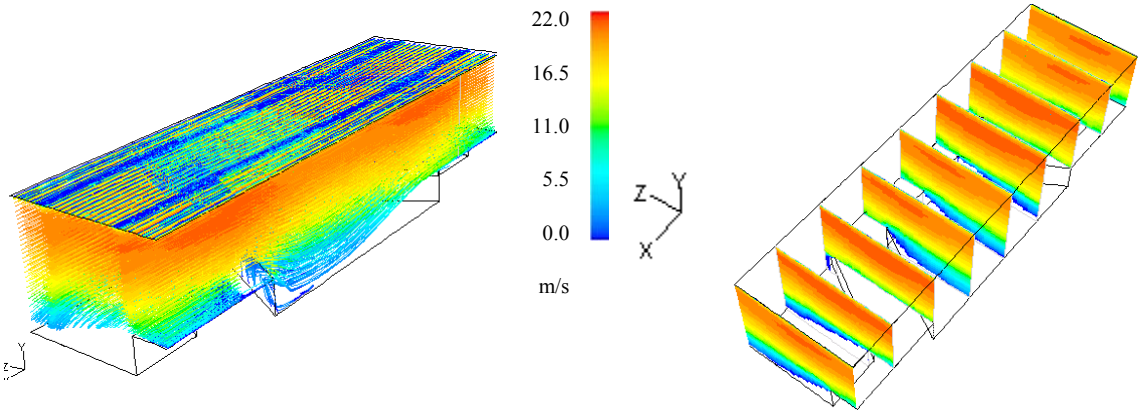


(c) Clearance = 1270 µm, Re~$4.3 \cdot 10^4$, PG= $5 \cdot 10^6$ Pa/m.

Path Lines  Flow Direction, X  Stream-wise velocity

Figure 164. Path lines and X-velocity contours, effect of the clearance, honeycomb pattern, turbulent flow.

In all clearances, flow velocities are significantly reduced by the presence of the pattern and the flow does dip considerably into the pattern in all clearances. Path lines were created releasing particles from span-wise planes located atop the walls separating each pattern. It is clear that the amount of dipping increases with clearance as the flow appears to reattached to the bottom in the intermediate and largest clearance. Similarly, stream-wise velocity contours along the periodic unit are not similar within the same clearance, and vary considerably depending on the actual value. The core flow in the upper mid-clearance that is basically two dimensional (no span-wise component) is considerably reduced in the largest clearance case. In the intermediate clearance, contours indicate that velocity reduces significantly but somewhat uniformly in the widest portion of the pattern. On the other hand, the flow appears entirely channeled towards the center of the pattern in the test clearance (the smallest value simulated), as larger velocities are predicted near the stream-wise symmetry planes of the periodic unit.

Similarly, Figure 165 compares vertical and span-wise velocity contours at horizontal planes located near the bottom clearance wall at a distance equivalent to 25% of the clearance. Predicted vertical velocities exhibit a common behavior, downward velocity magnitude values (flow dipping into the pattern) are much smaller than upward velocity magnitude values (flow ‘accelerating’ up in the trailing wall of each pattern). Span-wise contours shows that the flow going up in the trailing edge of each pattern, also promotes a zigzag path just as it has been predicted for the shallow round-hole of Fayolle[8] and the isogrid pattern of Iwatsubo [36]. The effect appears to intensify as the clearance is reduced, contributing to the channeling effect observed in the stream-wise velocity components.

Regarding recirculation paths within the pattern, Figure 166 compares velocity vectors in three planes located at the same coordinates on each periodic unit. In the stream-wise plane, the traditional vortex or cavity flow is virtually inexistent in all clearances. The significant dipping of the flow generates two weak vortexes in this plane located in both leading and trailed edges of the pattern, promoted by the mean flow separation on the former and the sudden change of direction due to flow impingement in the latter. These vortexes appear to loose strength as the clearance is decreased. Similarly, a couple of clock-wise single vortexes are observed in the span-wise plane located at the widest portion of the

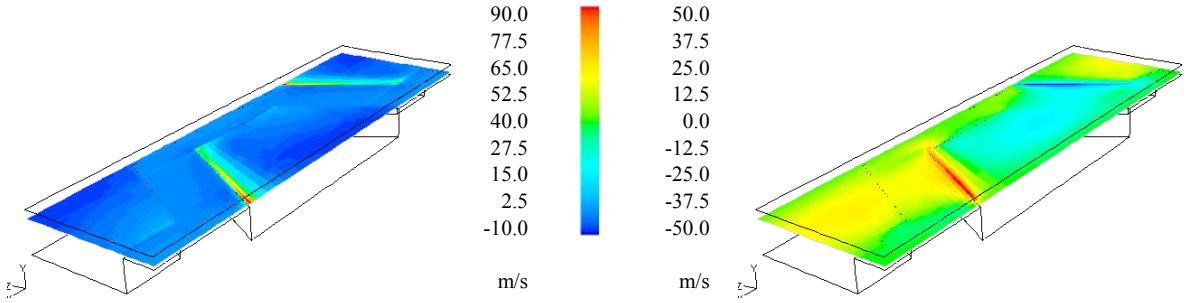


(a) Clearance = 176 µm, Re~$4.4 \cdot 10^4$, PG= $2 \cdot 10^9$ Pa/m.

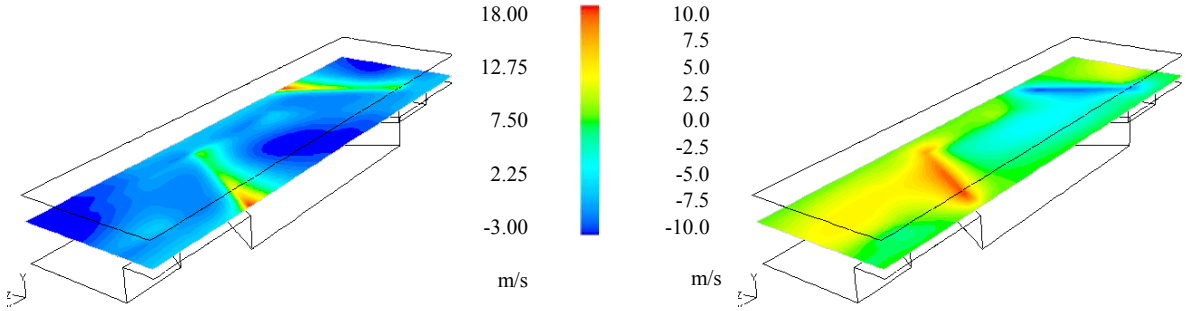


(b) Clearance = 508 µm, Re~$4.6 \cdot 10^4$, PG= $1 \cdot 10^8$ Pa/m.

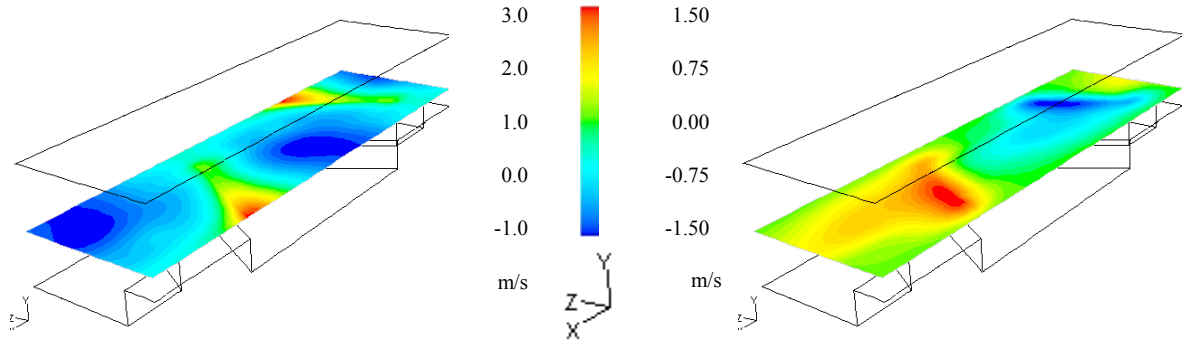


(c) Clearance = 1270 µm, Re~$4.3 \cdot 10^4$, PG= $5 \cdot 10^6$ Pa/m.

Vertical velocity at y=1/4·$C_r$ Flow Direction, X Span-wise velocity at y=1/4·$C_r$

Figure 165. Y and Z velocity contours, effect of the clearance, honeycomb pattern, turbulent flow.

pattern in all clearances. These vortexes get stronger as the clearance is reduced (the zigzag effect). The larger vortex is located inside the pattern located near the lateral walls, while a weak vortex exists within the clearance adjacent to the one located inside the pattern. On the other hand, the large dipping of the flow creates a single pair of counter rotating vortices in the horizontal plane of the pattern (clock-wise rotation in the half pattern shown). The strength and size of this vortex pair appear to increase as the clearance is reduced. (Vortex direction is established looking at each reference plane in the periodic unit).

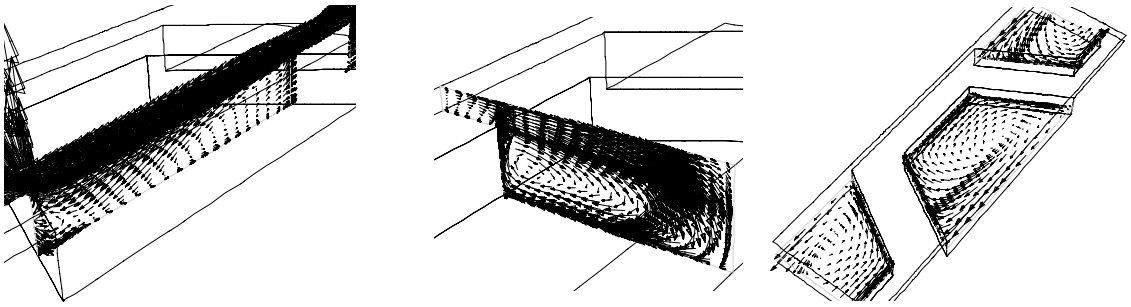

(a) Clearance = 176 μm, Re~$4.4 \cdot 10^4$ ($\overline{V}$ = 128.2 m/s), PG= $2 \cdot 10^9$ Pa/m.

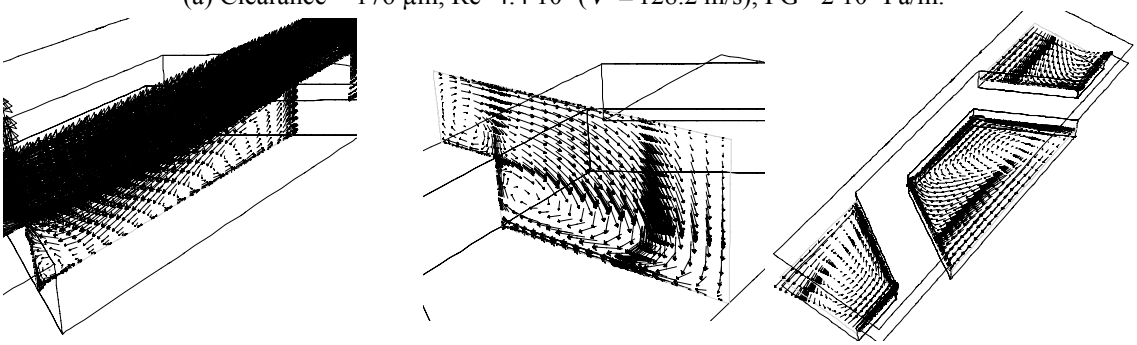

(b) Clearance = 508 μm, Re~$4.6 \cdot 10^4$ ($\overline{V}$ = 46.1 m/s), PG= $1 \cdot 10^8$ Pa/m.

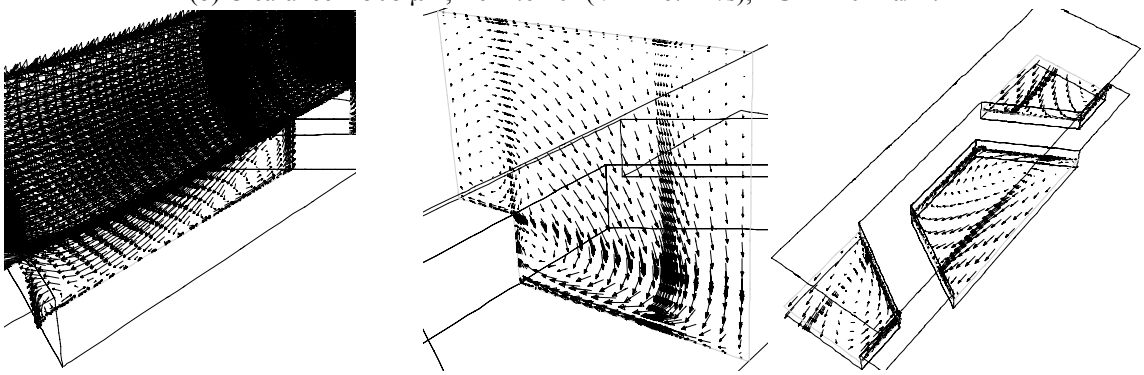

(c) Clearance = 1270 μm, Re~$4.3 \cdot 10^4$ ($\overline{V}$ = 17.4 m/s),, PG= $5 \cdot 10^6$ Pa/m.

Stream-wise plane (z=0.25·width), Scale $0.001/\overline{V}$ | Mid-length span-wise plane, Scale $0.002/\overline{V}$ | Mid-depth horizontal plane, Scale $0.001/\overline{V}$

Figure 166. Periodic unit velocity vectors, honeycomb pattern, turbulent flow.

Figure 167 compares turbulence intensity levels along several stream-wise planes and in the 25% clearance horizontal plane. Turbulence intensity levels are comparable in all clearances, although variability increases as the clearance is reduced, with larger values predicted in the trailing edge of the pattern where the mean flow goes upward coming out of the pattern. On the other hand, mass-weighted average turbulence intensity levels have a peculiar behavior; values are larger in the intermediate clearance of 508 μm (13.98%), while average levels are reduced in the test clearance, 176 μm (12.37%), and the largest

clearance simulated, 1270 µm (13.01%). In other words, mass-weighted average turbulence intensity levels have a maximum or 'plateau' at the intermediate clearance, 508 µm.

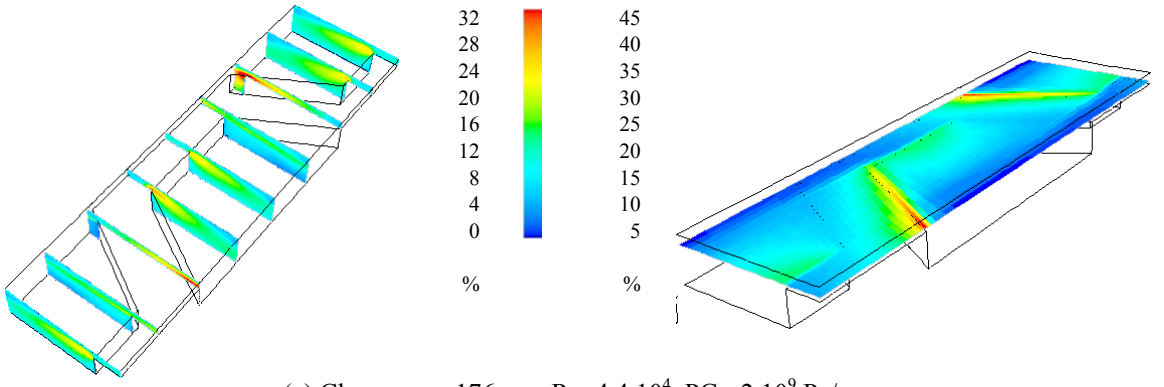


(a) Clearance = 176 µm, Re~$4.4 \cdot 10^4$, PG= $2 \cdot 10^9$ Pa/m.

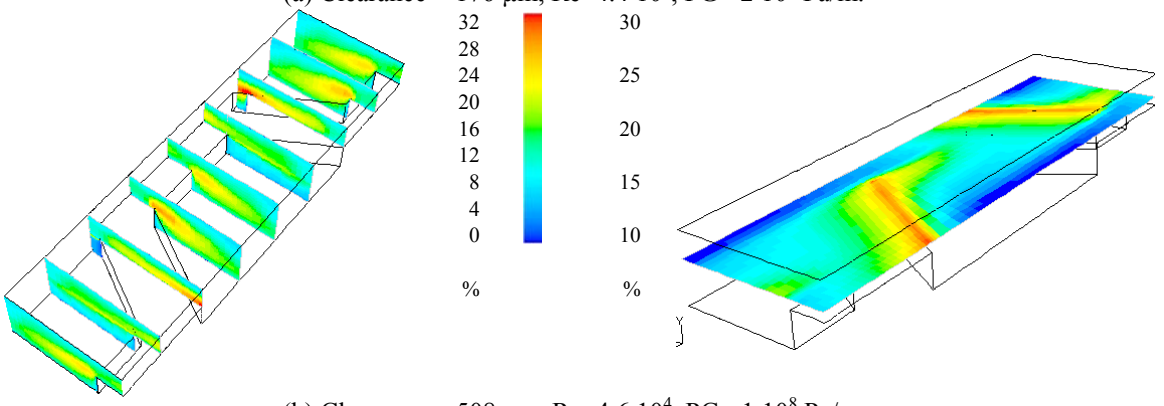


(b) Clearance = 508 µm, Re~$4.6 \cdot 10^4$, PG= $1 \cdot 10^8$ Pa/m.

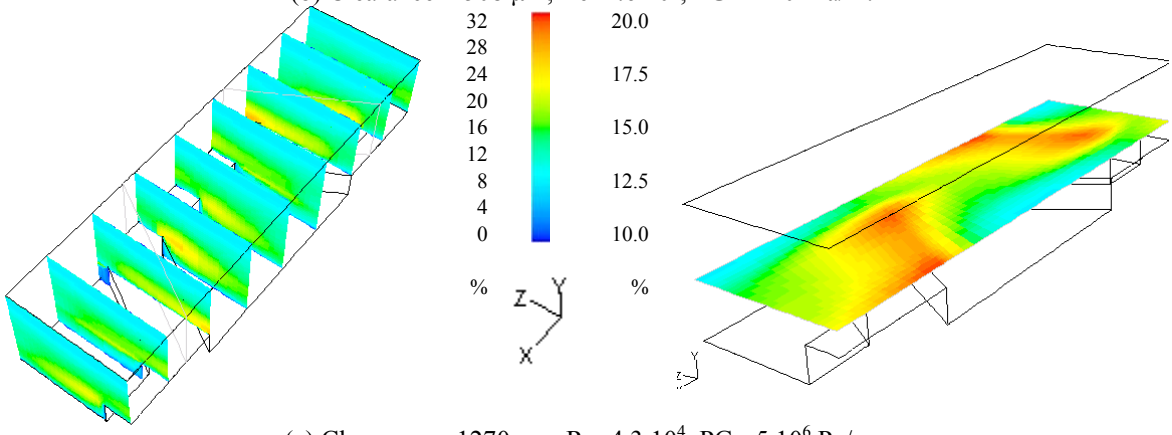


(c) Clearance = 1270 µm, Re~$4.3 \cdot 10^4$, PG= $5 \cdot 10^6$ Pa/m.

Equidistant X-planes Flow Direction, X Horizontal plane at y=1/4·$C_r$

Figure 167. Turbulence intensity, effect of the clearance, honeycomb pattern, turbulent flow.

Now, Figure 168 presents the static pressure force ratio versus the Reynolds number for all clearances simulated. In all cases the static pressure force ratio is well above 50%,

indicating that most of the friction factor is generated by the static pressure force imbalance in the pattern. On the other hand, values appear to have a maximum at the intermediate clearance of 508 µm, although values in all smaller clearances (176 to 762 µm) are comparable within 1%, while values in the largest clearance simulated (1270 µm) values are consistently lower up to 4%.

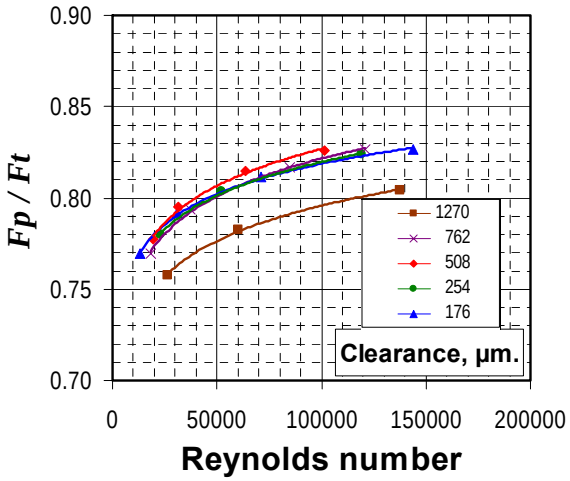


Figure 168. Stream-wise forces predicted proportion in the honeycomb pattern, turbulent flow regime.

Lastly, Figure 169 compares wall shear stresses and periodic static pressure contours. Regardless of the actual magnitude, contours are relatively similar in all clearances. In spite of dipping considerable inside the pattern at all clearances, the flow does not reattaches to the pattern bottom wall in any case, there are no positive values in the wall shear stresses distribution (in contrast to enhanced wall treatment predictions, wall functions results indicate that the flow reattaches to the bottom wall in all clearance cases). In addition, large separation zones with recirculation are predicted in the horizontal walls near the trailing edge of each pattern at all clearances. Separation zones are also clearly observed in the pressure contours where the largest negative periodic static pressure is predicted in the trailing edge of each pattern. On the other hand, the 'stagnation' point (highest static pressure point on the trailing wall of the pattern) clearly shifts from the upper center of the pattern trailing walls towards the center corner and down inside the pattern, as the clearance is reduced.

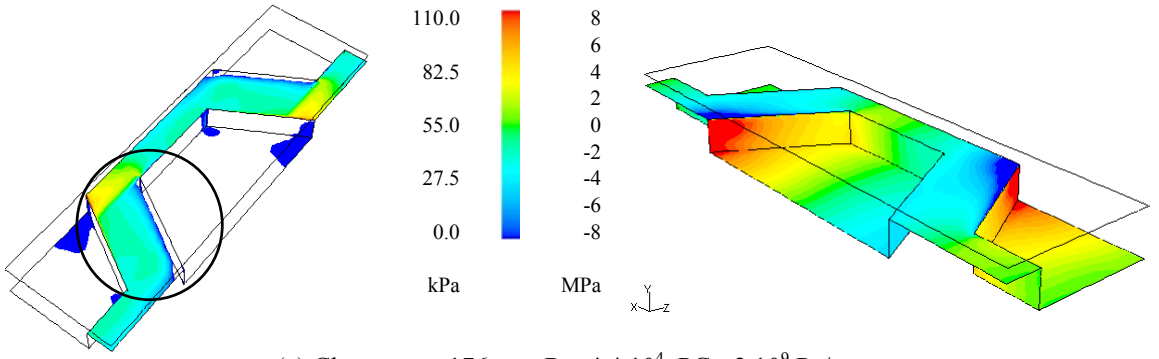


(a) Clearance = 176 µm, Re~$4.4 \cdot 10^4$, PG= $2 \cdot 10^9$ Pa/m.

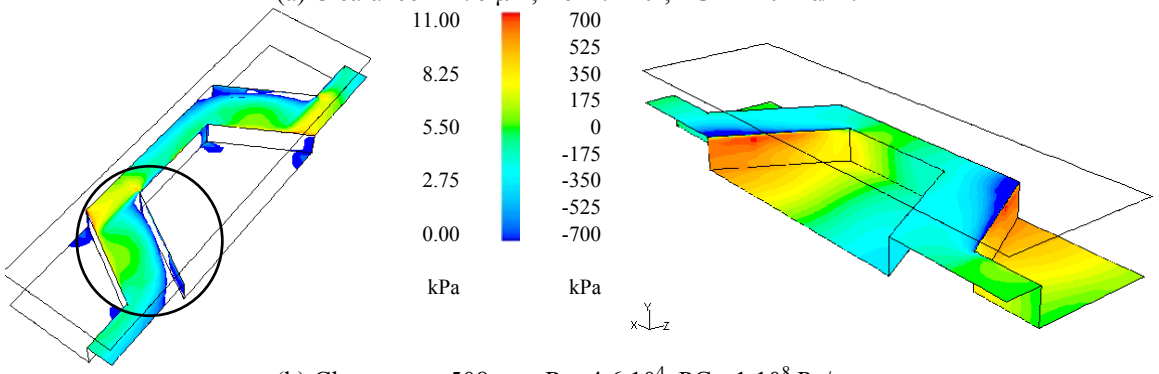


(b) Clearance = 508 µm, Re~$4.6 \cdot 10^4$, PG= $1 \cdot 10^8$ Pa/m.

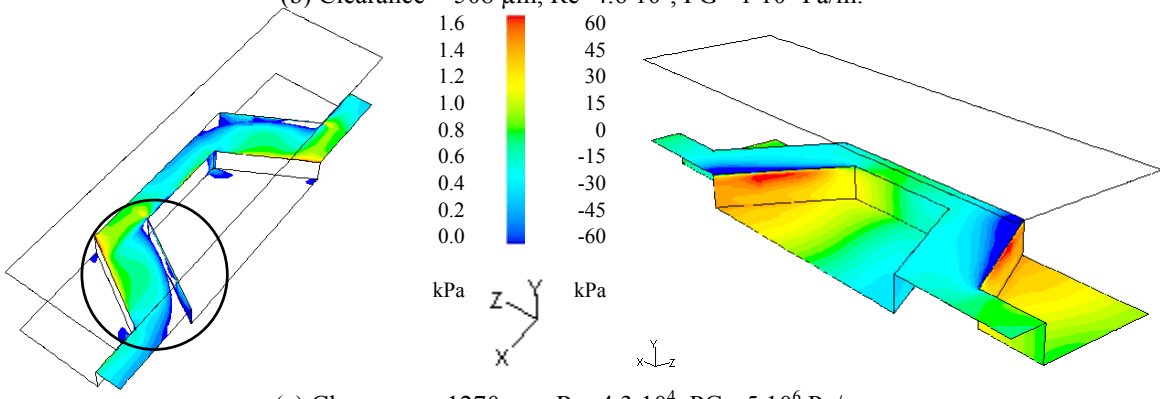


(c) Clearance = 1270 µm, Re~$4.3 \cdot 10^4$, PG= $5 \cdot 10^6$ Pa/m.

Wall shear stress (x-direction) Flow Direction, X Periodic static pressure

Figure 169. Bottom wall shear stresses and pressure contours, honeycomb pattern, turbulent flow.

Contrary to laminar results, friction factor predictions in the turbulent regime indicate that the intermediate clearance provide the largest resistance to flow, in other words, a 'plateau' like behavior is predicted. Predicted friction factors increase with clearances, reaching a maximum at the intermediate clearance, and reduces when the clearance is increased further, exhibiting the traditional behavior. The present analysis indicate that mass-weighted average turbulence intensity levels and static pressure force ratios are larger at this intermediate clearance and are responsible for this behavior.

### *5.2.4. Effect of the pattern orientation.*

As presented in section 3.5, friction factor predictions are significantly affected by the mean flow direction in the honeycomb pattern of Kaneko[37] while deviation in predictions in the isogrid pattern of Iwatsubo[36] are either comparable or smaller than the numerical uncertainty. First, flow features in the predictions based on the isogrid pattern are compared to evaluate whereas similarities in friction factor predictions correlate to any particular behavior. Secondly, flow predictions in the honeycomb pattern are reviewed to explore whereas significantly different flow features could explain the predicted sensitivity.

Starting with the isogrid pattern, Figure 170 compares stream-wise velocity contours along each periodic unit, and vertical and span-wise velocity contours at horizontal planes located near the bottom clearance wall at a distance equivalent to 25% of the clearance, 175 μm. In both directions, stream-wise velocities are reduced by the presence of the patterns but overall their magnitudes are comparable. A significant different feature is the 'spreading' of the velocity into the patterns (contours only include positive values so any blank portion on any plane indicate backward flow). In the original direction, the backward flow occupies most of the pattern as indicated by the zero velocity lines (end of the blue spectrum in the color code) that are somewhat parallel to the bottom of the pattern. On the other hand, the flow spreads out towards laterals walls of the pattern with the flat leading edge, while the flow appears to be channeled towards the center of the flat trailing edge pattern.

In the case of predicted vertical velocities, they exhibit an already described common behavior, downward velocity magnitude values that are much smaller than the upward magnitudes values. In both direction, the flow 'accelerates' up in the trailing corners of each pattern. Similarly, span-wise contours shows that the flow going up in the trailing corners of each pattern, also promotes a zigzag path in both directions, although velocity magnitudes are larger in the counter flow direction but only in the vicinity of the patterns with corners in the trailing side. In contrast, span-wise velocity variations appear to spread out in most of the pattern in the original flow direction.

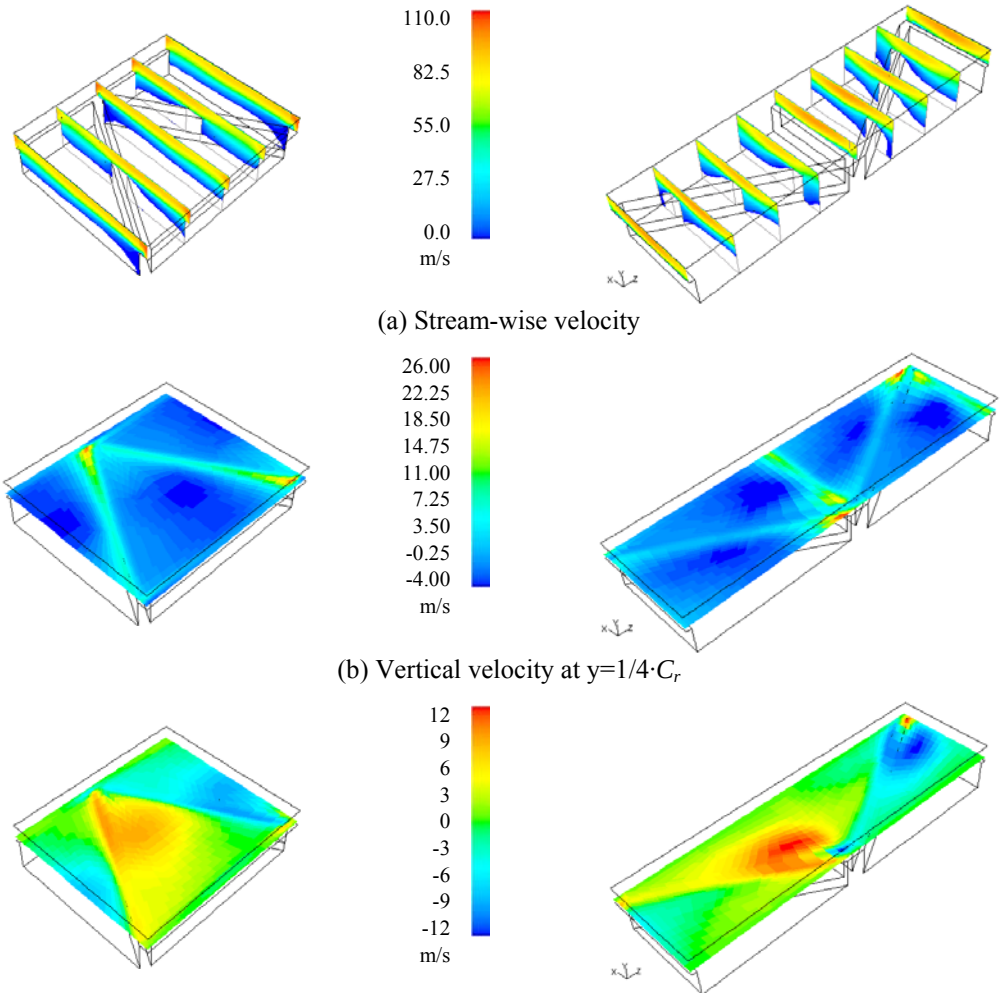


Figure 170. Velocity contours, effect of the orientation, Clearance = 175 µm, isogrid pattern, turbulent flow.

Similarly, Figure 171 compares velocity contours of the three components in both periodic units for the intermediate clearance. Likewise, stream-wise velocities are reduced by the presence of the patterns but overall magnitudes are comparable, although at this clearance in easier to visualize that the core flow concentrates in the center of the patterns 'avoiding' the corners in either case. The spreading of the velocity into each pattern at this larger clearance is roughly the same. Vertical and span-wise velocities also exhibit the behavior described above, much larger upward velocity values in trailing pattern corners, with stronger but concentrated zigzag effect in the counter flow direction.

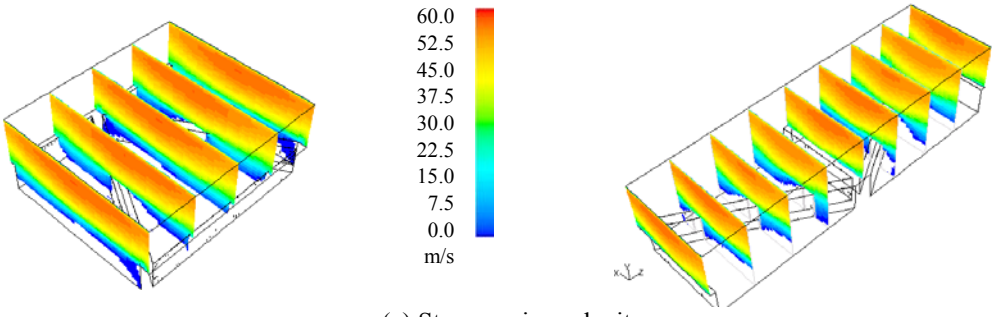


(a) Stream-wise velocity

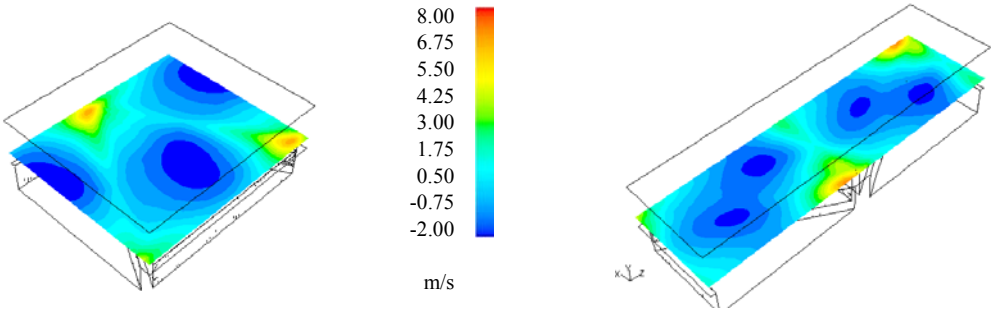


(b) Vertical velocity at y=1/4·$C_r$

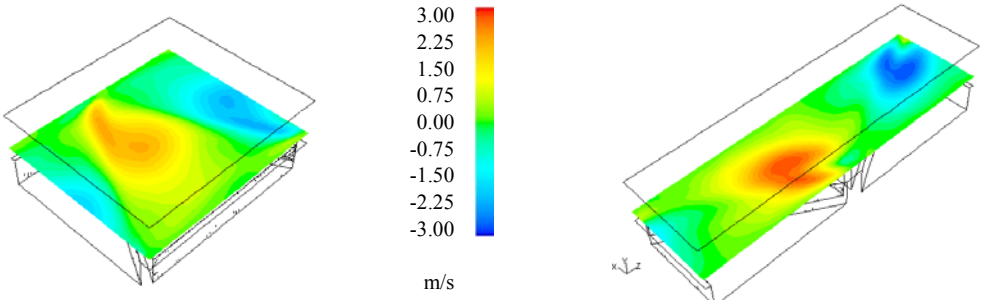


(c) Span-wise velocity

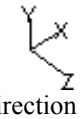


PG


Original flow direction (X), Re~$4.56 \cdot 10^4$ $1 \cdot 10^8$ Pa/m. Counter Flow direction (Z), Re~$4.50 \cdot 10^4$

Figure 171. Velocity contours, effect of the orientation, Clearance = 508 µm, isogrid pattern, turbulent flow.

Regarding recirculation paths within each pattern, Figure 172 compares velocity vectors in several planes (plane locations shown on the isometric views) on each periodic unit at the smallest clearance. As already discussed in previous sections, the traditional vortex or cavity flow is prevalent and skewed due to dipping in the stream-wise planes of the pattern with the original orientation. On the other hand, stream-wise vortexes are not well defined in the counter flow direction, where the flow dips significantly in the pattern with the flat trailing edge, but just barely in the one with the flat leading edge. This behavior is explained while observing the vortexes in the mid-depth planes. While in the original direction, the

flow appears only to move sideways with a weak vortex present in the leading corner of each pattern, there is a strong pair of counter rotating vortexes (indeed the strongest) on each pattern of the counter flow direction. While the flow dipping promotes the vortex pair in the flat trailing edge pattern, the 'cornering' of the flow creates a large backflow in the bottom of the pattern with the flat leading edge. Lastly, while the single span-wise vortex occupies the entire pattern width in the original flow direction, stronger vortexes are localized near the lateral walls in both patterns of the counter flow direction. These vortexes have the same direction, so while in one pattern they promote flow towards the walls (flat leading edge), they prevent such flow in the other pattern (flat trailing edge), explaining the peculiar behavior described in the analysis of the stream-wise velocity.

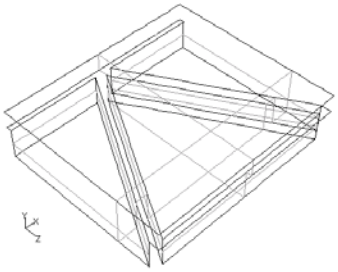

Stream-wise plane (z=0.75·width),
Scale $0.0005/\overline{V}$

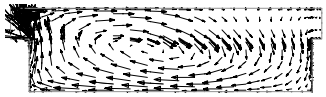

Mid-length span-wise plane,
Scale $0.001/\overline{V}$

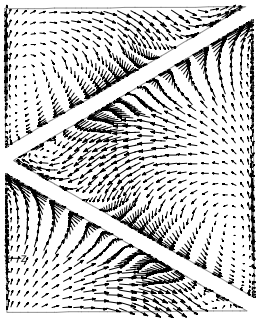

Mid-depth horizontal plane,
Scale $0.001/\overline{V}$

(a) Original flow direction, Re~$2.58\cdot10^4$ ($\overline{V}$ = 75.0 m/s), PG = $1\cdot10^9$ Pa/m.

Stream-wise plane (symmetry, x=width),
Scale $0.0005/\overline{V}$

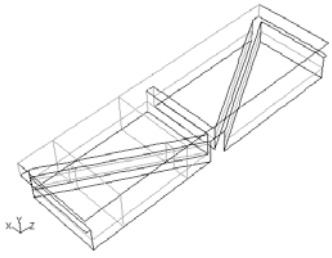

Span-wise plane (z=0.125·length),
Scale $0.001/\overline{V}$

Span-wise plane (z=0.375·length),
Scale $0.001/\overline{V}$

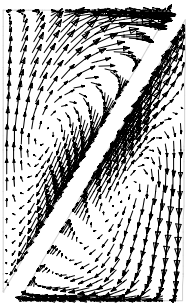

Mid-depth horizontal plane,
Scale $0.001/\overline{V}$

(b) Counter flow direction, Re~$2.61\cdot10^4$ ($\overline{V}$ = 75.8 m/s), PG = $1\cdot10^9$ Pa/m.

Figure 172. Velocity vectors, effect of the orientation, Clearance = 175 μm, isogrid pattern, turbulent flow.

In the case of the intermediate clearance, Figure 173, the flow dipping is considerable reduced as the clearance is increased in the original flow direction (already mentioned in section 5.2.2), and the stream-wise plane recirculation vortex is clearly established, with the localized weak horizontal vortex shifted from the trailing to the leading corner of each pattern (there are also smaller vortexes on the middle corners). Similarly, the flow paths inside each pattern remain comparable in the counter flow direction, with the flow dipping also reduced considerably at this larger clearance.

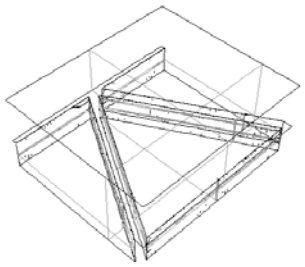

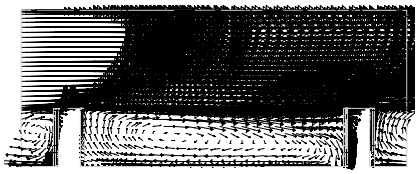

Stream-wise plane (z=0.75·width), Scale $0.0005/\overline{V}$

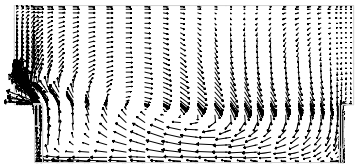

Mid-length span-wise plane, Scale $0.001/\overline{V}$

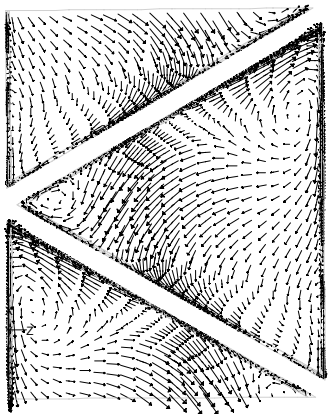

Mid-depth horizontal plane, Scale $0.001/\overline{V}$

(a) Original flow direction, Re~$4.56\cdot10^4$ ($\overline{V}$ = 45.6 m/s), PG = $1\cdot10^8$ Pa/m.

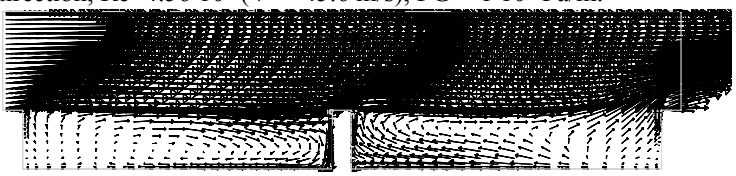

Stream-wise plane (symmetry, x=width), Scale $0.0005/\overline{V}$

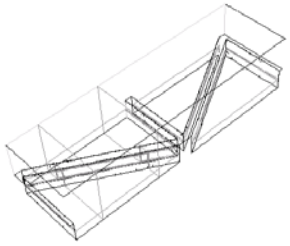

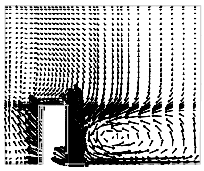

Span-wise plane (z=0.125·length), Scale $0.001/\overline{V}$

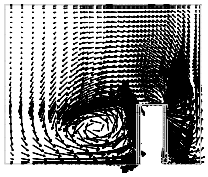

Span-wise plane (z=0.375·length), Scale $0.001/\overline{V}$

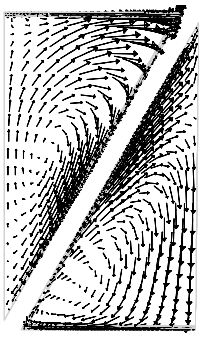

Mid-depth horizontal plane, Scale $0.001/\overline{V}$

(b) Counter flow direction, Re~$4.50\cdot10^4$ ($\overline{V}$ = 45.0 m/s), PG = $1\cdot10^8$ Pa/m.

Figure 173. Velocity vectors, effect of the orientation, Clearance = 508 μm, isogrid pattern, turbulent flow.

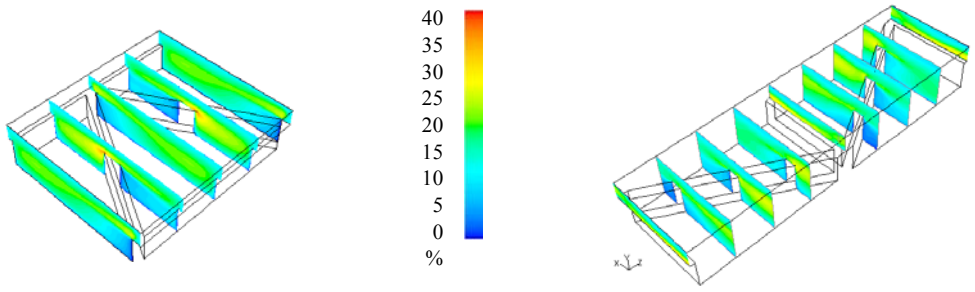


Equidistant stream-wise planes

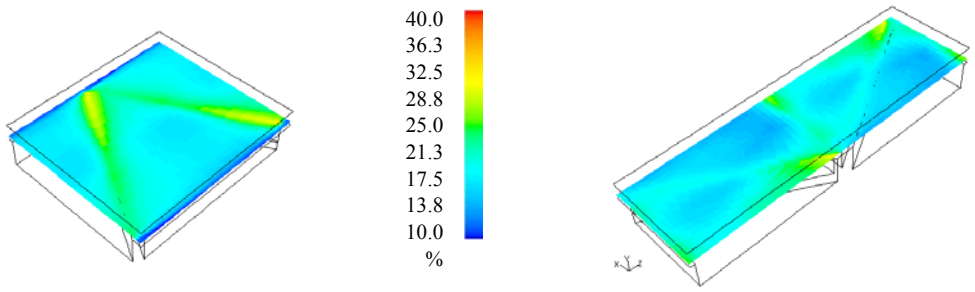


Vertical plane at y=1/4·$C_r$

Re~$2.58 \cdot 10^4$ . Re~$2.61 \cdot 10^4$

(a) Clearance = 175 µm, PG = $1 \cdot 10^9$ Pa/m.

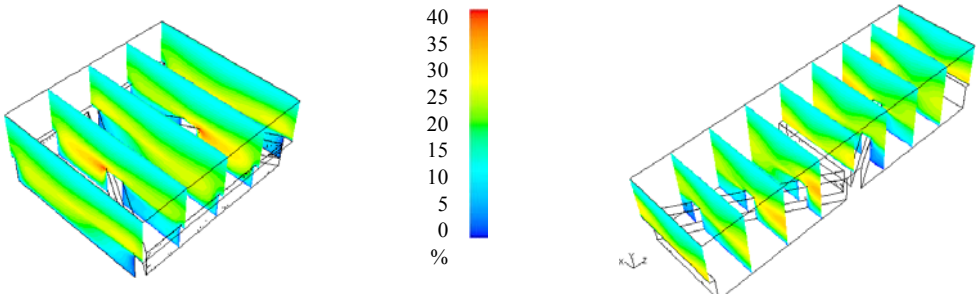


Equidistant stream-wise planes

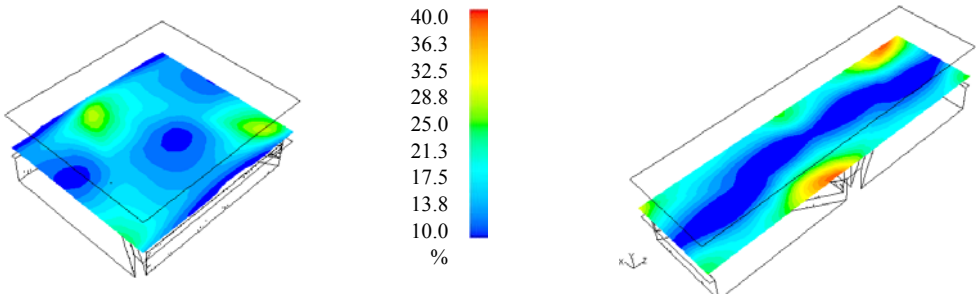


Vertical plane at y=1/4·$C_r$

Re~$4.56 \cdot 10^4$ Re~$4.50 \cdot 10^4$

(b) Clearance = 508 µm, PG = $1 \cdot 10^8$ Pa/m.


Original flow direction (X),


Counter Flow direction (Z),

Figure 174. Turbulence intensity, effect of the orientation and clearance, isogrid pattern, turbulent flow.

Figure 174 compares turbulence intensity levels in both flow directions along several stream-wise planes and the 25% clearance horizontal plane of both clearances. Turbulence intensity levels are comparable in both flow directions at the smaller clearances, with larger values in the 'spreading' of the shear flow into the patterns, and maximum levels predicted in the trailing edge and walls of each pattern, where the flow goes upward. Contrary to predictions in the original flow direction, variability in turbulence levels increases with clearance in the counter flow direction, where a stream-wise path of 'low' turbulence is clearly present in the horizontal planes, with larger maximum values in the trailing corner of the flat leading edge pattern, Figure 174 (b). On the other hand, mass-weighted average turbulence intensity levels maintain the same trend, they increase as the clearance is reduced, although actual magnitude and changes are smaller in the counter flow direction (13.45% at 508 μm, and 14.07% at 175 μm, versus 13.64% and 15.53% in the original direction.)

Now, Figure 175 presents static pressure force ratios versus the Reynolds number in both clearances. At the smallest clearance, the static pressure force ratio is identical (within 0.36%) in both flow directions. On the other hand, this proportion is slightly larger in the original flow direction at the intermediate clearance by up to 2%. This behavior is consistent in the flow range simulated.

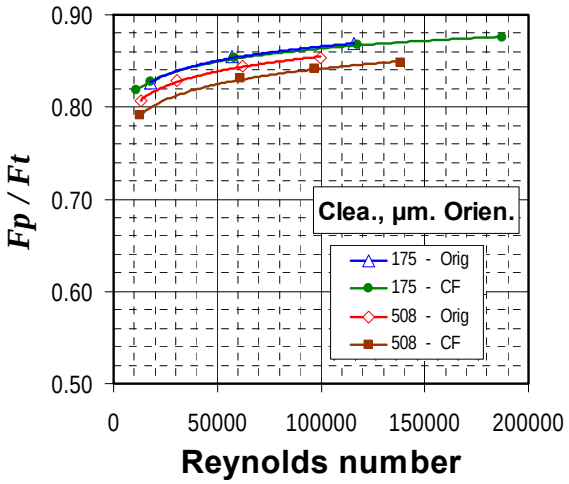


Figure 175. Stream-wise forces predicted proportion in the isogrid pattern, turbulent flow regime.

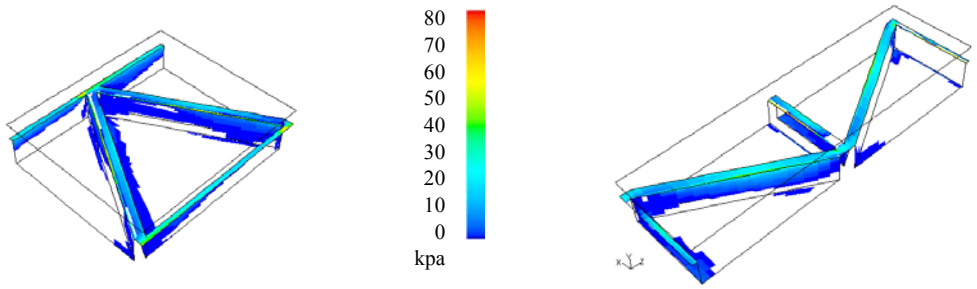


Stream-wise wall shear stresses

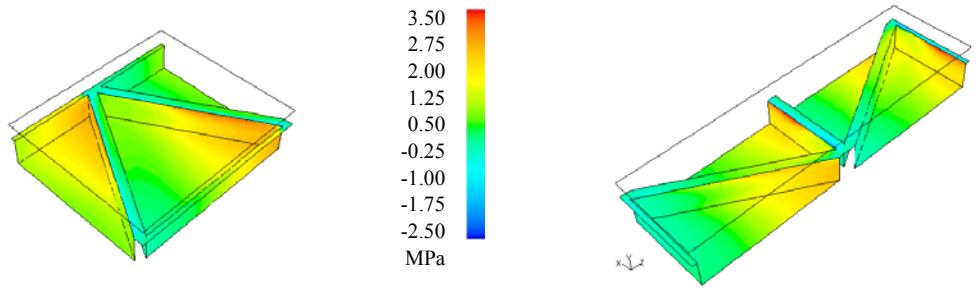


Periodic static pressure

Re~$2.58 \cdot 10^4$ Re~$2.61 \cdot 10^4$

(a) Clearance = 175 µm, PG = $1 \cdot 10^9$ Pa/m.

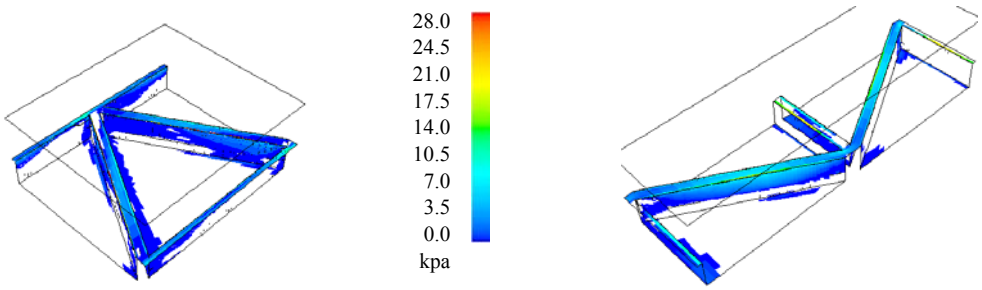


Stream-wise wall shear stresses

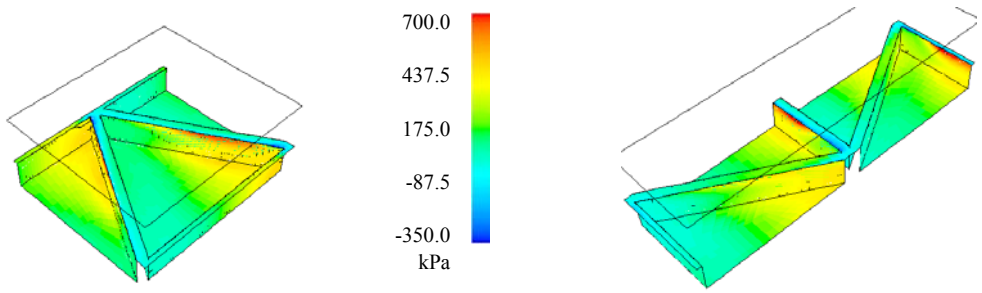


Periodic static pressure

Re~$4.56 \cdot 10^4$ Re~$4.50 \cdot 10^4$

(b) Clearance = 508 µm, PG = $1 \cdot 10^8$ Pa/m.


Original flow direction (X)


Counter Flow direction (Z)

Figure 176. Shear stresses/Pressure, effect of the orientation and clearance, isogrid pattern, turbulent flow.

Lastly, Figure 176 compares wall shear stresses and periodic static pressure contours. Regardless of the actual magnitude, contours are relatively similar in all clearances. From the wall shear stresses distribution, it is clearly observed that the flow does not reattaches to the pattern walls (no positive values) in any flow direction and clearance, although the localized recirculation and separation in the horizontal walls near corners of each pattern are stronger in the counter flow direction. Separation zones are also observed clearly in the pressure contours where largest negative periodic static pressures are predicted near corners of each pattern in the original direction, but only in the flat trailing edge pattern in the counter flow direction. On the other hand, the 'stagnation' point (highest static pressure point on the trailing wall of the pattern) that shifts slightly in the original flow direction as the clearance is reduced, remains in the same location in the counter flow direction. Indeed, a strong 'stagnation' only exists in the flat trailing pattern of the counter flow direction, as this pattern provides larger resistance forces (up to 7%) than the flat leading edge pattern.

In summary, although the flow path inside each isogrid pattern vary considerably depending on the flow direction, average static pressure force ratios and turbulence intensity levels remain similar in both clearances, translating into the apparent no effect of the orientation in the mean bulk flow behavior predicted by comparable overall friction factor values.

Moving on to the honeycomb pattern, Figure 177 compares velocity contours in comparable planes for the test clearance in both flow directions. In both cases, stream-wise velocities are reduced by the presence of the patterns, but flow velocities in the counter flow direction are more uniform on each stream-wise plane, with larger values near the center of the periodic unit, where there is a continuous wall that defines the clearance. In the case of the original flow direction, the flow dips significantly to the point of reattachment, as already discussed, and it is entirely channeled towards the center of each pattern.

In the case of predicted vertical velocities, they exhibit an already described common behavior, downward velocity magnitude values that are much smaller than upward magnitudes values. In both directions, the flow 'accelerates' up in the trailing wall of each pattern. On the other hand, span-wise velocities are significantly lower in the counter flow direction, as they are localized near lateral edges of pattern trailing corners and 'push' the mean flow towards the center of the periodic unit, rather than spreading it and promoting

the zigzag behavior observed in the original flow direction.

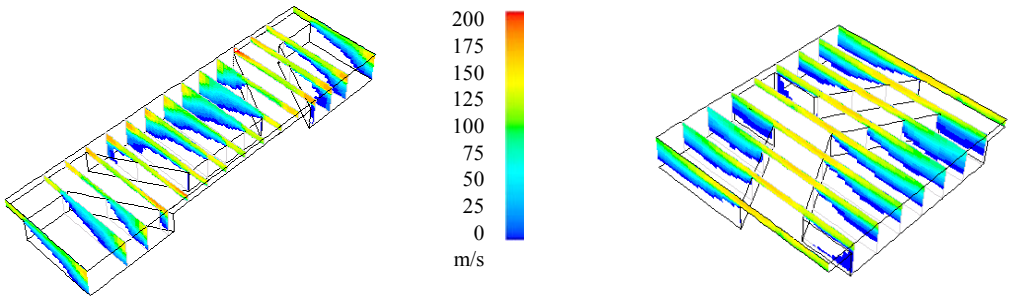


(a) Stream-wise velocity

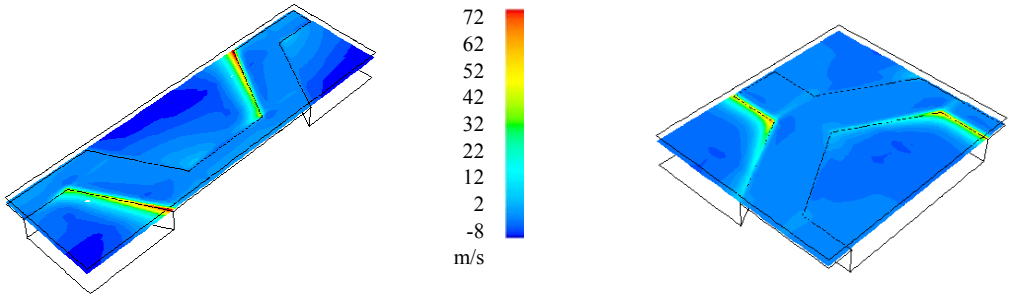


(b) Vertical velocity at y=1/4·$C_r$

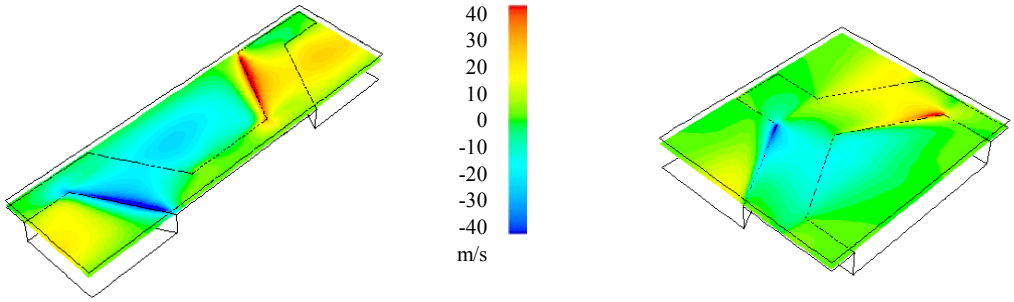


(c) Span-wise velocity

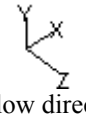


Original flow direction (X),
Re~4.44·10$^4$, PG = 2·10$^9$ Pa/m.


Counter Flow direction (Z),
Re~4.45·10$^4$, PG = 1.59·10$^9$ Pa/m.

Figure 177. Velocity contours, effect of the orientation, Clearance = 176 µm, honeycomb, turbulent flow.

Similarly, Figure 178 compares velocity contours of the three components in both periodic units for the intermediate clearance. Likewise, stream-wise velocities are reduced by the presence of the patterns and overall magnitudes are comparable, although at this clearance in easier to visualize that the core flow concentrates in the center of the periodic unit in the counter flow direction, while the flow is still somewhat channeled in the original flow direction although actual velocity values are more uniform. Vertical velocities also

exhibit the behavior described above for the smaller clearance, much larger upward velocity values in the trailing edges of each pattern, although values predicted in the original flow direction are larger. In the case of span-wise velocities, the predicted behavior is the same, actual values in the original flow direction are larger a promote a stronger zigzag effect, while weaker values concentrate the flow rather than spread it flow in the counter flow direction.

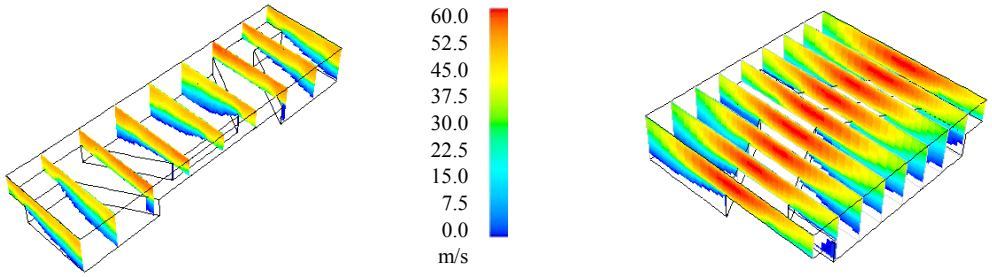


(a) Stream-wise velocity

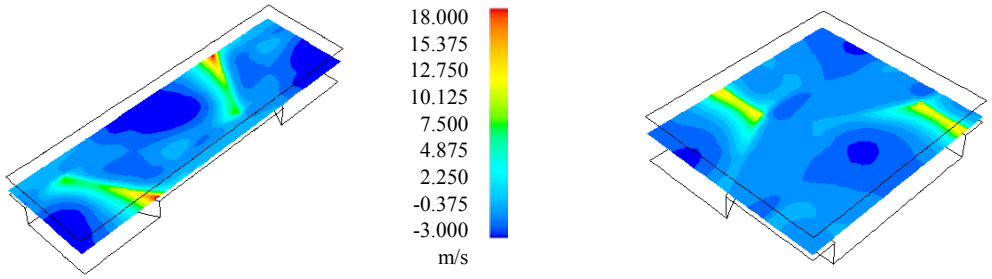


(b) Vertical velocity at y=1/4·$C_r$

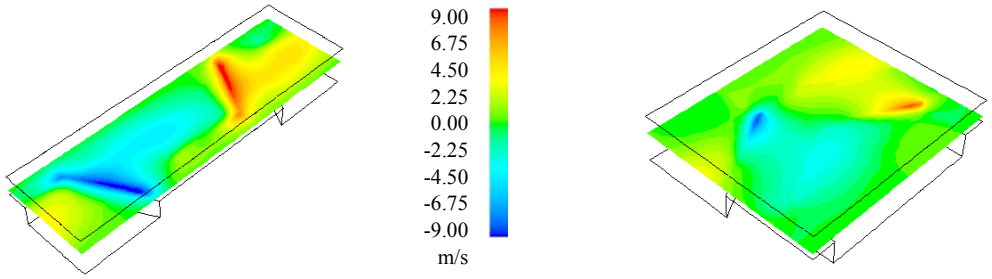


(c) Span-wise velocity


Original flow direction (X),
Re~$4.62 \cdot 10^4$, PG = $1 \cdot 10^8$ Pa/m.


Counter Flow direction (Z),
Re~$4.62 \cdot 10^4$, PG = $7.98 \cdot 10^7$ Pa/m.

Figure 178. Velocity contours, effect of the orientation, Clearance = 508 µm, honeycomb, turbulent flow.

Regarding recirculation paths within each pattern, Figure 179 compares velocity vectors

in several planes (plane locations shown on the isometric views) on each periodic unit at the smallest clearance. As already discussed in previous sections, the traditional vortex or cavity flow is not present due to dipping in the stream-wise planes of the pattern with the original orientation. On the other hand, this traditional vortex is present in the stream-wise planes of the counter flow direction but concentrated in the pattern center (not filling the whole length of the pattern) and it not particularly strong. Regarding span-wise planes, there are pairs of counter rotating vortexes of comparable strength in the widest portion of each pattern in both flow directions. On the other hand, while the flow dipping promotes stronger vortex pairs that fill horizontal planes of each pattern in the original flow direction, there are only weak and partial vortexes in the same planes of the counter flow direction.

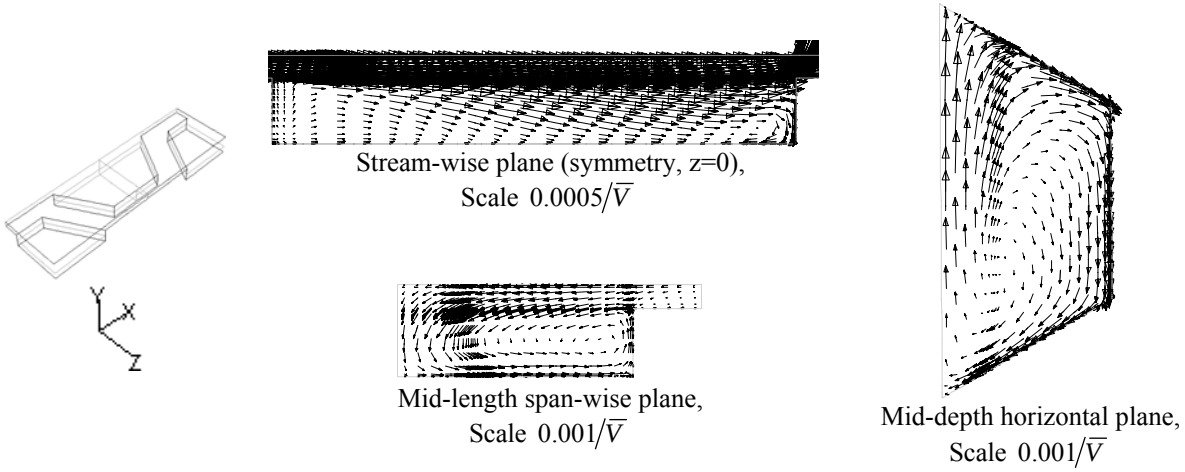


(a) Original flow direction, Re~$4.44 \cdot 10^4$ ($\overline{V}$ = 128.2 m/s), PG = $2 \cdot 10^9$ Pa/m.

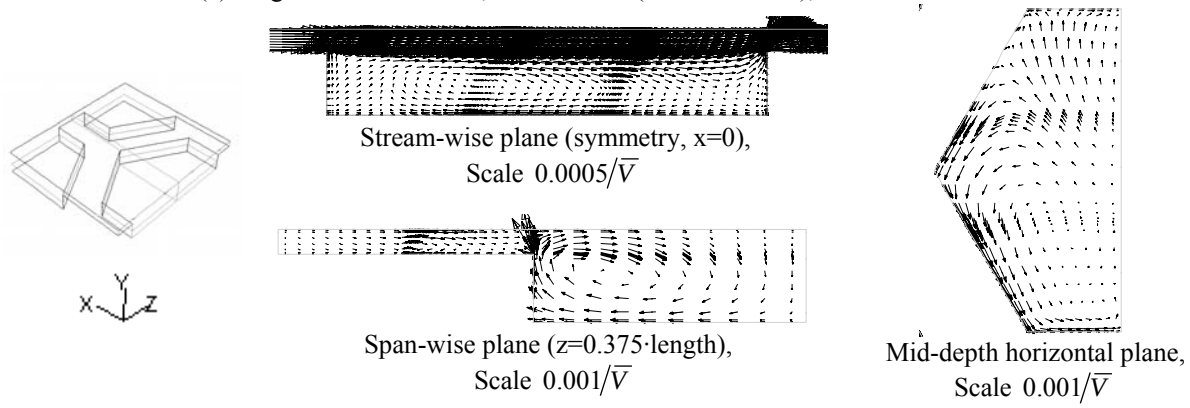


(b) Counter flow direction, Re~$4.45 \cdot 10^4$ ($\overline{V}$ = 128.3 m/s), PG = $1.59 \cdot 10^9$ Pa/m.

Figure 179. Velocity vectors, effect of the orientation, Clearance = 176 μm, honeycomb, turbulent flow.

In the case of the intermediate clearance, Figure 180, the flow path within each pattern does not vary significantly. Stream-wise planes in the original direction show the strong flow dipping preventing any major vortex, while the traditional vortex present in the counter flow direction is shifted to the back of the pattern. In the span-wise planes, the pairs of counter rotating vortexes appear to shift towards the lateral walls in the widest portion of each pattern. While horizontal planes shows a strong somewhat skewed vortex pair filling each pattern in the original flow direction, and only weak and partial vortexes in the counter flow direction.

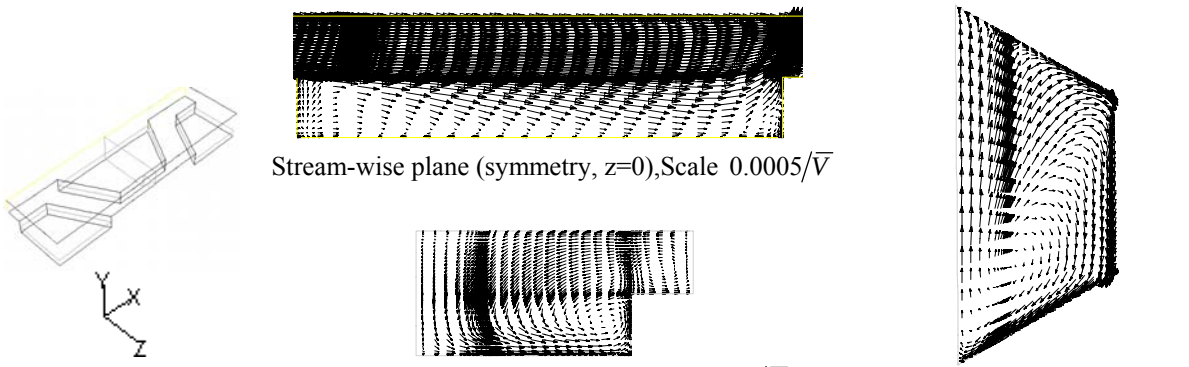


(a) Original flow direction, Re~$4.62 \cdot 10^4$ ($\overline{V}$ = 46.1 m/s), PG = $1 \cdot 10^8$ Pa/m.

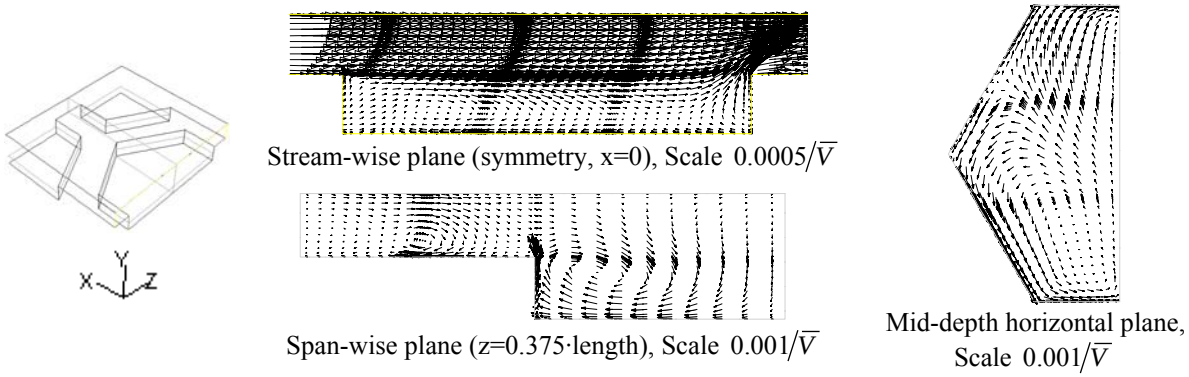


(b) Counter flow direction, Re~$4.62 \cdot 10^4$ ($\overline{V}$ = 46.1 m/s), PG = $7.98 \cdot 10^7$ Pa/m.

Figure 180. Velocity vectors, effect of the orientation, Clearance = 508 μm, honeycomb, turbulent flow.

Figure 181 compares turbulence intensity levels in both flow directions along several stream-wise planes and the 25% clearance horizontal plane of both clearances. Turbulence intensity levels are comparable in both flow directions at the smallest clearance, with larger

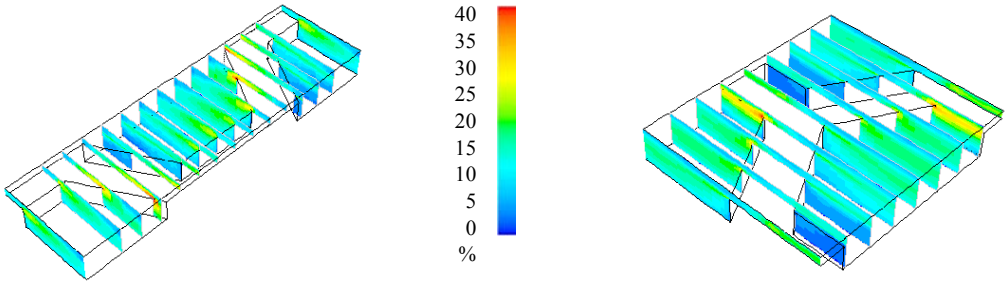


Equidistant stream-wise planes

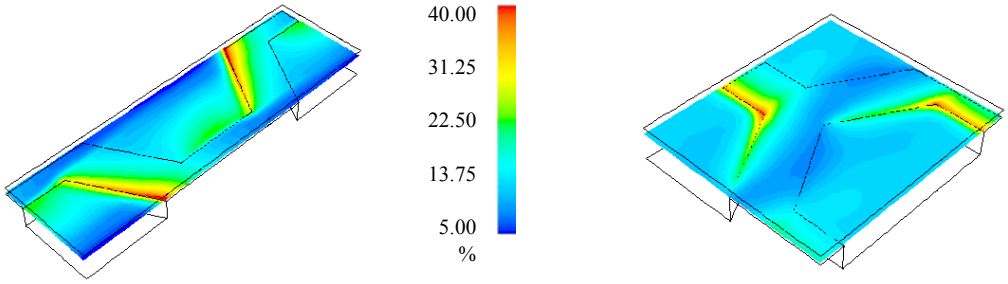


Vertical plane at y=1/4·$C_r$

Re~$4.44 \cdot 10^4$, PG = $2 \cdot 10^9$ Pa/m. Re~$4.45 \cdot 10^4$, PG = $1.59 \cdot 10^9$ Pa/m.

(a) Clearance = 176 µm

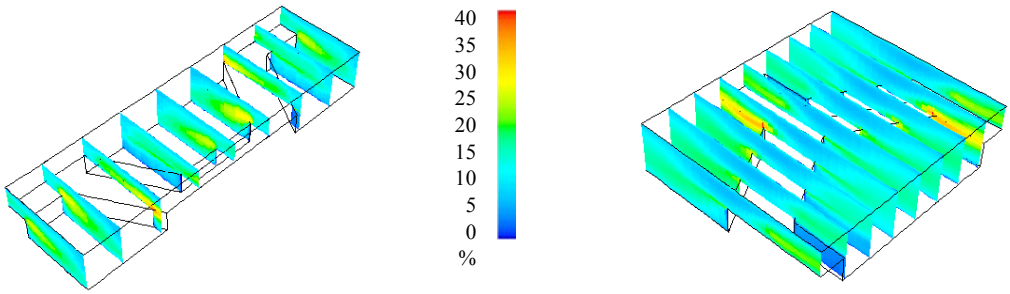


Equidistant stream-wise planes

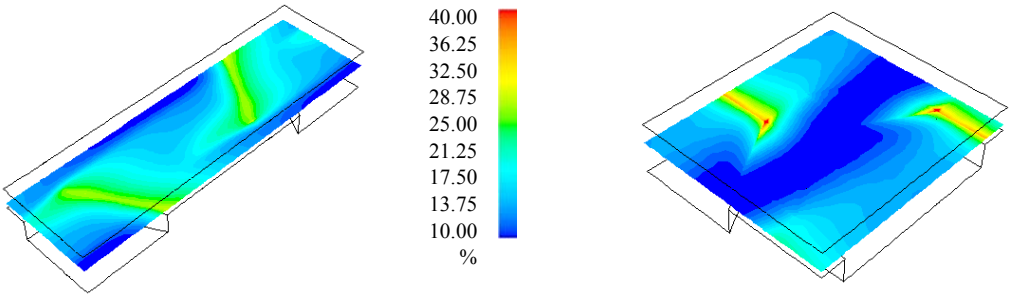


Vertical plane at y=1/4·$C_r$

Re~$4.62 \cdot 10^4$, PG = $1 \cdot 10^8$ Pa/m. Re~$4.62 \cdot 10^4$, PG = $7.98 \cdot 10^7$ Pa/m.

(b) Clearance = 508 µm


Original flow direction (X),


Counter Flow direction (Z),

Figure 181. Turbulence intensity, effect of the orientation and clearance, honeycomb, turbulent flow.

values present in the 'spreading' of the shear flow inside the patterns in the counter flow direction. On the other hand, the strong channeling of the flow in the original direction is evident in the lower levels of turbulence present near the symmetry planes of the periodic unit. Similarly, larger stream-wise velocities observed in the center of the periodic unit in the counter flow direction are correlated with lower turbulence levels in the same location. In both cases, maximum levels are predicted in the trailing edge and walls of each pattern, where the flow goes upward. Contrary to predictions in the original flow direction, variability in turbulence levels increases with clearance in the counter flow direction, where the stream-wise path of 'low' turbulence is now clearly present in the horizontal planes, and the intensified values remain located in the trailing edge of each pattern, Figure 181 (b). On the other hand, mass-weighted average turbulence intensity levels that increases significantly with clearance in the original flow direction (12.37% at 176 µm versus 13.98% at 508 µm), are somewhat comparable in the counter flow direction (11.98% at 176 µm versus 12.35% at 508 µm).

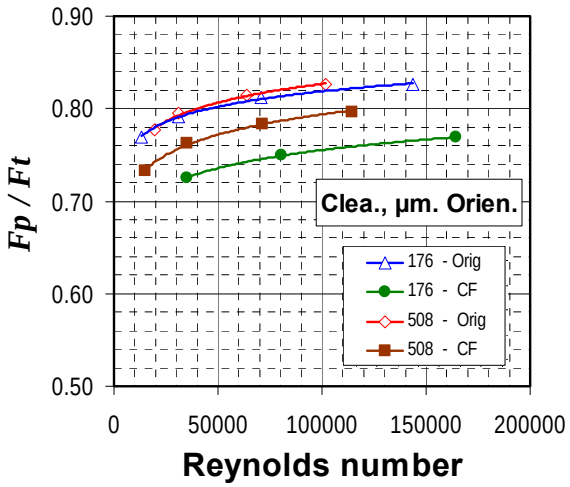


Figure 182. Stream-wise forces predicted proportion in the honeycomb pattern, turbulent flow regime.

Now, Figure 182 presents static pressure force ratios versus the Reynolds number in both clearances. At the smallest clearance, ratios in the original flow direction are up to 10% larger than the values in the counter flow direction. Similarly, values at the intermediate clearance are larger up to 5% in the original flow direction. This behavior is consistent in the flow range simulated.

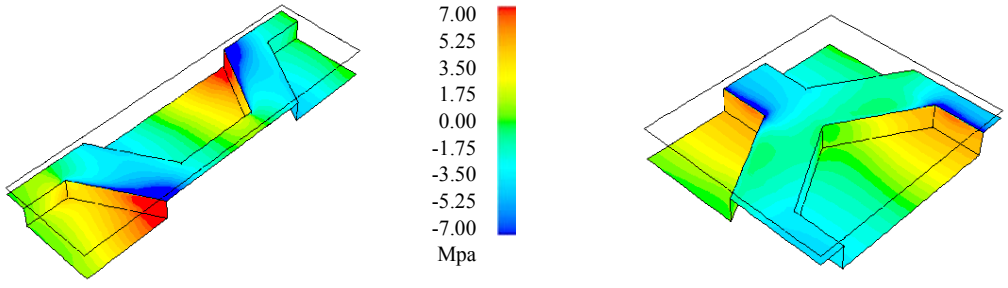


Periodic static pressure

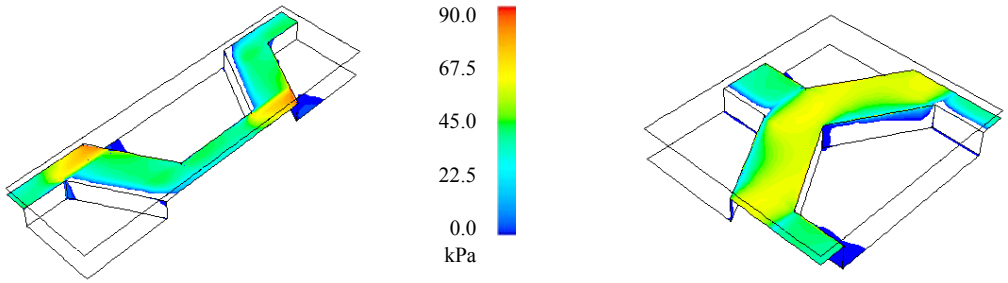


Stream-wise wall shear stresses

Re~$4.44 \cdot 10^4$, PG = $2 \cdot 10^9$ Pa/m. Re~$4.45 \cdot 10^4$, PG = $1.59 \cdot 10^9$ Pa/m.

(a) Clearance = 176 µm

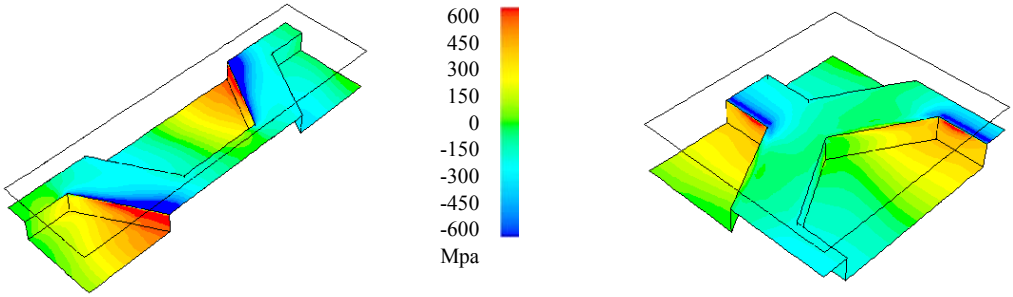


Periodic static pressure

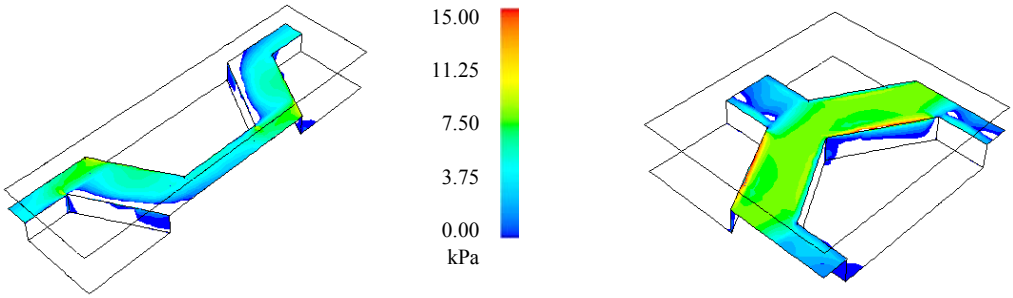


Stream-wise wall shear stresses

Re~$4.62 \cdot 10^4$, PG = $1 \cdot 10^8$ Pa/m. Re~$4.62 \cdot 10^4$, PG = $7.98 \cdot 10^7$ Pa/m.

(b) Clearance = 508 µm


Original flow direction (X),


Counter Flow direction (Z),

Figure 183. Pressure/shear stress, effect of the orientation, clearance = 508 µm , honeycomb, turbulent flow.

Lastly, Figure 183 compares wall shear stresses and periodic static pressure contours. At the smallest clearance, wall shear stresses are significantly larger in the original flow direction, with maximum values in the horizontal walls near the leading corner of the pattern. On the other hand, wall shear stresses are larger in the counter flow direction at the intermediate clearance, with maximum values along edges of each pattern lateral trailing walls. From the wall shear stresses distribution, it is clearly observed that the flow does not reattaches to the pattern walls (no positive values) in any flow direction and clearance, but localized recirculation and separation zones in the horizontal walls after trailing pattern edges are larger in the original flow direction. Separation zones are clearly observed in the pressure contours locating where largest negative periodic static pressures are predicted. It is also apparent that while separation zones increase with clearance in the original direction, they tend to reduce in the case of the counter flow direction.

Regarding static pressure contours, larger extreme values are predicted in both clearances for the original flow direction, with both extremes values located in the trailing corner of each pattern. Similarly, the ‘stagnation’ point (highest static pressure point on the trailing wall of the pattern) that strongly shifts down and towards the trailing corner in the original flow direction as the clearance is reduced, it remains in the same location in the counter flow direction, the upper side on the trailing edge near the side corners of each pattern.

In summary, the flow path inside each honeycomb pattern vary considerably depending on the flow direction. Similarly, average static pressure force ratios and turbulence intensity levels are considerably larger in the original flow direction for both clearances. The present analysis indicate these factors are responsible for the significant difference predicted in the friction behavior depending on the flow direction in this pattern.

*5.2.5. Summary, cross pattern geometry discussion.*

The more relevant observations derived by comparing main flow features predicted in each pattern for turbulent flow are the following:

- The mean flow moves sideways in all patterns, particularly near the bottom wall defining each clearance simulated. This zigzag effect is much marked in the shallow round-hole, Figures 152(a), and in the test clearance for the original mean flow direction in the honeycomb, Figure 165(a) (span-wise velocity components). The effect significantly diminishes in the deep round-hole depth, Figure 152(b), and the honeycomb by an increase in the clearance, Figure 165(b) and (c). Equally important, the flow orientation does not have a significant impact in the zigzag effect predicted for the isogrid pattern, Figure 171. On the contrary, the zigzag effect has a difference outcome in the honeycomb pattern. In the original flow direction, the effect promotes mixing in the horizontal planes of the periodic unit, while it concentrates the mean flow along the center of the periodic unit in the counter flow direction, Figure 177.
- The mean flow is channeled towards the pattern center and dips significantly to the point of reattachment at the bottom wall, in the shallow round-hole, Figures 149(a) and 150(a), and the honeycomb for all clearances in the original flow direction, Figures 164 (path lines) and 166 (stream wise plane velocity vectors). Nevertheless, the mean flow does not dip into the deep round-hole pattern, Figure 149(b), and the honeycomb for the counter flow direction, Figures 179(b) and 180(b) (stream wise plane velocity vectors).
- In all patterns, larger turbulence intensity levels are associated with the high mixing promoted by the localized higher vertical velocities in the trailing edges of each pattern (Figure 155, round-hole; Figures 161 and 174, Isogrid; Figures 167 and 181, honeycomb).
- Predicted static pressure force ratios (Figure 156, round-hole; Figure 168, honeycomb; Figure 162, isogrid) reveal the following trends:
  - Ratios increase with $\Gamma$. Predictions in the isogrid (83%) are larger than in the honeycomb (60%). While predictions in the honeycomb are larger that those in the round hole (44%). In contrast to laminar flow, the shallow round hole is predicted to

have significantly larger static pressure force ratios than the deep round hole.
  - Ratios are comparable in the smaller clearances of the honeycomb and the isogrid.
  - Ratios are above 50% in all cases, indicating that pressure forces play a primary role depending on the roughened surface area ratio, Γ.
- Within the same pattern, larger weighted average turbulence intensity levels explain why the test clearance in the isogrid pattern, 175 μm, and the intermediate clearance in the honeycomb pattern, 508 μm, are predicted to have larger friction factors.

In perspective, the presence of the roughness pattern in Poiseuille turbulent flow leads to a significant increase in friction factor. In addition, all parameters evaluated have a significant effect in the predicted flow resistance, i.e. friction factor, depending on the relative size of the roughness and the Reynolds number prevailing in the annular clearance of the seal.

### *5.2.6. How current 3-D results compare to 2-D predictions.*

The parametric analysis included in section 2.5 led to the conclusion that the flow resistance of liquid grooved seals is determined primarily by the grooved percentage area, Γ. At a fixed clearance, a larger grooved or roughened percentage area leads to larger flow resistance. For a given grooved percentage area, the groove aspect ratio is then the parameter defining flow resistance. Although flow resistance is affected by the actual length of the groove and the Reynolds number, the grooved percentage area and the aspect ratio of the groove are the parameters that make results similar.

Results from the original 2-D numerical analysis [19] of Nava's [30] experiments were included in the parametric analysis to confirm that larger grooved or roughened areas lead to larger flow resistance. In the 2-D approach, the large knurl is indeed a 'V' shape groove with a Γ ratio of 69%, while the large recess is indeed a rectangular groove with a Γ ratio of 50%. At a comparable clearance to the groove experiment of Iwatsubo[38], 0.127 mm (5 mils), large knurl predictions indicate a larger flow resistance than the large recess predictions.

Given the fact that the isogrid experiments of Iwatsubo[36] and the honeycomb experiment of Kaneko[37] were conducted at the same clearance that the groove

experiments of Iwatsubo[38], the results of 3-D predictions in both the isogrid and the honeycomb at the test clearances (175 and 176 μm) were added to the parametric analysis. Figure 184 presents again the low Reynolds number parametric analysis included in Figure 12(a) but for the groove length that maximizes flow resistance at each Γ ratio, and single prediction points corresponding to the 2-D large knurl, the 2-D large recess, the 3-D isogrid, and the 3-D honeycomb. Clearly, these predictions confirm the trend that flow resistance increases as the grooved or roughened surface area ratio is increased. On the other hand, when the flow resistance of each individual geometry is compared to the one predicted in each 'optimum' groove (per Γ ratio) at the same aspect ratio, actual values does not correlate linearly. This is due to the fact that these geometries correspond to the pattern sizes used in each experiment, which are not necessarily the optimum in each case, and most importantly, the flow features are significantly different in a 3-D pattern, particularly in large shallow patterns such as the isogrid and the honeycomb.

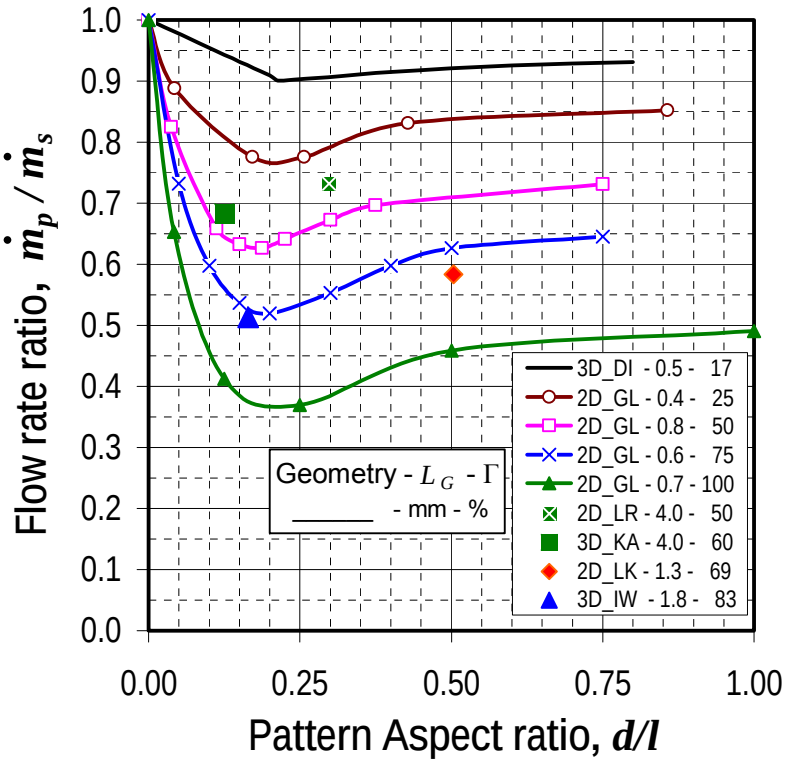


Figure 184. Groove seal parametric analysis, Low Reynolds number, $\Delta P_X \sim 10$ MPa/m.
DI = Dietzen and Nordmann, LR = large recess, LK = large knurl, KA = Kaneko's honeycomb, IW = Iwatsubo's isogrid, GL = Groove Length (largest stream-wise pattern length in 3-D geometries).

Regarding the relevance of the actual size of each pattern, Figure 185 compares the predicted flow resistance of each 'optimum' groove configuration per roughened area ratio as a function of the groove length but normalized by the clearance. Recall that a groove with an optimum aspect ratio is neither shallow nor deep, therefore the changes in predicted flow resistance are solely due to the roughened area ratio and the actual length of the groove. The groove length to clearance ratio predicted to minimize leakage is in the order of 2 to 8 at any Γ percentage. Although the Reynolds number affects the predicted optimum length-to-clearance ratio, it is the change in flow resistance with the groove length that is more affected as the Reynolds number is increased. The flow resistance, i.e. the friction factor, decreases at a lower rate with the groove length as the Reynolds number is increased.

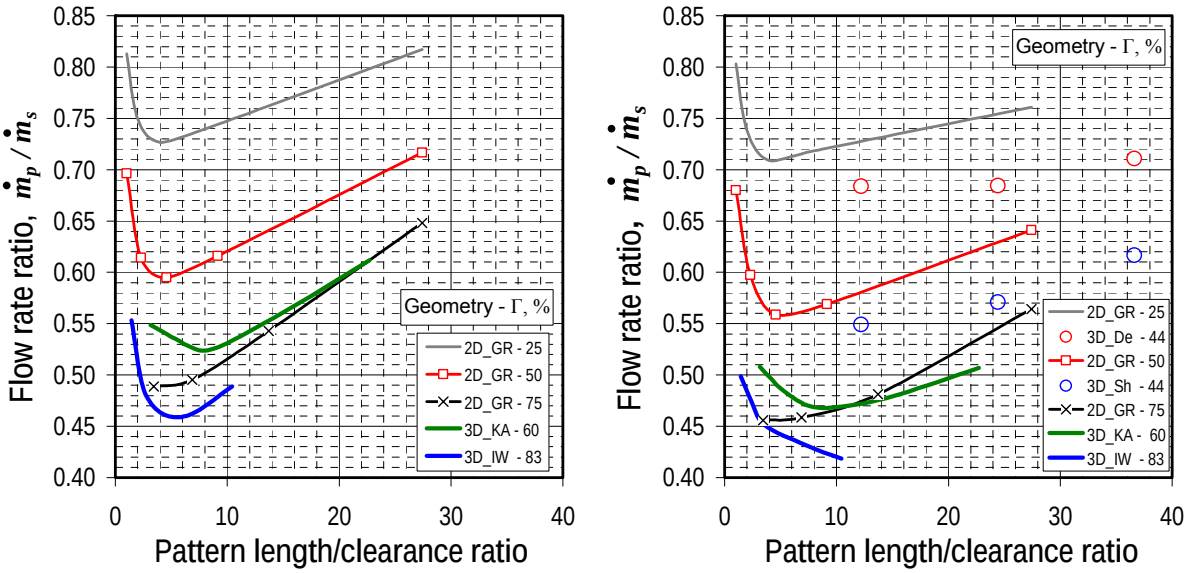


(a) Reynolds number = 6000 (b) Reynolds number = 20000

Figure 185. Predicted Flow Resistance, 2-D versus 3-D modeling.
GR = groove with the optimum aspect ratio at the given length, De = Fayolle's deep round-hole, Sh = Fayolle's deep round-hole, KA = Kaneko's honeycomb, IW = Iwatsubo's isogrid.

In Figure 185, the friction-factor-to-clearance behavior predicted for the isogrid and honeycomb pattern are also added, together with preliminary predictions at the smallest test clearance, and twice the largest test clearance of the round-hole pattern, deep and shallow. The similarities in the predicted flow resistance of the two analysis, 2-D varying the length

of the optimum groove at a fixed clearance versus 3-D varying the clearance of a fixed roughness pattern, is striking. As with Figure 184, 3-D predictions are consistent in pointing to Γ as a primary parameter defining flow resistance but with a lesser dependence that the one predicted by the 2-D groove parametric analysis. Similarly, 3-D predictions indicate that the optimum length-to-clearance ratio for a fixed pattern depends of the roughness type and the Reynolds number. Indeed, Reynolds number is predicted to affect more the flow resistance versus the length-to-clearance ratio behavior in 3-D patterns than in the optimum 2-D groove configuration.

In summary, all experimental pattern geometries studied in the original 2-D numerical analysis [19] and the ones under scrutiny in the present research are considerably much larger than the actual clearance in each experiment. In such large size pattern configurations, the actual length of the pattern has a comparable effect in the flow resistance to the one attributed to the roughened surface area ratio. Indeed, all simulations predict larger flow resistance in patterns with larger surface roughened area ratios. Although the aspect ratio defines the flow resistance of any particular pattern at a given clearance and Γ ratio, the actual size of the pattern has a comparable effect when the size is extremely large in relation to the actual clearance of the seal. In fact, this large relative size is the parameter that appears to markedly influence the friction-factor-to-clearance proportionality in annular seals with deliberately roughened surfaces.

# 6. CONCLUSIONS

An extensive 2-D and 3-D numerical analyses of several experiments with liquid annular seals, smooth and roughened, have been performed to further the understanding of the friction-factor behavior in fluid flow within seals with deliberately roughened surfaces. Present results support the following physical standpoint conclusions:

(a) After the clearance, the surface roughened area ratio is the primary parameter defining the actual flow resistance of a roughened seal; a larger surface roughened area ratio leads to larger flow resistance, indeed, to observed and predicted larger friction factors.

(b) After the surface roughened area ratio, the aspect ratio of the roughness pattern is the parameter defining the actual flow resistance of a roughened seal. At a fixed surface roughened area ratio, there exists an optimum aspect ratio that maximizes the flow resistance in any given flow range. Smaller ratios lead rapidly to decreased flow resistance, indeed, to lower friction factors where a smooth seal is the limiting solution. Larger ratios also lead to reduced flow resistance but to limiting solutions that depend only on the roughened surface area ratio. More specifically, the friction factor having a maximum at the optimum aspect ratio of any given roughness pattern is slightly reduced for larger aspect ratios but smoothly stabilizes as the aspect ratio is increased further.

(c) For a given roughened seal, where the surface roughened area and aspect ratios have already been established, the size of the roughness pattern relative to the actual clearance is the parameter that defines the observed and predicted flow resistance. As was found in the 2-D numerical analysis [19], larger roughness patterns lead to reduced flow resistance, indeed, to predicted lower friction factors. Even so, the actual size of the roughness pattern in a particular seal has a comparable effect in the flow resistance to the one predicted for the roughened surface area ratio for extremely large sizes of the roughness patterns. In addition, the effect of the actual pattern size in the flow resistance depends on the averaged Reynolds number of the flow. Indeed, varying the actual size of the roughness pattern in a seal for a given Reynolds number has a comparable effect in the friction factor, that varying the actual flow rate in a given seal with equally sized roughness patterns.

(d) The flow resistance in a roughened seal might also be sensitive to the mean flow

orientation relative to each roughness pattern within the seal. Experimental verification on this subject is scarce, but predictions consistently indicate that the shape of a particular constant depth roughness pattern has an effect in the flow resistance that is even larger than the effect of the clearance itself. This behavior was predicted in the honeycomb pattern and not in the isogrid pattern.

In general, present results confirm that the friction-factor behavior of these surfaces is determined by the roughness pattern's ability to develop high static pressures in its trailing faces. Particularly when comparing roughness patterns with a significant different Γ ratio. However, static pressure forces ratios alone do not explain the friction factor differences predicted in the smaller clearances of both isogrid and honeycomb, while weighted average turbulence intensity levels correlate well with the difference in friction factor predictions.

The friction-factor 'plateau' phenomenon, the associated shift in proportionality of the friction factor, and the friction-factor-to-clearance indifference behavior were also reproduced clearly in the largest pattern, the honeycomb. This behavior is also predicted in the smaller pattern but for low Reynolds number only. In both cases, the 'plateau' is predicted to be the same intermediate clearance reported as the one providing the largest friction factor in the experiments of Nava[30] and Hess[34]. There is no current explanation to why this intermediate clearance is observed and predicted to be an apparent universal 'plateau' for liquid roughened seals.

Although more research is needed, particularly in relation to the apparent discrepancy of the predictions versus the experiments at low Reynolds number, and extending the groove parametric analysis or even performing one with 3-D geometries, the following design practices are recommended if the primary intention of the liquid seal is to reduce leakage:

- Use the largest feasible roughened surface area ratio.
- Use a shallow pattern, with an aspect ratio between 0.125 and 0.200.
- Use a pattern size comparable to the intended seal clearance, roughly 4 to 5 times larger.
- Use sharp edges shaped patterns with no edge being perpendicular to flow direction.

Regarding the friction-factor-to-clearance proportionality, numerical predictions and experiments suggest it is defined by the roughness pattern length to the seal clearance ratio.

Very large patterns are more likely to have a flow resistance that will increase with clearance in a certain Reynolds number range.

From a numerical modeling point of view, it was found that:

(e) All simulations performed in the laminar regime in every 3-D pattern and any clearance appear to have the theoretical channel flow line (96/Re) as the limiting friction factor solution. Several transitional studies and stability analysis [51,52] indicate that is the case for flow in a channel with periodic grooves.

(f) The original 2-D numerical analysis [19] developed to simulate the experiments of Nava[30] and Hess[34] was validated by replicating the leakage of a liquid grooved seal within 2%. Similarly, 3-D numerical analysis performed in several new patterns predict leakage values within reasonable margins when compared to each experiment. The excessively large and constant over prediction in the numerical results based on Nava experiments is most likely related to post-processing errors in the original data.

(g) The standard k-ε turbulence model is more stable than the RNG version from a iterative convergence point of view when simulating steady flow over roughened surfaces, particularly at low Reynolds number.

(h) The Reynolds stress model appears to be extremely sensitive to the use of highly stretched 3-D conformal grids intended to resolve the laminar sub-layer. More research is needed to clarify the performance of this model, but stretched grid cells create artificial turbulent stresses and variations in the flow field that does not diminish as more stricter convergence criteria are enforced during the iterative convergence process.

(i) The previously reported sensitivity [19] of the wall function approach to the location of the first grid point near the wall is a combination of two aspects. First, larger gradients in the mean flow velocity occur near the wall. By definition, the wall function approach does not resolve the near-wall profile of the velocity. The default integration method over estimates the mass flow rate in this region. As the grid is refined, mass flow rate estimations are more accurate as the profile near the wall is better reproduced, as long as the first grid point near the wall is located within the overlap region. Second, enforcing the laminar velocity profile reduces considerably mass flow rate predictions when this point is mistakenly or inadvertently located in the laminar sub-layer, while exaggerated

boundary values calculated for the turbulence dissipation do not play a role.

(m) The Grid Convergence Index of Roache[31] is a good indicator of numerical accuracy and grid convergence only when used in uniform grids with simple turbulence models and basic geometries. Once the grid is refined or modified in complicated geometries to comply with the restrictions of more complex turbulence models or to capture particular features within the flow, its application is dubious at best. This shortcoming was already mentioned by Roache[31] but appears to be exacerbated when it is used to analyze the results obtained in turbulent flow over roughened surfaces. The relative error, in which the GCI is based, was the main indicator of grid convergence used in this research.

(n) Direct Numerical Simulations of turbulent channel flow [35] and smooth seal experiments at low Reynolds number [36,37] are better predicted when using the enhanced wall treatment (the two layer zonal model of Chen[25] when the laminar sub-layer is properly resolved). Using the standard wall function approach results in replicating the Blasius solution for turbulent flow in a smooth pipe.

(o) Turbulent flow in grooved seals at low Reynolds number [38] was better predicted using standard wall functions. The enhanced wall treatment predicts larger turbulence levels within the clearance leading to a non-negligible under prediction in the leakage.

(p) Turbulent flow in deliberately roughened seals [8,36,37], with 3-D equally spaced patterns, was not well predicted with either the enhanced wall treatment or using wall functions. Indeed, neither of the turbulence model combination tested, core flow and near-wall treatment, reproduced the leakage measured in the experiments within the same predicted accuracy as in turbulent channel flow and for grooved seals. In addition, contrary to the findings of the 2-D numerical analysis[19], both near wall treatments predict comparable friction factors, trends, and sensitivity to the change in clearance. The enhanced wall treatment predicts lower values, mostly associated with significantly different flow field predictions inside each pattern. The comparison in the 2-D numerical analysis was made with a different turbulence model for the core flow.

In summary, a fair estimation provided by solving the Reynolds-averaged Navier-Stokes equations might not be sufficient to predict the turbulent flow field in liquid annular seals with deliberately roughened surfaces.

# REFERENCES


1. Childs DW. *Turbomachinery Rotordynamics: Phenomena, Modeling and Analysis*. John Wiley & Sons, Inc: New York, NY, 1993 (Chapter 4).
2. Hirs GG. A Bulk-Flow Theory for Turbulence in Lubricant Films. *ASME Journal of Lubrication Technology* 1973; **1**(2):137-146.
3. Moore J. Three-dimensional CFD Rotordynamics Analysis of Gas Labyrinth Seals. In *Proceedings of DETC*, Pittsburgh, PA, September 9-12, 2001, DETC2001/VIB-21394.
4. Arghir M, Frêne J. A Bulk-Flow Analysis of Static and Dynamic Characteristics of Eccentric Circumferentially-Grooved Liquid Annular Seals. In *Proceedings of STLE/ASME Joint International Tribology Conference,* Ponte Vedra Beach, FL October 26-29, 2003, 1-10.
5. Florjancic, S. Annular Seals of High Energy Centrifugal Pumps: A New Theory and Full Scale Measurements of Rotordynamics Coefficients and Hydraulic Friction Factors. PhD Dissertation, Swiss Federal Institute of Technology, Zürich Nr. 9087, 1990.
6. Marquette OR, Childs DW. Theory versus Experiment for Leakage and Rotordynamic Coefficients of Circumferentially-Grooved Liquid Annular Seals with L/D of 0.45. In *Fluid Engineering Division Summer Meeting FEDSM97-3333*, ASME: Vancouver, British Columbia, Canada, June 22-26, 1997, 1-16.
7. Von Pragenau G. Damping Seals for Turbomachinery. NASA Technical Paper No. 1987, 1982.
8. Childs DW, Fayolle P. Test Results for Liquid 'Damper' Seals using a Round-Hole Roughness Pattern for the Stators. *Journal of Tribology, ASME Transactions* 1999; **121**:42-49.
9. Ha TW, Childs DW. Friction-Factor Data for Flat-Plate Tests of Smooth and Honeycomb Surfaces. *Journal of Tribology, ASME Transactions* 1992; **114**:722-730.
10. DeOtte R, Morrison GL, Nava DL, Hess JC. A Study of Friction Factors in Channel Flow Between Plates with Highly Roughened Surfaces. In Fluid Machinery Forum, *Fluid Engineering Division Summer Meeting FED-Vol.195*, ASME: Lake Tahoe, NV, June 19-23, 1994, 23-27.
11. Al-Qutub A, Elrod D, Coleman H. A New Friction Factor Model and Entrance Loss Coefficient for Honeycomb Annular Gas Seals. *Journal of Tribology, ASME Transactions* 2000; **122**:622-627.
12. Dietzen FJ, Nordmann R. Calculating Rotordynamic Coefficients of Seals by Finite-Difference Techniques. *Journal of Tribology*, *ASME Transaction* 1987; **109**:388-394.
13. Childs DW. Finite Length Solutions for Rotordynamic Coefficients of Turbulent Annular Seals. *Journal of Lubrication Technology* 1982; ASME Paper No. 82 Lub. 42.
14. Rhode DL, Hibbs RI. Labyrinth Seal Rotordynamic Forces using a Three-dimensional Navier-Stokes Code. *Journal of Tribology*, *ASME Transaction*, 1992; **114**:683-689.

15. Athavale MM, Przekwas AJ, Hendricks RC, Liang A. SCISEAL: A 3D CFD Code for Accurate Analysis of Fluid Flow and Forces in Seals. In *Proceedings of the Advanced ETO Propulsion Conference*, NASA CP3282, Marshall Space Flight Center, Huntsville, AL., May 1994; 337-345.

16. Peletti J. A Comparison of Experimental Results and Theoretical Predictions for the Rotordynamics Coefficients of Short (L/D=1/6) Labyrinth Seals. M.S. Thesis, Texas A&M University and Turbomachinery Laboratory Report No. TL-Seal-1-90, College Station, TX.

17. Schramm V, Willenborg K, Kim S, Wittig S. Influence of a Honeycomb Facing on the Flow through a Stepped Labyrinth Seal. In *Proceedings of the ASME TURBOEXPO,* Munich, Germany, May 8-11, 2000-GT-0291.

18. Chochua G. Computations of Gas Annular Damper Seal Flows. Ph.D. Dissertation, University of Florida, Gainesville, FL, 2002.

19. Villasmil LA. Understanding the Friction Factor Behavior in Liquid Annular Seals with Deliberately Roughened Surfaces, a CFD Approach. M.S. Thesis, Texas A&M University, College Station, TX, 2002.

20. Pope SB. *Turbulent Flows*. Cambridge University Press: Cambridge, United Kingdom, 2000 (Chapter 11).

21. Gerolymos GA, Vallet I. Wall-Normal-Free Reynolds-Stress Model for Rotating Flows Applied to Turbomachinery. *AIAA Journal* 2002; **40** (2):199-208.

22. Hsieh WD, Chang KC. Two-Layer Approach Combining Reynolds Stress and Low-Reynolds-Number $k$-$\varepsilon$ Models. *AIAA Journal* 1999; **37** (2):283-287.

23. Chien KY. Predictions of Channel and Boundary-layer Flows with a low-Reynolds-number Turbulence Model. *AIAA Journal* 1982; **20**:33-38.

24. FLUENT 6.1 User's Guide, No. 2003-01-25, Fluent Incorporated, Lebanon, NH.

25. Chen HC, Patel VC. Near-wall Turbulence Models for Complex Flows including Separation. *AIAA Journal* 1988; **26**(6):641-648.

26. Lam CKG, Bremhorst KA. Modified Form of the $k$-$\varepsilon$ Model for Predicting Wall Turbulence. *Journal of Fluids Engineering* 1981; **103**:456-460.

27. Launder BE, Sharma BI. Application of the Energy-dissipation Model of Turbulence to the Calculation of Flow near a Spinning Disc. *Letters in Heat and Mass Transfer* 1974; **I**:131-138.

28. Patel VC, Chen HC. Turbulent Wake on a Flat Plate. *AIAA Journal* 1987; **25** (8):1078-1085.

29. Rahman MM, Siikonen T. Low-Reynolds-Number $k$-$\varepsilon$ Model with Enhanced Near-wall Dissipation. *AIAA Journal* 2002; **40** (7):1462-1464.

30. Nava DL. Observations of Friction Factors for Various Roughness Patterns in Channel Flow. M.S. Thesis, Texas A&M University, College Station, TX, 1993.

31. Roache PJ. *Verification and Validation in Computational Science and Engineering.* Hermosa Publishers: Albuquerque, NM, 1998 (Chapter 5).

32. Arghir M, Roucou N, Helene M, Frêne J. Theoretical Analysis of the Incompressible Laminar Flow in a Macro-Roughness Cell. *Journal of Tribology* 2002; **125**: 309-318.

33. Bergström J, Gebart R. Estimation of Numerical Accuracy for the Flow Field in a Draft Tube. *International Journal of Numerical Methods for Heat & Fluid Flow* 1999; **9**(4):472-486.

34. Hess JC. Dynamic Pressure Response of Water Flow between Closely Spaced Roughened Flat Plates. M.S. Thesis, Texas A&M University, College Station, TX, 1993.

35. Moser RD, Kim J, Mansour NN. Direct Numerical Simulation of Turbulent Channel Flow up to $Re_\tau = 590$. *Physics of Fluids* 1999; **11**(4):943-945.

36. Iwatsubo T, Sheng B. An Experimental Study on the Static and Dynamic Characteristics of Damper Seals. In *Proceedings of the Third IFToMM International Conference on Rotordynamics*, Lyons, France, 1990; 307-312.

37. Kaneko S, Ikeda T, Saito T, Ito S. Experimental Study on Static and Dynamic Characteristics of Liquid Annular Convergent-Tapered Damper Seals with Honeycomb Roughness Pattern. *Journal of Tribology, Transactions of the ASME* 2003; **125**:592-599.

38. Iwatsubo T, Sheng B. Evaluation of Dynamic Characteristics of Parallel Grooved Seals by Theory and Experiments. In *Proceedings of the Third IFToMM International Conference on Rotordynamics*, Lyons, France, 1990; 313-318.

39. Verstappen RWCP, van der Velde RM, Veldman AEP. DNS of Turbulent Flow and Heat Transfer in a Channel with Surfaces Mounted Cubes. In *Proceedings of the European Congress on Computational Methods in Applied Science*, Barcelona, Spain, September 11-14, 2000.

40. Villasmil LA, Childs DW, and Chen HC. Understanding Friction Factor Behavior in Liquid Annular Seals with Deliberately Roughened Surfaces, *ASME Journal of Tribology* 2005; **127**:213-222. Issue 1.

41. Ha TW, Ju YC, Lee Y-B, Kim C-H, Characteristics of Friction Factor for Artificially Roughened surfaces, in Korean, *Journal of the Fluid Machinery* 2003; **6**(3):15-20.

42. Villasmil LA, Chen HC, Childs DW, Evaluation of Near-wall Turbulence Models for Liquid Annular Seals with Roughened Walls, *AIAA Journal* 2005; **43**(10):2137-2146.

43. Ha, TW. Test Results of Friction Factor for Round-Hole Roughness Surfaces in Closely Spaced Channel Flow of water, *Korean Society of Mechanical Engineers International Journal* 2004; **18**(10):1849-1858.

44. Staat DG. Investigation of Friction Factor in Channel Flow based upon Variation in surface Geometry and Channel Spacing, a Senior Project, December 1994, Texas A&M University, College Station, TX.

45. Billy F, Arghir M, Pineau G, Frêne J, Texier A. Modèle théorique et validations expérimentales pour un écoulement de film mince en présence d'une surface texturé. Application aux joints annulaires d'étanchéités. Advanced Topics and Technical Solutions in Dynamic Sealing Workshop, EDF-LMS Futuroscope, Poitiers, France, 2005, M1-M8.

46. Patankar SV, Liu CH, Sparrow EM. Fully Developed Flow and Heat Transfer in Ducts having Streamwise-periodic Variations of Cross-sectional Area. *ASME Journal of Heat Transfer* 1977; **99**:180-186.

47. Shyy W, Thakur SS, Ouyang H, Liu J, Blosh E. *Computational Techniques for Complex Transport Phenomena*. Cambridge University Press: Cambridge, United Kingdom, 1997.

48. Celik I. Procedure for Estimation and Reporting of Discretization Error in CFD Applications. In: Freitas C. (Ed.), Editorial Policy Statement on the Control of Numerical Accuracy, *ASME Journal of Fluids Engineering*, 2005. http://journaltool.asme.org/Templates/JFENumAccuracy.pdf.Accessed November 2005.

49. Launder BE, Spalding, DB. *Lectures in Mathematical Models of Turbulence. Academic Press*: London, England, 1972.

50. Moser RD, Kim J, Mansour NN. DNS Predictions for Turbulent Channel Flow. http://www.tam.uiuc.edu/Faculty/Moser/channel. Accessed May 2004.

51. Adachi T, Uehara H. Linear stability analysis of flow in a periodically grooved channel. *International Journal for Numerical Methods in Fluids* 2003; **41**:601-613.

52. Sahan RA, Gunes H, Liakopoulos A. A modeling approach to transitional channel flow. *Computers & Fluids* 1998; **27**:121-136.

# APPENDIX

# GRID SUMMARY

## Geometries for the grooved seal of Iwatsubo[38]:

| Name | Nodes(Cells) | Type | Size(μm) Δx, Δy, Δw |
|---|---|---|---|
| *a. Clearance = 175μm (original clearance)* | | | |
| GG01U | 2963(2808) | Uniform | 29.2,29.2,14.6 |
| GG01Ur | 11541(11232) | GG01U refined in both directions except near walls | 14.6,14.6,14.6 |
| GG01Urr | 39327(38718) | GG01Ur refined in both directions except near walls | 7.3,7.3,14.6 |

Note: GG01U is the 'BASE' grid for grove parametric analysis.

## Geometries for the round-hole seal of Fayolle[8]:

| Name | Nodes(Cells) | Type | Size(μm) Δx, Δy, Δz, Δw |
|---|---|---|---|
| *b. Shallow hole, clearance = 130μm (original largest clearance)* | | | |
| GG01U | 110044(99360) | Mixed | 10-85,22,10-85,11 |
| *c. Deep hole, clearance = 130μm (original largest clearance)* | | | |
| GG01UBL | 260134(243360) | Mixed | 10-85,22-44,10-85,11-22 |

## Geometries for the Isogrid seal of Iwatsubo[41]:

| Name | Nodes(Cells) | Type | Size(µm) Δx, Δy, Δz, Δw |
|---|---|---|---|
| *c.1 Clearance = 175µm (original clearance)* | | | |
| GG01cr | 70262(63920) | Mixed | 10-45,10-24,10-60,5 |
| GG04 | 39470(35356) | Mixed | 10-75,10-24,10-90,5 |
| GG04-1 | 63375(57768) | GG04 with boundary layer in all walls | (Δw) 1.0, top/bottom walls. (Δw) 0.5-1.5, hole walls. |
| GG04-2 | 88356(81416) | GG04 with boundary layer in all walls | (Δw) 0.25, top/bottom walls. (Δw) 0.25-0.75, hole walls. |
| *c.2 Clearance = 254 µm* | | | |
| GG03 | 26658(23576) | Mixed | 20-90,25-38,20-75,10-12.5 |
| GG03-1 | 48594(44152) | GG03 with boundary layer in horizontal walls | (Δw) 0.25, top/bottom walls. (Δw) 10, hole walls. |
| GG03-2 | 51742(47152) | GG03 with boundary layer in horizontal walls | (Δw) 1.25, top/bottom walls. (Δw) 10, hole walls. |
| GG03-1 a05* | 237570(170670) | GG03-2 locally refined for $y^+$ compliance | adapted 5 times near hole walls, (Δw) 1.1-10. |
| *c.3 Clearance = 508 µm* | | | |
| GG01cr | 132082(123760) | Mixed | 10-45,10-24,10-60,5 |
| GG03 | 42398(38576) | Mixed | 20-90,25-38,20-75,10-12.5 |
| GG03-1 | 64334(59152) | GG03 with boundary layer in horizontal walls | (Δw) 0.25, top/bottom walls. (Δw) 10, hole walls. |
| GG03-1 b08* | 343687(247809) | GG03-1 locally refined for $y^+$ compliance | adapted 8 times near hole walls, (Δw) 1.1-10. |
| *c.4 Clearance = 762 µm* | | | |
| GG03 | 42398(38576) | Mixed | 20-90,38,20-75,10-19 |
| GG03-1 | 80074(74152) | GG03 with boundary layer in horizontal walls | (Δw) 0.25, top/bottom walls. (Δw) 10, hole walls. |
| GG03-1 a04* | 199898(153035) | GG03-1 locally refined for $y^+$ compliance | adapted 4 times near hole walls, (Δw) 2.2-10. |
| *c.5 Clearance = 1270 µm* | | | |
| GG01cr | 175356(165648) | Mixed | 10-45,10-40,10-60,5-8 |
| GG02 | 90686(84224) | Mixed | 20-90,10-40,20-75,5-10 |
| GG03 | 61286(56576) | Mixed | 20-90,38-40,20-75,10-20 |
| GG03-1 | 88053(81728) | GG03 with boundary layer in horizontal walls | (Δw) 1.0, top/bottom walls. (Δw) 5-10, hole walls. |
| GG03-1 a05* | 229826(176088) | GG03-1 locally refined for $y^+$ compliance | adapted 5 times near hole walls, (Δw) 1.1-10. |

* This is a typical grid in the clearance, each case ran has a different grid.

Note: GG03 is the 'BASE' grid for this pattern.

## Geometries for the Honeycomb seal of Kaneko[42]:

| Name | Nodes(Cells) | Type | Size(µm) Δx, Δy, Δz, Δw |
|---|---|---|---|
| *d.1 Clearance = 176 µm (original clearance)* | | | |
| GG01 | 134418(121820) | Mixed (BL in walls, Uniform in core) | 10-100,10-75,10-70,5-10 |
| GG01r | 306495(281224) | Mixed (BL in walls, Uniform in core) | 10-50,10-75,10-35,5-10 |
| GG04U | 208854(191200) | Uniform | 25-50,22-25,49-50,11-25 |
| GG04Ucrxczcyh | 21346(18240) | Uniform | 100-200,22-50,95-100,11-100 |
| nGG04Ucrxczcyh-1 | 82818(75264) | GG04Ucrxczcyh | (Δw) 0.5, top/bottom walls. |
| | | with boundary layer in all walls | (Δw) 1.1-4.3, hole walls. |
| nGG04Ucrxczcyh-2 | 103318(94608) | GG04Ucrxczcyh | (Δw) 2.5, top/bottom walls. |
| | | with boundary layer in all walls | (Δw) 0.5-2.5, hole walls. |
| *d.2 Clearance = 254 µm* | | | |
| GG01 | 134418(121820) | Mixed (BL in walls, Uniform in core) | 10-100,14-75,10-70,7-10 |
| GG04Ucrxczcyh | 27202(23760) | Uniform | 100-200,21-50,95-100,11-100 |
| GG04Ucrxczcyh-1 | 63610(57552) | GG04Ucrxczcyh | (Δw) 1.0, top/bottom walls. |
| | | with boundary layer in all walls | (Δw) 2.4-8.1 hole walls. |
| GG04Ucrxczcyh-2 | 88866(81120) | GG04Ucrxczcyh | (Δw) 1.0, top/bottom walls. |
| | | with boundary layer in all walls | (Δw) 0.25-1.25, hole walls. |
| *d.3 Clearance = 508 µm* | | | |
| GG04Ucrxczcyh | 43306(38940) | Uniform | 100-200,22-50,95-100,11-100 |
| GG04Ucrxczcy | 24274(21000) | Uniform | 100-200,50,95-100,25-100 |
| nGG04Ucrxczcy-2 | 81862(74440) | GG04Ucrxczcy | (Δw) 0.5/0.8, top/bottom wall. |
| | | with boundary layer in all walls | (Δw) ~1.0, hole walls. |
| nGG04Ucrxczcyh-3 | 195528(183024) | GG04Ucrxczcyh | (Δw) 1.0, top/bottom walls. |
| | | with boundary layer in all walls | (Δw) 0.25-1.0, hole walls. |
| *d.4 Clearance = 762 µm* | | | |
| GG04Ucrxczcyh | 43606(38940) | Uniform | 100-200,33-50,95-100,16-100 |
| nGG04Ucrxczcyh-1 | 122598(113484) | GG04Ucrxczcyh | (Δw) 2.5, top/bottom walls. |
| | | with boundary layer in all walls | (Δw) 2.5-5.0 hole walls. |
| nGG04Ucrxczcyh-2 | 124309(115052) | GG04Ucrxczcyh | (Δw) 0.5, top/bottom walls. |
| | | with boundary layer in all walls | (Δw) 0.25-1.0 hole walls. |
| nGG04Ucrxczcyh-3 | 219678(206424) | GG04Ucrxczcyh | (Δw) 0.25, top/bottom walls. |
| | | with boundary layer in all walls | (Δw) 0.25-0.50 hole walls. |
| *d.5 Clearance = 1270 µm* | | | |
| GG04Ucrxczcyh | 103330(95520) | Uniform | 100-200,20-50,95-100,10-100 |
| nGG04Ucrxczcyh-1 | 150138(139944) | GG04Ucrxczcyh | (Δw) 2.5, top/bottom walls. |
| | | with boundary layer in all walls | (Δw) 2.5-5.0 hole walls. |
| nGG04Ucrxczcyh-2 | 162972(152236) | GG04Ucrxczcyh | (Δw) 1.25, top/bottom walls. |
| | | with boundary layer in all walls | (Δw) 0.5-2.5 hole walls. |
| nGG04Ucrxczcyh-3 | 267978(253224) | GG04Ucrxczcyh | (Δw) 0.5, top/bottom walls. |
| | | with boundary layer in all walls | (Δw) 0.25-1.25 hole walls. |

Note: GG04Ucrxczcyh is the ‘BASE’ grid for this pattern.

# VITA

Larry Alfonso Villasmil Urdaneta was born in the city of Maracaibo, Zulia State, Venezuela. He attended “Universidad Nacional Experimental del Táchira” in San Cristóbal, Venezuela, from 1983 to 1988 graduating with honors earning a Bachelor of Science degree in mechanical engineering. He is a registered Professional Engineer in Venezuela. After graduation he worked for the state owned Venezuelan Oil Company, PDVSA. He served in several positions, addressing the selection, installation, and troubleshooting of a multiple variety of rotating machinery, and was a senior design engineer when he was admitted to Texas A&M University in 2000. He graduated in 2002 earning a Master of Science degree in mechanical engineering from Texas A&M, and continued his studies enrolling in the Mechanical Engineering Doctor of Philosophy program.

Permanent Address:
Av. 16-A c/c 84, # 83-13, Sector “El Carmen”, Delicias, Maracaibo, ZULIA, 4001,
VENEZUELA.